UNIVERSITAT POLITÈCNICA DE VALÈNCIA

Doctoral Thesis

Dark matter searches towards the Sun with ANTARES and positioning studies for KM3NeT

Candidate:
Chiara Poirè

Supervisors:
Prof. Miguel Ardid
Dr. Vincent Bertin

July 2022

A Mamma e Papà.
And to all the girls and women
who do not have the same luck as me.

"In life one should never give in, surrender oneself to mediocrity, but rather move out of that grey area where everything is habit and passive resignation. One has to grow the courage to rebel."
Rita Levi Montalcini

Abstract

High energy Neutrinos are elusive particles: they are chargeless, have a very small cross section with ordinary matter and their mass is extremely small. Neutrinos are an important probe in the study of the origin of cosmic rays but also, following some models of physics Beyond the Standard Model, they can be produced from the decay of Standard Model particles produced by dark matter annihilation.

In the last century, many new approaches have been developed in astroparticle physics, trying to solve the unsolved puzzles of the Universe such as the origin of Cosmic Rays and the existence of Dark Matter. Among the many experiments, neutrino telescopes certainly stand out. Neutrinos telescopes, made of large volume of a transparent medium observed by optical sensors, can detect high energy neutrinos from galactic or extra-galactic sources, and they can also be used for the study of neutrino properties.

ANTARES and its successor KM3NeT are two neutrino telescopes located in the Mediterranean sea. ANTARES operations started in 2007 and it has taken data almost continuously until the beginning of 2022. KM3NeT, taking advantage from the experience of ANTARES, aims to be the most sensitive neutrino telescope in the next generation of detectors.

This thesis presents my contributions to both detectors. In particular, the technical part of the work has been developed in collaboration with KM3NeT. It is devoted to the the study of data from the compasses installed in the KM3NeT detection elements: from their calibration before deployment to the analysis of their data in the sea. These compasses allow a tracking of the movements of the detector elements in the sea. In collaboration with ANTARES a physics analysis related to the search of dark matter annihilation in the Sun has been developed analyzing thirteen years of data. New upper limits for neutrino and antineutrino fluxes from dark matter annihilation in the Sun have been obtained, and from these upper limits on the Dark Matter - Nucleon scattering cross section have been obtained. These results improve previous ANTARES results by a factor of 2 and are competitive with those obtained by other experiments.

Resumen

Los neutrinos de alta energía son partículas esquivas: no tienen carga, tienen una sección transversal de interacción muy pequeña con la materia ordinaria y su masa es extremadamente pequeña. Los neutrinos son una sonda importante en el estudio del origen de los rayos cósmicos, y también, siguiendo algunos modelos de la física más allá del modelo Stardard, pueden producirse a partir de la propagación de partículas del modelo estándar producidas por la aniquilación de la materia oscura.

En el último siglo, se han desarrollado muchos enfoques nuevos en la física de astropartículas, tratando de resolver los enigmas no resueltos del Universo, como el origen de los rayos cósmicos y la existencia de la materia oscura. Entre los diferentes experimentos destacan, sin duda, los telescopios de neutrinos. Los telescopios de neutrinos, consistentes en un gran volumen de un medio transparente monitorizado por sensores ópticos para detectar luz de Cherenkov, pueden detectar neutrinos de alta energía de fuentes galácticas o extragalácticas, y también pueden usarse para el estudio de las propiedades de los neutrinos.

ANTARES y su sucesor KM3NeT son dos telescopios de neutrinos ubicados en el mar Mediterráneo. El telescopio ANTARES empezó a estar operativo en 2007 y ha tomado datos de forma casi continua hasta principios de 2022. KM3NeT, aprovechando la experiencia de ANTARES, pretende ser el telescopio de neutrinos más sensible de la próxima generación de detectores.

Esta tesis presenta mis contribuciones en ambos detectores. En concreto, la parte técnica del trabajo se ha desarrollado en colaboración con KM3NeT. Está dedicado al estudio de los datos de los sensores de orientación instalados en los módulos de detección ópticos de KM3NeT: desde su calibración antes del despliegue en el mar hasta el análisis de sus datos in situ. Estos sensores permiten una monitorización de los movimientos de los elementos detectores en el mar. Por otro lado, en colaboración con ANTARES se ha desarrollado un análisis de física relacionado con la búsqueda de la aniquilación de la materia oscura en el Sol analizando trece años de datos. Se han obtenido nuevos límites superiores para los flujos de neutrinos y antineutrinos a partir de la aniquilación de materia oscura en el Sol, y a partir de estos, se han derivado límites superiores a la sección eficaz de dispersión de Materia Oscura - Nucleón. Estos resultados mejoran en un factor dos los resultados anteriores de ANTARES y son competitivos con respecto a otros experimentos.

Resum

Els neutrins d'alta energia són partícules esquives: no tenen càrrega, tenen una secció transversal d'interacció molt petita amb la matèria ordinària i la massa és extremadament petita. Els neutrins són una sonda important en l'estudi de l'origen dels raigs còsmics, i també, seguint alguns models de la física més enllà del Model Stardard, es poden produir a partir de la propagació de partícules del model estàndard produïdes per l'aniquilació de la matèria fosca.

A l'últim segle, s'han desenvolupat molts enfocaments nous a la física d'astropartícules, tractant de resoldre els enigmes no resolts de l'Univers, com l'origen dels raigs còsmics i l'existència de la matèria fosca. Entre els diferents experiments destaquen, sens dubte, els telescopis de neutrins. Els telescopis de neutrins, consistents en un gran volum d'un medi transparent monitoritzat per sensors òptics per detectar llum de Cherenkov, poden detectar neutrins d'alta energia de fonts galàctiques o extragalàctiques, i també es poden utilitzar per a l'estudi de les propietats dels neutrins.

ANTARES i el seu successor KM3NeT són dos telescopis de neutrins ubicats al mar Mediterrani. El telescopi ANTARES va començar a estar operatiu el 2007 i ha pres dades de forma gairebé contínua fins a principis del 2022. KM3NeT, aprofitant l'experiència d'ANTARES, pretén ser el telescopi de neutrins més sensible de la propera generació de detectors.

Aquesta tesi presenta les meves contribucions a tots dos detectors. Concretament, la part tècnica del treball s'ha desenvolupat en col·laboració amb KM3NeT. Està dedicat a l'estudi de les dades dels sensors d'orientació instal·lats als mòduls de detecció òptics de KM3NeT: des del calibratge abans del desplegament al mar fins a l'anàlisi de les seves dades in situ. Aquests sensors permeten una monitorització dels moviments dels elements detectors al mar. D'altra banda, en col·laboració amb ANTARES s'ha desenvolupat una anàlisi de física relacionada amb la recerca de l'aniquilació de la matèria fosca al Sol analitzant tretze anys de dades. S'han obtingut nous límits superiors per als fluxos de neutrins i antineutrins a partir de l'aniquilació de matèria fosca al Sol, i a partir d'aquests, s'han derivat límits superiors a la secció eficaç de dispersió de Materia Fosca - Nucleó. Aquests resultats milloren en un factor dos els resultats anteriors de ANTARES i són competitius respecte a altres experiments.

Contents

List of Figures

List of Tables

Introduction

There are still many open questions in the study of our Universe, and almost all branches of astrophysics must deal with them. Some of these require further connections with the study of particle physics, and thus fall into the realm of what is commonly referred to as *astroparticle physics*. In order to address these questions, this broader approach must be undertaken. From the particle physics perspective the properties of neutrinos constitute a major problem in the Standard Model of particles; similarly the origin of high energy neutrinos is still an unknown of astroparticle physics; the Standard Model of cosmology in its attempt to understand the evolution of the Universe requires the presence of forms of matter and energy that are not directly observable. These are only a few of these open questions, to which cosmology, astrophysics and astroparticle physics are trying to give an answer.

In the last century, the field of astroparticle physics has seen many new experiments come to life, using different detection techniques and new approaches to solve new questions coming up as more observation of our Universe arrived. The current scenario sees the full development of the multi-messenger approach, where different probes such as gamma-rays, neutrinos and gravitational waves are used as new tools that can be exploited to solve the puzzle of our Universe.

The quest for dark matter is the main subject of this thesis and represents one of the fundamental questions to be answered if we want to obtain a complete picture of the Cosmos. Dark matter, which some theoretical predictions interpret as weakly interactive massive particles, constitutes a significant part of the matter content of the Universe, being more than a factor of 5 more abundant than ordinary baryonic matter. When put together with the Dark Energy component, roughly 95% of the energy density of our Universe is currently unknown. Dark matter influences the structure the Universe gravitationally but it cannot be observed as ordinary matter. However, in the multi-messenger astroparticle physics scenario described above, probes for the existence of Dark Matter beyond the sole gravitational interaction can be used. Neutrinos constitute a very intriguing one. Some models, indeed, predict that the annihilation of dark matter particles into Standard Model particles can yield a measurable neutrino flux, after the decay chains of the latter. Therefore, neutrino detectors can play an important role for this purpose.

Neutrinos can be elusive. Thus, specific detectors have been built over time in order to study them. In particular, neutrino telescopes are large volume apparatus where neutrinos can be detected with an array of photo-sensors optimized for recording the Cherenkov light coming from the products of neutrino interactions. These detectors can be used to study fundamental neutrino properties, by observing the oscillations phenomena, and to detect high energy neutrinos from Galactic or extra-Galactic sources. In the same way as these objects can be used as target for astrophysical searches, they can also be candidates for Dark Matter detection. Among these, the Galactic centre, the Sun, and the centre of the Earth are the most studied ones.

The ANTARES detector (Astronomy with a Neutrino Telescope and Abyss environmental RESearch) was the largest neutrino telescope in the Northern Hemisphere and the first operating in sea water. Its operations started in 2007 and it has taken data almost continuously until the beginning of 2022. The successor of ANTARES, taking advantage of the return of experience coming from 15 years of ANTARES data taking, is KM3NeT. This research infrastructure is split over two different locations. In the Italian site of KM3NeT, 100 km far from Porto Palo di Capo Passero in Sicily a high energy neutrino telescope, ARCA, is being set-up. In the French site, not far from the location of the ANTARES telescope near Toulon in France, the ORCA neutrino detector is also being constructed.

This thesis presents my contributions to activities carried out by the the ANTARES and KM3NeT Collaborations. The manuscript is divided into three parts: the first is an introduction to the physics of neutrinos and to Cherenkov neutrino telescopes, in order to provide the reader with a broad view of the field, that will also be necessary in the later stages of the thesis to understand better how the analyses are performed. This first part comprises the first four chapters. Chapter I is an introduction to neutrinos as a new messenger for astroparticle physics, describing its interaction with matter and properties. Also, in order to better contextualise how neutrino telescopes operate, the production of high energies neutrinos from the interactions of cosmic rays is presented. Chapter II illustrates the method of neutrino detection using the Cherenkov radiation and consequently the properties of Cherenkov neutrino detectors, also giving a general overview of the currently active apparatuses. Chapter III and Chapter IV are dedicated respectively to the ANTARES and KM3NeT neutrino telescopes. In these chapters an overview of the specific characteristics of these two detectors are provided, with particular attention to the positioning and data acquisition system.

The second part is dedicated to my work in the KM3NeT Collaboration. This covers the more technical aspects of my work and it is mainly dedicated to the compasses installed in the KM3NeT detection elements. These compasses play an important role in the tracking of the positions and movements of the apparatus. Chapter V covers the details of the compass calibration procedure, the monitoring of compass data *in situ* and their usage in the reconstruction of the positions of the Detection Units. Even though this is mainly a technical subject, it required a significant amount of development for the data analysis on an almost entirely new subject.

The third and final part is dedicated to the physics analysis done using data from the ANTARES neutrino telescope. The goal of this part is to show how Dark Matter annihilation processes in the Sun can be investigated by means of a neutrino telescope, an instrument that had been built for a different goal. This part includes three different chapters. Chapter VI gives an introduction to the physics of dark matter: from dark matter experimental evidences, evidences on a cosmological and astrophysical scale, to its properties, to particle physics candidates and the ways to possibly detect them. Chapter VII is dedicated to the description of the technical tools used in the analysis, such as the ANTARES Monte Carlo simulations and the event reconstructions strategies. Finally in Chapter VIII the steps of the analysis are described. New limits for neutrinos and antineutrinos fluxes coming from dark matter annihilation in the Sun have been obtained and are presented at the end of the chapter, comparing the dark matter scattering cross sections, derived from these upper limits, to those produced by other experiments.

Part I

Introduction to the high energy neutrino world

A scientist in his laboratory is
not a mere technician: he is also
a child confronting natural
phenomena that impress him as
though they were fairy tales.

Maria Skłodowska-Curie

Chapter 1

High energy neutrinos in astroparticle physics

This chapter presents an overview on astroparticle physics, and its connection to the fundamental physics of neutrinos. The importance of neutrinos in many different astrophysical searches is underlined in this Chapter, and some of the basic knowledge required to understand all the following parts of this thesis are given here. This includes the astrophysical production of neutrinos, their possible sources, the interactions of neutrinos with matter that make neutrino observations possible and the oscillation processes that modify how neutrinos are actually observed with respect to their production.

1.1 Introduction

The existence of the neutrino was first postulated by Wolfgang Pauli in 1930 to explain how the observed problem of non-conservation of energy, momentum, and angular momentum in beta decays could be solved, by adding an invisible neutral particle. The first who introduced the word for this small neutral particle (*neutrino*, indeed, in Italian) was Enrico Fermi, who used it during a conference in Paris, then this word entered in the scientific vocabulary [128].

Neutrinos are neutral leptons, i.e. they have half-integer spin (fermions) and do not have electrical charge. As neutral leptons, they interact with matter only via the weak force, mediated by the $W^{\pm}$ and Z bosons. Neutrinos come in three different flavours, electron, muon and tau neutrinos, coupled to the respective charged leptons [218], [92]. A variety of neutrino sources exists in Nature: from the low energy neutrinos of the cosmic background radiation [131] to the high energy neutrinos possibly produced inside Active Galactic Nuclei [17].

Neutrinos are the lightest known massive particles, and in fact they were supposed to be mass-less [82]. Since neutrinos are electrically chargeless, they are not deflected by magnetic fields as they travel through the Universe, maintaining their trajectory even when passing through strong magnetic fields.

Given these characteristics, and since their interaction cross section with matter is, in most cases, practically negligible, how can these particles be used to do astronomy? A solution to this experimental problem was suggested by M. Markov, in the 1960s: a large volume of transparent medium can be instrumented to create an experiment that detects the secondary particles produced by neutrino interactions [170]. Such *neutrino telescope* will measure the Cherenkov light from the charged particles produced by the interaction of high energy neutrinos with the medium. The general characteristics of this kind of experiment as proposed in the 60s would then be:

- both the detector and the medium must have a large volume, to offer as many target nuclei as possible, on which neutrinos could interact;
- the medium is transparent to Cherenkov light;
- the detector is at a great depth, to reduce the background from various types of radiation in the atmosphere.

The main goal of these detectors is to discover the sources of Cosmic Rays, by means of observing point-like or diffuse high-energy neutrino fluxes in the sky.

To date, there are different operational experiments which take advantage of these features and the majority of them are located in the Northern Hemisphere, as ANTARES and KM3NeT in the Mediterranean sea, Baikal-GVD in the namesake lake, and an R&D project P-ONE in the Pacific Ocean. Instead only one, IceCube, is in the Southern Hemisphere. More details about these neutrino telescopes will be given in the next chapters.

1.2 Cosmic rays

One of the main open questions of the astroparticle physics is the origin and the nature of cosmic rays (CRs). Early measurements of this cosmic radiation where held by Victor Hess in 1912, when he measured the intensity of ambient radiation in balloon flights, showing that this radiation was increasing as he went higher in altitude and thus suggesting an extra-terrestrial (*cosmic*) origin [152].

The majority of high-energy particles in cosmic rays is made of protons (hydrogen nuclei); about 10% are helium nuclei (i.e. α particles), and 1% are neutrons or nuclei of heavier elements. Together, these account for 99% of the cosmic rays: electrons and photons make up the remaining 1%.

The primary CRs energy spectrum (Figure 1.2.1) follows almost precisely a power-law of form:

$$\frac{d\Phi}{dE} \propto E^{-\alpha}. \tag{1.2.1}$$

where the parameter α is the differential spectral index of the cosmic ray flux. From Figure 1.2.1, where a compilation of cosmic ray spectral measurement

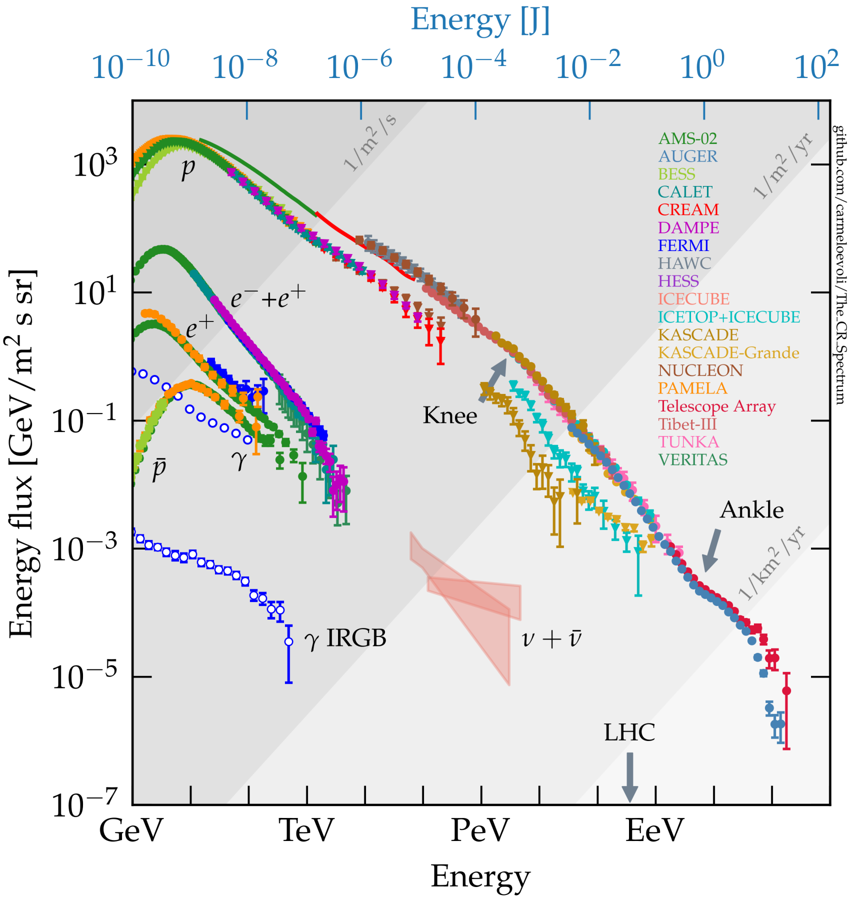

Figure 1.2.1: Energy flux of the different types of cosmic radiation as observed at Earth by several experiments. Figure taken from [123].

is reported, it is possible to distinguish three different energy ranges on the basis of the value of the observed spectral index:

- The first is characterized by $\alpha \sim 2.7$ for energies from 10^9 eV to about $3 \cdot 10^{15}$ eV. The origin of cosmic rays with these energies is generally linked to local production sites in our Galaxy, such as Supernovae Remnants [201], [138].

- The second interval includes energies between 10^{15} eV and 10^{19} eV, where the value of α is $\sim$ 3.1. Most of the particles produced at such high energy should have a Galactic origin. This energy intervals is comprised between two spectral breaks called the *knee*, where the spectrum first steepens and *ankle*, where it flattens [201], [138].

- At energies higher than E$\sim$ 10^{19} eV, the region above the *ankle*, the cosmic ray intensity becomes lower than 1 particle per km^2 per year, and the spectral index again assumes a value $\alpha \sim 2.7$. The particles produced with such high energy can only be accelerated by extremely energetic events such as those happening in the jets produced by Active Galactic Nuclei (AGN), Radio Galaxies or Gamma-Ray Bursts, outside our Galaxy.

The steepening of the spectrum that happens at the knee can be justified if the maximal energy at which Cosmic Rays can be accelerated in their source depends on the Cosmic Ray charge Ze. If this is the case, lighter elements can "escape" their acceleration region earlier than "heavier" nuclei, which can in turn then be accelerated to higher energies. This is the case in the Supernovae Remnant (SNR) scenario for Galactic Cosmic Ray acceleration [201].

For energies below 10^{14} eV, the primary CR flux is very high and it is possible to measure it directly, i.e. with a particle-by-particle identification, in balloons or satellites. At high energies ($>$ PeV), the particle flux is considerably reduced (about 10 particles $/m^2yr$), so direct measurements are not possible due to the limited size of the experimental apparatus. Thus, "indirect" measurements are necessary. In these experiments, the products of Cosmic Ray interactions in the atmosphere are measured to investigate the primary CR flux properties [138].

CRs with very high energies travel through the interstellar medium and can interact with other particles. The results of these interactions are mostly short-lived mesons, whose decay chains can produce neutrinos. Thus, high energy neutrinos at TeV energies and above from extra-terrestrial sources may help to study the sources and the acceleration mechanisms of very high energy cosmic rays.

1.2.1 Acceleration mechanism

A first model of cosmic ray acceleration was proposed by Enrico Fermi[129]. In Fermi's original theory, particles are accelerated via collisions through an uneven galactic magnetic field, in random motion in the interstellar medium. This perturbation of the field behaves like a magnetic mirror, running at speed $V = \beta \cdot c$. Following any reflection on that mirror, the particles acquire energy statistically. The percentage gain of energy ($\Delta E/E$) is proportional to β^2 and for this reason, the first version of Fermi's theory is known as

mechanism of Fermi I or *second order*. It has been shown that if the particles remain confined inside the acceleration region for a characteristic time τ_{esc}, the final energy spectrum follows a power-law [159].
The mechanism just described is, however, too inefficient to accelerate high energy particles since the β of the magnetic mirror can be rather low. A more efficient mechanism is known as *Fermi II* or *first order*, where particles are accelerated by flat-shock collisions and in this case the energy gain dependence on β is of the first order [201]. This acceleration mechanism will produce an energy spectrum at the source that can be described by a power-law with $\alpha \sim 2.1$.
Cosmic Rays propagating through the Galaxy can then exit it over a certain time scale τ_{ex}. According to the measurement of this exit time from the Galaxy [165], this would cause a steepening of the primary spectrum by a factor $\sim$0.6. Thus, the observed energy spectrum at Earth with α 2.7 is reproduced.

1.3 Neutrino astronomy

The study of the Universe has been limited for centuries to observations with optical telescopes. The spectrum of photons provides accurate information on the physical and chemical properties of the bodies that produce them. On the other hand, the central regions of many astronomical sources are dense and therefore are opaque to the photons. For example, some important information we have on the inner nature of the Sun can also come from indirect observations such as those obtained with neutrinos [79]. Neutrino astronomy, often conjugated with γ-ray astronomy in the multi-messenger approach, aims at understanding the CR acceleration mechanisms, with the main goal of discovering CR sources.
γ-rays are easier to detect, when compared to neutrinos, since they have a much larger cross section with ordinary matter, given their electromagnetic interactions. This however hinders the possibility of observing gamma-rays from opaque regions. Both neutrinos and γ-rays can be produced by CRs; however, γ-rays might come from both hadronic (π^0 decays produced by CRs interactions) or leptonic processes (electron CRs producing high-energy photons by inverse Compton effect or Bremsstrahlung radiation). On the other hand, neutrinos can be produced only via hadronic processes ($\pi^{\pm}$ decays from the same processes producing neutral pions described above).

1.3.1 Hadronic production mechanisms of high energy neutrinos

The experimental evidence of the existence of cosmic rays with energies up to $\sim 10^{20}$ eV and the observation of high-energy gamma rays shows us that astrophysics with neutrinos can be done [148]. This is strictly connected with the possibility that an hadronic emission can be observed. In this scenario, astrophysical neutrino production is given by the interaction of accelerated protons (or nuclei) with photons or matter fields in the proximity of astrophysical objects. In these interactions, many pions (and other mesons) can be produced:

$$p + \gamma(p) \rightarrow N_1\pi^{\pm} + N_2\pi^0 + X \tag{1.3.1}$$

$$p + P \rightarrow N_1\pi^{\pm} + N_2\pi^0 + X \tag{1.3.2}$$

where N_1 and N_2 are the numbers of produced pions, and X a generic hadronic state. P is a generic target nucleon. And then pions decay in the following way:

$$\pi^0 \rightarrow \gamma + \gamma \tag{1.3.3}$$

$$\pi^+ \rightarrow \mu^+ + \nu_\mu \tag{1.3.4}$$

$$\pi^- \rightarrow \mu^- + \bar{\nu_\mu} \tag{1.3.5}$$

The ratio between the number of charged pions and neutral pions depends on the type of the reaction that has generated them ($p+p$ or $p+\gamma$) and from the energy of the center of mass. The number of produced photons is of the same order of magnitude as the number of neutrinos. Thus the high-energy neutrino and high-energy photon fluxes are closely related. On average, each neutrino carries away 1/20th of the primary cosmic ray energy while each γ-ray photons will have ~1/10th of the CRs energy. Thus a PeV Cosmic Ray would produce signals in the 50-100 TeV energy range in neutrinos and gamma-rays respectively [201]. This constitutes the basic starting point of high-energy neutrino astrophysics.

1.4 Neutrino sources

Neutrinos can be found in our Universe at very different energies. Their spectra will also vary according to their origin. In Figure 1.4.1 the predicted neutrino flux as function of the energy for different neutrino sources is shown. Both Galactic and Extra-Galactic sources are accredited to be sources of high-energy neutrinos.
A large amount of neutrinos is also produced, on Earth, by CRs interacting in the high atmosphere and producing an atmospheric neutrino flux. While the former represent the target for neutrino astronomy, the latter constitute the main background for these searches, and in general for all searches of extra-terrestrial neutrinos in neutrino telescopes, as it will be explained later in this manuscript.

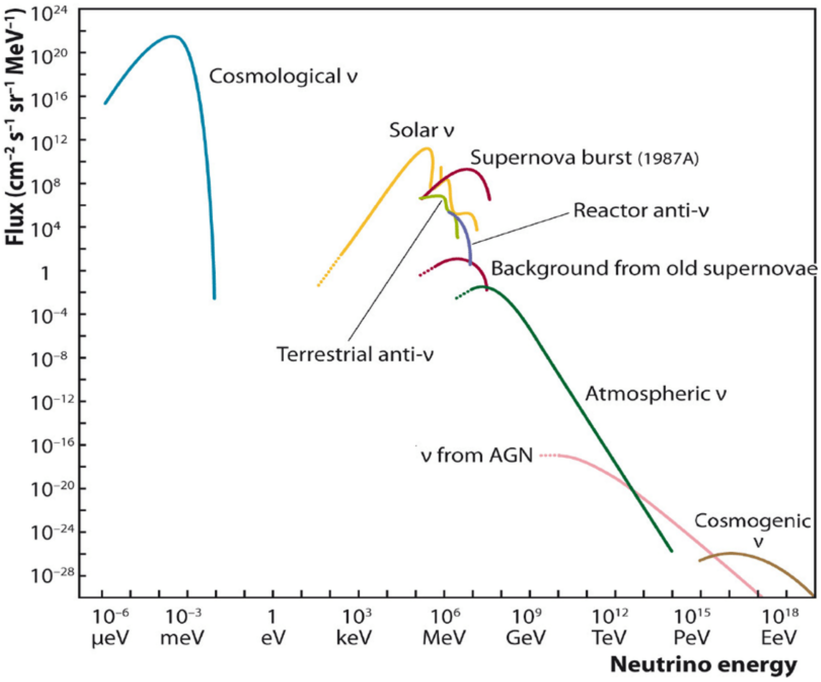

Figure 1.4.1: Example of the predicted neutrino fluxes that are expected from different neutrino sources as a function of energy. Adaptation by C. Spiering [199] of an original plot from [200]

1.4.1 Galactic sources

As pointed out in Section 1.3, Galactic sources and accelerators of CRs must also be the main source of neutrinos in our Galaxy. Indeed, we expect that Galactic CR sources should fill the CR spectrum up to the ankle region, and thus also high-energy (hundreds of TeV) neutrinos can come in turn. The presence of a neutrino emission from a Galactic source can be considered a "smoking gun" for CR acceleration, provided the hadronic mechanism previously explained in Section 1.3.1.

Supernova remnants

What remains after catastrophic end-of-stellar-life events, known as Supernova Remnants (SNRs), are the most suitable candidate for Cosmic Ray acceleration below the knee; thus, they also are the most suitable candidates for the production of an observable neutrino flux. Indeed, considering the total energy distributed into the Cosmic Rays in our Galaxy, a rate of a few SN explosions per century could provide the required energy to accelerated them and fill the Milky Way [138].

Explosions of massive stars produce shock fronts of expanding material that can accelerate charged particles to high energy via the Fermi II mechanism. The shock waves following the explosion of a supernova are generated by successive and repeated expansions and compression of matter. Charged particles are accelerated when scattering across the shock front, which travels at speed $v \sim 0.1\,\mathrm{c}$. This acceleration process can last a very long time, if magnetic fields are strong enough to keep charged particles contained in the acceleration area. In this recursive shock acceleration, charged particles can cross the shock-front multiple times until the density of the shock becomes too low to constitute a "wall" against which the particle can be efficiently rebounded. As a result, SNRs of few thousands years of age are most efficiency in accelerating 100 TeV Cosmic Rays, while the acceleration efficiency becomes lower as the SNR ages. The shock life limits the maximum energy that can be achieved by cosmic rays [177].
An example of such an object is the supernova remnant in Vela Jr. Neutrino emission from any SNRs has not been established yet.

Pulsar Wind Nebulae

Pulsar Wind Nebulae (PWNe) can also accelerate Cosmic Rays in our Galaxy. A pulsar is a rapidly rotating neutron star, deriving from the gravitational collapse of stellar matter during a supernova event, and surrounded by a nebula of relativistic particles and magnetic flux [83]. According to theoretical models, particles accelerated in pulsars by SNR can reach very high energies, up to $\sim 10^{18}\,\mathrm{eV}$ [85]. This is mainly due to the very intense magnetic fields that are expected in the proximity of the Pulsar. These strong magnetic fields can contain particles within the acceleration region allowing multiple acceleration processes. Given the presence of high energy particles, if these are protons or nuclei, a significant neutrino flux could be detected as emerging from energetic PWNe.
The most known PWN is the Crab Nebula even though its high-energy gamma-ray emission should be dominated by leptonic mechanisms rather than the hadronic ones [62].

1.4.2 Extra-Galactic sources

Galactic sources are too small and too weak to work as accelerators of Cosmic Rays at extremely high-energies. Thus, Extra-Galactic sources are invoked [61]. In Extra-Galactic environments, particle accelerators can reach larger sizes, thus allowing more iterations of the acceleration mechanisms. Also, these energetic environment can produce particle jets with highly relativistic boots that can enhance the maximal energy up to which particles are accelerated. Two examples of possible Extra-Galactic sources, among many others, are Active Galactic Nuclei and Gamma-Ray Bursts.

Active Galactic Nuclei

Active Galactic Nuclei (AGN) are large compact regions at the centre of many Galaxies that show a very bright core. The photon spectrum from the AGN shows a different spectral behaviour with respect to the thermal spectrum produced by the stars in the galaxy. For this reason it is supposed that the AGN emission is due to the accretion of matter by a supermassive black hole at the center of its host galaxy. Given their properties, AGN should be the most intense sources of high energy cosmic rays and thus likely neutrino sources at the highest energies [178].

Very often, AGNs show two relativistic jets that are emitted perpendicular to the accretion disk. These jets can be responsible for the acceleration of high energy cosmic rays up to energy of 10^{20} eV. AGNs whose jets point towards the observer (the Earth) are called Blazars [180].

Cosmic Ray acceleration can happen in AGN as a strong jet of matter is produced by the central black hole. This jet is typically relativistic and can either form shocks that will accelerate particles, or boost the energy of particles that have already been accelerated in the surroundings of the black hole by SNRs and other local accelerators [193].

Gamma Ray Bursts

Gamma Ray Bursts (GRB) are among the most energetic phenomena of the Universe. They are characterised by the emission of fast γ rays flash with duration between milliseconds and dozens of seconds. Most of the high-energy GRB emission that is observed at Earth is in the MeV range, especially in the first phases of the emission. This prompt phase is then accompanied by a long "afterglow" where the source can be very luminous from the x-ray, to the optical and radio wavelengths.

The astrophysical models that explain these explosions are various. Short (gamma-ray emission duration smaller than 2 s) GRBs are connected to the merger of two neutron stars as proved by the observation of a GRB and a Gravitational Wave signal in GW170817 [26]. Long (emission times larger than 2 s) can be connected to stellar explosion where matter is accreted and jets are formed.

The standard model for GRBs is the fireball model [173]. A jet of matter is produced in the GRB, expanding outside and creating shock-waves as it propagates through the local matter and radiation fields, thus causing CR acceleration and possibly neutrino production. As the jet expands through the surrounding matter and radiation fields, emission over the whole photon wavelengths is also produced.

The transient nature of these phenomena can offer the chance of greatly reducing the background in a neutrino detector by requiring a spatial and temporal coincidence with the flux of photons from the same object. The very narrow time window offers a unique opportunity for a neutrino detector to observe neutrinos associated with a single explosion [202], [91].

1.4.3 Atmospheric neutrinos

Cosmic rays that reach the Earth interact with the layers of the atmosphere at a height between 10 and 20 km. These interactions produce pions and kaons which in turn decay into neutrinos. The decay process is described in the following scheme [115]:

$$\pi^+ \rightarrow \nu_\mu + \mu^+ \tag{1.4.1}$$
$$\pi^- \rightarrow \bar{\nu_\mu} + \mu^- \tag{1.4.2}$$

Kaons (K^+, K^-) can decay similarly.
The produced muons can then decay in the following way:

$$\mu^+ \rightarrow e^+ + \bar{\nu_\mu} + \nu_e \tag{1.4.3}$$
$$\mu^- \rightarrow e^- + \nu_\mu + \bar{\nu_e} \tag{1.4.4}$$

These muons can also propagate through the atmosphere, and underground or underwater, and constitute the majority of events detected in a very large volume neutrino telescope.
The resulting atmospheric neutrino flux out of these decay chains is the convolution of the primary cosmic ray flux at the top of the atmosphere and the neutrino yield per primary and secondary particle. This yield is affected by several factors, mostly related to the efficiency in producing the mother particles of neutrinos, i.e. hadrons decaying into leptons [138]. Similarly, the uncertainties on the primary cosmic ray flux intensity and composition affect the resulting atmospheric neutrino flux. More details will be provided in Section 2.3.1.

1.5 Neutrino propagation

High-energy neutrinos produced by astrophysical cosmic ray sources can exit their production site and move towards us. Once out of their production site, neutrinos will propagate in vacuum along the same direction as they were produced. Finally, they might reach Earth - even propagate through it - without any further interaction. During their journey, in vacuum, through the Earth or inside their sources, neutrinos will be affected by oscillation phenomena, and even though with very low probability, by their Neutral Current (NC) and Charged Current (CC) Weak Interactions.
Most importantly, these properties will be fundamental to understand the possibility of even detecting them, and how they will show up in the detector.

1.5.1 High Energy Neutrino interactions with matter

The interaction of leptons with matter is described by the two terms in the Lagrangian of weak interactions in the Standard Model [141]. These two terms describe the interaction of neutrinos, the *Charged Current* (CC) term and the *Neutral Current* (NC) term. The two contributions can be written:

- Interaction term via Charged Current [82]:

  $$L_{CC} = \frac{g}{2\sqrt{2}} \sum_{f=1}^{n} [\bar{\nu}_f \gamma^{\mu}(1-\gamma_5) l_f W_{\mu}^{+} + \bar{l}_f \gamma^{\mu}(1-\gamma_5)\nu_f W_{\mu}^{-}] \tag{1.5.1}$$

  where g is one of the SM parameters and f is the leptonic family. γ_μ are the Dirac matrices and γ^5 is the chirality operator. This is mediated by the W bosons and has a charged lepton coming out of the interaction vertex.

- Interaction term with Neutral Current [82]:

  $$L_{NC} = \frac{e}{4\cos\theta_W \sin\theta_W} \sum_{f=1}^{n} \bar{\nu}_f \gamma_\mu (1-\gamma_5)\nu_f Z^{\mu} \tag{1.5.2}$$

  where θ_W is the weak mixing angle or Weinberg angle, γ_μ and $\gamma 5$ as defined before.

These two terms can be involved in the interaction of neutrinos with electrons or with nucleons.

Neutrino interaction with a nucleus

Neutrinos can elastically scatter on nucleons releasing some of them from the target. In the case of CC interactions this process is called quasi-elastic scattering, while for NC interactions it is called elastic scattering (Figure 1.5.1). These interaction can be resumed as [141]:

$$CC : \nu_f(p) + N(q) \rightarrow l_f^-(k_1) + X \tag{1.5.3}$$

$$NC : \nu_f(p) + N(q) \rightarrow \nu_f(k_1) + X \tag{1.5.4}$$

where N is the target and X is the hadronic final state of the interaction.
In addition neutrinos can also excite the nucleon into a resonant state. The resulting baryon resonance (Δ; N) then decays into a variety of possible final meson states [132]. This type of interaction can be the result of neutrino interactions with energy up to 20 GeV [132]. At higher energy, the Deep Inelastic Scattering process become more relevant. In this case the neutrino can interact with the individual quarks of the nucleon. This scattering manifests itself in the creation of a hadronic shower [132], [92].

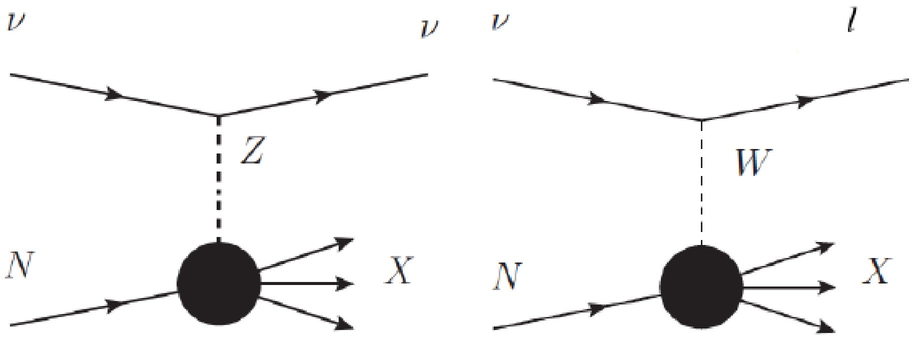

Figure 1.5.1: NC - CC interactions with nuclei.

Neutrino - electron interaction

Another possible interaction of neutrinos and antineutrinos in matter is with electrons. In this case it is possible to consider two different type of scattering: the elastic scattering and the quasi-elastic scattering.
The first case can involve all flavor (anti-)neutrinos and it does not have a threshold, since the initial state is equal to the final. The only effect of such a scattering is the redistribution of the total energy and the momentum between the interacting particles. The process can be written as:

$$\nu_f + e^- \to \nu_f + e^- \tag{1.5.5}$$
$$\bar{\nu}_f + e^- \to \bar{\nu}_f + e^- \tag{1.5.6}$$

If the neutrino flavor correspond to the electron, both charged currents and neutral currents contribute. Instead, if the flavor is μ or τ, only the neutral current contribute to the process [92]. Considering a generic process 1.5.6, it can be shown that the cross section is given by [141]:

$$\sigma \propto G_F^2 s \text{ with } G_F^2 = 5.297 \cdot 10^{-44} \frac{cm^2}{MeV^2} \tag{1.5.7}$$

Where G_F is the Fermi's costant and $s = (p_{\nu_i} + p_{e_i})^2 = (p_{\nu_f} + p_{e_f})^2$ is one of the Mandelstam variables and represents the square of the energy of the centre of mass.
In the quasi-elastic scattering, muon neutrinos, with an energy higher than the muon production energy threshold, can interact with electrons through charged currents: the so called *inverse muon decay* [169]. The process can be written as:

$$\nu_\mu + e^- \to \nu_e + \mu^- \tag{1.5.8}$$

1.5.2 Neutrino oscillation

As mentioned above, neutrinos can oscillate during their propagation both in matter and in vacuum, so that the flavour state (e, μ, τ) in which they can be detected is different from the flavour state in which they were produced at their source. This change is due to the fact that flavour and mass eigenstates do not coincide. The first who supposed and proposed the phenomenon of neutrino oscillation was Pontecorvo, in analogy with $K^0 - \bar{K^0}$ oscillations [184]. The discovery of neutrino oscillation [81] is the most sensitive probe for the existence of non-zero neutrino masses.

The oscillation probability changes significantly if neutrinos travel in matter instead of vacuum; this is due to the fact that ordinary matter in which neutrinos can travel contains electrons, but not muons or tau leptons [214], [141]. The presence of electrons modifies the propagation Hamiltonian via an interaction potential which changes the oscillation patterns.

The time evolution of the flavour state of a neutrino with flavour f, created in a charged-current weak interaction process from a charged lepton l_f, can be written as:

$$|\nu_f\rangle = \sum_{k=1}^{3} U^*_{f,k} e^{iE_k t} |\nu_k\rangle \tag{1.5.9}$$

where $f = e, \mu, \tau$ and $k = 1, 2, 3$.

Using the unitarity relation properties the Equation 1.5.9 can be written as:

$$|\nu_f\rangle = \sum_{k=1}^{3} U^*_{f,k} e^{iE_k t} |\nu_k\rangle = \sum_{k=1}^{3} \sum_{f'=e,\mu,\tau} U^*_{f,k} U_{k,f'} e^{iE_k t} |\nu_{f'}\rangle \tag{1.5.10}$$

The *mixing* is described by the Pontecorvo - Maki - Nakagawa- Sakata (PMNS) matrix [184] [168], through which the basis change is realized. The matrix PMNS can be parametrized in the following way:

$$U = \begin{pmatrix} 1 & 0 & 0 \\ 0 & c_{23} & s_{23} \\ 0 & -s_{23} & c_{23} \end{pmatrix} \cdot \begin{pmatrix} c_{13} & 0 & s_{13}e^{-i\delta} \\ 0 & 1 & 0 \\ -s_{13}e^{-i\delta} & 0 & c_{13} \end{pmatrix} \cdot \begin{pmatrix} c_{12} & s_{12} & 0 \\ -s_{12} & c_{12} & 0 \\ 0 & 0 & 1 \end{pmatrix} \cdot$$
$$\cdot \begin{pmatrix} e^{i\phi_1/2} & 0 & 0 \\ 0 & e^{i\phi_2/2} & 0 \\ 0 & 0 & 1 \end{pmatrix} \tag{1.5.11}$$

where $s_{12} = \sin\theta_{12}$, $c_{23} = \cos\theta_{23}$ and so on. θ_{12}, θ_{23} and θ_{13} are mixing angles, while δ and $\phi_{1,2}$ are the phases respectively of Dirac and of Majorana who interfere in the CP violation [135].

The three neutrino states that interact with the charged leptons in weak interactions are each a different superposition of the three neutrino states of

definite mass. Neutrinos are created in weak processes in their flavour eigenstates. As a neutrino propagates through space, the quantum mechanical phases of the three mass states advance at slightly different rates due to the slight differences in the neutrino masses. This results in a changing mixture of mass states as the neutrino travels, but a different mixture of mass states corresponds to a different mixture of flavour states.
The oscillation probability is given by:

$$P(\nu_f \to \nu_{f'}) \equiv |\left\langle \nu_f | \nu_{f'} \right\rangle|^2 = \sum_{i=1}^{3} |U^*_{f,i} U_{i,f'} e^{-i\frac{m_i^2 L}{2E}}|^2 \tag{1.5.12}$$

The first experiment that detected the effects of neutrino oscillation was Ray Davis's Homestake experiment in the late 1960s [80], in which he observed a deficit in the flux of solar neutrinos with respect to the prediction of the Standard Solar Model, using a chlorine-based detector. The Sudbury Neutrino Observatory (SNO) measured all-flavour neutrino interactions and thus the all-flavour neutrino flux from the Sun in 2001 [185]. This allowed to establish the correctness of the neutrino flux estimations and the identifications of neutrino oscillations as the source of this deficit. The year after, the KamLAND experiment measured the oscillation of neutrinos from reactors and unambiguously identified the phenomenon of the electron neutrino oscillations to explain the solar neutrino problem [119]. It is worth mentioning that neutrino oscillations had already been observed in the atmospheric neutrino flux by the Super-Kamiokande experiment in 1998 [134].

Chapter 2

Neutrino telescopes

In this chapter the most important characteristics and properties of neutrino telescopes are described, with particular attention to those underwater. In these telescopes, where a large volume of a trasparent medium is instrumented with a three dimensional matrix of photo-sensors placed at great depths, Cherenkov radiation is detected. Once this is explained, an overview of the main neutrino telescopes currently operating in the world is presented.

2.1 Neutrino detection principle

The neutrino detection principle is based on the measurements of optical and ultra-violet photons produced by the Cherenkov radiation (Section 2.2) by secondary particles produced by the interaction of high energy neutrinos with matter. The detector structure is based on a large matrix made of light sensors, built inside a transparent medium at great depths. The medium could be ice or water. The three main characteristics of these telescope can be resumed as:

- large volume, which offers a large volume of free target nucleons for neutrino interactions;
- great depth, which provides shielding against secondary particles produced by CRs;
- transparent medium, which allows the propagation of Cherenkov photons emitted by relativistic particles produced by neutrino interaction.

2.2 Cherenkov radiation

Neutrino telescopes can detect the light emitted by the Cherenkov radiation of the charged particles produced by the interaction of the neutrinos with the medium.

In particular, the Cherenkov radiation is emitted when charged particles travel through a dielectric medium with a speed v that is larger than the speed of light in this medium, so when:

$$v > \frac{c}{n} \tag{2.2.1}$$

where c is the speed of light in vacuum and n is the refractive index of the medium.

The radiation produced by depolarisation of molecules in the medium is emitted in the form of a light cone (Figure 2.2.1). The opening angle of the cone θ_c is given by [218],[158]:

$$\cos\theta_c = \frac{c}{nv} = \frac{1}{n\beta} \tag{2.2.2}$$

If we consider the case where the medium used is water, the refractive index is $n \sim 1.33$. Furthermore for ultra - relativistic particle $v/c = \beta \sim 1$. Therefore, the emission angle of Cherenkov photons in water with respect to the original direction of the particle is $\theta_C \sim 41°$.

The number of Cherenkov photons N emitted per unit wavelength interval $d\lambda$ and unit travelled distance dx by a charged particle of charge ze is given by [218]:

$$\frac{d^2N}{dxd\lambda} = \frac{2\pi\alpha z^2}{\lambda^2} \cdot \left(1 - \frac{1}{n^2\beta^2}\right) \tag{2.2.3}$$

The wavelengths of Cherenkov emission that propagate in water are in the range $300 - 600\,nm$, so in the visible and UV region. It is possible to compute that the number of Cherenkov photons emitted is $\sim 3.5 \cdot 10^4\,m^{-1}$.

2.3 Background

Although neutrino telescopes are positioned at large depths in order to limit the particle backgrounds from Cosmic Rays interacting in the atmosphere, this is not null. The main sources of the physical background in neutrino telescopes are the atmospheric neutrinos and the secondary atmospheric muons, which are produced by the primary cosmic ray interaction with the atmosphere. In addition to this physical background, an optical background is present in underwater neutrino telescopes, given for example by the presence of living organisms that can emit light, or Cherenkov light produced in ^{40}K decays, present in the dissolved salts.

2.3.1 Atmospheric muons and neutrinos

When cosmic rays reach the upper atmosphere, they interact with the air and produce *secondary* or *atmospheric* cosmic rays which include hadrons

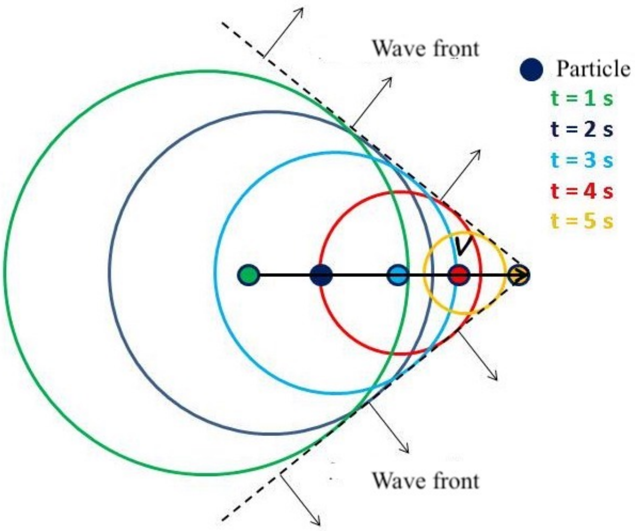

Figure 2.2.1: Scheme of the Cherenkov effect.

and their decay products. The energy spectrum of the secondary cosmic rays ranges from few GeV up to 100 TeV [137], [138]. The principal channels which produce atmospheric muons or neutrinos are [201]:

$$p + X \rightarrow \pi^\pm (K^\pm) + Y \tag{2.3.1}$$

$$\pi^\pm \rightarrow \mu^\pm + \overset{(-)}{\nu}_\mu \tag{2.3.2}$$

$$\mu^\pm \rightarrow e^\pm + \overset{(-)}{\nu}_e + \overset{(-)}{\nu}_\mu \tag{2.3.3}$$

The production mechanisms of atmospheric muons and neutrinos are strongly correlated. However, due to the different interaction and decay kinematics, the energy spectra of muons and muon neutrinos are different [201].
The atmospheric neutrino flux from pion and K decay is dominated by ν_μ. This flux is indicated as *conventional* atmospheric neutrino flux which in the energy range from 1 TeV to 100 TeV has the form:

$$\frac{d\Phi_\nu}{dE}(E) \propto E^{-\alpha_\nu} \tag{2.3.4}$$

with $\alpha_\nu \simeq 3.7$ [201] which asymptotically becomes $\alpha+1$, being α the primary spectral index. The atmospheric neutrino flux as a function of the energy for muon and electron neutrinos as measured by different experiments as predicted by the theory is reported in Figure 2.3.1.
Above 100 TeV another reaction mechanism plays a role in the production of muons and neutrinos: the semi-leptonic decays of charmed mesons like $D^\pm$,

D°. Since these particles have a very short lifetime, of the order of 10^{-12} s, they do not lose too much energy before decaying, nor they re-interact, so the muons produced in the decay process may have very large energies. These muons are accompanied by very energetic atmospheric neutrinos, originating the so-called *prompt* neutrino flux, with an energy dependence similar to the primaries CRs ($\Phi_{prompt} \sim E^{-\alpha}$ with $\alpha \sim$2.7) [201], [138].

The atmospheric muon flux at depths up to 12 km of water equivalent is still relevant. This represents the largest physical background in neutrino telescopes, along with the optical noise that could be present in sea-water due to bio-luminescence and ^{40}K decays (see Section 2.3.2). Therefore, in order to minimise this atmospheric muon background, a neutrino telescope must be located at large depths, 2000 m below surface or deeper. The atmospheric muon flux at these depths is reduced by several orders of magnitude [101]. Given the fact that the background coming from CR interactions in the atmosphere is almost isotropic at the surface of the Earth, the atmospheric muon background can be further reduced by selecting up-going events. Indeed, up-going atmospheric muons would be absorbed since they cannot traverse the Earth, while neutrinos could be able to propagate through the whole Earth almost unaffected. This represents the most efficient way to remove this background in the search for extra-terrestrial (and atmospheric) neutrinos. If, on the other hand, the goal is to look for a signal with neutrino events coming from above, no simple selection would eliminate atmospheric muons. This challenge is usually undertaken by means of sophisticated strategies at analysis level, such as requesting starting events.

2.3.2 Optical background

Even if the physics background could be removed, underwater neutrino telescopes that are positioned both in deep lakes and sea water will suffer from enviromental optical noise. In sea water there are two main sources of optical background:

- the decays of radioactive elements, such as ^{40}K;
- bioluminescence.

^{40}K can decay as:

$$^{40}K \rightarrow ^{40}Ca + e^{-} + \bar{\nu}_e \tag{2.3.5}$$

$$^{40}K + e^{-} \rightarrow ^{40}Ar + \nu_e + \gamma \tag{2.3.6}$$

In the first channel, the decay kinematics allows for electrons that are often above the Cherenkov threshold. Hence, if the ^{40}K decays close to a photo multiplier tube (PMT), some photons might be detected. In the second reaction, γ has an energy of 1.46 MeV and can induce electrons above the

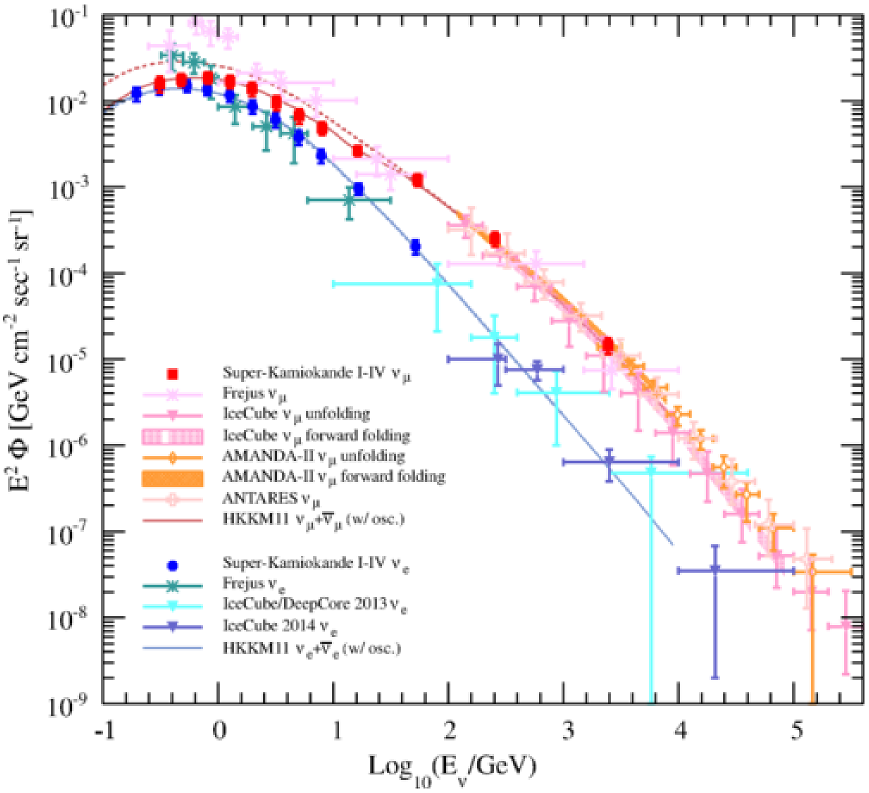

Figure 2.3.1: Measured atmospheric electron and muon neutrino flux by several experiments: Frejus [16], Super-K [191], AMANDA [22], IceCube [25], [23] and ANTARES [31]. The figures includes also shows the HKKM11 flux model predictions for the conventional atmospheric neutrino fluxes. Figure taken from [191].

Cherenkov threshold via Compton scattering. This background is proportional to the salinity of water, which is almost constant in all the Mediterranean Sea [65], [70], . The corresponding signal rates on the photo-sensors from ^{40}K decays will depend on the size and the efficiency of the PMT; for example, for the ANTARES neutrino telescope the size of a single PMT is 10″ and the rate is around 40 kHz.

In addition, in sea water there are also photons produced by living organisms, the so-called *bioluminescence*. Two sources are present in deep sea: steady glowing bacteria and flashes produced by marine animals. Seasonal effects in bio-luminescence are also present and they reach their maximal intensity during spring where, for 10″ PMTs ∼ MHz, single rates on PMTs can be detected in the form of bursts. The time evolution of the observed rates on PMTs in the ANTARES site is presented in Figure 2.3.2.

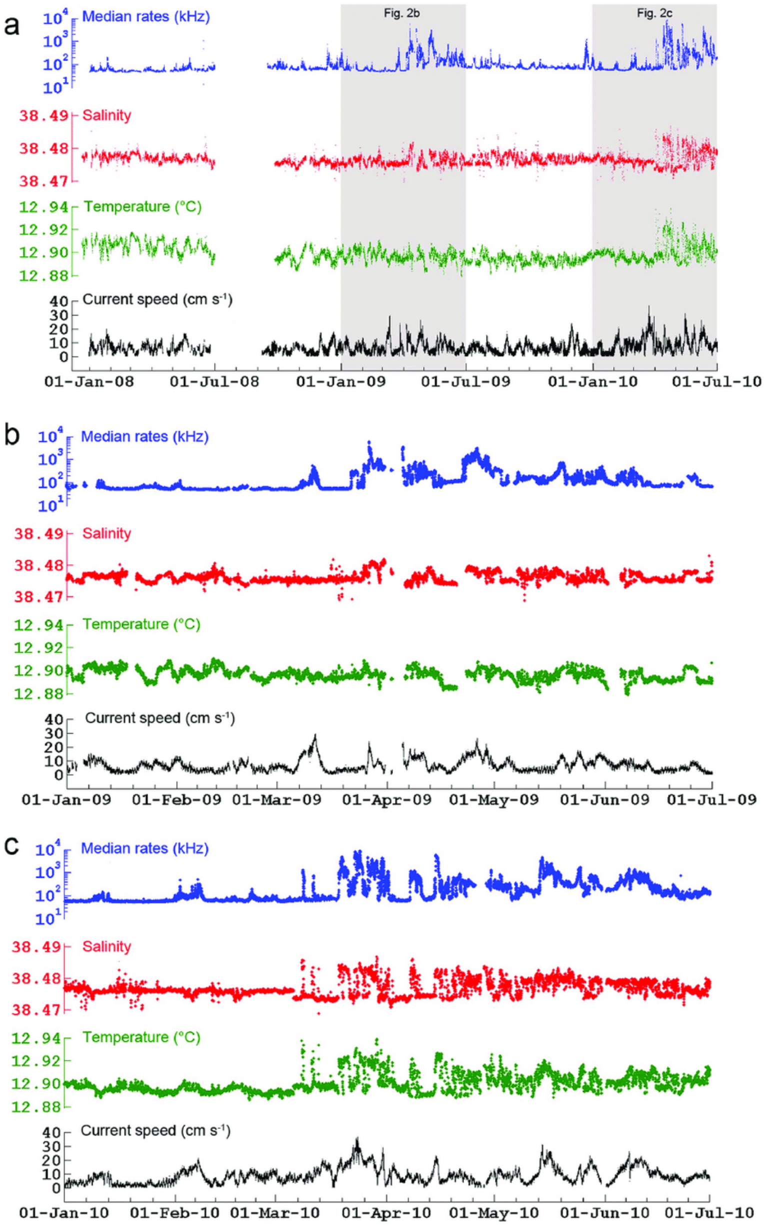

Figure 2.3.2: Time series measured at the ANTARES IL07 mooring line. All three figures shows median PMTs counting rates (log scale), salinity, potential temperature and current speed. The figure at the top (a) for the period from December 2007 to June 2010; the figure in the middle (b) for the period from January to June 2009; the figure at the bottom (c) for the period from January to June 2010. Figure taken from [203].

2.4 Number of optical sensors in a neutrino telescope

Neutrino telescopes must cover a large instrumented volume, of the order of the kilometre cube. This large size is necessary to detect high energy cosmic neutrinos which have a small interaction cross section and a very low flux. The number of photo-sensors to be put in water will be estimated here, in order to give the reader an idea of the quantities at play.

In order to perform this kind of evaluations, it is necessary to take into account the dimensions of the PMT, its detection area (A_{pmt}) and its efficiency (ϵ_{pmt}). The latter can be affected, other than the typical quantum effects, also by the material used on the glass sphere hosting the PMT, the presence of a mu-metal cage to magnetic shielding, the optical glue used to make the PMT adhere to its glass sphere and so on.

Then, we can define the quantity λ_{abs} as the ice or water absorption length; this will be better explained in the next section, but it roughly corresponds to the distance at which photons can be properly detected. The volume inside which a PMT can observe light is approximated by the volume of a cylinder $V_{pmt} = A_{pmt} \cdot \lambda_{abs}$. This simplification comes from the assumption that light travels on a straight line towards a PMT which is omnidirectionally sensitive. If we consider PMTs with $10''$ diameter and $\lambda_{abs} = 50\,m$ in the wavelength interval where the PMT quantum efficiency is not null, the volume $V_{pmt} \sim 2.5\,m^3$, assuming that only a photon propagating inside the effective PMT volume can induce a photoelectron (p.e.).

If N_{pmt} is the number of optical sensors inside the instrumented volume, the ratio R between the effective PMT volume of N_{pmt} and the instrumented volume (which it is assumed $1\,\mathrm{km}^3$) is [105]:

$$R = \frac{V_{pmt} \cdot N_{pmt}}{10^9 m^3} = 2.5 \cdot 10^{-9} N_{pmt}. \tag{2.4.1}$$

N_{pmt} is the unknown number to be determined.

In the case of a km-long muon track, the number of Cherenkov photons emitted is $N_C \simeq 3.5 \cdot 10^7$ [201]. Only a small fraction falling inside the effective volume of one PMT can be converted with efficiency ϵ_{pmt} into photoelectrons. If we assume $\epsilon_{pmt} \sim 0.2$, the total number of p.e. produced by the muon track will be

$$N_{p.e.} = N_C \cdot R \cdot \epsilon_{pmt} \simeq (3.5 \cdot 10^7) \cdot (2.5 \cdot 10^{-9} N_{pmt}) \cdot \epsilon_{pmt} = 1.8 \cdot 10^{-2} N_{pmt}. \tag{2.4.2}$$

Requiring that $N_{p.e.} \simeq 100$ are needed for the proper detection of the muon track, it is possible to obtain:

$$N_{pmt} \simeq 100/1.8 \cdot 10^{-2} \simeq 5000. \tag{2.4.3}$$

The IceCube collaboration uses 5160 PMTs, while ANTARES 885 PMTs even though in a much smaller volume than IceCube thus guaranteeing a good neutrino detection efficiency. The KM3NeT collaboration uses PMTs with 3″ of diameter and 31 PMTs inside each Digital Optical Module (DOM) or a total of more than 60-120 thousands PMTs according to the detector design described in Chapter 4.

2.5 Water and ice properties

As described before, neutrino telescopes must be built inside a transparent medium in order to measure the Cherenkov radiation. The options that could provide a large volume of transparent media are ice or water. In these media, the propagation of light is affected by two different effects: absorption and scattering of the Cherenkov photons.

Absorption reduces the total amount of Cherenkov light arriving at PMTs. Scattering, instead, changes the direction of the Cherenkov photons and consequently delays their arrival time on the PMTs; this has direct consequences in the measurement of the track direction and the determination of the direction of the incoming neutrino.

For the case of ice, in particular deep polar ice, the maximum value of the *absorption length* is $\lambda_{abs} \sim 100\,\mathrm{m}$ in the blue-UV range. On the contrary for clear sea waters the absorption length is $\lambda_{abs} \sim 70\,\mathrm{m}$. Water is thus less transparent than ice [201].

On the other hand, the effective scattering length for ice is smaller than water. This causes a greater degradation of the angular resolution of muons induced by neutrinos detected in ice compared to water.

The optical properties of the ice at South Pole change with depth; in the Antarctic ice it is possible to find trapped impurities, as well as the presence of air bubbles, which represent scattering targets for photons and thus contribute in reducing the effective scattering length of light in ice. The quality of the ice depends on atmospheric events and events on Earth, such as volcanic eruptions, during the various millennia. Ice is almost background-free from radioactivity.

Also the optical properties of water depend on many factors as the environmental parameters such as water temperature and salinity [45]. Water absorption and scattering depend also on the density and the sizes of the floating particulate, which affects the telescope response also in terms of detector aging. In addition, due to bio-fouling (a microscopic film of biological material) and sediments sticking on the optical modules, efficiency in photon detection can be reduced for long-term operations [66]. The location of the neutrino telescope in water should be far from continental shelf breaks and river estuaries, which can induce turbulent currents and spoil the purity of water, but also close to scientific and logistic infrastructures on shore.

2.6 Operating neutrino telescopes

The first project of a neutrino telescope started in the early 1970 and it was a collaboration between Russia and the USA [201], but after some political events this cooperation effort broke down and the two states started two different projects: DUMAND [1], [96] for the USA (cancelled in 1995) and BAIKAL for Russia.

Nowadays there are four neutrino telescope which are collecting data: one in the Southern hemisphere, IceCube, and three in the Northern hemisphere, ANTARES, GVD-Baikal and KM3NeT. There is also a new project, called P-ONE, but it is at the R&D stage [188].

Baikal-GVD

The Baikal Gigaton Volume Detector (Baikal-GVD) is located in the homonyms lake in southern Siberia, Russia. A neutrino detector is operative there since 1993 [76], [2].

Lake Baikal is the deepest lake in the world, reaching a depth of more than 1600 m. The ice which forms in winter on the surface of the lake can be used for assembly and deployment of instruments, instead of using ships and underwater remotely operated vehicles.

The disadvantage of lake water is that the scattering length is much shorter than in seawater, with a consequent very poor determination of the neutrino direction.

Over the years this experiment has increased its detection volume. To date the experiment includes a total of 2304 PMTs at a maximal depth of 1366 m. The detector elements are arranged along vertical strings, each of which is anchored to the bottom of the lake and kept taut by a bunch of buoys at the top. Each string holds 36 optical modules. The optical module (OM) comprises a 10-inch high-quantum-efficiency PMT which is oriented downwards. The OMs are arranged with 15 m vertical spacing, for a total active string length of 525 m, starting 90 m above the lake-bed [86]. A scheme of the Baikal-GVD is reported in Figure 2.6.1.

IceCube

IceCube is the evolution of the AMANDA (Antarctic Muon and Neutrino Detector Array) detector in South Pole ice [15][3]. The first AMANDA string was deployed in 1993 and the first data used for physics analysis were taken between 1997 and 1999 [151].

The IceCube instrumented detector volume is a cubic kilometre of highly transparent Antarctic ice and it was built between 2005 and 2010. IceCube consists of an array of 5,160 Digital Optical Modules (DOMs) deployed on 86 strings at a depth of 1.5–2.5 km below the surface just above the bedrock in

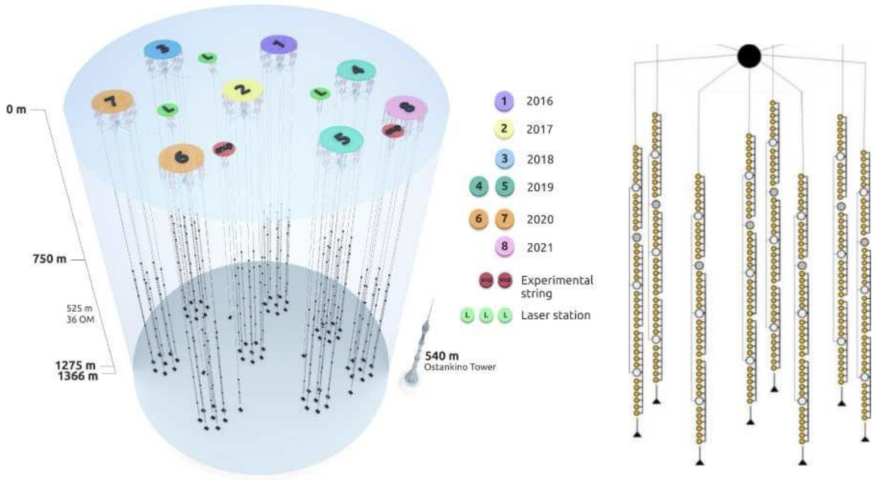

Figure 2.6.1: Left: Schematic view of the Baikal-GVD detector with the yearly progression of the detector deployment is shown in the legend. Right: The Baikal-GVD cluster layout (vertical scale compressed) [86].

the clear, deep ice. Strings are arranged at the vertices of equilateral triangles that have sides of 125 m. The DOMs are spherical, pressure resistant glass housings, each containing a 25 cm diameter photomultiplier tube (PMT) plus electronics for waveform digitization. DOMs are vertically spaced by 17 m from each other along each string. High quantum efficiency PMTs are used in a denser sub-array located in the centre of the detector (Figure 2.6.2). This sub-array, called DeepCore, enhances the sensitivity to low energy neutrinos [15]. Finally, a surface CR detector, called IceTop, completes the IceCube Observatory [3], [15]. Data acquisition with the complete configuration started in May 2011.
In the search for cosmic neutrinos the trigger consists of at least 8 DOMs recording a signal within a 5 μs time window. Most of the events selected with this trigger are atmospheric muons (rate of ~ 2.2 kHz) entering the detector from above. Only about one in 10^5 recorded events can be a candidate signal neutrino among the atmospheric muon background. In 2014 IceCube has seen the first detection of cosmic neutrinos [18].

ANTARES

The ANTARES detector [35] was the largest neutrino observatory in the Northern Hemisphere, taking advantage of a privileged view of the most interesting areas of the sky, like the Galactic Centre, where many neutrino source candidates are expected.
The ANTARES detector was completed in 2008, after several years of site

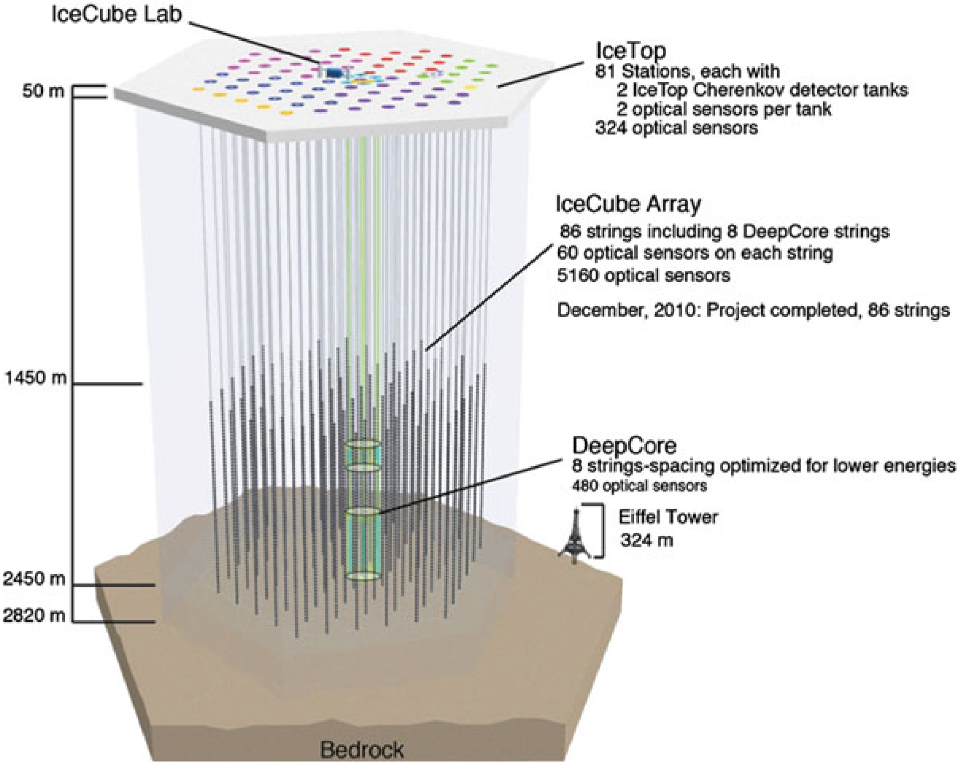

Figure 2.6.2: Side view of the IceCube detector, consisting of 86 buried InIce strings. The IceTop surface array and the DeepCore are also shown. Credit: IceCube/NSF.

exploration and detector R&D. The detector is located at a depth of 2475 m, in the Mediterranean Sea, 40 km from the French town of Toulon.
The ANTARES detector is being dismantled at the time of the writing of this manuscript, in Spring 2022, after 15 years of operation. More details about ANTARES will be given in Chapter 3.

KM3NeT

KM3NeT, once its construction phases have been completed, will be a future deep-sea research infrastructure hosting a neutrino telescope with a volume of several cubic kilometers in the Mediterranean Sea.
This telescope is composed of 2 complementary detectors deployed in two locations: one is close to the ANTARES site and it is called ORCA and the second one is close to Sicilian coast and it is called ARCA. At the time of the writing of this manuscript, KM3NeT is under construction and there are 10 lines installed for ORCA and 9 for ARCA. More details about KM3NeT will be given in Chapter 4.

Chapter 3

ANTARES

In this chapter the most important characteristics of the ANTARES Telescope are described, focusing on the detector structure and the data acquisition system. Also, the studies on the water properties around the detector site are presented.

3.1 The ANTARES neutrino telescope

ANTARES, which stands for Astronomy with a Neutrino Telescope and Abyss environment RESearch [4], was the first neutrino telescope in the Mediterranean Sea and it was the largest neutrino telescope in the Northern Hemisphere, and the first to operate in the deep sea. It was completed in 2008 and it was located 40 km offshore from Toulon (France) at 2475m depth (Figure 3.1.1). ANTARES has acquired high-quality data almost continuously for 15 years and has been switched off in February 2022. At the time of the writing of this manuscript (Spring 2022), the detector is being de-commissioned and dismantled.

The detector infrastructure has 12 detection lines holding pressure-resistant glass sphere, the Optical Modules (OMs), which host light sensors used to detect Cherenkov radiation (see Section 2.2).

The main purpose of the detector is to perform neutrino astronomy and particle astrophysics, but the apparatus also offers facilities for marine and Earth sciences [35].

3.2 Detector structure

The overall detector structure is a three-dimensional matrix of photo-sensors. The array is composed of 12 vertical lines anchored to the sea-bed; eleven of these are equipped with a chain of 25 storeys, with each storey defining a *floor* along the line. The twelfth line is equipped with 20 storeys and it is completed on the uppermost 5 floors by devices dedicated to acoustic

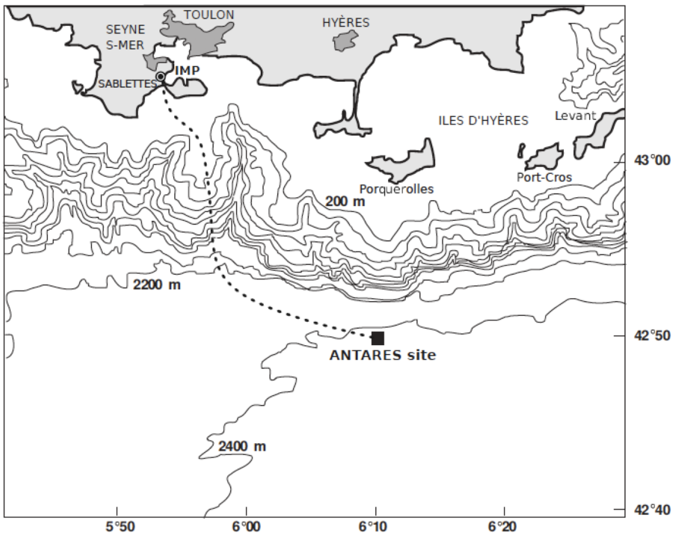

Figure 3.1.1: This picture shows the map where the detector is located.

detection.
Each storey supports with a mechanical structure made of titanium three Optical Modules (OMs), which are looking downwards at 45°. Each OM houses a 10-inch PhotoMultiplier Tube (PMT), so the entire array is made by a total of 885 PMTs.
The average horizontal spacing between each line is $\sim 60\,\text{m}$ and the vertical distance between two consecutive storeys is $\sim 14.5\,\text{m}$; the total length of a line is $\sim 480\,\text{m}$ with the first 100m left without equipment in order to allow light from below to be produced and propagated before being detected. The line is anchored to the sea-bed with the Bottom String Socket (BSS) and is held vertical by a buoy at the top.
In Figure 3.2.1 a scheme of the ANTARES detector is presented.

3.2.1 The lines

As indicated above there are 12 lines which are composed of 25 storeys, equally spaced by 14.5 m and grouped in five sectors. The total length is $\sim 450\,\text{m}$. In order to maintain the vertical position of the line, a buoy is attached at its top and the line is anchored to the sea bed thanks to the Bottom String Socket (BSS). The BSS contains the String Power Module (SPM), that controls the power supply to all instrumentation of the line. In each sector, a Master Local Control Module (MLCM) contains the Ethernet switch to control data distribution from the storeys of the sector. Two of the lines have in their BSS also a Laser Beacon used for time calibration.

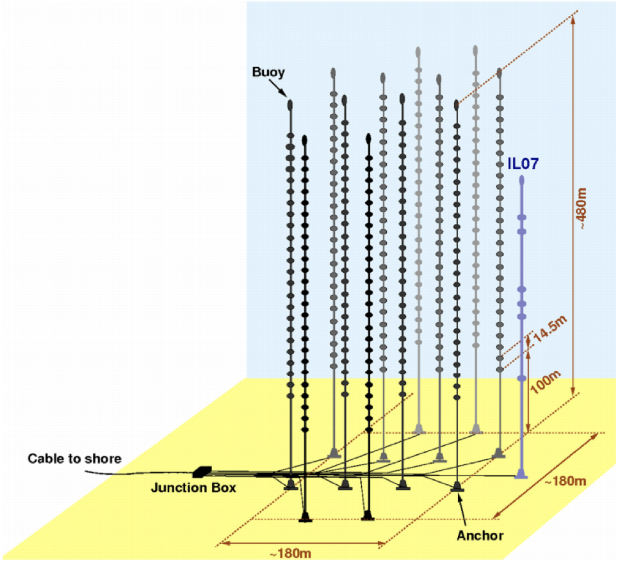

Figure 3.2.1: This picture shows the scheme of ANTARES Telescope. Figure taken from [35].

3.2.2 The Storeys

The storey structure is made of a titanium container called Local Control Module (LCM). Attached to it, titanium bars hold the Optical Modules housing the PMTs. Additional instruments used for the positioning and calibration of the detector are present. The storey structure is about 2 meters long (Figure 3.2.2).

The three OMs that are attached to the LCM are equally spaced by 120° in the azimuth angle and facing 45° downwards, in order to increase the efficiency in the detection of upward-going particles.

The LCM is water-tight sealed, and it contains and protects the electronics from water. All the electronic boards are contained in the LCM, as well as the Slow Control (SC) instrumentation. The electronic boards control the distribution of the clock signal, the PMT HV supply and the readout of PMT signals. The signals coming from the OMs, providing information about their amplitude, arrival time and shape are digitized in the Analogue Ring Sampler (ARS) [41].

3.2.3 The Optical Module

The Optical Module (OM) consists of a glass sphere of 17″ diameter, that contains a photomultiplier of 10″ in diameter, to detect Cherenkov light [68]. The PMT model selected by the ANTARES collaboration is the Hamamatsu

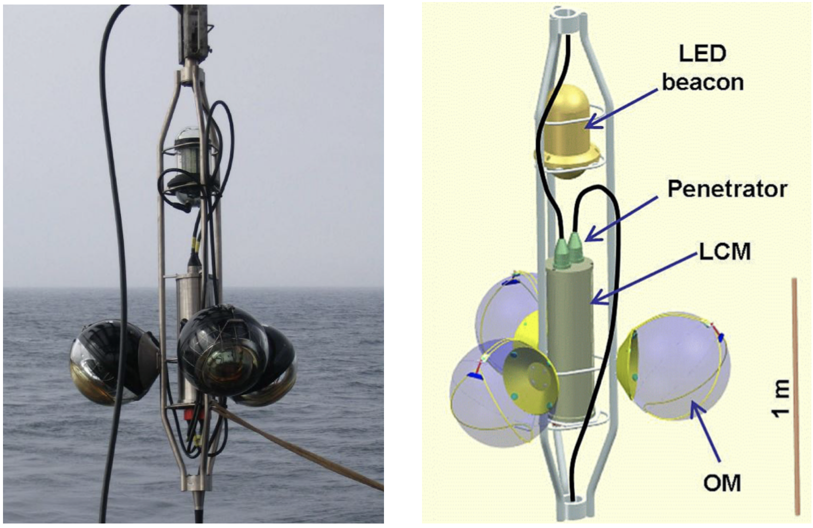

(a) Storey photo during sea operations.

(b) Storey scheme.

Figure 3.2.2: In Figure (a) a photo of a storey is shown. In Figure (b) the scheme of a storey is shown. Figures taken from [35]

R7081-20 [42]. This model has a gain of about $5 \cdot 10^7$ at the operating high voltage, that is tuned in situ during the charge calibration procedures described in Section 3.4.2. The Transit Time Spread (TTS) of the PMTs is below 3 ns (FWHM) and the dark noise rate is below 1 kHz for a 0.25 photoelectron threshold [42].
The glass sphere is designed to endure at high pressures: about 260 atm during operation and 700 atm during qualification tests. The glass refractive index is about 1.47 for wavelength between 300 and 650 nm and the glass allows for a peak in response at 420 nm. The sphere consists of two halves that are joined by a watertight tape and the surrounding pressure. The upper hemisphere is blackened in order to avoid light detection from aback. On the opposite side of the OM with respect to the window for the PMT, there is a penetrator to connect the OM to the rest of the electronics. Inside the glass sphere there is a μ–metal grid to reduce the effect of the Earth's magnetic field on the PMT. The PMT is glued to the glass sphere by an optical gel. Attached to the side of the PMT there is a LED emitter that is used for calibration purposes and onto the inside of the blackened part of the glass sphere there is a manometer to check the pressure inside the OM. In Figure 3.2.3(b) it is possible to see the scheme of a OM.

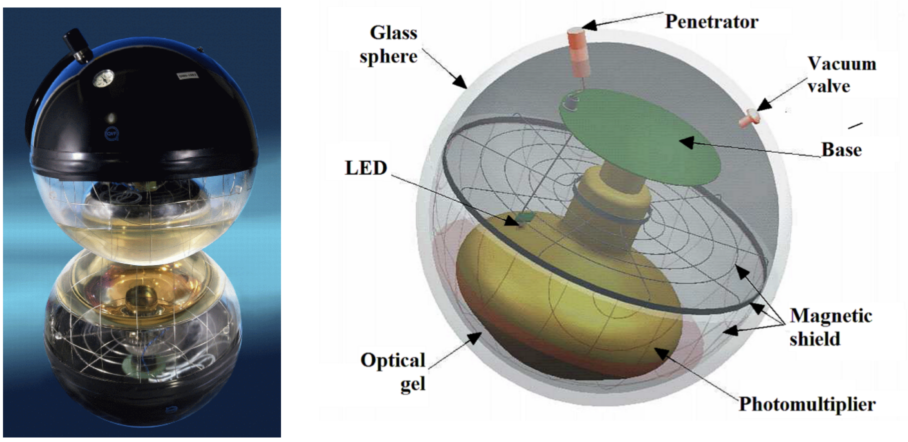

(a) OM photo. (b) OM scheme.

Figure 3.2.3: In Figure (a) a photo of an OM is shown. In Figure (b) the scheme of a OM is shown. Figures taken from [35]

3.2.4 The Junction Box and the electro-optical cable

The detector is connected to the shore station, located in La-Seyne-Sur-Mer, close to Toulon, by the Main Electro-Optical Cable (MEOC), that is 42 km-long. The cable consists of 48 mono-mode pure silica optical fibres with a total diameter of 50 mm. Through this cable the data acquisition control commands, the clock signal and the power supply to the entire detector and / or its specific components are distributed, and the transmission of data to shore is ensured. The MEOC arrives to the Junction Box (JB), a titanium egg-shaped vessel connected to the lines. In the JB, the electrical and optical signals are split from the MEOC to the BSS of the lines. The junction box is responsible for the distribution of clock signal, power and data transmission to the BSS and it is the point where bi-directional communication between shore and the detector are exchanged [41].

3.3 Water properties

Since ANTARES was the first neutrino telescope installed in deep sea waters and the first in the Mediterranean sea, different studies on the properties of sea-water, on the optical backgrounds, and on the possible impact of biofouling and sedimentation have been carried out before its construction. These studies were also important in order to prepare the accurate Monte Carlo simulations used by the ANTARES Collaboration that will be described later on in this document.

3.3.1 Light transmission

The transmission of light in water is characterized by the absorption and diffusion processes of photons, as discussed in the Section 2.5.

The propagation of light in a transparent medium can be quantified, for a given wavelength λ, by the medium optical properties coefficients: namely the absorption a(λ), the scattering b(λ) and the attenuation c(λ) = a(λ) + b(λ) coefficients.

The measured value of the effective attenuation length, which is the inverse of the attenuation coefficient, for a wavelength of 466 nm, in the ANTARES site [46], is:

$$L_c(\lambda = 466\,nm) = 41 \pm 1(stat) \pm 1(syst)[m] \tag{3.3.1}$$

The measurement had been repeated during the course of one year to understand the time variability of water properties at the experimental site. Small differences were found at different times, compatible with the accuracy of the measurement. As a result, it is assumed that these properties remain constant with time and do not differ significantly in the volume of the detector.

3.3.2 Optical background

A steady source of optical background in sea water is due to the decays of radioactive elements, the most abundant of which, in sea-water, is ^{40}K. The abundance of these elements depends on the water salinity. Section 2.3.2 shows a detailed view about this problematic. More details on this are given in [65].

In addition to the steady contribution from ^{40}K decays, seasonal and short-term effects are observed in the measured rates at the ANTARES detector, see Figure 2.3.2. These effects are attributed to biological activity. Bioluminescent creatures, both micro- and macroscopic, produce light emissions that can last up to few seconds. This biological activity usually peaks during the spring season when water rich in nutrients reaches the detector site and stimulates biological activity. During some periods, burst with single rates of the order of $\sim$MHz have been measured on the ANTARES PMTs. In order to not compromise the functionality of the detector, sometimes the ANTARES data acquisition is switched off by removing HV from the PMTs.

3.3.3 Biofouling and sedimentation

A study of the effect of particle sedimentation and biofouling [108] on the OM glass has been performed in 1998 [67]. These effects can reduce the light transmission through the glass sphere of the OMs.

The experimental setup consisted of two pressure-resistant glass spheres, similar to those used for the OMs. One of them was equipped with five photodetectors glued to the inner surface of the sphere at different inclinations (zenith angles) which were illuminated by two blue light LEDs contained in the second sphere. The measurements went on during periods of immersions lasting several months and the results were extrapolated to longer periods of time.

As expected, the fouling shows a decreasing tendency when the zenith angle on the glass sphere increases. The loss of transparency in the equatorial region of the OM dropped only of about 2.7% in eight months of operation of the test system and then seems to saturate. Extrapolations indicate a global loss after 1 year of about 2% [67] (taking into account the two glass spheres used in the setup). Considering that the PMTs of ANTARES point 45° downward (zenith angle of 135°), the biofouling and the sedimentation does not represent a major problem for the experiment.

A recent study, published in 2018, and considering ANTARES data from 2008 to 2017 [56] has shown an average decrease of the OM efficiency by 20% over 10 years of operation, which can be translated to a loss of only 15% in detection efficiency of an astrophysical signal with an E^{-2} power-law spectrum. This study have been performed using ^{40}K trigger (see Section 3.5). The results obtained indicates that undersea neutrino telescope can be operative for a decade without major efficiency degradation. The loss of efficiency measured using this approach has also been implemented in the Monte Carlo simulations of the experiment, as described in Chapter 7 so that the expectation at analysis level can be reproduced in a realistic manner.

3.4 Detector calibration

The precision with which events can be reconstructed strictly depends on the accuracy of the detector calibrations. In the case of the ANTARES detector three different calibrations have been performed: time, charge and position calibration. The calibration details are written into the database as a calibration set. There are two types of sets: sets which are used for the online detector data processing, like those needed for the event triggering, and more precise offline calibration which come after the analysis of collected data, which are in particular used for the event reconstruction.

3.4.1 Time calibration

In order to have a good reconstruction of the events, a time synchronization between OMs better than 1 ns is needed. To ensure this, time calibrations are performed in two separate steps: the first one is done in a dedicated dark room before the undersea installation; the second one is done once lines are deployed *in situ* [44].

In the first calibration procedure, a laser and a clock system are employed. The laser is used to flash a group of OMs to measure the time offset between the modules. The time delay from the String Control Module (SCM) to each Local Control Module (LCM) is measured with the clock system calibration. The contribution of the cable linking the LCM to the OM, the transit time of the PMTs and the front-end electronics time delay are measured.
The in-situ time calibration is performed regularly to assess the stability of the absolute time calibration of the signals. The absolute time calibration allows assigning a universal time to each event. This is performed by interfacing the shore station master clock to a card receiving the Global Positioning System (GPS) time with an accuracy of about 100 ms with respect to the Universal Time Coordinated (UTC). The time of PMT hits is measured by a self-calibrated 20 MHz master clock system generated on-shore. The independent time offsets of each specific detection unit are measured in situ using the optical beacons (OBs). The difference between the signal time recorded in the OM and the emission time of the corresponding LED flash is considered taking into account also the time offsets measured on-shore. Then the nominal travel of the light from the OB to the OM is subtracted, the time distribution of the "time residuals" should be centred at zero.
The time calibration, as well as an estimation of the PMT efficiency, can be performed exploiting the ^{40}K present in the sea water by using the Cherenkov light induced by the electron released in the β decay and e-capture process. If the ^{40}K decays within a few meters from the storey, a coincident signal is expected to be seen in a couple of OMs in the same storey. An Incorrect time calibration would be seen as an offset in the time coincidence distribution, since there would be a shift from the exact coincidence of a single ^{40}K decay detected by two neighbouring OMs. [34].

3.4.2 Charge calibration

Charge calibration is performed during the so called *shift* and special data runs are dedicated to this scope. In these runs, the output signal of the PMT is digitised at random times. PMTs are instruments which amplify the secondary emission of the number of electrons generated by photoelectric effect when a photon strikes the photo-cathode surface. The charge of the signal generated by the photo-electrons (p.e.) is digitised by an Amplitude to Voltage Converter (AVC) into a value related to the number of p.e., Q_{pe}, that caused the signal through the equation:

$$Q_{p.e.} = \frac{AVC - AVC_{0p.e.}}{AVC_{1p.e.} - AVC_{0p.e.}} \tag{3.4.1}$$

where $AVC_{0p.e.}$ is the value of AVC corresponding to zero p.e. (pedestal value) and $AVC_{0p.e.}$ corresponds to the single p.e. peak. Regular charge calibration runs are acquired in order to determine these two values as they evolve with the usage of the PMTs. The pedestal value is obtained by digitising the output signal of the PMT at random times, while the single p.e. peak is determined exploiting the optical background which produces primarily single photons at the photo-cathode level. Over the years, the measured amplitudes can degrade and so, in order to maintain the 0.3 p.e. threshold, it is necessary to tune the high-voltage supply of the PMT, the so called *high-voltage tuning.*

3.4.3 Position calibration

The detector lines, although the structure is built to float and hold a vertical position, are subject to sea currents that can rotate or displace them from their vertically-aligned positions [32]. In order to ensure optimal track reconstruction accuracy, it is necessary to monitor the relative positions of all OMs with an accuracy better than 20 cm, which is equivalent to the 1 ns precision of the timing measurements. In addition, to properly reconstruct muon track and its energy the OM orientation with a precision of few degrees is required.

In order to obtain a suitable precision on the overall positioning accuracy, two different and independent system are used:

- A High Frequency Long Base Line acoustic system (HFLBL) giving the 3D position of hydrophones placed along the line. These positions are obtained by triangulation from emitters anchored in the base of the line plus autonomous transponders on the sea floor.
- A set of tiltmeter-compass sensors giving the local tilt angles of each storey with respect to the vertical line (pitch and roll) as well as its orientation with respect to the Earth magnetic north (heading).

The combination between the two systems, hydrophones plus compasses-tiltmeters, allow to reconstruct the shape of each line performing a global fit of the positions of all the elements as a function of time, using the effective sea current velocity as free parameter.

The water current flow and the sound velocity in sea water are measured using acoustic Doppler current profilers (ADCP) for the water current flow, conductivity-temperature-depth (CTD) sensors to monitor the temperature and salinity of the water and sound velocimeters to monitor the sound velocity in sea water. This information is taken into account for the global fit of the detector shape.

The reconstruction of the line shape is based on a model which predicts the mechanical behaviour of the line under the influence of the sea water flow taking into account the weight and drag coefficients of all elements of the line.

A 20 cm precision is achievable on the position of each detector element. This alignment calibration is continuously updated every 2 minutes [32]. In this way, for each event the best estimation of the OM position can be applied when analyzing data.

3.5 Data acquisition system

The Data Acquisition system (DAQ) of ANTARES is based on the all-data-to-shore principle. In other words, all hits acquired by the PMTs are sent to the on-shore control station and, only afterward, filters are applied. Only hits exceeding a certain threshold are digitized by a custom application-specific integrated circuit called Analogue Ring Sampler (ARS) and then sent to shore [125]. The ARS is a chip that samples the PMT signal continuously at a tunable frequency up to 1 GHz [41]. The ARS can measure different characteristics of the signal, as the amplitude, the time of threshold crossing and the presence of multiple peaks within the time gate, but it records only charge and amplitude. The charge of the signal is integrated by the ARS using two 8-bit Analog-to-Digital Converter (ADC) with an integration gate of 40 ns. Instead a 20 MHz reference clock is used for time stamping the signals. A Time-to-Voltage Converter (TVC) device is used for high-resolution time measurements between clock pulses. In each storey there are 6 ARS, which are read out by a Field Programmable Gate Array (FPGA). This phase of the data acquisition is called *level-0* trigger, and the hits recorded at this stage are called *L0-hits* [43].
Once the signals are digitized are transferred to shore, the data output rate can be between 0.3 GB/s to 1 GB/s, depending on the background level and on the number of active strings. Since most of the hits are optical background, these need to be filtered.
This filtering stage is divided in two phases: the *level-1* trigger (*L1-hits*) and *level-2* trigger (*L2-hits*). The *L1-hits* conditions consist of a correlation between hits in the same storey, since the background is expected to be uncorrelated. In other words, a L1 trigger requires hits in the same storey with a difference in time smaller than 20 ns. Two L1-hits (i and j) are considered causally related by imposing the following condition:

$$|t_i - t_j| \leq |\overrightarrow{r_i} - \overrightarrow{r_j}| \cdot v_g + 20ns \tag{3.5.1}$$

where t_i and t_j are the arrival times, $\overrightarrow{r_i}$ and $\overrightarrow{r_j}$ the position of the corresponding OM and v_g is the group velocity of light in water. A triggered event is defined when a number (typically ≥ 5) of causally correlated L1-hits are found.
The trigger level L2-hits comprises the high level triggers. The first of them is the *T-level* trigger, which is of two different types. In the case of a hit having at least one coincidental hit in an adjacent floor on the same line are called T2 hits. The coincidence windows is 100 ns. Instead in case of a

hit in a adjacent or next to adjacent floor on the same line it is called a T3 hit. The coincidence windows is 200 ns. Usually the filtering of data requires multiple T2 and T3 hits in order to reduce the background.
In addition to these triggers it is possible to apply additional filters, which depend on the analysis. There are specific triggers for analyses directed towards the to the Galactic Centre, or triggers dedicated for the ^{40}K decay. In this work also the trigger called 3N is used. The 3N trigger selects events in which hits follow a causality connection condition compatible with the presence of a muon crossing the detector.
It is possible conclude that the data acquisition control system involves about 750 processes, of which 300 are offshore processes for data acquisition, 300 are offshore processes for slow control, and about 120 are processes running on the onshore computers for data processing and filtering, monitoring and user interface.

3.5.1 Data taking

Data taking is divided into *runs* whose duration ranges from 2 to 12 hours, or 2 to 8 GB according to the settings. At each run change a run setup is loaded, in which the trigger settings for the data acquisition and the configuration of each storey is set. Run setups can be changed according to the environmental conditions at the detector to handle possible problems induced by high rates, eventually also by turning off the High Voltage (HV) on PMTs. If no changes are to be done, the runs are stopped and restarted automatically by the run control program, otherwise detector shifters have to intervene. Finally, periodically, calibration run setups are taken, which allow to collect specific data runs for calibration purposes, such as Laser-beacon or LED beacon data.
Continuity in data taking is fundamental in a neutrino telescope, since rare signal events might appear at any moment. For this reason, data run changes are automated and do not induce any significant deadtime. A periodic contribution to a loss of detector exposure is given by the weekly calibration runs, but also these take at most 1h. During the first years of data taking, significant increases in bioluminescence had been observed during spring time, and the detector HV was removed during these periods of a few weeks. This has not effected the last years of data taking, though. Overall, an average 95-98% uptime has been reached in the last years of ANTARES.

Chapter 4

KM3NeT

In this chapter the characteristics of the KM3NeT detectors will be described. At first the general characteristics of the two detectors, ARCA and ORCA, will be given; this will be followed by a description of the KM3NeT Detection Units (DUs) and the Digital Optical Modules (DOMs). Finally, the data transmission and the data acquisition are discussed.

4.1 KM3NeT

KM3NeT is the successor of ANTARES as the next generation neutrino observatory in the Mediterranean Sea. The two main goals of this experiment are [29]:

- The identification, observation and study of high-energy neutrino sources in the Universe;
- The study of the properties of neutrinos.

KM3NeT, as a research infrastructure, will not only focus on astroparticle and particle physics with neutrinos, but it will also operate as a multidisciplinary scientific installation. Indeed, the apparatus will also be connected to monitoring instruments for Earth and sea science [164]. The KM3NeT Collaboration has indeed had a strong cooperation, since many year with the EMSO Consortium for Earth and sea science research [5].

The KM3NeT Collaboration is proceeding in building and deploying its two constituent detectors in parallel in two different sites. KM3NeT/ARCA, a high-energy neutrino telescopes, is being built in the KM3NeT Italian site, 100km off the coast of Capo Passero, in Sicily. The KM3NeT/ORCA experiment, for the observation of low energy atmospheric neutrinos and the precise measurement of the neutrino oscillation phenomena, is being built off-shore Toulon, France.

The ARCA detector final configuration will be made of two building blocks, large three dimensional arrays of optical modules aiming to reach a km^3 volume, while ORCA will consist of one block with a final configuration that will instrument ~ 7 Mton of sea-water.

Each block is made of by 115 Detection Units (DU), each consisting of 18 Digital Optical Modules (DOMs). 31 PhotoMultiplier Tubes are hosted inside each DOM.

The Collaboration, to date, comprises 55 institutes and groups in 16 countries [6].

4.1.1 KM3NeT/ARCA: Astroparticle Research with Cosmics in the Abyss

The main research goal of KM3NeT/ARCA is the detection of high-energy neutrinos of cosmic origin. The main sources that KM3NeT/ARCA will investigate are the candidate cosmic ray accelerator in our Galaxy, in order to find neutrinos from these sources. The detector design has been optimised in order to improve the sensitivity to neutrino fluxes from these sources. The KM3NeT/ARCA infrastructure is located at $36°16'$ N $16°06'$ E at a depth of 3500 m, about 100 km offshore from Porto Palo di Capo Passero, Sicily, Italy. The final design of the structure foresees the installation of two blocks providing an instrumented volume of about one cubic kilometre and each block is made by 115 DUs. Each DU is about 700m in height and with the 18 DOMs spaced 36 m apart in the vertical direction, starting about 80 m from the sea floor. The horizontal spacing between detection strings is about 95 m (Figure 4.1.1) [29].

At the time of the writing of this manuscript, Spring 2022, the detector consists of nine DUs installed on the sea-bed.

4.1.2 KM3NeT/ORCA: Oscillation Research with Cosmics in the Abyss

The main scientific objective of KM3NeT/ORCA is to study the fundamental neutrino properties as the neutrino mass ordering, and the properties of neutrino oscillation phenomena. This will be accomplished by collecting a large statistic of atmospheric neutrinos, mainly in the 1-100 GeV energy range.

The KM3NeT/ORCA infrastructure is located at $42°48'$ N $06°02'$ E at a depth of 2450 m, about 40 km offshore from Toulon and is about 10 km west of the site of the ANTARES telescope (Figure 4.1.2(a)).

The final design of the apparatus foresees the construction of one block of 115 DUs, where each DU is 200 m in height and holds 18 DOMs that are spaced by 9 m apart in the vertical direction, starting about 40 m from the sea floor. The horizontal spacing between detection strings is about 20 m (Figure 4.1.2(b)) [29].

(a) Map of ARCA location.

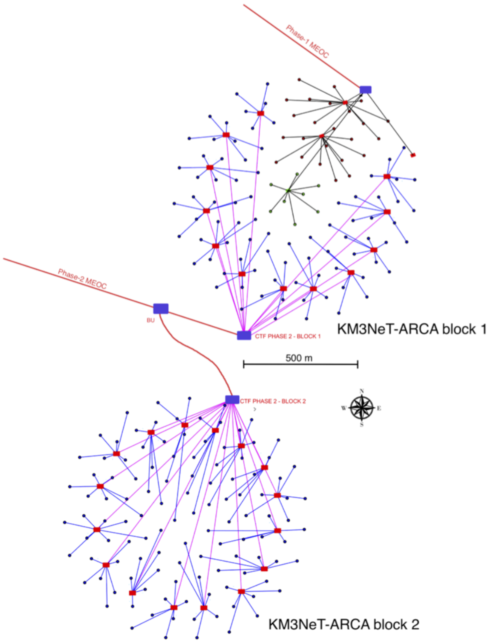

(b) ARCA scheme.

Figure 4.1.1: In Figure (a) the site location of ARCA using Google Maps. In Figure (b) the two blocks structure of ARCA. Figure taken from [29]

The control room is located at the Institute Michel Pacha, La Seyne-sur-Mer, and and hosts the data transmission and acquisition computing elements [29]
.

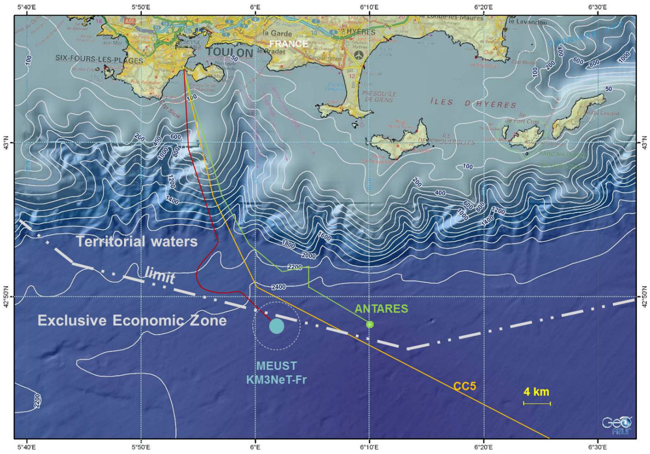

(a) Map of ORCA location.

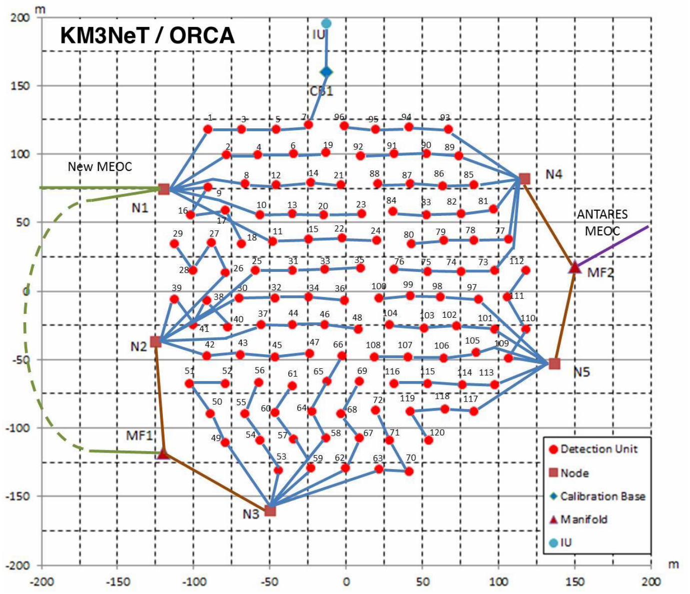

(b) ORCA scheme.

Figure 4.1.2: In Figure (a) the site location of ORCA, which is close to the ANTARES site. In Figure (b) the block structure of ORCA. Figure taken from [29]

4.2 Digital Optical Module

The Digital Optical Module (DOM) (Figure 4.2.1) is a transparent glass sphere of 432 mm in diameter. It is made of two separate hemispheres, housing 31 PMTs [49] and their associated readout electronics [29] [53].

In other experiments, such as in IceCube and ANTARES, optical modules host only one large PMT. However, this single-PMT design offers a limited angular coverage. The new multi-PMT design of the KM3NeT Optical Modules foresees the usage of smaller, 3″ PMTs, arranged on 5 rings of 6 PMTs each and the thirty-first placed on the bottom pointing vertically downwards [51], [52]. The PMTs are spaced by 60° in azimuth and successive rings are staggered by 30°. There are 19 PMTs in the lower hemisphere and 12 PMTs in the upper hemisphere. The PMTs are held in place by a 3D printed support. In this way a complete angular coverage is obtained.

Figure 4.2.1: Photo of a a Digital Optical Module. Figure taken from [29].

The photon collection efficiency is increased by 20–40% by a reflector ring around the face of each PMT. In order to assure optical contact, an optical gel fills the cavity between the support and the glass. The support and the gel are sufficiently flexible to allow for the deformation of the glass sphere under hydrostatic pressure.

Each PMT has its own individual very-low-power high voltage base with integrated amplification and adjustable discrimination. The arrival time and the time-over-threshold (ToT) of each PMT, are recorded by an individual time-to-digital converter implemented in a FPGA. The threshold is set at the level of 0.3 of the mean single photon pulse height and the high voltage is set to provide an amplification of $3 \cdot 10^6$. The FPGA is mounted on the Central Logic Board (CLB), which transfers the data to shore via an Ethernet

network of optical fibres. Each DOM in a string has a dedicated wavelength for data transmission, to be later multiplexed with other DOMs wavelengths to allow data communication via a single optical fibre to shore [51].
The PMTs specifications foresee a photo-cathode diameter of at least 72 mm and a length smaller than 122 mm. The reflector effectively increases the diameter to about 85 mm. The photo-multiplier tube has a ten stage dynode structure with a minimum gain of 10^6. The front face of the photo-multiplier tube is convex with a radius smaller than the inner radius of the glass sphere. Due to the small size of the PMT, the influence of the Earth's magnetic field is negligible and a μ-metal shield is not required.
The optical module also contains three calibration sensors [51]:

- The LED nano-beacon, which illuminates the optical module(s) vertically above;
- A compass and tilt-meter for orientation calibration;
- An acoustic piezo sensor glued to the inner surface of the glass sphere for position calibration.

In Figure 4.2.2 a scheme of the components of a DOM is presented.

4.3 Detection Units

The detector is made by a matrix of strings anchored to the sea-bed. These strings are called Detection Units (DUs). Each DU, see Figure 4.3.1 and Figure 4.3.2, hosts 18 DOMs.
Each DU comprises two thin (4 mm diameter) parallel Dyneema ® ropes to which the DOMs are attached via a titanium collar [33]. Additional spacers are added in between the DOMs to keep the ropes parallel. Attached to the ropes, there is the vertical electro-optical cable, a pressure balanced, oil-filled, plastic tube that contains two copper wires for the power transmission (400 VDC) and 18 optical fibres for the data transmission. At each DOM two power conductors and a single fibre are branched out via the breakout box. The power conductors and optical fibre enter the glass sphere via a penetrator [29].
In order to minimize the horizontal displacement in case of large sea currents, an additional buoyancy is introduced at the top of the string.
For deployment and storage, the string is coiled around a large spherical frame, the *launcher vehicle* (LOM), in which the DOMs slot into dedicated cavities (Figure 4.3.3(a)). The anchor is external to the launcher vehicle and is sufficiently heavy to keep the string fixed on the sea-bed. The anchor houses an interlink cable, equipped with a wet-mateable connectors, and the base container. The base container incorporates dedicated optical components and an acoustic receiver used for positioning of the detector elements.

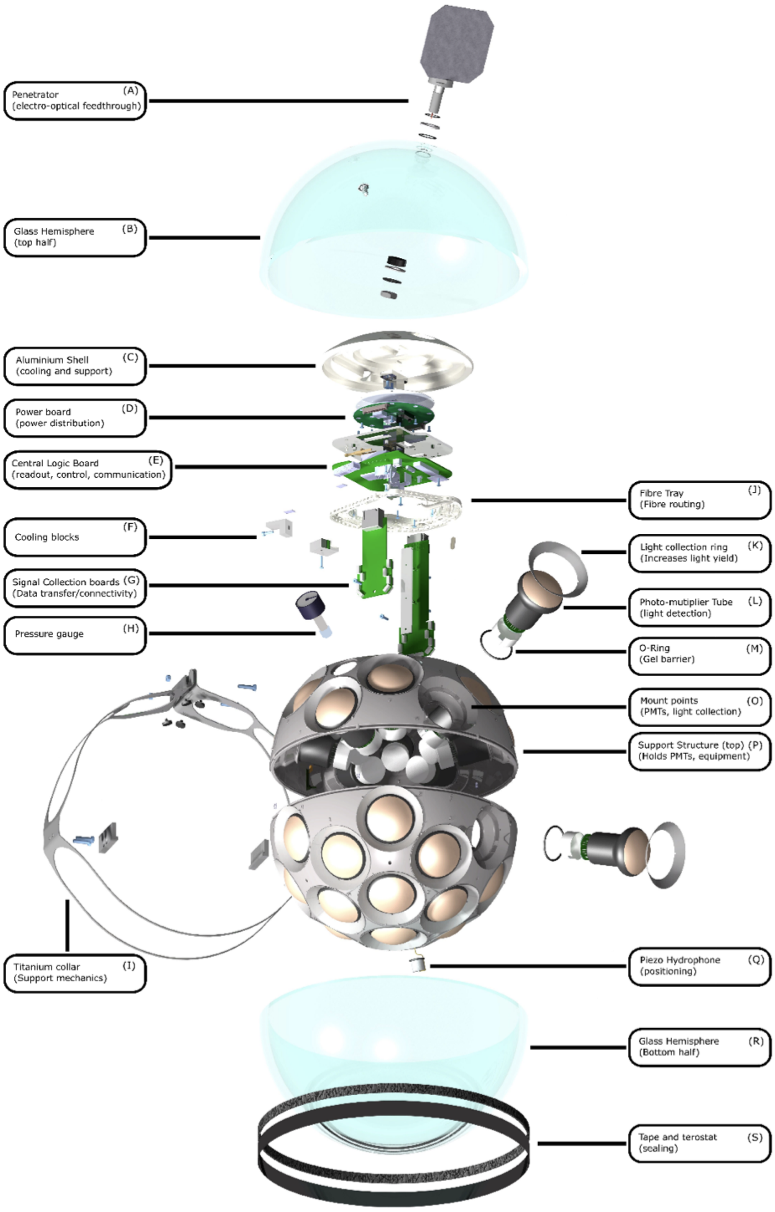

Figure 4.2.2: Scheme of a a Digital Optical Module. Figure taken from [51].

A surface vessel, with dynamic positioning capability, is used at each site to deploy the launcher vehicle at its designated position on the sea-bed with an accuracy of 1 m. A Remotely Operated Vehicle (ROV) is used to deploy and connect the interlink cables from the base of a string to the junction box. Once the connection to the string has been verified onshore, the ROV open

(a) Detection string (b) The fixation of the DOM on the two parallel Dyneema® ropes.

Figure 4.3.1: In Figure (a) a simplified scheme of the string. In Figure (b) a photo of a single DOM showing how it is fixed on the ropes of the DUs. Figure taken from [29]

a hook which releases the LOM [50].

During this process, the launcher vehicle starts to rise to the surface while slowly rotating and releasing the DOMs (Figure 4.3.3(b)). The empty launcher vehicle floats to the surface and is recovered by the surface vessel. The usage of this compact string-deployment techniques allows for the transportation of multiple units onboard a single vessel, and thus multiple deployments during a single cruise [50]. This method reduces costs and also has advantages in terms of risk reduction for ship personnel and materials during the deployment.

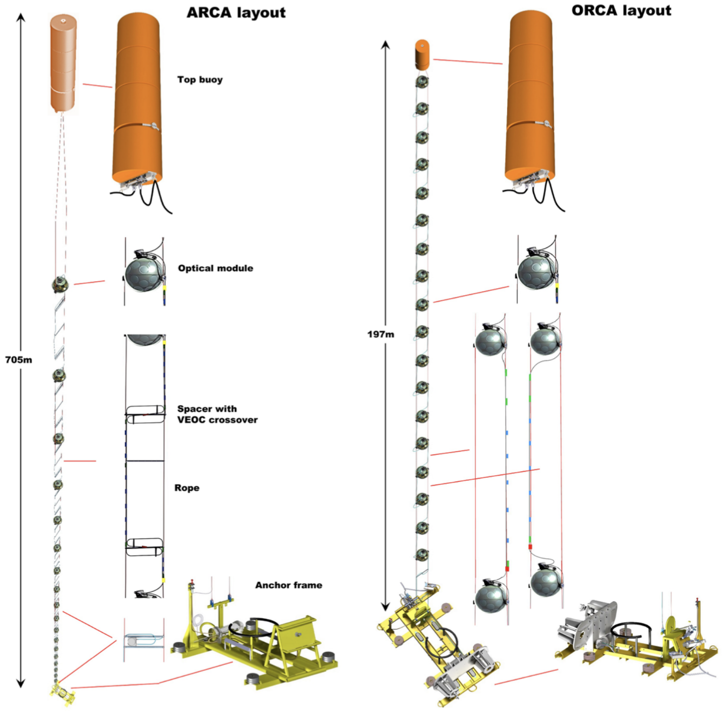

Figure 4.3.2: ARCA (left) and ORCA (right) DU-string layouts showing the 18 optical modules on one DU- string, the VEOC guided along the DU-string, as well as the top buoys and anchor frames. Figure taken from [50]

4.4 Positioning system

The KM3NeT detector uses two different instrumental system for the in-situ positioning procedure: one consists of compass chips installed on the CLB inside each DOM (for details the reader can refer to Chapter 5); the second is an array of acoustic emitters installled in the detector site and the acoustic sensors installed in the DUs [190].

Regarding the compass, two kinds of boards have been used in KM3NeT: LNS-AHRS and LSM303-AHRS, both developed within the collaboration. The LNS-AHRS (Attitude Heading Reference Systems) contains two sensor blocks: 3D accelerometres and 3D magnetometers to provide body angles (AHRS mode). The core of the board is the LSM303 commercial compass and tilt chip, from *ST microelectronics* [51]. Both of these two chip types provide the components of the acceleration and of the magnetic field, from these data it is possible to reconstruct the Yaw, Pitch and Roll value (see Chapter 5).

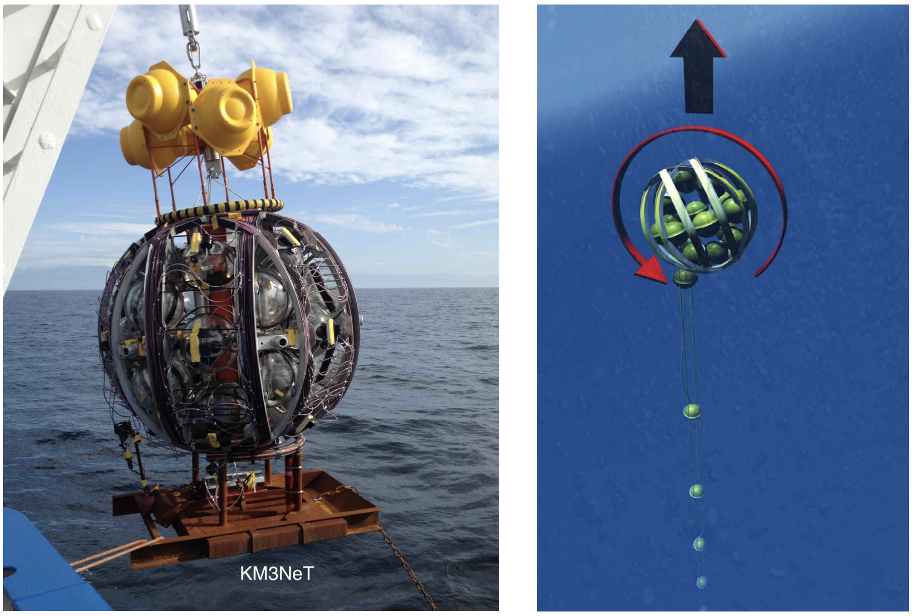

(a) Launcher vehicle (b) Simulation of unrolling.

Figure 4.3.3: In Figure (a) the launcher vehicle of a DU. In Figure (b) a simulation of the deployment in the water of the DU.

The Acoustic Positioning System (APS) consists of Acoustic Beacons (ABs) installed at the Sea bottom around the detector, hydrophones installed on the DU base and piezo-electric sensors installed inside DOMs [113] [209]. The APS works in the frequency range between 20 and 50 kHz [208]. The APS uses a triangulation method for positioning the receivers. In order to exploit this method, it is extremely important not only to know with precision the position of the ABs, but also the Time of Emission (ToE) of the signals. The accuracy of the deployment location of the DU-bases and the ABs is of about 2 m (absolute positioning system), but the accuracy of the relative APS on KM3NeT is few tens of centimetres [209]. For the moment, the ABs used by KM3NeT are autonomous, which means that the ToE is not controlled by the system and thus must be fitted in the triangulation procedure. The autonomous ABs are mounted in tripods with a height of 5 m. They are programmed to emit acoustic waves for 1 min and switched off for 9 min after that. During the minute of emissions, the AB emits 1 pulse signal every 5 s. The pulse has a duration of 5 ms, and it is a linear sweep-signal along 2 kHz in the frequency band of the emitter. Each AB has a unique sweep signal that permits distinguishing and detecting it in the reception. The AB's Sound Pressure Level (SPL) is around 180 dB in the 20–60 kHz range which allows for a good reception in the receivers [208]

[113]. The hydrophone is a Colmar DG0330. It is omnidirectional, stereo to avoid signal saturation, and it works in the 5–90 kHz range. The piezo-ceramic sensor installed inside each DOM is an acoustic receiver basically used to monitor the position of the DOM. It is in an aluminum capsule with the pre-amplifier board glued to the glass of the DOM facing downwards.

4.5 Time calibration

In order to reconstruct the neutrino tracks, all DOMs need to be synchronized with nanosecond precision and their position must be determined with less than 20 cm accuracy. The time calibration in KM3NeT between different detector components consists of three different steps executed directly in situ [195].

The first consists in the synchronisation of the PMTs in the same DOM, and time delays between pairs of PMTs are computed. Since the light emitted by the decay products of potassium in sea water can be seen simultaneously from neighboring PMTs, and a single decay occurring near the DOM has the potential to produce a true coincidence between signals from different PMTs, this can be exploited for this step of the DOM time calibration [109]. This calibration phase is called *Intra-DOM* calibration and has been pioneered by the ANTARES Collaboration [56], [44].

The second time calibration phase, called *Inter-DOM*, consists of the synchronisation of DOMs in the same DU. A first part is done in a dedicated dark room before the DU deployment, where two PMTs of each DOM of a DU line are illuminated by a blue laser. The purpose is to measure the time delays between DOMs of a single DU. Then, once the DU is deployed, another check is done using a LED installed on the top of each DOM, so the DOMs above can be illuminated. Since the distances between DOMs are known, it is possible to compute the time delays. This is further cross-checked by measuring the Cherenkov light emitted by down-going muons, which also shows a precise time-dependent pattern and can be used to estabilish the time synchronisation of the DOMs in a DU.

The third calibration, the so called *Inter-DU*, consists of the synchronisation of each DU with the others. In this phase the time calibration is done synchronising the master clock on shore with the DUs. The measurements then needs to be corrected by including all relevant latencies and asymmetries, i.e. the time delay for the one-way propagation of the clock signals from shore to the base of each DU. A final validation of the whole time calibration procedure exploits the reconstruction of down-going muons [109].

4.6 Data acquisition

In KM3NeT all signals recorded in the PMTs which pass a preset threshold (typically 0.3 photo-electrons [29]) are digitised and these data are sent to shore where they are processed in real time, the so called *all data to shore*. The optical data contain the time of the leading edge and the time over threshold of every analogue pulse, commonly referred to as a hit. Each hit corresponds to 6 Bytes of data [29]. The least significant bit of the time information corresponds to 1 ns. The total data rate for a single building block amounts to about 25 Gb/s. A reduction of the data rate by a factor of about 10^5 is thus required to store the filtered data on disk. In addition to physics data, summary data containing the singles rates of all PMTs in the detector are stored with a sampling frequency of 10 Hz. This information is used in the simulations and the reconstruction to take into account the actual status and optical background conditions of the detector.

In parallel to the optical data, the data from the acoustic positioning system are processed and represents a data volume of about one third of that of the optical data.

A dedicated software is used in order to filter physics events from the background. Since data have to be managed for offline analyses, in order not to lose any significant information, each event will contain a snapshot of all the signals recorded in the detector during the event.

The trigger algorithms are designed to filter the signals of possible neutrino interactions from the background dominated stream and store them for further analysis. The underlining principle, shared by the trigger algorithms is that photon arrival times (hits) from a neutrino interaction are causally related in a known way [53] [99], similarly to what has been already explained for the ANTARES event filtering.

As for ANTARES (Section 3.5.1), the uptime is maximised by the data acquisition system. As a consequence, $> 95\%$ up-time has been reached in both the ARCA and ORCA detectors in their first years of data acquisition, showing that, despite the youth of these experiments, no severe critical issues hindered data taking.

Part II

Analysis of KM3NeT compass data

The earth began to cool,
the autotrophs began to drool
Neanderthals developed tools

The History of Everything,
Barenaked Ladies

Chapter 5

Calibration, monitoring and position reconstruction using KM3NeT compass data

In this chapter the technical part of the thesis is presented. This work occupied the first part of my PhD studies, and consituted a fundamental development for the innovative procedures carried out in the KM3NeT collaboration in the understanding of the detector movement when put under-sea. This work can be divided into three parts:

1. compass calibration on the Central Logic Board (CLB);

2. monitoring compass data;

3. DU line reconstruction using compass data.

The first part is one of the fundamental steps in the construction of the detector. In this chapter the calibration procedure of the compass and tilt chips that are installed on the KM3NeT CLBs will be described.
The second item refers to the in-situ monitoring of compass data that I performed, using the KM3NeT DOMs installed under-sea after deployment.
Finally, the third item covers my contribution to the work developed in the KM3NeT Collaboration for the reconstruction on the DOM positions under-sea by means of a reconstruction procedure of the DU shape. This DU Line-fit is based on the mechanical model of the string and allows to determine the position of the DOMs using also data collected by the compasses. The main outcome of this study will be that the usage of this information can be very relevant especially when strong sea currents act on the lines.

5.1 AHRS: Attitude Heading Reference System

As it is described in Section 4.4, the positioning system in KM3NeT [190] consists of the Acoustic Positioning System (APS), based on sound measurements, and of the Attitude Heading Reference System (AHRS) which makes use of the array of compasses and tilt-meters installed inside the DOMs.
Regarding the AHRS [7], it consists of a chip mounted on-board each CLB (Figure 5.1.2(b)). This chip provides a measurement of the three components of the Magnetic field (H_x, H_y, H_z) and the three components of the Acceleration (A_x, A_y, A_z). From these components it is possible to determine the orientation of the DOMs, for instance the Yaw, Pitch, and Roll (YPR), the rotation angles around three perpendicular axes z, y, and x respectively (Figure 5.1.1). They can be calculated as:

$$Pitch = atan2(A_x, \sqrt{A_y^2 + A_z^2}) \tag{5.1.1}$$

$$Roll = atan2(-A_y, -A_z) \tag{5.1.2}$$

$$\begin{aligned} Yaw = atan2(&-H_y \cdot \cos(Roll) + H_z \cdot \sin(Roll), \\ &H_x \cdot \cos(Pitch) + H_y \cdot \sin(Pitch) \cdot \sin(Roll) + H_z \cdot \sin(Pitch) \cdot \cos(Roll)) \end{aligned} \tag{5.1.3}$$

This convention is the same used for the aircrafts.
In the KM3NeT data acquisition system the AHRS recordings are provided every 10 seconds and stored in the KM3NeT Database.

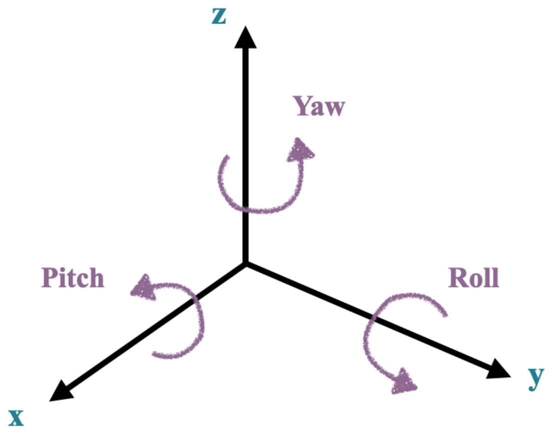

Figure 5.1.1: Representation of the Yaw, Pitch and Roll rotation around the respective axes.

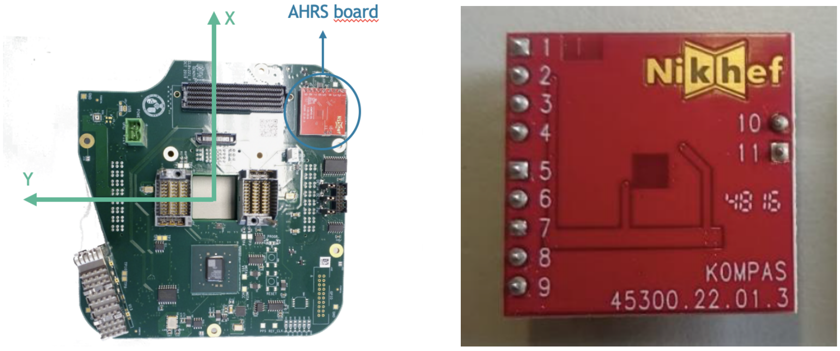

(a) Central Logic Board (CLB).

(b) The LSM303-AHRS developed at Nikhef.

Figure 5.1.2: In Figure (a) it is reported the picture of a CLB, where the coordinate system is reported. In Figure (b) the picture of the AHRS chip.

5.2 Calibration of the compass and tilt board

Before the installation of a CLB inside a DOM, it is necessary to calibrate the AHRS in order to have a magnetic field measurement with respect to the Magnetic North. This procedure is delicate since the environment where the measurements are carried out could affect it; for example it is necessary to verify if any ferromagnetic material, like iron, or possible magnetic field sources are present in the surroundings of the measurement site.
The calibration procedure can be summarised in three consecutive phases:

1. the CLB setup;
2. the compass and accelerometer calibration;
3. the check of the calibration outcome.

The CLB mechanical setup consists of fixing the board on the gimbals (shown in Figure 5.2.1). The CLB is then connected to a computer and to the power supply. Once this connection is established, data from the CLB compass and accelerometers are acquired by a custom-designed application that is connected to the central KM3NeT database. At this point, the second phase of the procedure starts. The CLB is rotated with respect to the different axes. Each rotation has a duration of about one minute. The details related to this procedure are reported in the Appendix B, where also some figure of the different rotations are shown. The magnetometer module variation should not exceed 2% and the accelerometer module variation should not exceed 2.5%. These limits are thought in order to avoid systematic errors on the DOM orientation exceeding the requirements described later. Data

flow is constant and smooth so it is necessary to be aware that frequently twisting the cables may lead to rupture of the power supply cable, with the CLB data flow suddenly disappearing.
Once calibration parameters for a compass/accelerometer have been obtained, the outcome needs to be checked. The CLB is positioned face-up, with the z-axis pointing downwards, and the x-axis oriented in the direction of the four cardinal point, using the Magnetic North as first. These check measurements have a duration of about two minutes, where each position is maintained of about 30 s.

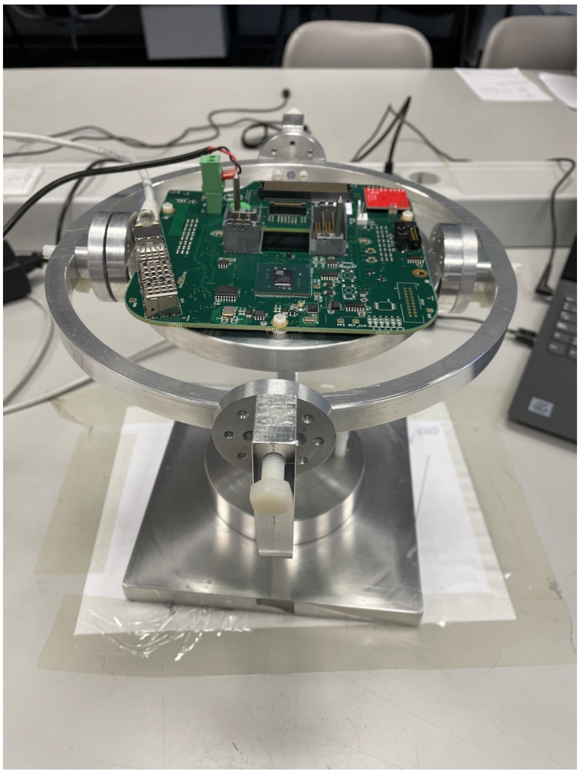

Figure 5.2.1: The CLB installed on the gimbals for the calibration procedure.

5.2.1 Calibration in different environment

During the development of this work I had the chance to supervise a bachelor's thesis, whose the main goal was to understand the impact of environmental conditions in the CLB calibration procedure [78]. The main causes of alteration of the measurements can usually be the presence of iron or the presence of an external magnetic field in the laboratory where the calibration is carried out. This study has been performed calibrating three different

CLBs in different conditions: in the laboratory where the the CLBs are usually calibrated, with or without an external magnetic field; in a laboratory where some iron was added near the calibration table; in another laboratory where other computers and machines were active. It has been observed, as expected, that the accelerometer components do not show significant variations in the different calibration environments for all the three CLBs; instead, the magnetic field readings vary visibly both in presence of iron and when the measurements are carried out in the presence of a magnetic field.
Naturally this was the expected result, but it was interesting to study how much the environment conditions could affect the calibration in order to understand possible systematic effects in this calibration procedure. In Figure 5.2.2 the mean values of the acceleration and of the magnetic fields measured in the six different locations used in the study are reported. It is possible to notice that the acceleration readings are stable and constant in all environments. Instead, magnetic field measurements can increase by a factor of about 3, especially in the presence of an external magnetic field. In the laboratory 1 and laboratory 2 the value of the magnetic field is comparable to the Earth magnetic field.

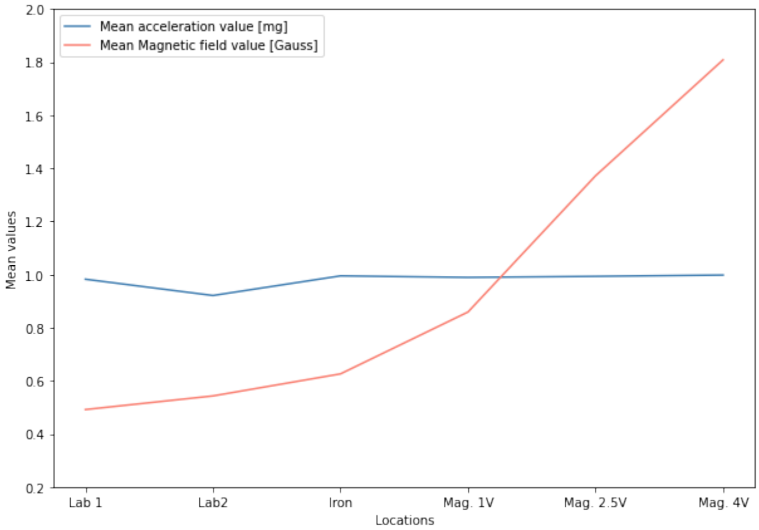

Figure 5.2.2: Mean values of the accelerometer and magnetometer readings measured in the six different locations described in the text. The mean accelerometer measurements have standard deviation $\sigma_A \sim 0.03$ while the magnetometer have $\sigma_H \sim 0.5$, not shown in figure.

5.3 Monitoring compass data

In order to properly reconstruct neutrino tracks, it is very important to know the positions and the orientations of all the DUs and DOMs underwater. For this, it is essential to know how the environmental conditions, i.e. the sea current, could affect the orientations. In order to monitor and study the orientations of DOMs, I have developed a dedicated code in *Python language* [207].

This code can be subdivided into three parts; the first part takes care of the connection to the KM3NeT database, which allows to access the AHRS data as well as to select the KM3NeT detector and data taking run to be analysed. The second part is dedicated to the treatment of the data, consisting of a clean-up of the selected data set by *stacked* data, i.e. fake duplicated data for a given time, or data out of range. Once data are cleaned, offsets are applied for each compass; these offsets are the ones computed during the calibration procedure of the CLBs. The third part consists of finally computing the YPR values. To do this, data are averaged in order to manage a lighter data set. The results presented here are averaged every 10 minutes. Once the YPR values are obtained, statistical data analyses can be carried out in order to monitor the orientation of the DOM. This mainly concerns the monitoring of the Yaw values, since they are related to the orientation of each floor of the DU and the value that is most affected by the influence of sea currents. Indeed, DOMs are fixed to two parallel ropes so the Pitch and Roll rotations are close to zero and effects given by strong sea current are not so visible. In addition, thanks to this monitoring procedure it is possible to visualize issues that could affect the DOMs and to intervene in due time in order to avoid further problems.

Many periods of data taking have been analysed, both when KM3NeT/ORCA was made by only four lines (before January 2020) and when other two additional lines were deployed. In this work results of the compass monitoring for KM3NeT/ORCA with 6 working DUs are presented covering some period samples. In the period when this study was done the KM3NeT/ARCA detector was not operative, but the same analysis could be applied to that detector and similar results are expected.

5.3.1 Low sea current period

The first monitoring study, presented here, has been done on a period when the environmental conditions do not affect much the positions of the lines. This allows us to get a *reference* measurement where we know that the detector is rather stable and *vertical*. This is for example the case shown in Figure 5.3.1, which covers a data taking periods where no strong sea currents where measured on the detector site, and the Yaw values show great stability. Each DU has its own orientation with respect to the magnetic North which

depends on how the base anchor is oriented. A preliminary measurement of the DU orientation is done during the deployement operation when the anchor is inspected with the Remotely Operated Vehicle (ROV) as it stands in front of it, and the ROV's compass measurement is acquired. Since the height of the DUs is very large, it can happen that the orientation of each floor could change by to some degrees with respect to the orientation of the base, and the higher is the floor, the larger is this difference.
In the Table 5.1 the orientation measured by the ROV and the mean value of the Yaw measured in all DOMs of the line in a period with low sea current for each DU of KM3NeT/ORCA are reported. The period of low sea current considered is from 7/02/2020 to 14/02/2020.

Table 5.1: Table with the orientation of the base line given by the ROV (anchor heading) and the mean Yaw given by the mean of measured Yaw of each DOM of the DU. The period considered for this measurement is data recorded from February 7th 2020 to February 14th 2020; in this period with low sea currents.

Detection Unit	Anchor Heading (°)	Mean Yaw (°)
DU 1	190	197
DU 2	255	250
DU 3	280	265
DU 9	120	145
DU 10	260	268
DU 11	285	272

Looking at the Figure 5.3.1, it is possible to notice that in general the higher DOMs twist more than the lower ones. Also the different colors of the floors create a kind of *rainbow effect* in these plots. Deviations from the *rainbow* configuration would allow spotting anomalies in the DOMs behaviour.
The orientation of the bases, which could help in the monitoring, is not shown in any of the plots. Unfortunately the compass and tilt measurement of the DU Base Module are affected by the presence of a large quantity of iron in the anchor, so these values cannot be used for any YPR computation. For completeness, additional plots for the YPR of other DUs are reported in the Appendix A.

5.3.2 Strong sea current study

At the depths where the KM3NeT detectors are installed, periodic sea currents are present. These can have sufficient intensity to twist and displace the DOMs in the lines from their vertical position. To monitor the sea currents

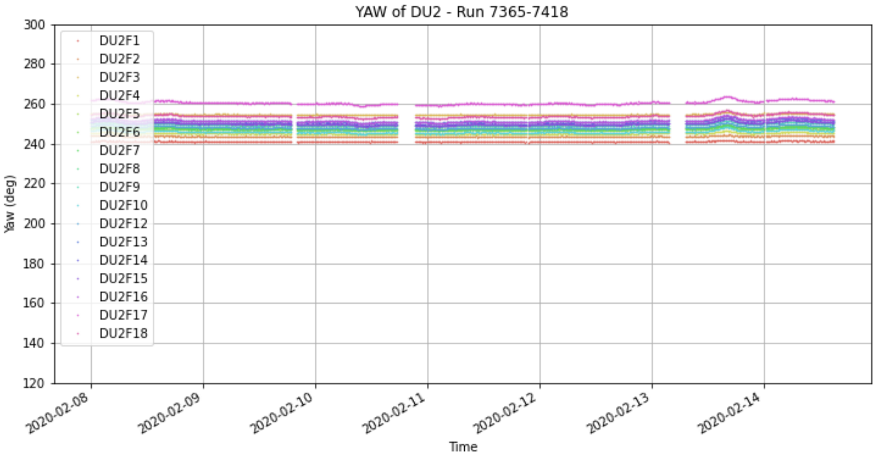

Figure 5.3.1: Yaw value of the DU2 for the period with low sea current.

close to the KM3NeT/ORCA detector, the MII current-meter AQUADOPP is used. Its measurements are available in ERDDAP [8], which is a data server that provides oceanographic data. This tool provides the speed and the direction of the sea current in the proximity of the detector.
During the periods when strong sea currents are observed in the vicinity of the KM3NeT/ORCA detector, the study of how large the displacement of the DOMs or the twisting of the lines can be very valuable.
In Table 5.2 the details of two data taking periods where a strong sea current was measured at the site are reported. Data from the DOMs are then analysed to understand the effect on the lines. In Figure 5.3.2 the sea current speed and orientation are shown. The sea currents in the two periods are comparable in intensity but with a 125° difference in orientation.

Table 5.2: In this table the details of the two period with strong sea current considered are shown.

	Data Period	Run	Peak period	Current Speed (m/s)	Current Orientation (°)
Period 1	22/02/20	7495	24/02/20	0.095	225
	02/03/20	7590	25/02/20	0.130	250
Period 2	07/06/20	8085	03/06/20	0.080	95
	30/05/20	8130	04/06/20	0.110	130

In Figures 5.3.3 and 5.3.4 the Yaw value as a function of the time for the

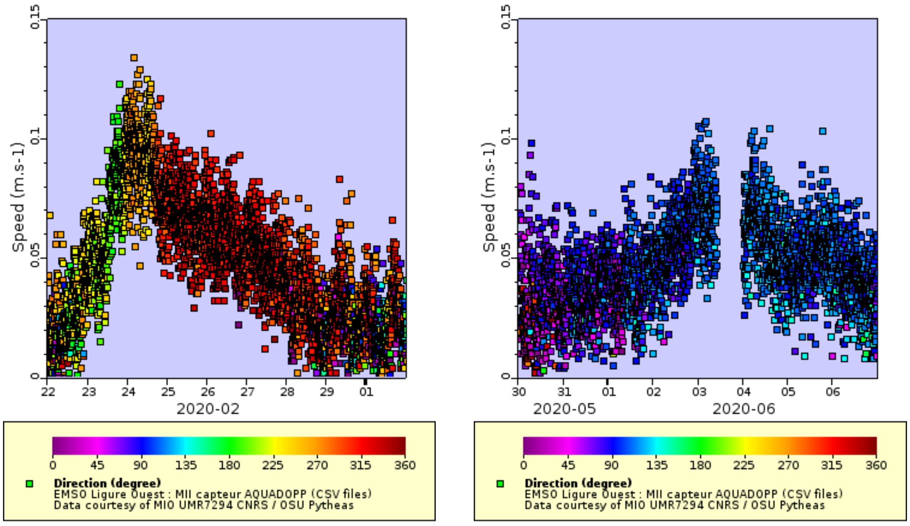

(a) Sea current speed and direction for Period 1.

(b) Sea current speed and direction for Period 2.

Figure 5.3.2: In Figure (a) there is the plot representing the speed of the sea current as a function of the time and in color the speed direction for Period 1. In Figure (b) the same for Period 2. Both plots are taken from [8].

two periods for DU2 are shown. In the Appendix A more plots for the Yaw, Pitch and Roll can be found, including those from other DUs.

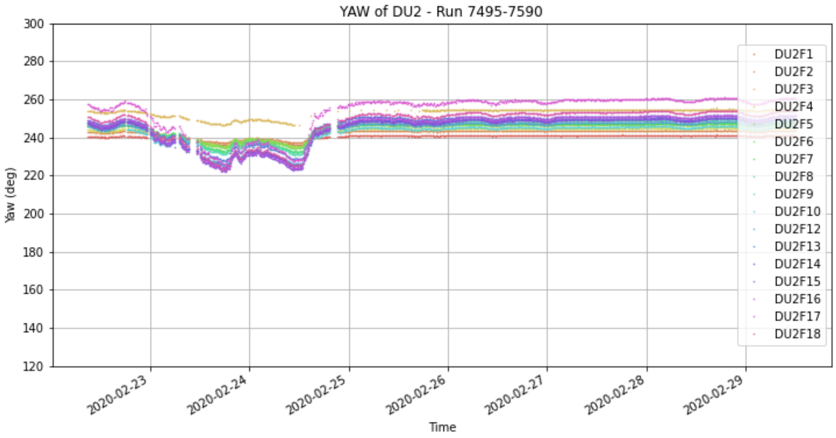

Figure 5.3.3: Yaw of the DU2 for the Period 1, with strong sea current.

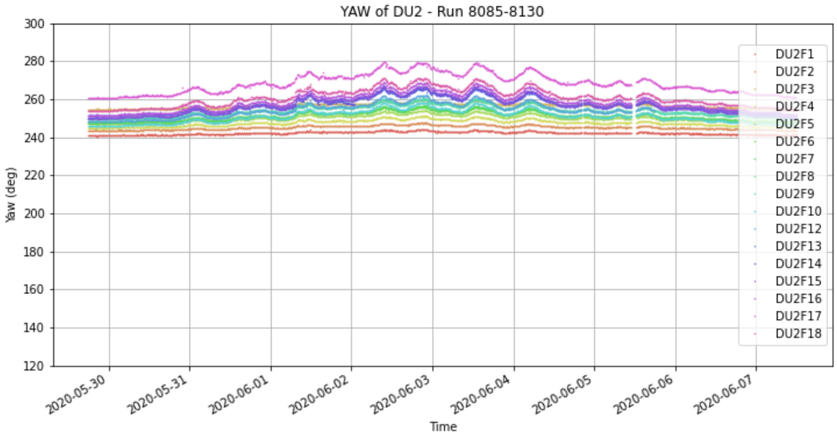

Figure 5.3.4: Yaw of the DU2 for the Period 2, with strong sea current.

From the Figures 5.3.3 and 5.3.4 it can be seen that higher DOMs are subject to larger displacements from the vertical line positions than lower DOMs. Secondly, it can be seen that for Period 1 the Yaw values decrease while for Period 2 they show an increase. This indicates that the different current directional orientation can be directly monitored with compass data. In addition, looking at the Figure A.1.22 and Figure A.2.4, in the Appendix A, it is possible to observe that DU9 has a different behaviour with respect the the other lines; this is due to the fact that DU9 is oriented in a different direction with respect to the other lines, as it is reported in Table 5.1. Moreover, DU9 does not have a top buoy since it had to be cut due to some technical problems during deployment so it can be more (or differently) affected by strong sea currents.
For completeness, in Appendix A the Pitch and Roll plots are also reported; from them it is possible to observe that the strong sea current affect also these two values, but the displacements are really small with respect to what is observed for the Yaw.
I carried out further investigations using the measured Yaw values. The two strong sea current periods of Table 5.2 and the quiet period in Section 5.3.1 were used. First of all it is necessary to pick a reference value for the Yaw value of each DOM in each DU. These reference values have been computed for the period of low sea current, since the Yaw values are stable: the mean value of the measured Yaw of each DOM in each DU has been considered. For the two periods of strong sea current, for each DOM in each DU, the minimum (in the case of Period 2 with the exception of DU9) or the maximum (in the case of Period 1 with the exception of DU9) have been

considered. Using these values described above, two different checks have been performed.
The difference between the minimum or maximum Yaw values during the strong sea current periods and the Yaw mean value during the period of low sea current have been studied at first. These have been plotted as a function of the DOM floor and an example of these is reported in Figure 5.3.5 and Figure 5.3.7 for DU2, for period 1 and period 2 respectively. It is possible to notice that the increasing behaviour of these differences is linear with the DOM height, positive in the case of period 1 and negative for period 2. This is explained by the different orientation of the sea current in period 1 with respect to period 2, as already described above.
Another check has been done computing the difference between the minimum and the maximum Yaw values recorded in the periods of strong sea current for each DOM. An example of this is reported in Figure 5.3.6 and Figure 5.3.8 for DU2, respectively for period 1 and period 2. As in the previous study, and as expected, also in this case the difference between the values has an increasing behaviour which is linear as function of DOM height.
These studies confirm that higher DOMs are more affected by the sea current not only in terms of displacement but also of twist. The Mechanical Model of the DU that will be presented in the next section takes this into account.
These studies have been performed for all DUs of KM3NeT/ORCA, but here only the results of DU2 are reported as an example. A systematic error of 3° is attributed to the Yaw value measurements.
My analysis and the checks that came with it have shown the importance of the monitoring of compass data and the valuable information they carry. Such monitoring, both qualitative and quantitative, is necessary to establish the reliability of this data in input for the position and orientation calibration procedures.

5.4 Detection Unit Line fit

The work shown above has paved the way for further developments, in particular related to the reconstruction of the DOM positions under-sea, first and foremost for the development of the *Detection Unit Line fit*. This part of my work has been developed in collaboration with D. Diego-Tortosa, a PhD student of the KM3NeT group at Universitat Politècnica de València.
The *Detection Unit Line fit* has been developed from the past experience of ANTARES [32] and allows the reconstruction of the position of the DUs using as input raw data from the AHRS or from the Acoustic Positioning System (APS) in KM3NeT. The procedure includes the application of equation from a Mechanical Model (MM) that can be applied to two different analyses, depending on the input data to study: *tilt* and *position* methods.
In Figure 5.4.1 a complete scheme of this DU Line Fit is reported.

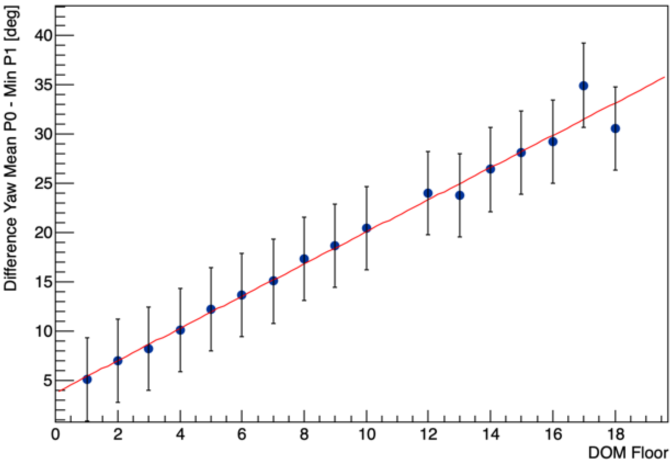

Figure 5.3.5: Differences between the Yaw mean value for the period with low sea current and the Yaw minimum value of each DOM for period 1. The result of DU2 as example is reported.

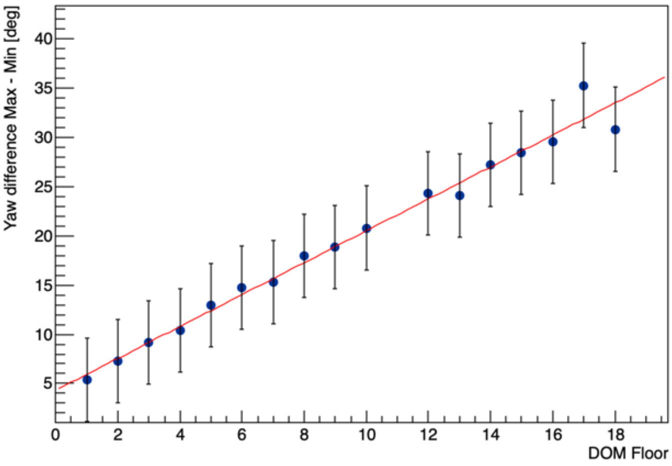

Figure 5.3.6: Differences between the Yaw maximum value and the Yaw minimum value of each DOM for period 1. The result of DU2 as example is reported.

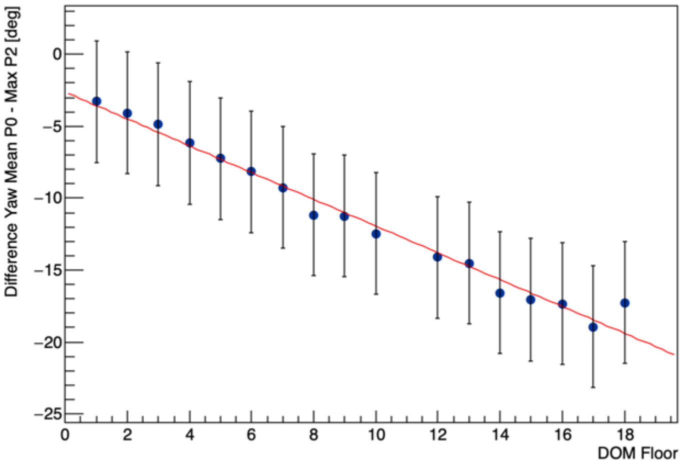

Figure 5.3.7: Differences between the Yaw mean value for the period with low sea current and the Yaw maximum value of each DOM for period 2. The result of DU2 as example is reported.

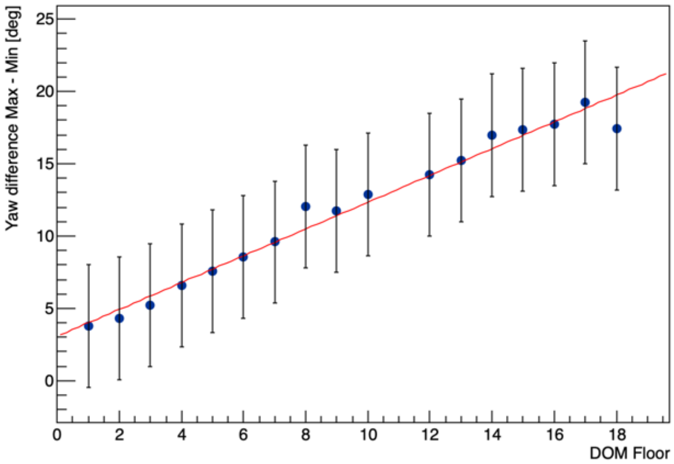

Figure 5.3.8: Differences between the Yaw maximum value and the Yaw minimum value of each DOM for period 2. The result of DU2 as example is reported.

5.4.1 Application of the Detection Line Fit Model using compass data

The goal of the Detection Line Fit Model is to reconstruct the position [X,Y,Z] in space of the DOMs using as input the AHRS raw data. In the

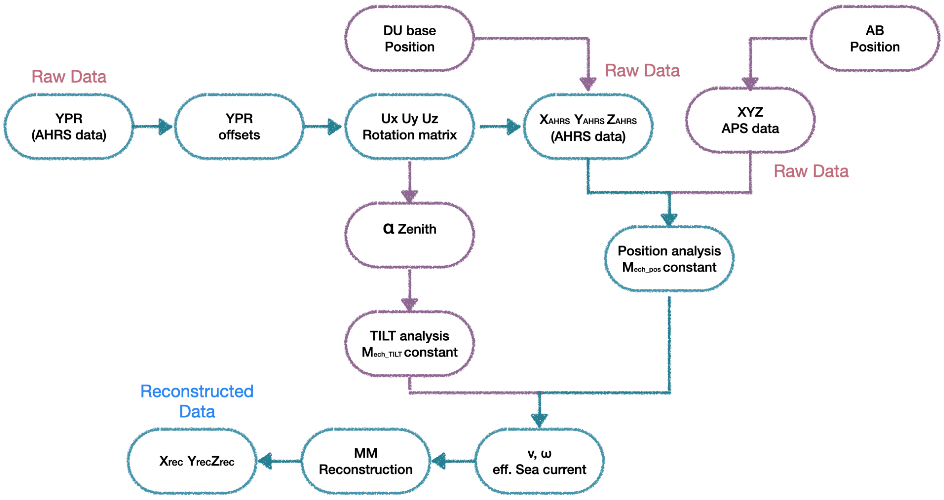

Figure 5.4.1: Detection Unit Line Fit analysis procedure in KM3NeT. The results presented in this work follow the strategy marked in blue.

first step of the procedure, the offset corrections are applied to Yaw, Pitch, and Roll; these offsets are obtained by studying the shapes of the lines in periods in which strong sea currents are absent and assuming that the lines are perfectly vertical. Once the offsets are applied, the YPR values are transformed into position in space; in order to do this, a rotation matrix is applied [183].

After this, it is necessary to recover the information related to the sea current properties, as velocity and direction. In order to achieve this a Mechanical Model (MM) is applied. The MM for KM3NeT uses the sea current properties (velocity and direction) to eventually provide the line shape and, in other words, the DOMs positions. The MM determines the coordinates in space [X,Y,Z] from the velocity (ν) and direction (ω) of the sea-current using the mechanical properties of the string in terms of buoyancy of its elements and tensions along the DU [205]. The MM can work in two different ways, depending on the data provided for the fit: *tilt* and *position* methods. In this thesis only the results obtained with the *position* methods are presented and described.

For this case, the MM equations are:

$$r = M_{pos} \cdot \nu^2 \tag{5.4.1}$$

where r is the displacement from the vertical position (which can be calculated from XYZ data), M_{pos} is the *mechanical constants* calculated for the position method of the MM which takes into account the drag and buoyancy forces of the different elements, and ν represents the sea current velocity.

The MM performs a linear fit using the mechanical equations to estimate the effective sea current velocity (ν) and the effective sea current direction (ω) from the input data.
Once the sea current properties are obtained, then it is possible to apply the Mechanical Model to get the reconstructed position XYZ.
An example of the results coming from this reconstruction method is reported below; the period considered is February 24th 2020, from 6:00 am to 9:00 am, and all six DUs of KM3NeT/ORCA have been considered. The results of the fit computing the sea current velocity and direction are shown in Figure 5.4.2. The Figures 5.4.3, 5.4.4, 5.4.5 show the final results of the

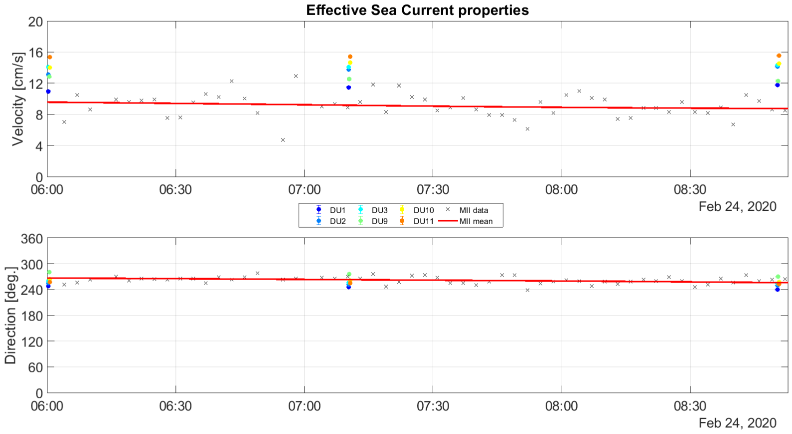

Figure 5.4.2: Sea Current properties deduced from the the Line Fit Mechanical Model as a function of time: Top: the sea current velocity; Bottom: the sea current direction.

DU Line Fit: the reconstructed position [X,Y,Z] during the three hours considered in the different dimension/point of view. It is possible to see the DU movements due to the strong sea current.
This model has been applied to all six DUs of KM3NeT/ORCA; also it is applied to DU9 that does not have a top buoy, and its absence ts taken into account in the M_{pos} factors. The results presented here show that the developed DU line fit model using AHRS data with the *position method* looks promising. This method has been developed to be used for cross-checks on periods where there is a strong sea current that can displace the top DOMs of the DUs by a few metres from the vertical position. These results show the possibility to reconstruct the positions of the main components of the detector independently of the acoustic positioning system.

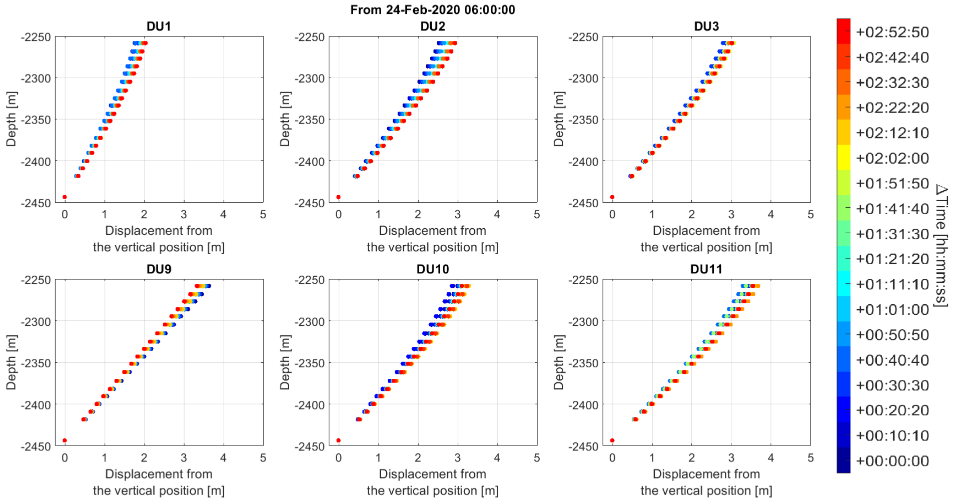

Figure 5.4.3: Detection Unit Line Fit position reconstruction with horizontal displacement.

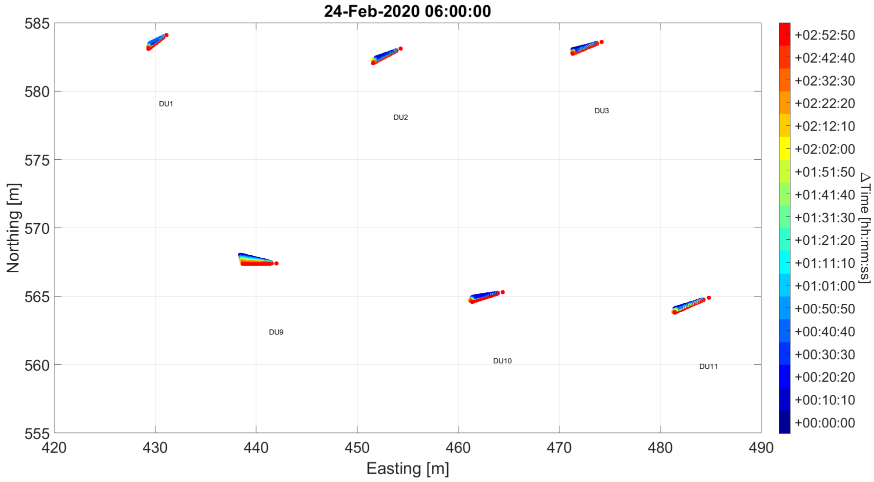

Figure 5.4.4: Detection Line Fit position reconstruction with top-view for each line with respect to their position on the sea-bed.

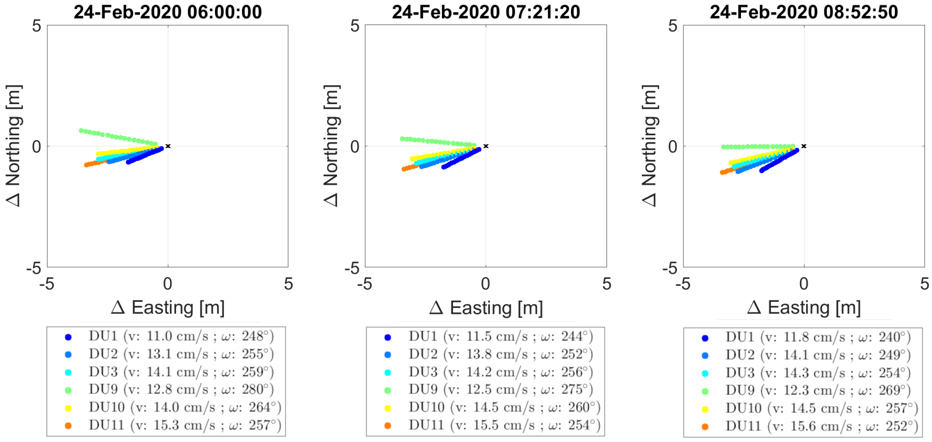

Figure 5.4.5: Detection Line Fit position reconstruction with top-view in three different moments: at the beginning of the considered period (left plot), in the middle (plot in the middle), at the end (plot on the right).

Part III

Dark Matter searches towards the Sun with ANTARES

Leela: Dear Captain's Diary: I may not have found love on this mission but I did find a cute little companion who excretes starship fuel. And that's just as good.
Bender: Aw man, that crap's heavy!
Fry: And warm...

E4S1, Futurama

Chapter 6

Dark Matter phenomenology

Dark matter (DM) is one of the pillars of the Standard Cosmological Model but its nature remains unknown today, despite the convincing evidence of its effects on large astrophysical scales. The possible connection with theories beyond the Standard Model of particle physics makes it one of the most important open problems in modern cosmology and particle physics, as evidenced by the enormous theoretical and experimental efforts that have been made to identify it.
In this chapter the evidences and the candidates of DM are shown, with particular attention to the Weakly Interactive Massive Particles (WIMPs) candidates. The final part of this chapter is dedicated to the different techniques that can be exploited in order to detect DM, and in particular those using neutrinos and for which neutrino telescopes represent the ideal detectors. The possible DM sources, and the reasons why they can be ideal targets for neutrino telescopes will be presented, with a particular focus on the Sun as an emitter of neutrinos from dark matter.

6.1 Introduction to the Dark Matter problem

The Swiss astronomer Firtz Zwicky, while examining the Coma galaxy cluster, discovered in 1933 the existence of a possible gravitational anomaly in the velocity distribution of galaxies in the cluster [216]. Indeed, luminous matter in the cluster showed an excessive velocity when compared to the calculated gravitational attraction within the cluster from the same luminous matter. Using the Virial Theorem, he computed the gravitational mass of the cluster from the galaxy velocities and obtained a value at least 400 times greater than expected from their luminosity. He attributed this difference to a *Dark Matter* [217] component that was present in the cluster, of unknown origin. Even though the same calculation today shows a smaller discrepancy, since larger values for the mass of luminous material have been estimated, it is still clear that the great majority of matter could have been attributed to this DM component.

Many other studies have been carried out since then, and other many experimental evidences have given proof for the existence of *something different*, i.e. the existence of dark matter. In particular the usage of gravitational lensing to estimate the matter content of astrophysical objects and compare it to the *luminous* component, as well as the detailed measurement of the Cosmic Microwave Background (CMB), have shown that most of the matter in our Universe must be in this *dark* form. The most precise measurement of the CMB [97], combined with the results from the simulations of the formation of the large scale structures, such as galaxy and galaxy clusters, indicates that baryonic matter only contributes to 4.9% of the total mass-energy of the Universe, while dark matter represents 26.8%. The remaining 68.3%, called dark energy, is a hypothetical form of energy that creates a negative, repulsive pressure in space-time, behaving like the opposite of gravity and thought to be responsible for the acceleration of the expansion of the Universe in the current times. Figure 6.1.1 shows a pie chart of the matter-energy content of our Universe.

The Standard Model (SM) of particle physics is a Gauge theory and for many years this theory was believed to be complete. The discovery of the oscillations of neutrinos, explained by the hypothesis that neutrinos are not mass-less as in the SM, demonstrated that the SM was not complete. Over the years, various theories have been formulated proposing to move beyond the Standard Model. In particular, these Beyond Standard Model (BSM) theories usually try to accommodate some kind of particle dark matter. An example is the Supersymmetry (SUSY) [212], which involves a symmetry between fermions and bosons, being the neutralino the best candidate for dark matter [90]. This will be shown more in details in Section 6.3

In any case, the nature of dark matter is still unknown nowadays: whether it is a particle, or a set of particles, whether it comes from BSM theories, whether its effects could actually come from deviations from our standard gravitational theories and not from an additional form of matter, this is still all questionable [175]. For this reason DM remains one of the most important and challenging mystery of particle physics and cosmology.

6.2 Evidences of existence of Dark Matter

The existence of dark matter, a non-luminous - i.e. which, per se, does not emit light - and non-absorbent - i.e. that does not produce observable effects by absorbing surrounding or background light - is pretty well established because of the different independent observations, on different astrophysical scales, that have been conducted over the last century. This great wealth of observations has allowed an estimation of its density in the Universe. These observations can be divided into two categories: direct evidence and indirect

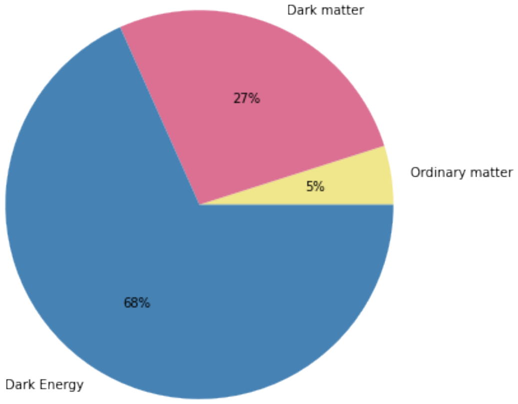

Figure 6.1.1: Relative abundances of mass-energy elements in the Universe.

indications.

Direct evidences come from those measurements that show that some measured gravitational effects cannot be explained by considering only the observed distribution of luminous matter. Indirect evidences are provided by the measurements of the properties of anisotropies of the CMB, by the distribution of cosmic structures and cosmic structure formation in our Universe along its life.

6.2.1 The Galactic scale

The measurement of the rotation curves of galaxies, that are the distribution of velocities of stars and gas as a function of their distance from the center of host galaxies, can provide a direct evidence for the existence of dark matter [90]. Considering Newton's laws and assuming that the stars of a spiral galaxy have a circular orbit around the center of the galaxy, the rotation speed is given by:

$$v(r) = \sqrt{\frac{GM(r)}{r}} \tag{6.2.1}$$

where the mass distribution is $M(r) = 4\pi \int_0^r \rho(r')r'^2 dr'$ assuming a spherical symmetry, and $\rho(r)$ is the mass density. Considering the mass distribution of visible matter in spiral galaxies, for large radii, the trend of the velocity should be proportional to $1/\sqrt{r}$ since most of the mass of spiral galaxies is in their bulges. Experimental data show, however, that velocity distributions appear to have a constant trend in the outskirts of all spiral galaxies; this would require that the total mass of the galaxy is directly proportional to

the distance from the galactic center $M(r) \propto r$ and thus the matter density is $\rho(r) \propto 1/r^2$. In Figure 6.2.1 the discrepancy between the newtonian model and the experimental results is shown for the particular case of the spiral galaxy NGC 6503. This same behaviour has been observed in many other similar objects. The flattening of the rotation curves therefore suggests the presence of non luminous (dark) matter distributed as a massive halo around the galaxy and extending to distances much greater than its visible radius. As it will be explained in Section 6.2.2, anomalies are not only visible when considering Newtonian Gravitation, but also General Relativity. As a consequence, one can then assume that there is in fact a missing mass problem and not a modification of the gravitational attraction.
Following the indications described above, in order to provide a flattening of the rotation curves, the DM density should then follow a distribution:

$$\rho(r) \propto \frac{M(r)}{r^3} \sim r^{-2} \tag{6.2.2}$$

which thus corresponds to a spherically symmetric halo around the galaxy center.

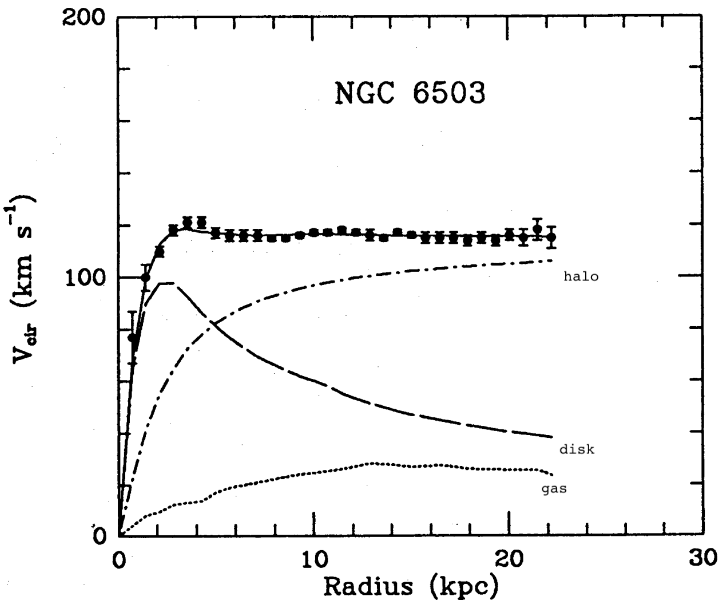

Figure 6.2.1: Galactic rotation curve for NGC 6503 showing disk and gas contribution plus the dark matter halo contribution needed to match the data. Figure taken from [84].

6.2.2 Gravitational lensing

According to the theory of General Relativity, light propagates along geodesics. A geodesic, $x(\tau)$, is the shortest curve connecting two arbitrary points in a space and which, in general, depends on a parameter τ, which may be the proper time. Light travels along a curved geodesic when it passes close to a gravitational field, and the stronger the field, the greater the deflection. A schematic description of this effect is reported in Figure 6.2.2. This deflection generates what is commonly known as *gravitational lensing*.

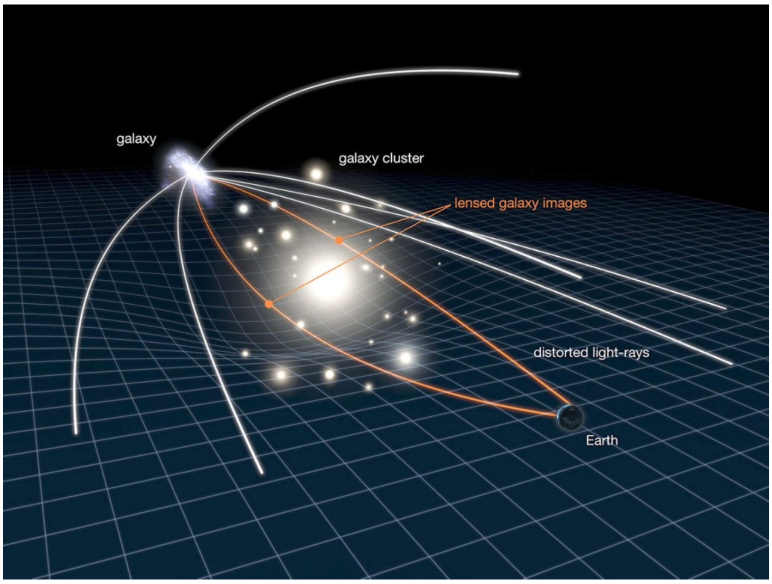

Figure 6.2.2: Scheme of what happens to the trajectories of light rays when they pass near large masses such as clusters of galaxies. Figure taken from ESA [9], Credit: NASA, ESA & L. Calçada.

A clear display of these effects appears in clusters of galaxies, since they are extremely massive and can thus produce extreme deflections of light coming from further beyond them. Since space-time is curved in proximity of a cluster, the light emitted by objects behind it travels along a curved path to reach our telescopes. The distortion of images of objects that are behind a cluster of galaxies can be used to better understand the shape of the gravitational potential and therefore the mass of the object [211]. In Figure 6.2.3 it is possible to observe the deflection of the light induced by the galaxy cluster in the foreground of the image, which create a kind of different arcs. These are the deformed images of objects that are placed further beyond the cluster whose mass is deflecting light from there.
The deflection angle caused by a certain object of mass M, for a given impact

parameter b, is defined as:

$$\alpha \sim \left(\frac{GM}{bc^2}\right)^{1/2}. \tag{6.2.3}$$

The deflection angle can be measured experimentally while the impact parameter can be obtained from the red-shift difference between the cluster and the source behind it; from these values it is possible to obtain the total mass M. In all galaxy clusters, the total mass M measured using gravitational lensing is much larger than the mass that can be inferred for the components that emit light, for example stars in galaxies or gas in the inter-cluster medium [114].

Thanks to the observation of gravitational lensing, which is an effect directly connected with the amount of mass of the object coming from General Relativity, it is possible to assume that it is indeed necessary to add an additional component to the mass composition of large astrophysical objects. In fact, one could possibly think of modifying Newton's law to accommodate for the difference in rotational velocity in Clusters. However, the measured masses coming from the observation of lensing end up corroborating the need of additional mass in these objects.

A very peculiar case is the Bullet Cluster [107]. In this celestial object, two galaxy clusters have collided. After the collision, the intra-cluster gas of the two have interacted and heated up, producing a strong X-ray emission. However, gravitational lensing measurements show that the largest part of the mass of the two went through the collision without interaction - in galaxy clusters, hot gas carries most of the luminous mass, and still it is smaller than the gravitational content of the whole object. It is very difficult for every theory to accommodate such effects without adding a significant amount of dark matter.

6.2.3 The Cosmological scale

The experimental evidences presented in Sections 6.2.1 and 6.2.2 demonstrate the existence of dark matter in some particular objects but do not provide information on the total amount of of dark matter that is present in the Universe. This information can be extracted from the analysis of the Cosmic Microwave Background (CMB). In 1948, G. Gamow predicted the existence of a background radiation originating from the propagation of photons in the early Universe, once decoupled from matter [60]. About 380,000 years after the Big Bang, due the Universe expansion, the temperature decreased to a point where the energy of particles fell below the ionisation threshold. From this moment began an epoch called recombination during which baryons and electrons started to form neutral atoms; after this period the Universe became transparent and photons were able to freely travel in space. Up to that moment, photons had scattered continuously with matter,

Figure 6.2.3: The galaxy cluster Abell 2218 photographed by the Hubble telescope. The arcs of light that are observed are an optical effect due to gravitational lensing. Figure taken from ESA [10], Credit: NASA, ESA, and Johan Richard (Caltech, USA).

thus assuming a black body spectrum. Since the "last scattering", their spectrum has remained almost unchanged from that black body spectrum, just cooling down in temperature as the Universe expanded. Photons that have free streamed until today are what we call cosmic microwave background.

The first experimental test that proved the existence of the CMB was in 1965 by A. Penzias and R.W. Wilson using the Holmdel Horn Antenna [182]. Over the years, with the development of more precise instruments, various measurements have been carried out on the CMB and to date we know that the black body spectrum corresponds to a temperature of $T = 2.726\,\mathrm{K}$ and furthermore it is spatially isotropic within one part in 10^5 [218]. In Figure 6.2.4 the most updated temperature fluctuation of the CMB is shown.

The existence of the CMB is an indication that there must have been a primordial phase in which the Universe was in thermal equilibrium. In fact, different black body distributions, corresponding to regions of the Universe with different temperatures, could not give a single black body distribution, but it would result in a frequency distribution of another shape.

The most accredited cosmological model is the Λ Cold Dark Matter (ΛCDM) [204], [163], which refers to the main components of the Universe. The Cold Dark Matter component is indeed what we have referred to so far as Dark

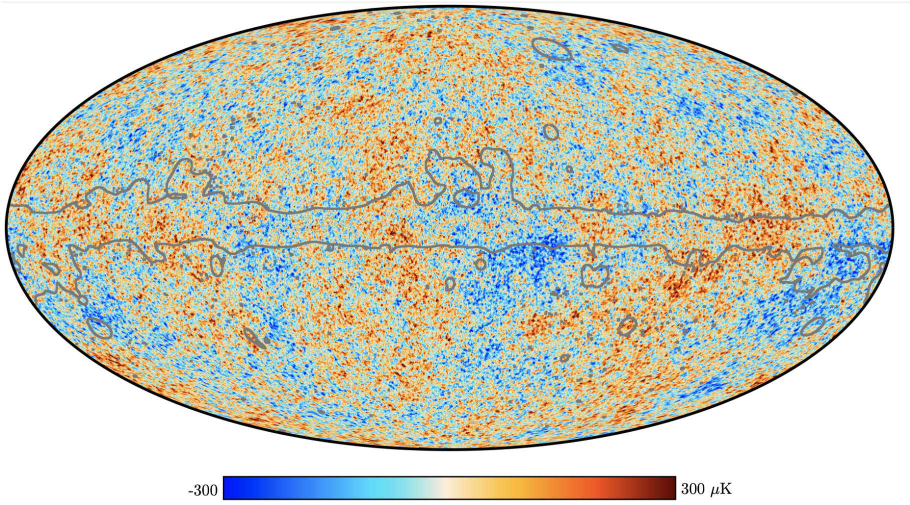

Figure 6.2.4: Plank sky: 2018 SMICA temperature map. Figure taken from [37]

Matter (with the attribute *Cold* that will be explained later). The Λ term is the cosmological constant in the General Relativity equations. This model is based on the assumption that cold dark matter and a cosmological constant Λ, usually referred to as Dark Energy, exist alongside photons, neutrinos, charged leptons and baryons. It is expected that in the early phases of the Universe, radiation dominated the equation of state; then, as the Universe cooled down, it entered a matter-dominated phase. The current phase, where the Universe is expanding at an accelerated rate, is dominated by the Λ term in the equation of state. In the first phases, due to the rapid rate of particle interactions with respect to the expansion rate of the Universe, thermal equilibrium was present [218].

A detailed analysis of the CMB anisotropy maps, such as the one shown in Figure 6.2.4, can be used to extract physical information such as baryonic and matter density. Over the last decades, the CMB radiation has been analysed with the purpose of extracting high precision measurements of its properties by different satellites such as WMAP and Planck. In particular, the Planck experiment, an European Space Agency mission launched in 2009, has recently published the results obtained from the last Legacy data release in 2018 [37]. The cosmological parameter results, from the final full-mission Planck measurements of the CMB anisotropies, combining information from the temperature and polarization maps and the lensing reconstruction, show that the densities of matter at 68% C.L. [38] are:

$$\Omega_b h^2 = 0.02226 \pm 0.00023 \tag{6.2.4}$$

$$\Omega_{nbm} h^2 = 0.1186 \pm 0.0020 \tag{6.2.5}$$

where h is the Hubble constant in units of 100 km/(s Mpc), Ω_b is the density of baryonic matter and Ω_{nbm} is the density ratio of non-baryonic matter. From these numbers it is possible to notice that the density of non-baryonic matter is about five times that of ordinary matter. From the same analysis the updated value of the Hubble constant $h = 67.8 \pm 0.9$ km/(s Mpc) is obtained [38].

Combining observations of our galaxy with data from other galaxies, such as the rotation curves, it is possible to estimate the value of the local dark matter density (68% C.L.) [194]:

$$\rho_{DM}^{local} = (0.387 \pm 0.036)\, GeV/cm^3 \tag{6.2.6}$$

6.3 Dark Matter candidates

What is dark matter made of? This is one of the main questions in the fields of Particle and Astroparticle Physics and in Cosmology. Since the first hypotheses of its existence, and even after several observations that provided more and more evidences for its existence, nowadays, the answer is not known yet.

Several dark matter candidates with different characteristics have been proposed. Anyway, DM candidates have to satisfy some minimal requirements:

1. They have to be electrically neutral: if they were not neutral, they would have electromagnetic interactions and thus either emit or absorb some light - making them not anymore *dark*.

2. They have to interact very weakly with ordinary matter: their long-ranged interactions can indeed only be gravitational, without electromagnetic interactions which otherwise would emit/absorb light.

3. They have to be stable on the cosmological time scale.

4. They must be non-relativistic: indeed, simulations of structure formation in the Universe show that adding a relativistic component washes out anisotropies in the matter distribution in the early Universe and slows down structure formation such as galaxy clusters. For this reason the Dark Matter must be *cold* - non relativistic.

In Table 6.1 some of the most popular DM particle candidates are resumed. In Figure 6.3.1 the interaction probability of DM candidates as a function of the DM particle mass is reported. There are other theories not discussed

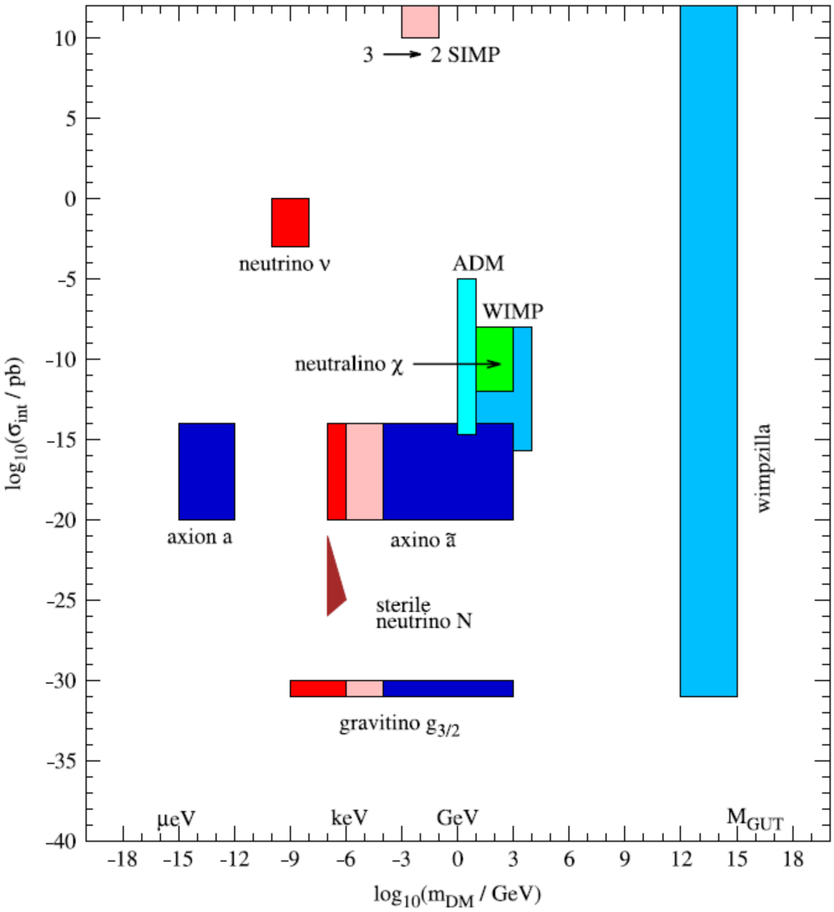

Figure 6.3.1: Most of the favourite DM candidates: σ_{int}, representing the typical strength of interactions with ordinary matter, as a function of the DM mass. The red, pink and blue colors represent Hot DM, Warm DM and Cold DM, respectively. Figure taken from [77].

here that try to explain the observations without the requirement of particles that satisfy the aforementioned minimum requirement, such as the MOdified Newtonian Dynamics (MOND) [175] introduced by M. Milgrom in 1983. According to this model, the intensity of gravitational attraction does not decrease with the typical trend. However, it is not consistent with observations of clusters of colliding galaxies [172], as explained in Section 6.2.2.
Other interesting theories are based on the Kaluza-Klein theory [197] using physics in extra dimensions. This theory came from the attempt to unify electromagnetism with gravity. The basic idea is that every multidimensional field correspond to a Kaluza-Klein tower of four-dimensional particles with

increasing masses. The most promising theory are based on extra dimension is the Randall-Sundrum set-up [187], using a slice of 5D anti de Sitter spaces. Also neutrinos were taken in consideration as DM candidates but there are two main problems to account for: the first one is related to the total fossil density of neutrinos, measured from the analysis of the CMB anysotropies, which is not large enough, and thus does not satisfy requirement on the cosmological time scale; also neutrinos do not satisfy requirement number 4, since they are relativistic particles.
In the next subsections the characteristic of baryonic and non baryonic candidates are presented. A particular attention will be given to WIMP candidates (Section 6.4) since the work of this thesis is based on them.

Table 6.1: Characteristics of the most famous DM candidates for Baryonic and Non-Baryonic families.

Family	Sub-Family	Mass range	Candidates
Baryonic	MACHO	10^{-2}-10^{14} $M_\odot$	Brown Dwarf Neutron star
Non-Barionic	Hot DM	$< 1\,\mathrm{keV/c^2}$	Axions Neutrinos Light Goldstone Bosons
Non-Barionic	Warm DM	$1\,\mathrm{keV/c^2}$ - $10\,\mathrm{GeV/c^2}$	Sterile neutrinos
Non-Barionic	Cold DM	$> 10\,\mathrm{GeV/c^2}$	Neutralino Gravitino WIMP

6.3.1 Baryonic candidates

It is possible to build a dark matter model where ordinary matter actually plays its role, as long as there are objects made of baryons which do not emit light. MAssive Compact Halo Objects (MACHOs), which could be white dwarfs, brown dwarfs, dark stars, neutron stars and black holes, could indeed modify the gravitational potential of galaxies without being visible. Experimental measurements of the Large Magellanic Cloud, using microlensing observations (i.e. gravitational lensing on small scales), concluded that MACHOs can only explain a few percent of the mass of the DM halo in our galaxy [59].
In addition, since these astrophysical objects must have been created at a "late" stage of the Universe evolution, i.e. at least after the creation of elements in the Big Bang (the Big Bang Nucleosynthesis), and since the amount

of primordial elements in the Universe allows to constrain the baryonic content [111], an overabundance of such object would violate these limits [130]. A possible alternative is given by Primordial Black Holes [215]. Indeed, these astrophysical objects consist of baryonic matter but have been created before the formation of primordial elements, and thus are not subject to the cosmological constraints of Section 6.2.3, since the material of which they are made is subtracted very early on from the baryonic content of the Universe. Exotic scenarios must be invoked to create these primordial black holes [104]. However, also in this case, the experimental limits tend to exclude a significant contribution from these objects [192].

6.3.2 Non-Baryonic candidates

As it is schematized in the Table 6.1, there are different non-baryonic DM candidates, and they could be divided into three different families.
The *Hot DM* (HDM) candidates are particles with really small masses under the keV and and thus should travel with ultra-relativistic velocities. The most popular particle candidate in the Hot DM family is the **Axion**, postulated in 1977 by Robert Peccei and Helen Quinn [181]. This particle is introduced to resolve the problem of CP violation in quantum chromodynamics (QCD) [147] [186]. Since dark matter must be non-relativistic, their small mass requires that axions, as valuable candidates, were not produced in the early Universe in thermal equilibrium with the rest of matter, but through vacuum realignment mechanisms [118], thus *at rest*. In addition, it is expected that they interact very weakly with ordinary matter. Computations of their density yield different results as a function of the axion production mechanism. However it is possible to find an acceptable range of parameters which satisfies the minimum requirements to be a DM candidate [140]. HDM models are today disfavored and small amounts of HDM can still be tolerated, provided that it is compatible with large scale structure and CMB data [204].
The *Warm DM* (WDM) candidates with masses in the range of keV up to 10 GeV are chargeless, have zero weak hypercharge, zero weak isospin, and zero color charge. They are supposed to interact only via gravity and not via any of the other fundamental interactions of the Standard Model. WDM particles are supposed to be relativistic at decoupling, but non-relativistic at the radiation-to-matter dominace transition. The most popular candidate is the **sterile neutrino**, proposed for the first time as DM candidates in 1993 by Dodelson and Widrow [117]. As the name suggests, it has similar characteristics to the SM neutrinos, but it does not interact via the weak force. The addition of 3 right-handed neutrinos in the Standard Model Lagrangian, which can be used to make neutrino masses emerge, could provide a prediction of these sterile neutrinos [142]. These candidates are supposed to be produced in the early Universe by oscillation conversion of thermal ac-

tive neutrinos, with a momentum distribution significantly suppressed and distorted from a thermal spectrum. If the production rate is always less than the expansion rate, then these neutrinos will never be in thermal equilibrium. However, they may still play a significant role in the dynamics of the Universe and possibly provide the missing mass necessary for closure.
Cold DM (CDM) candidates have masses above 10 GeV. The adjective *cold* refers to the fact that they should move slowly with respect to the speed of light, thus they should be clearly non-relativistic and they have become non-relativistic well before the matter-dominated era. The most popular CDM candidates are **WIMPs** (Weakly Interactive Massive Particles), and **Neutralinos** are among the favourite ones among particle physicists. In the Supersymmetry model, each SM particle has a correspondent superymmetric particle. In the Minimal Supersymmetric Model (MSSM) [197], 4 neutralinos are present. These are the 4 symmetric particles of the Standard Model Electro-Weak Bosons. The lightest of them should be stable, and thus could be a proper DM candidate. Neutralinos, as supersymmetric partners of the SM Electro-Weak Bosons, are fermion and are electrically neutral.

6.4 Weakly Interactive Massive Particles

The production mechanism of WIMPs assumes that in the early Universe they were in thermal equilibrium with the ordinary matter plasma [139]. At high temperatures there was a continuous exchange between WIMPs and standard model particles via production and annihilation reactions. With the expansion of the Universe and its consequent cooling, the lighter particles no longer had enough kinetic energy to produce DM. Therefore the density of DM collapsed with an exponential trend ($n_\chi \propto e^{-M_\chi/T}$) and the annihilation rate fell below the expansion rate ($\Gamma_\chi = \langle\sigma v\rangle n_\chi < H$). This moment is called *freeze-out* and WIMPs decoupled from plasma resulting in the relic density of DM observed today [127].
WIMPs are the most popular dark matter particles because they appear spontaneously in several supersymmetric (SUSY) [161] models and also in some models of extra-dimension [196], [197]. In SUSY models it is expected that to each SM particle a supersymmetric partner is assigned; these partners share all quantum numbers except spin, which should differ by 1/2. This symmetry is called *R-parity* [161], in which ordinary particles have $R = 1$ and the super-partner $R = -1$. If R-parity is not violated in the model, the lightest supersymmetric particle (LSP) will be stable and it is a good WIMP candidate.
Despite strong theoretical motivations, no experimental evidence has yet been found for the existence of supersymmetric particles. Their research is one of the objectives for the current generation of particle accelerators, as the Large Hadron Collider (LHC) at CERN in Geneva.

6.5 Detection of Dark Matter

Considering the WIMPs as DM particle candidates and considering that these particles interact weakly, they can be detected in three different ways following the scheme in Figure 6.5.1:

- production at colliders;
- direct detection;
- indirect detection.

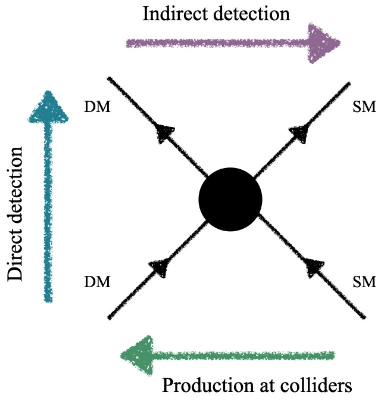

Figure 6.5.1: Scheme of WIMP detection.

6.5.1 Dark Matter at colliders

DM particles can be produced in colliders from the interaction of SM particles. In particular, the production of DM in colliders with $p-p$ collisions can be inferred from the transverse momentum of particle against which the DM recoils. Indeed, since DM particles that could come out of the collision will not interact in the detector elements, an imbalance in the deposited energy and momentum out of the interaction vertex should be observed. This is know as missing transverse momentum and would be a probe or DM signals [13] [14].

Searches at colliders can only prove the stability of WIMPs on the required timescale by these particles in order to exit from the detector and thus the discovery of a WIMP-like particle at colliders would require validation from astrophysics or cosmology, where its stability on long time-scales could be possibly proven. Different searches at LHC collider at CERN have been carried out, the results can be found in [122], [133], [98].

6.5.2 Direct detection

It is expected that our Galaxy, and so the Solar System, is pervaded of WIMP particles and some of them, close to the Earth, can interact with ordinary matter. In these conditions, the direct DM experiments try to detect DM by measuring the recoil energy of nuclei as WIMPs scatter off them [93]. The ingredients that are necessary for the study are the density and velocity distribution of WIMPs in the Solar System and the scattering cross section of WIMP-Nucleon. Density and velocity distributions can be estimated beforehand by means of N-body simulations [69], and on the basis of this assumptions the strength of the WIMP-Nucleon interaction can be estimated. The WIMP-Nucleon scattering can be elastic or inelastic, and the scattering cross section can be either Spin-Dependent (SD) or Spin-Independent (SI).
The WIMP-nucleon elastic scattering in the detector is the interaction of the WIMP with the whole nucleus causing its recoil. From an experimental point of view, the energy spectrum of the nuclear recoil can be measured. In order to have an idea of the type of spectrum that we expect to observe, the WIMPs velocity distribution should be known. Supposing that it is smaller than the escape velocity from the Galaxy (and typical estimate for the DM velocity distribution are of the order of 270 km/s) and that WIMP masses can be in the range between 10 GeV and 10 TeV, typical nuclear recoil energies are of the order of 1 to 100 keV [197].
Inelastic scattering, on the other hand, is not observed by the recoil of a target nucleus. In this case WIMP interacts with electrons of the target atoms by exciting or ionizing them. Alternatively the WIMP can interact with the nuclei leaving them in an excited nuclear state. This process produces the same signal of a recoil, followed by a delayed emission of photons from the de-excitation of the atoms or the nuclei. Such signal have to compete with the natural radioactivity [121].
In general, the nature of the scattering process depends on the nature of the coupling between the particles that are scattering. For non-relativistic WIMPs a distinction is made between spin-dependent and spin-independent couplings. Spin-dependent interactions involve axial vectors and obviously can only exist if the WIMPs have spin. The cross section for spin-dependent scattering depends on the spin of the $J(J+1)$ nucleus rather than on the number of nucleons. Spin-independent scattering can involve axial and vector currents for nucleons and WIMPs (vector currents are absent for Majorana's WIMPs, i.e. neutralino). Due to coherence effects, this cross section increases with the square of the mass of the nucleus, so nuclei with higher mass are preferred and typically dominates spin-independent scattering in current experiments using heavy atoms as targets [197].
In order to ensure the feasibility, and to evaluate the sensitivity of a direct detection experiment, the event rate must be estimated because, when compared to the expected background, it gives an indication of the signal-to-

noise ratio. To be more general, we introduce the differential event rate: it is defined as the number of WIMP events per unit of time and detector sensitive mass. It is given by [197]:

$$\frac{dR}{dE_R} = \frac{\rho_0}{m_N m_\chi} \int_{v_{min}}^{\infty} v f(v) \frac{d\sigma_{\chi N}}{dE_R}(v, E_R) dv \tag{6.5.1}$$

where ρ_0 is the local WIMP density, $d\sigma_{\chi N}/dE_R((v, E_R)$ is the differential cross-section for the WIMP–nucleus scattering and $f(v)$ is the WIMP speed distribution, normalized to 1 and expressed in the detector frame. The integral starts from $v_{min} = \sqrt{\frac{m_N E_R}{2\mu_N^2}}$ which is the minimum velocity that produces a recoil of energy E_R.
The Spin Independent cross section is given by:

$$\sigma_{SI} = \sigma_N \frac{\mu_{\chi N}^2}{\mu_N^2} \frac{(f_p Z + f_n(A - Z))^2}{f_n^2} = \sigma_N \frac{\mu_{\chi N}^2}{\mu_N^2} A^2 \tag{6.5.2}$$

where $\mu_{\chi N}$ is the reduced mass of WIMP-nucleus and μ_N the reduced mass of the nucleus, σ_N is the WIMP-nucleus cross section. The terms f_p and f_n are, respectively, the factors of the WIMP coupling strength to protons and neutrons, while Z is the atomic number and A is the mass number of the target. The second term of the formula is derived in the approximation of $f_p = f_n$. We can thus state that the heavier is the nucleus of the target, the larger will the event rate be.
The cross sections that are typically computed in the MSSM models induce rates of at most 1 event per day per kg of detector, much smaller than the radioactive background. This explains the need for underground laboratories to protect against cosmic ray induced backgrounds, and the use of extremely radio-pure materials. The current generation of direct detection experiments measuring DM scattering on nucleons takes advantage of the Liquid Noble Gas Time Projection Chamber technologies, in particular with Liquid Argon as in the DarkSide experiment [39] and Liquid Xenon as in the XENONnT experiment [73].
In Figure 6.5.2 the limits of the spin independent cross section for direct detection experiments are presented. In this plots, also other direct detection techniques, not relying on the measurement of the recoil spectrum, are shown. These will not be treated in detail in this, but a review of experimental effors can be found in [93]

6.5.3 Indirect detection

Experiments for the indirect detection of dark matter look for signals of annihilation or decay of dark matter particles. These experiments search for signals of Dark Matter, for example, in massive celestial bodies in which it is expected that DM accumulates, and following the minimal requirements

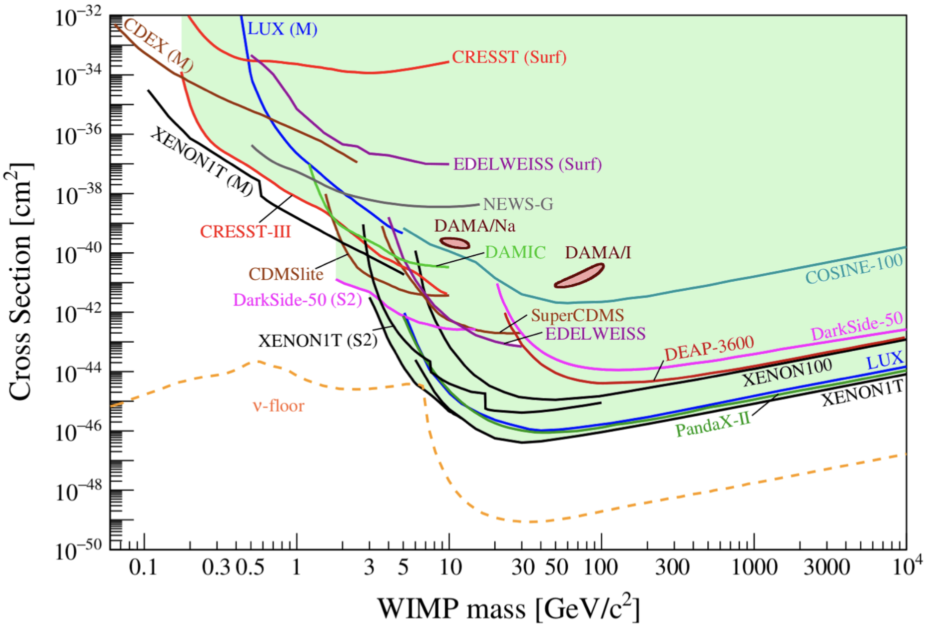

Figure 6.5.2: Current status of searches for spin-independent elastic WIMP-nucleus scattering (90% C.L.) as a function of the WIMP mass for different direct DM detection experiments. Figure taken from [93].

that DM have to be stable in a cosmological time scale. The word *indirect* suggests that these experiments do not detect directly the DM interaction, but instead its interaction or annihilation indirect products, such as neutrinos, cosmic rays and gamma rays, are measured. Gamma-ray and neutrino telescope are indeed some of these experiments performing indirect Dark Matter searches. Many experimental efforts in this field are also done using direct cosmic ray experiments; this will not be discussed in this thesis but an overview can be found in [112].

Imaging Air Cherenkov telescopes, located at different sites on Earth, provide the gamma-ray coverage in indirect searches. The two most active ones are HESS in Namibia [154], [176] and MAGIC in the Canary Islands [167]. At lower gamma-ray energies, the satellite-bound experiment FERMI-LAT [110], [54] which is a gamma-ray converter-tracker, can also scan large portions of the sky. These experiments can search for indirect dark matter signals over a broad energy range, but suffer from great uncertainties from the unknowns in photon propagation from the source to the detector. Even though a signal could be detected, the presence of many other astrophysical sources producing high-energy photons would not help in assessing this signal as a clear dark matter one.

Neutrino telescopes are based on the detection of Cherenkov light, as shown in detail in Chapter 2. Indirect searches using neutrinos, when compared to gamma-rays, benefit from the much smaller systematic coming from propagation effects since neutrinos can travel over very large distances without interference from matter or radiation fields [89]. In addition, astrophysical background in neutrino telescopes are much lower than in gamma-ray telescopes, since only hadronic mechanisms can produce high-energy neutrinos from cosmic sources and these are more rare then the plethora of possible high-energy photon emission phenomena.

In the same way as direct detection experiments, also indirect experiments are sensitive to both Spin Dependent and Spin Independent DM-nucleon scattering cross sections, through DM capture and annihilation in celestial bodies.

As it will be explained in Section 6.7, using the Sun as a target for Dark Matter searches, one can directly constrain the SD and SI cross section under certain assumptions. For other objects, indirect searches are mostly sensitive to the annihilation DM cross section. This is the case, for example, of the center of our galaxy. In this case, the flux of neutrinos can be connected to the DM annihilation cross section considering the velocity distribution of DM particles in the Galactic Halo.

6.6 Dark Matter using neutrinos

Indirect searches, using neutrinos as messengers, can look into different celestial objects for dark matter annihilation and decay signals. It is expected that DM scatters with ordinary matter, in particular with nucleons, and after losing energy is thus slowed down and can be captured gravitationally inside the source. Since one of the minimal requirements is that DM is stable over cosmological time scales, it is expected that inside a dense source, as for example the Sun, a sufficient quantity of DM has accumulated over billion years, and thus the DM density in the centre of the Sun is large enough to allow annihilation processes. According to each particular WIMP model, these DM particles could annihilate into SM particles, which in turns can produce neutrinos as end-products of their decay processes. All other particles produced in the decay process or annihilation process might be absorbed inside the source and only neutrinos might escape. Some of the different sources in which to look for DM signal with neutrino telescopes are:

The Earth

The Earth can be used for indirect dark matter searches with neutrino telescopes. The center of the Earth is indeed the closest available target in which DM can accumulate, but also the less promising. WIMPs can be captured gravitationally in the Earth only if their velocity is smaller than the

escape velocity from the planet. The escape velocity is $\sim 11.1\,\mathrm{km/s}$ at surface and $\sim 14.8\,\mathrm{km/s}$ at the centre. Considering that the velocity dispersion is $270\,\mathrm{km/s}$, only a small fraction of WIMPs would lose enough energy to become captured. Capture of WIMPs in the Earth is expected to be dominated by spin-independent elastic scattering on the most abundant heavy nuclei, mainly iron and nickel [58].
The process of WIMP annihilation in the centre of the Earth produces standard model particles that include neutrinos in their final-state decay products. The number of DM particles in a celestial object depends on time: they accumulate in the central part, where some of them undergo annihilation process. The variation of the number of DM particles as a function of the time can be written as [197]:

$$\frac{dN(t)}{dt} = C_C - C_A N(t)^2 - EN \tag{6.6.1}$$

where C_C is the capture rate, C_A is the annihilation cross section multiplied by the relative WIMP velocity per volume, E is the inverse time for a WIMP to escape the object via evaporation. This last term can be usually neglected [144]. The WIMP annihilation rate $\Gamma_A(t)$ in the Earth can be written as [161]:

$$\Gamma_A = \frac{1}{2} C_A N^2(t) = \frac{1}{2} C_C \tanh \frac{t}{\tau}^2 \tag{6.6.2}$$

where $N(t)$ is the total number of WIMPs at time t after the formation of the Earth. The equilibrium time scale τ determines the time needed for WIMPs to reach equilibrium between capture and annihilation in the core of an astrophysical object and it is $\tau = 1/\sqrt{C_C C_A}$. The annihilation factor C_A depends on the annihilation cross-section, the WIMP mass and the effective volume of the Earth [88]. Instead the capture rate C_C depends on the unknown WIMP mass and cross-section for interactions with Earth nuclei, the velocity of WIMPs in the halo and their local mass density [88]. Knowing the halo mass density, the WIMP dispersion velocity and the age of Earth it is possible to compute that the time needed to reach equilibrium is $\tau \sim 10^{11}$ years, but the Earth is only $4.5 \cdot 10^9$ years old.
Indeed, no equilibrium between capture and annihilation is expected given the limited gravitational potential of the Earth. It is thus necessary to consider both the annihilation cross section terms and the DM capture by scattering in the Earth in order to establish the amount of neutrinos which could be produced. This introduces significant systematic uncertainties in the evaluation of the scattering cross section [143]. Furthermore, the Earth is so close that the excess dark matter in its core must be treated as an extended source and different models of DM halo distribution can be considered. However, depending on the alleged annihilation cross section, the limits for the Earth may be reasonably good, although not as good as those for the Sun.

The Sun

Also the Sun is very close to neutrino detectors. Dark Matter accumulates in the centre of the Sun, which consists mainly of hydrogen, by gravitational capture. In the Sun, given its composition, a dark matter annihilation signal is particularly sensitive to spin-dependent scattering. Furthermore, the negligible astrophysical neutrino background from the Sun makes it a very clean source. This will be explained more in detail in Section 6.7.

The Galactic Centre

Given the large amount of gravitational matter in the Galactic Centre (GC), it can produce the largest dark matter signal expectations in indirect searches. In this case, dark matter is not accumulated through scattering but it is more likely to be a thermal relic from the early Universe. Theoretical models tell us that the GC cannot be treated as a point-like source in searches for a dark matter signal, but as an extended source [179]. The extension of this source and the size of the DM halo around the GC will depend on different factors which eventually lead to the DM accumulation in the GC. Various computation of the shape of this distribution are available. The differential flux of secondary neutrinos from dark matter self-annihilation in the Galactic Centre is defined as [90]:

$$\frac{d\phi_\nu}{dE_\nu} = \frac{1}{4\pi}\frac{\langle\sigma_A v\rangle}{2m_{DM}^2}\frac{dN_\nu}{dE_\nu}J \tag{6.6.3}$$

where $\langle\sigma_A v\rangle$ is the thermally-averaged self-annihilation cross section, m_{DM} is the mass of the dark matter particle and dN_ν/dE_ν is the differential number of neutrinos per annihilating dark matter pair. The factor $1/4\pi$ arises from the assumed spherical symmetry of the dark matter self-annihilation. The J-factor is expressed as:

$$J = \int_{\Delta\Omega} d\Omega(\Psi)\int_{l.o.s} \rho_{DM}^2(r(l,\Psi))dl \tag{6.6.4}$$

and is defined as the integral over the solid angle, $\Delta\Omega$, of the squared dark matter density evaluated along the line of sight (l.o.s.). The J-factor depends on the opening angle to the Galactic Centre, Ψ. The squared dark matter mass and dark matter density, as well as the factor $1/2$, result from the fact that two dark matter particles are needed for each annihilation. Given the dependence of the J-factor with the dark matter density, the final results will be dependent on the profile model considered. The two most used profile models are the Navarro-Frenk White (NFW) [179] and the Buckert profiles [102]. These two models differ by orders of magnitude close to the Galactic Centre, they become rather similar outside the solar circle in agreement with uncertainty estimations from galactic rotation curves [87]. Upper limits for

the same experiment can vary by as much as two orders of magnitude from the same search channel.
In Figure 6.6.1 the 90% C.L. upper limits on the thermally averged cross-section for WIMP pair annihilation obtained by indirect detection experiments are shown, together with the sensitivity that could be obtained by the complete KM3NeT/ARCA neutrino telescope in 1 year of operation. This is shown as a function of the WIMP mass for the $\tau^+\tau^-$ annihilation channel with the NFW dark matter halo profile [179]. The experiments shown in figure are: ANTARES with 14 years of data taking [36], IceCube [21], FermiLAT+MAGIC [47], HESS with 10 years of data taking [28] and VERITAS [74]. NFW dark matter halo in the Galactic Centre for neutrino telescopes. The galactic center is also the target for HESS searches, but a different DM halo profile has been used (Einasto [120]); this has a very large effect on the obtained upper limit, which makes it not-easy to directly compare it to the others. For the MAGIC and VERITAS results, Dwarf Spheroidals are used [75], [48].

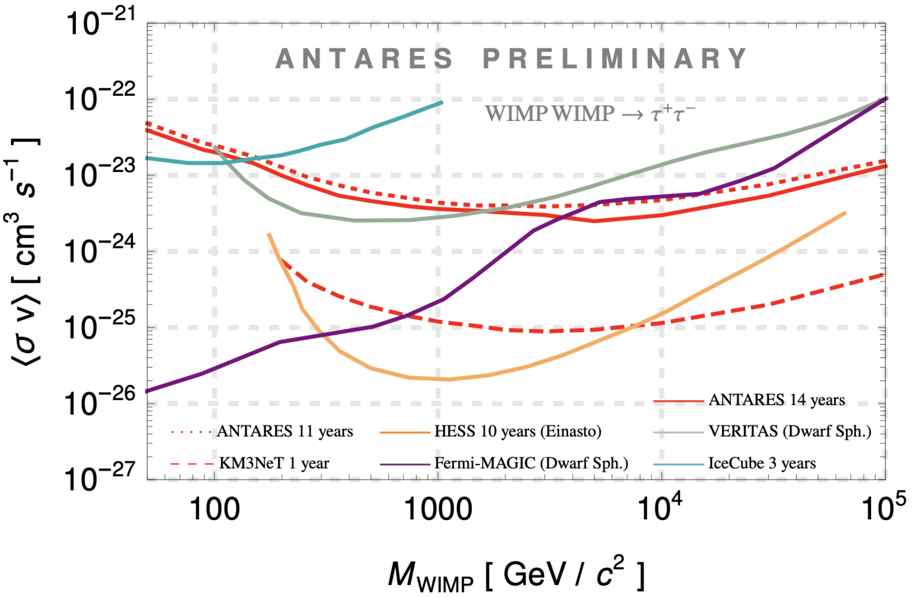

Figure 6.6.1: Upper limits at 90% C.L. on the thermally averaged cross-section for WIMP pair annihilation as a function of the WIMP mass for indirect detection experiments and the sensitivity that could be reached with KM3NeT in 1 year, for the $\tau^+\tau^-$ channel and NFW dark matter halo in the Galactic Centre. Figure taken from [36].

Dwarf Galaxies

Dwarf Galaxies are thought to have been created by gravitational forces in the early stages of the creation of larger galaxies, or as a result of collisions between galaxies, forming from streams of material and dark matter ejected from the parent galaxies. The Milky Way galaxy features at least 14 satellite dwarf galaxies orbiting it.
Dwarf galaxies have a very large dark matter to visible matter ratio [116]. Furthermore, among the various extra-galactic sources they are generally the closest ones. The amount of dark matter in dwarf galaxies is also quite well known, so they can be good candidates for indirect DM searches.
Different indirect dark matter search experiment have combined 20 different observation of dwarf galaxies, in order to to maximize the sensitivity of DM searches and improve the current results; the final results can be found in [27].

6.7 Dark Matter from the Sun

The Solar System is located, with respect to the Galactic Center, on the periphery of our galaxy (8 kpc from the GC). The Sun and the Solar System move thus inside the Milky Way DM halo. In this way some WIMPs can cross the Sun and could scatter elastically with nuclei inside it, and lose enough momentum to become gravitationally trapped [198]. Supposing that WIMPs are stable, and since the lifetime of the Sun is quite long ($4.6 \cdot 10^9$ years), an equilibrium is reached between the DM capture and annihilation rate as from Equation 6.6.1 and as it is described in Section 6.7.1.
Neutrino telescopes have low efficiency in the detection of neutrinos below 10 GeV. As a consequence, in general, neutrino searches from the direction of the Sun start from this range of energies [89]. These neutrinos could actually be the decay products of the SM particles produced in the DM annihilation processed [94] making the Sun a proper target for indirect searches. Neutrinos produced in the core of the Sun can then escape and travel towards the Earth undisturbed, with only a small fraction of them being absorbed. Indeed, the absorption lenght λ_ν for a 100 GeV neutrino is around $7.9 \cdot 10^{12}$ g/cm^2; since the maximal depth of the Sun is $3 \cdot 10^{12}$ g/cm^2 most of these neutrinos will not be absorbed. At 1 TeV, $\lambda_\nu \sim 2.8 \cdot 10^{11}$ g/cm^2, thus causing some neutrino absorption [171]. The SM particles that can generate neutrinos could be quarks, Gauge bosons or leptons.
The Sun is a good source where to look for DM for several reasons. The Sun model [206] [145] is well known: indeed, the Solar Standard Model predicts with great accuracy the elemental densities in our star, its internal structure and the reactions that take place inside of it. The WIMP capture rate onto the Sun depends only on the WIMP density in the halo and the particles velocity distributions [198]; the annihilation rate depends on the total num-

ber of WIMPs accumulated over 4.5 billion years in the core of the Sun. In addition the annihilation rate does not depend on the distribution of dark matter in the Galaxy or on the properties of the Galactic magnetic [100] or radiation field [197].

6.7.1 Capture rate in the Sun

As described above, DM particles which lose energy due to the scattering with nucleons can be captured gravitationally by the Sun. The capture rate in the Sun is given by [197]:

$$C^{\odot} \sim \phi_{\chi}\Big(\frac{M_{\odot}}{m_p}\Big)\sigma \tag{6.7.1}$$

where ϕ_{χ} is the local dark matter flux, the ratio $(M_{\odot}/m_p) \simeq 10^{57}$ is an estimate of the number of target nucleons in the Sun and σ is the DM-nucleon scattering cross section, which can be spin-dependent or spin-independent. Readapting the Equation 6.6.1 for the case of the Sun, we get:

$$\frac{dN(t)}{dt} = C^{\odot} - A^{\odot}N(t)^2 - E^{\odot}N \tag{6.7.2}$$

Since the analysis of this work is focused on WIMPs with masses larger than few GeV and since evaporation affects WIMPs with smaller masses, this effect can be neglected [146].
Hence the annihilation rate can be written as:

$$\Gamma = \frac{1}{2}A^{\odot}N(t_{\odot})^2 = \frac{1}{2}C^{\odot}\tanh^2(\sqrt{C^{\odot}A^{\odot}}t_{\odot}) \tag{6.7.3}$$

DM particles accumulate in the Sun for a long time, as long as the age of the Solar System ($t_{\odot} \approx 4.6$ billion years) and this time is long enough to have an equilibrium between the capture and the annihilation rate. This occur when $\sqrt{C^{\odot}A^{\odot}}t_{\odot} \gg 1$ and so the annihilation rate at equilibrium is:

$$\Gamma = \frac{1}{2}C^{\odot} \tag{6.7.4}$$

This final relation is really important because it means that the annihilation rate has no dependence on the DM annihilation cross section.

6.7.2 Neutrino spectra

WIMPs, once captured and trapped in the core of the Sun, can annihilate into Standard Model particles which can produce neutrinos in the process of decay or interaction with other particles [160]. These particles could be leptons, as τ, or Gauge bosons, as W, or quarks, as b. In the first case, due to the conservation of the lepton flavour number, a neutrino is always emitted. The W boson can decay leptonically, producing neutrinos, with a 32.6%

branching ratio [218]. Similarly, its hadronic decays can produce particles which in turn yield neutrinos. If the DM annihilation produces quarks, these will generate hadronic showers, with neutrinos emerging from them [218].
The WimpSim software [157] is used to simulate the self-annihilation of dark matter particles in the Sun, and to obtain the corresponding SM signal energy spectrum at Earth. In this work, neutrino fluxes from three decay channels are considered, i.e. $b\bar{b}$, $\tau^+\tau^-$ and W^+W^-, assuming that the DM branching ratio for each of them is 100%. The choice of these three channels allows to cover from the hardest neutrino spectra (W^+W^-) to the softest ($b\bar{b}$), thus giving an optimistic or pessimistic scenario for DM searches.
In Figure 6.7.1 some example for neutrino and anti-neutrino spectra for a dark matter mass of 100 GeV and 1000 GeV are reported . From these examples it can be observed that the neutrino spectra are different for different channels and masses. In particular, for channels that yield a harder spectrum ($\tau^+\tau^-$, W^+W^-), neutrino absorption in the Sun can become relevant. In any case, spectral features are present and the behaviour of these neutrino spectra is non trivial; for example, the integral flux might not increase as the dark matter mass increases since other effects, for example connected to neutrino interactions within the Sun as well as neutrino oscillations, might mitigate the increase in neutrino production at the annihilation vertex when neutrino spectra on the surface of the Sun or at Earth are considered. [95].

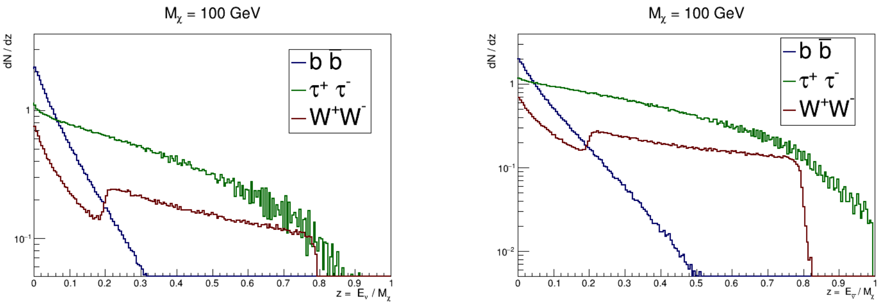

(a) Neutrino spectrum for WIMP mass equal to 100 GeV.

(b) Anti-Neutrino spectrum for WIMP mass equal to 100 GeV.

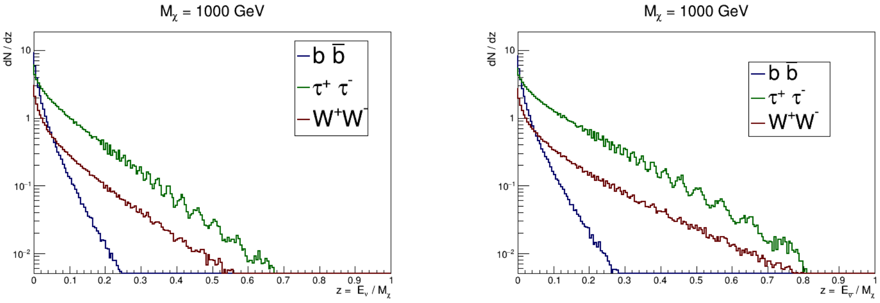

(c) Neutrino spectrum for WIMP mass equal to 1000 GeV.

(d) Anti-Neutrino spectrum for WIMP mass equal to 1000 GeV.

Figure 6.7.1: Examples of neutrino and antineutrino spectra for the three channels considered: $b\bar{b}$, $\tau^+\tau^-$, W^+W^-. In Figure (a) and (c) the neutrino spectrum for WIMP mass set to 100 GeV and 1000 GeV. In Figure (b) and (d) the anti-neutrino spectrum for WIMP mass set to 100 GeV and 1000 GeV. The wiggles in the $\tau^+\tau^-$ spectra are due to tau regeneration in the sun and electron neutrino oscillations [95]

Chapter 7

Inputs for ANTARES data analysis

In this chapter the necessary ingredients for the data analysis of this work, indirect searches for dark matter in the Sun, are described. These ingredients include: the ANTARES Monte Carlo simulations, the event reconstruction strategies, the data selection, the tracking of the Sun's position which is a moving source.

This chapter starts with the description of the Monte Carlo simulation method used in ANTARES, with particular emphasis on the efforts to reproduce at best the environmental and particle backgrounds. Then the event reconstruction strategies are presented. The Monte Carlo simulations and the reconstruction algorithms are general tools developed in the ANTARES Collaboration that constitute the common basis of all data analyses. Then, the data sets used are introduced, with a description of the preliminary event selection that I performed on these data. The comparison between data and MC simulations are also shown. Finally, the Sun coordinates computations and the Sun path tracking are presented.

7.1 Monte Carlo simulations

In all experiments it is very important to know the detector's response in different situations. The ANTARES Collaboration uses Monte Carlo simulations to assess the response of the detector and to help monitoring its performance, taking into account the variability of the environmental conditions. These Monte Carlo simulations have been developed in order to account for the functionality and efficiency of the different parts of the detector as they evolve in time, and, naturally, to properly simulate the physics of signal and background events in order to distinguish them at the analysis level.

The Monte Carlo simulations for ANTARES consist of three different steps

[57]:

- Generation of events;
- Particle tracking;
- Data acquisition.

The goal of the first step is to generate a simulated set of information of those particles that, following a neutrino interaction or the passage of an atmospheric muon, have a high probability of reaching the detector and produce Cherenkov light. Then, the second step takes care of propagating particles through the detector, and to generate and track photons up to the optical modules. Finally, the third step simulates the signals on the PMTs and the data acquistion filtering.
In these simulations, the detector is schematized as in the Figure 7.1.1. From the figure it is possible to distinguish two different cylinders: the biggest one, in yellow, is the so called *can* and it represents the sensitive volume of the detector. The second cylinder, in blue, represents the instrumented volume of the ANTARES detector. The *can* is a stretched out extension of the instrumented volume, with this stretching depending on the optical properties of water. The Cherenkov photons produced outside of this volume have a low probability to be detected by a PMT and are not simulated. Only energy losses of long tracking particle generated outside of the *can* volume are considered.

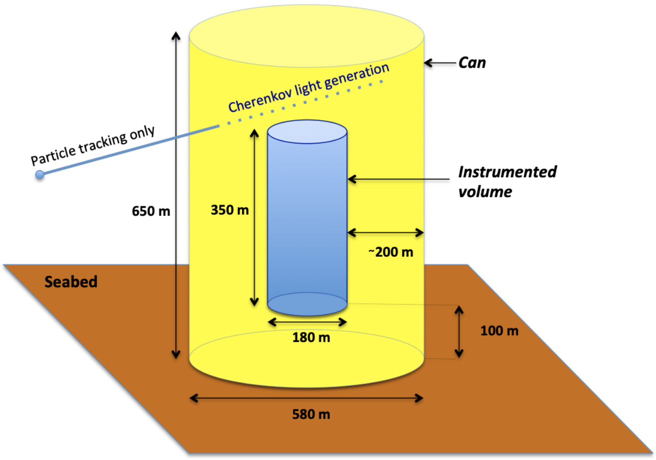

Figure 7.1.1: Schematic view of the ANTARES detector used in the simulation. Figure taken from [57].

7.1.1 Atmospheric muons

Atmospheric muons are produced by the interactions of the CRs with the atmosphere, as shown in Section 2.3.1. They represent the majority of the events triggered and reconstructed by the detector and they are a significant part of the background in searches for extra-terrestrial neutrinos.

The flux of atmospheric muons bundles at the detector can be reproduced using a complete simulation of the atmospheric showers induced by the arrival of a primary cosmic ray, or evaluating the underwater muon flux with a set of parametric formulae. Both strategies have been considered by the ANTARES Collaboration: CORSIKA [149] has been used for the full simulation and MUPAGE [103] for the parametric approach. In this work the second software has been used.

The MUPAGE package is based on a set of parametric formulae extracted from a full simulation of events. This package had been developed specifically for underwater neutrino telescopes, starting from the experience in the measurement of cosmic ray muons from the MACRO experiment at the Gran Sasso National Laboratories [63].

At the ANTARES detector the rate of atmospheric muons that are triggered during data taking is of the order of 1-10 Hz, depending on the trigger settings.

7.1.2 Neutrinos

The simulation of neutrino interactions is preformed by the GENHEN (GENerator of High-Energy Neutrinos) code, developed in the ANTARES collaboration. Neutrinos of all flavours with energies from 5 GeV up to 10^8 GeV, and both Charged Current (CC) and Neutral Current (NC) interactions are considered. This code relies on the LEPTO package for the simulation of the interaction kinematics [156], to simulate deep inelastic scattering at high energies, and the CTEQ6D [162] parton distribution functions are used.

The estimated rate of atmospheric neutrinos [31] in the ANTARES detector after event selection is of the order of 1-3 neutrinos per day, thus ~ 5 orders of magnitude smaller than the atmospheric muon rates. For what concerns cosmic neutrinos, a few events per year should be observable in ANTARES [136].

7.1.3 Particle and light propagation

The second part of the MC simulation chain aims at reproducing the passage of particles in water, together with their light emission. In order to accomplish this, a tool called KM3, also developed in the ANTARES Collaboration, is used [57]. In turn, this tool is divided into three distinct codes, each with its own function.

The first code is called *gen* and it computes the amount of Cherenkov photons generated by the passage of muons or electrons. In order to perform a realistic simulation, light absorption and scattering are considered. The absorption length follows the results from various measurements performed in different sites in the Mediterranean sea [189], [46]. The light scattering is simulated using a combination between Rayleigh and Mie scattering, with the ratio between Rayleigh and total scattering set to $\eta = 0.17$ [124], [174].
The second part of the KM3 package is called *hit* and, as the name suggests, uses the photon fields produced with the *gen* code to evaluate the probability of registering a hit on the PMTs given the its distance from the particle and the incidence angle of the simulated photons. The effective area of the OMs is used as input of the code and a set of tables, containing the probability for photons induced by electrons of different energy and by relativistic muon track segments to produce a detectable signal on an OM, is computed by a full GEANT simulation [11].
The third program is called *km3mc* and it performs the simulation of the propagation of the particle and the light through the *can* volume. Muon energy loss process are simulated using the MUSIC code [71].

7.1.4 Data acquisition simulations

The third and last step of the MC simulation chain is the creation of a data-set in the same format as real data from the simulated hit signals in the PMTs. In order to do so, also the environmental background must be considered and a simulation of the light induced by the optical background in sea-water is performed. This uses for each data taking run (see Chapter 3) the hit rates measured on each PMT and creates a realistic simulation of the average optical noise. Also partial malfunctioning of parts of the detector can be handled in the simulation by inspecting the detector conditions from the real data-taking runs. By using the results from the OM efficiency monitoring [56], the time dependent loss of efficiency of the detector is accounted for. Finally, the run-setups are read from the ANTARES data base and the same filtering algorithms that were applied to real data taking runs are also reproduced in the simulations, whose output is, at this level, in the same format as the real data runs. In the same step, also, calibration information is retrieved from the ANTARES data base and applied on simulated hits. All this procedure constitute the *run-by-run* approach and allows a detailed simulation of the ANTARES detector over its full livetime [57].

7.2 Reconstruction strategies

The ANTARES data-taking output files report information on each triggered event in terms of hits delivered by the PMTs. These consist of the incidence time and the integrated charge of the hit. From these recorded hits, the

properties of the particle that produced those hits are obtained using an event reconstruction algorithm. In this thesis only track–like events have been used.
The track reconstruction algorithms developed by the ANTARES Collaboration that are used in this analysis are: AAFit [150] and BBFit [40]. Each of these algorithms uses different procedures, resulting in different efficiency for different energies. After an initial fit to a hit distribution, a preliminary selection of hits has to be performed to reject background light. This hit selection is different for each strategy and mostly depends on coincidence criteria.

7.2.1 AAFit

The AAFit algorithm [150] performs a maximum likelihood fit of the probability of observing (or not observing) a set of hits in the detector from Cherenkov light emitted from a straight track. This track is defined by five parameters: two angles (θ,ϕ), and a position in space (x, y, z).
The first step for this reconstruction method is to perform a χ^2-like fit which is used as a starting point for the likelihood fit. This fitting procedure is repeated for different starting points and directions of the track, until one is selected as the best final likelihood. AAfit is a *multi-line* fitting strategy, i.e. it requires hits on at least two separate lines in order to reconstruct the muon track. For this reason it does not perform at its best for neutrino energies below 250 GeV. The parameter that measures the quality of the reconstruction is called λ and it is proportional to the likelihood value from the final likelihood fit and it is defined as:

$$\lambda = \frac{log(L)}{N_{DOF}} + 0.1 \cdot (N_{comp} - 1) \tag{7.2.1}$$

where N_{DOF} is the effective number of degrees of freedom in the fitting process and is equal to the number of hits minus the number of free parameters, which is five; N_{comp} is the number of convergences on the same final result from different initial steps. L is the maximum value of the likelihood function used for this fit.
An estimate of the angular uncertainty, β, is calculated from the error matrix of the final fit that yields the errors on the zenith angle, σ_θ, and the azimuth angle, σ_ϕ. The angular uncertainty is defined as [150]:

$$\beta = \sqrt{\sin^2(\theta_{rec}\sigma_\theta^2 + \sigma_\phi^2)} \tag{7.2.2}$$

These two parameters, λ and β, are strictly correlated since if a good fit is performed a better angular uncertainty is computed.
In this work different cuts on λ have been considered, while the cut on β is set to a fixed standard value of 1 degree. The typical angular resolution

achievable with this reconstruction strategy is of the order of 0.5° at high energies ($>$ 100 TeV). In the energy range of interest for DM searches, this worsens to $\sim$ degree level.

7.2.2 BBFit

The second reconstruction strategy is called BBFit [40] and it is possible to use it in two cases: in the reconstruction of events which have hits recorded on only one line, called *singleline*, of events with hits on two or more lines which is the *multiline* case. This reconstruction algorithm performs a χ^2 - like fit. Unlike AAFit, this strategy best performs in analyses where events with energies below 250 GeV are studied. Indeed, while AAFit uses the full hit information after a causality-relation selection, BBFit considers hits by merging them on a storey-by-storey level. This reduces the influence of noise hits in the reconstruction of low energy tracks, as explained in [40]. These simplifications cause however a loss in angular resolution. Given the scarcity of information generated in the hit pattern for the singleline case, it is not possible reconstruct the Azimuth angle value of the track.
In this work, both multiline and singleline are considered and are treated separately. In this algorithm the parameter that measures the quality of the reconstruction is called χ^2 and can be expressed as:

$$\chi^2 = \sum_{i=1}^{N_{hit}} \left(\frac{(t_i^{fit} - t_i)^2}{\sigma_i^2} + \frac{A(a_i)D(d_i^{fit})}{< a > d_0} \right) \tag{7.2.3}$$

where N_{hit} is the number of hits selected for the reconstruction and t_i^{fit} is the expected incident time from the current iteration of the fit, while t_i is the measured time of the ith hit. $A(a_i)$ and $D(d_i^{fit})$ are the so–called factor functions of the hit charge a_i and the fitted distance of the current iteration d_i^{fit}. $< a >$ is the average hit charge in the event and σ_i^2 is the timing uncertainty.
The function $A(a_i)$ can be written as:

$$A(a_i) = \frac{a_0 a'_i}{\sqrt{a_0^2 + a_i'^2}} \tag{7.2.4}$$

where a'_i is the corrected hit charge and a_0 is the artificial saturation. The correction applied to a'_i takes into account the angular acceptance. The function $A(a_i)$ makes sure that the charge of a hit is artificially saturated at a_0 $(A(a_i \ll a_0) \sim a_0)$. Similarly the function $D(d_i^{fit})$ assures that there is a minimum distance d_0 that is used for the fit $(D(d_i^{fit} \ll d_0) \sim d_0)$. The function $D(d_i^{fit})$ can be expressed as:

$$D(d_i^{fit}) = \sqrt{d_0^2 + d_i^{fit2}} \tag{7.2.5}$$

This approach with the BBFit algorithm produces the best efficiency for the lowest neutrino energies due to the inclusion of single line events. In this work different cuts on the χ^2 value have been considered for the singleline and multiline event samples selection.
A further simplified version of the BBFit algorithm, which assumes a rigid detector geometry (i.e. the storeys do not move in the water stream), is used to provide real-time event reconstruction . This introduces further uncertainty but increases the reconstruction speed and allows for the on-line execution of the reconstruction code [40].

7.3 Data set and pre-selection cuts used in this work

Before proceeding to the final steps of the analysis, described in the next chapter, the track event data sets are prepared, for both real data and MC simulations. In both cases, events have been partitioned according to the reconstruction strategy, i.e. AAFit, BBFit multiline and BBFit singleline samples are created. The analysis steps are then processed in parallel over the three strategies. In the run-by-run approach, the same selection should be applied to both data and MC. In addition, MC sets are produced separately for neutrinos and muons, each properly weighted and then summed up in order to evaluate the background and signal expectations.
The data set considered for this work covers the period from 2007 to the end of 2019, corresponding to a total of 10.45 years of livetime in the ANTARES detector, after a basic run quality selection is applied. The MC simulations are weighted according to the respective fluxes [155], [103] and in order to reproduce the same livetime as data.
For all the three strategies considered in this work, AAFit, BBFit multiline and BBFit singleline, different values of the respective quality parameters have been considered.
At this stage, I applied preliminary cuts for all strategies in order to ease the computational effort of analysing all the events. In the next chapter the specific optimisation strategy of the analysis will be described in detail. The preliminary cuts considered and applied to the whole data set are:

- Data Quality Basic > 0;
- Trigger 3N and T3;
- number of lines used in the track fit of the event $nline \geq 1$;
- $\cos\theta > 0$ to select up-going events.

Data Quality Basic is a parameter computed at the end of each run to establish whether a data-taking run can be used for analyses. Runs with this

parameter equal to 0 are not suitable for analysis. This is usually related to severe malfunctioning of the detector during these periods.
The selection of up-going events is necessary in order to minimise the background given by atmospheric muons, using the Earth as a shield, as previously described in Chapter 2.
The preliminary selection for the AAFit strategy cuts on the two track quality parameters described previously:

- $\lambda > -6$;
- $\beta < 1.5°$.

These values allow to reject unsimulated optical backgrounds without affecting in any way the detection of neutrinos [150]. Figure 7.3.1 shows the comparison between data and MC at pre-selection level, with the distribution of the number of events plotted as a function of the likelihood parameter λ; Figure 7.3.2 shows the same for the number of ANTARES lines having hits used in the fit procedure; Figure 7.3.3 provides the same plot as a function of the number of hits in the event; Figure 7.3.4 with the $\cos\theta$. In all of these figures the MC livetime is normalized by the detector livetime.
As written before, the MC sample presented here is the sum of the atmospheric neutrinos MC and the atmospheric muons MC. These two samples are affected by different uncertainties and the trend of data vs MC (neutrino + muon) changes as a function of λ . Indeed, for $\lambda > -5.2$ the MC sample is dominated by neutrinos; vice versa for $\lambda < -5.4$. The ANTARES MC simulations usually overestimate the amount of atmospheric muons and this is clearly visible in the figures. In the same way the atmopheric neutrino MC is $\sim 25\%$ below data [31]. This is evident in all figures and is a feature observed in all ANTARES analyses. As it will explained in the next Chapter, data are used to evaluate the atmospheric backgrounds in order to remove the uncertainties coming from these features. In any case most of the discrepancies, between data and MC, appear for λ values that are far from the region where optimal cuts are usually found. Figure 7.3.5 shows the MC simulations separately for muons and neutrinos compared with data.
For the BBFit strategy, the same preliminary selection is applied to both multiline and singleline events. The separation between the two is done at the later stages of the analysis described in the next Chapter. The preliminary cuts for the BBFit strategy are on the number of hits selected by the algorithm and its quality parameter:

- minimum number of hits: $nhits \geq 5$;
- $\chi^2 < 2.2$.

The motivation for these cuts is the same as for the AAFit preliminary cuts. Figure 7.3.6 shows the comparison between data and MC for the pre-selected

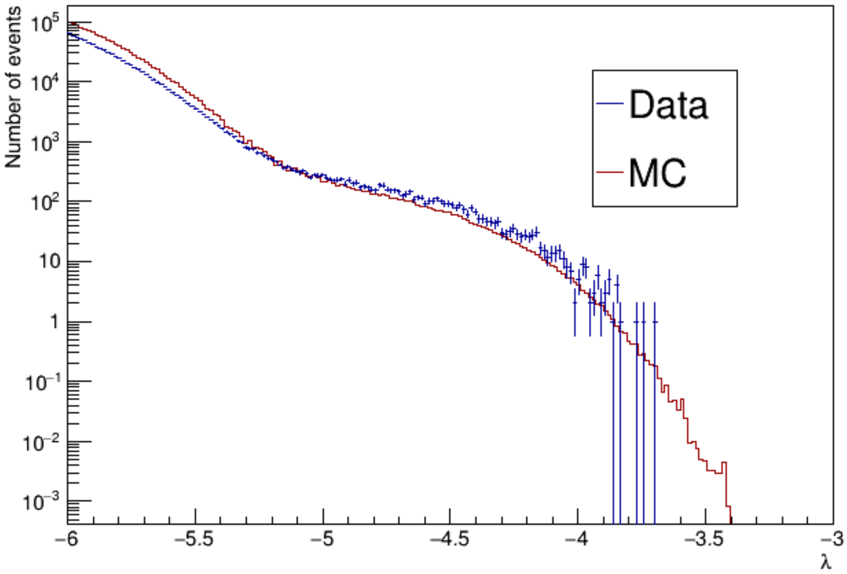

Figure 7.3.1: The number of events as a function of the event reconstruction quality λ for the AAFit algorithm. The events reconstructed in the 2007-2019 period are shown. The histogram shows the background estimate generated by Monte Carlo simulation, the crosses represent the recorded data.

events in terms of number of events as a function of the quality parameter χ^2; Figure 7.3.7 shows the same as a function of the number of lines with hits used in the event reconstruction; Figure 7.3.8 shows it as a function of the number of hits in the event; Figure 7.3.9 as a function of the $\cos\theta$. As for AAFit, also for BBFit there are some discrepancies between data and MC. The same motivations for these discrepancies given above for the AAFit strategy also apply here. In particular when $\chi^2 > 1.0$ the MC sample is dominated by atmospheric muons events while for $\chi^2 < 1.0$ it is mostly dominated by atmospheric neutrinos. In Figure 7.3.10 the MC reconstructions of muons and of neutrinos for BBFit compared with data are shown.

7.4 Moving sources

Since the analysis goal of this work is to search for dark matter towards the Sun, we should also understand how to determine a coincidence between the Sun direction and neutrino direction. The Sun is a moving source and its position must be translated in a consistent reference frame to the coordi-

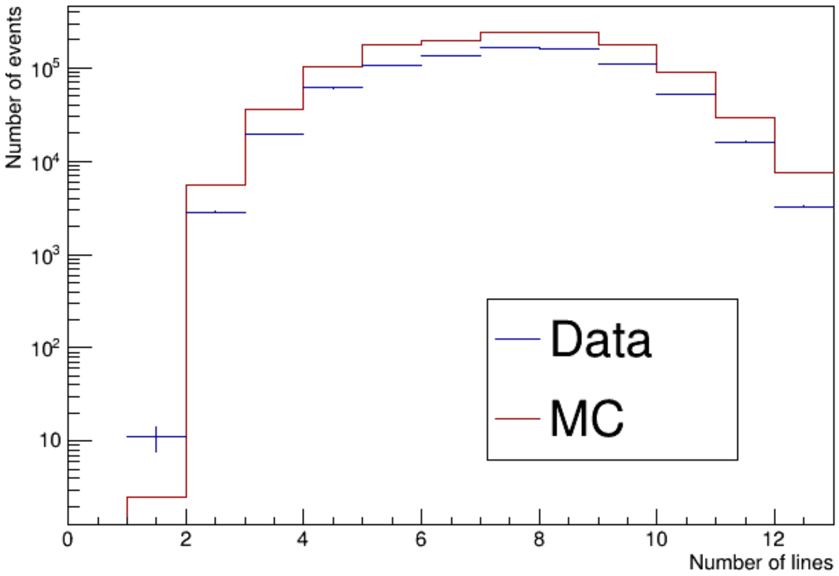

Figure 7.3.2: The number of events as a function of the number of lines with hits used in the reconstruction of the event for the AAFit algorithm. The events reconstructed in the 2007-2019 period are shown. The histogram shows the background estimate generated by Monte Carlo simulation, the crosses represent the recorded data.

nates of the experiment. The coordinate system in which the positions of all ANTARES detector elements are given is the Universal Transverse Mercator (UTM) system [12]. Therefore, also the directions and position coordinates of reconstructed objects such as muon tracks are usually given relative to this UTM system. The same reference system is used for MC simulations. The coordinate system is given by:

$$(x, y, z) = (Easting_{UTM}, Northing_{UTM}, up) \tag{7.4.1}$$

with the $x - axis$ corresponding to UTM Easting ($\phi = 0$ degrees) and the $y - axis$ corresponding to UTM Northing ($\phi = 90$ degrees, hence increasing in the counter-clockwise sense).

The Northing of the UTM system is not identical to the geodetic North. Its direction with respect to the geodetic North varies with the position on the Earth due to the local Mercator projection. The angular difference of the Northing direction to the geodetic North is called meridian convergence angle. Coordinates of data are selected using the Horizontal coordinate system, which use Azimuth and Zenith values, instead for the Sun the coordinates

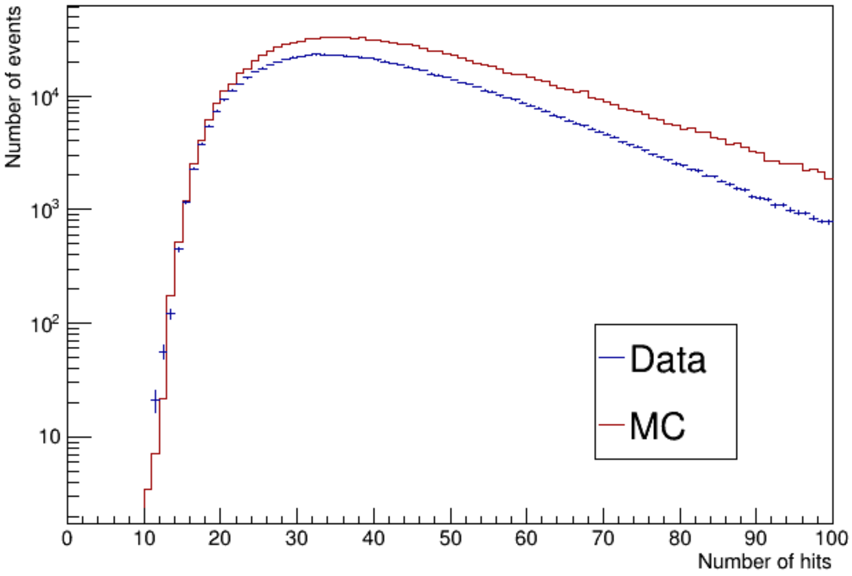

Figure 7.3.3: The number of events as a function of the number of hits of the event for the AAFit algorithm. The events reconstructed in the 2007-2019 period are shown. The histogram shows the background estimate generated by Monte Carlo simulation, the crosses represent the recorded data.

are expressed in spherical coordinates (ϕ, θ). For this reason from the Horizontal coordinate system it is necessary to move to spherical coordinates properly.

7.4.1 Conversions of the celestial coordinates

In order to properly convert the Horizontal coordinates into spherical coordinates, a preliminary check is performed. This check is done considering the Sun path for June 21st 2011 and consequently the data run for that day. The choice of this date is due to the fact that June 21 corresponds to the day of the Summer solstice: the number of daytime hours is the largest of the year, the Sun reaching is highest elevation in the sky. For this date, no selection cut is applied and both (Azimuth,Zenith) and (ϕ, θ) are studied. Figure 7.4.1 and Figure 7.4.2 show the Zenith vs θ and the Azimuth vs ϕ plots. From these plots one can conclude that the conversion to apply to convert Zenith into θ is:

$$\theta = 180^\circ - Zenith. \tag{7.4.2}$$

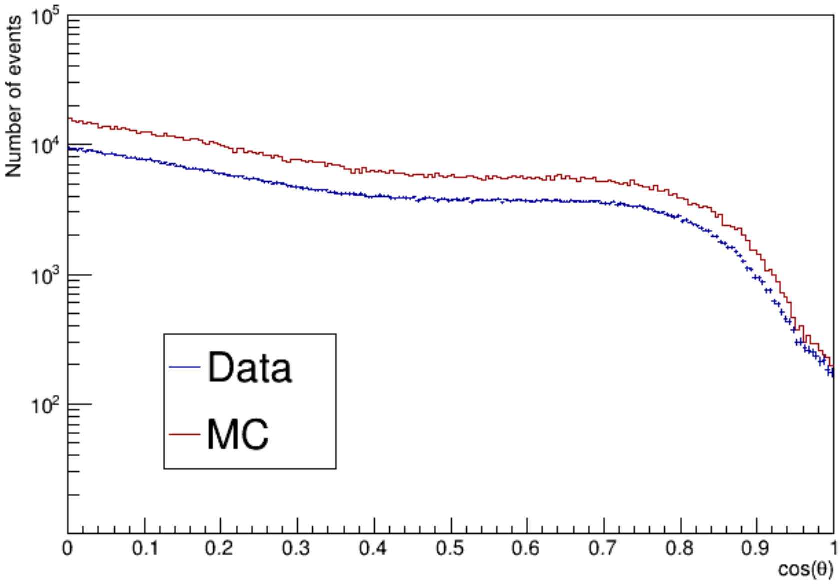

Figure 7.3.4: The number of events as a function of the $\cos\theta$ of the event for the AAFit algorithm. The events reconstructed in the 2007-2019 period are shown. The histogram shows the background estimate generated by Monte Carlo simulation, the crosses represent the recorded data.

and the conversions to convert Azimuth into ϕ are:

$$\begin{aligned} \phi &= Azimuth + 180°, \text{if Azimuth} < 180° \\ \phi &= Azimuth - 180°, \text{if Azimuth} > 180° \end{aligned} \tag{7.4.3}$$

7.4.2 Sun path

Given the coordinate system definition and the conversions described above, I used the *astro* package [210] to simulate the Sun position at any given time along the ANTARES data taking. The path covered by the Sun between the considered ANTARES livetime in 2007-2019 is shown in Figure 7.4.3. In order to do so, the event time of each ANTARES event in this livetime has been extracted from data and the Sun's position as then been computed in the local coordinates θ and ϕ. Given the fact that in this analysis events coming from below the detector are considered, the Sun is actually observed during the night. Also, given the position of ANTARES in the Northern Hemisphere, the Sun is visible for more time during the winter, and at directions corresponding to West-North-East, so for ϕ between 180° and 360°.

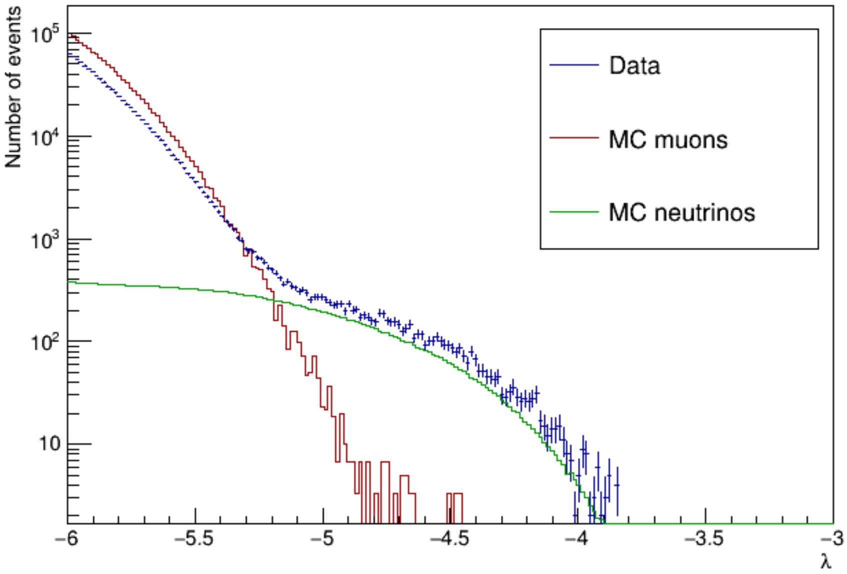

Figure 7.3.5: The number of events as a function of the event reconstruction quality λ for the MC neutrinos and MC muons for the AAFit algorithm. The events reconstructed in the 2007-2019 period are shown. The histogram shows the background estimate generated by Monte Carlo simulation.

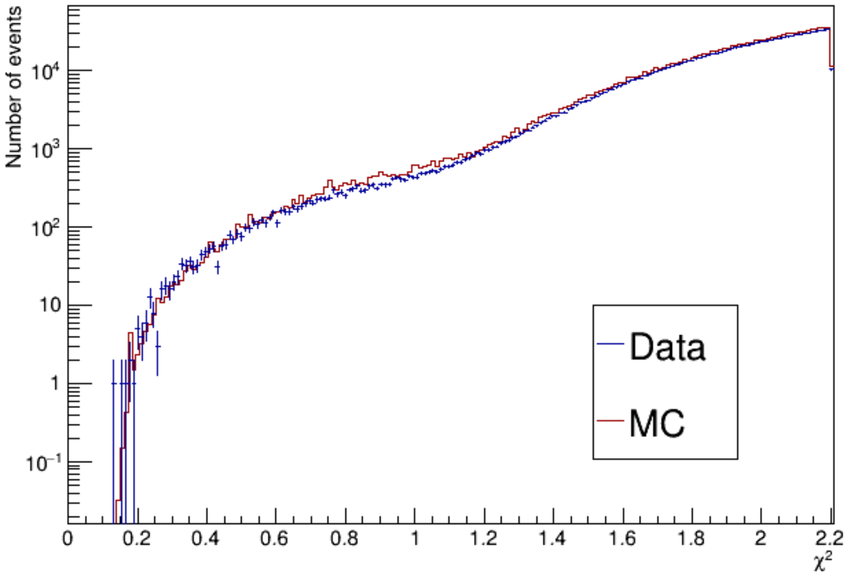

Figure 7.3.6: The number of events as a function of the event reconstruction quality χ^2. The events reconstructed in the 2007-2019 period with the BBFit algorithm are shown. The line shows the background estimate generated from the Monte Carlo simulation, the crosses represent the recorded data.

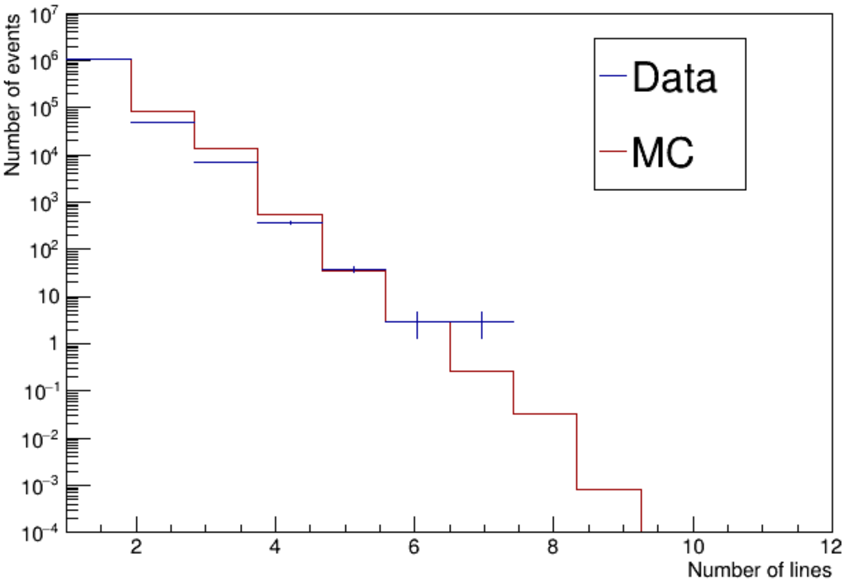

Figure 7.3.7: The number of events as a function of the number detector lines used in the reconstruction of the event. The events reconstructed in the 2007-2019 period with the BBFit algorithm are shown. The line shows the background estimate generated from the Monte Carlo simulation, the crosses represent the recorded data.

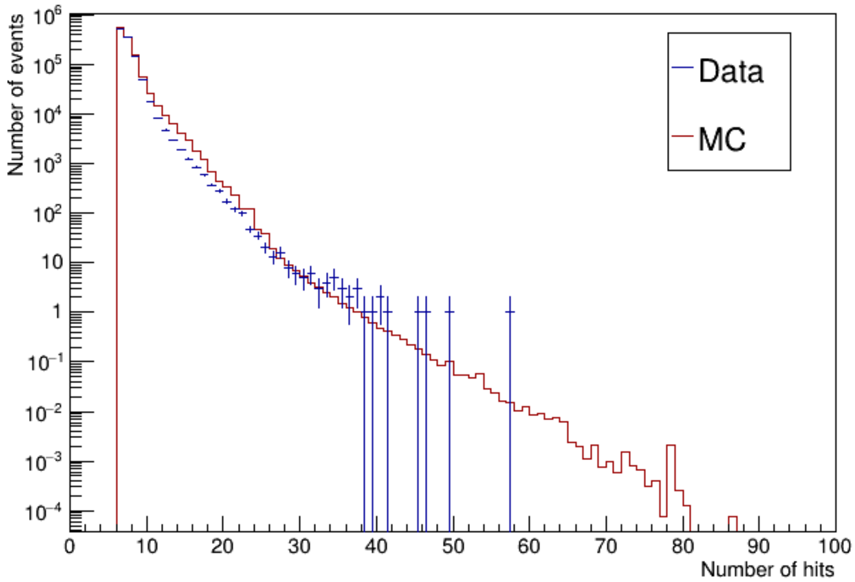

Figure 7.3.8: The number of events as a function of the number of hits of the event. The events reconstructed in the 2007-2019 period with the BBFit algorithm are shown. The line shows the background estimate generated from the Monte Carlo simulation, the crosses represent the recorded data.

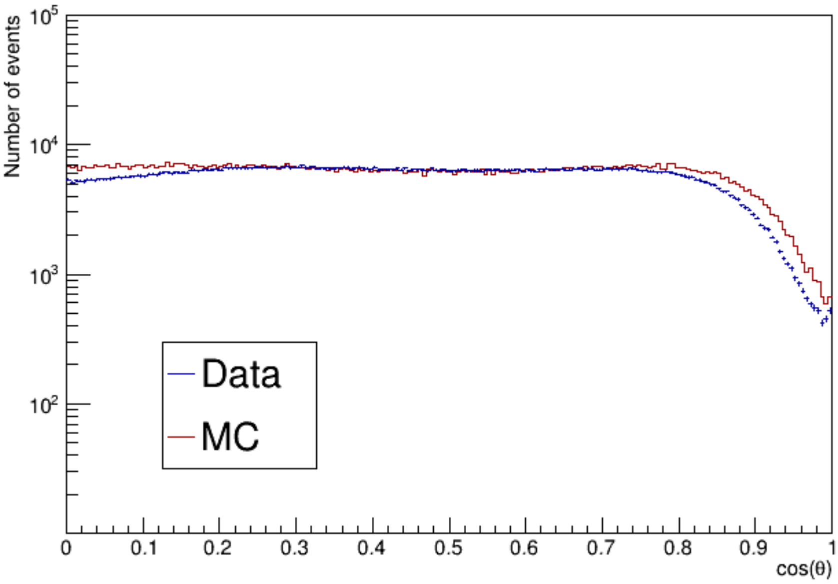

Figure 7.3.9: The number of events as a function of the $\cos\theta$ of the event. The events reconstructed in the 2007-2019 period with the BBFit algorithm are shown. The line shows the background estimate generated from the Monte Carlo simulation, the crosses represent the recorded data.

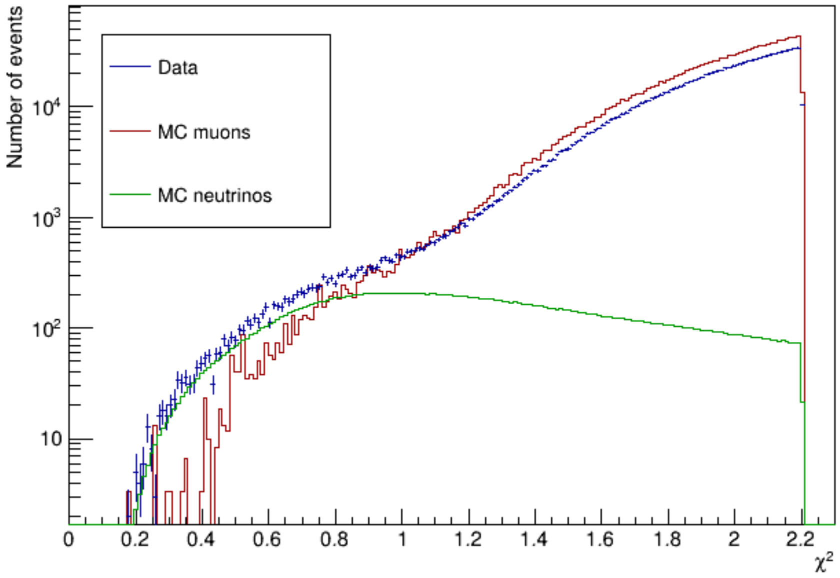

Figure 7.3.10: The number of events as a function of the event reconstruction quality χ^2 for the MC neutrinos and MC muons for the BBFit algorithm. The events reconstructed in the 2007-2019 period are shown. The histogram shows the background estimate generated by Monte Carlo simulation.

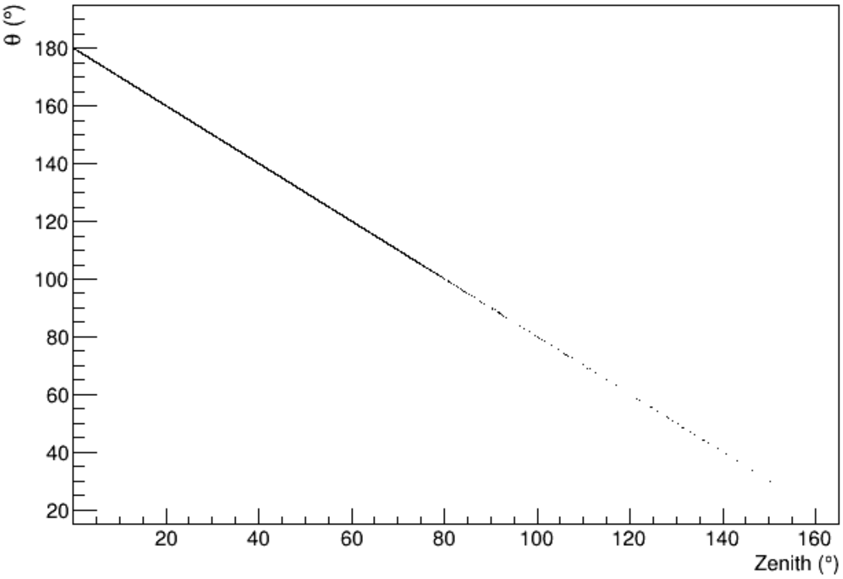

Figure 7.4.1: Zenith vs. θ of the events for data recorded on June 21st 2011. The AAFit data set was used for this test.

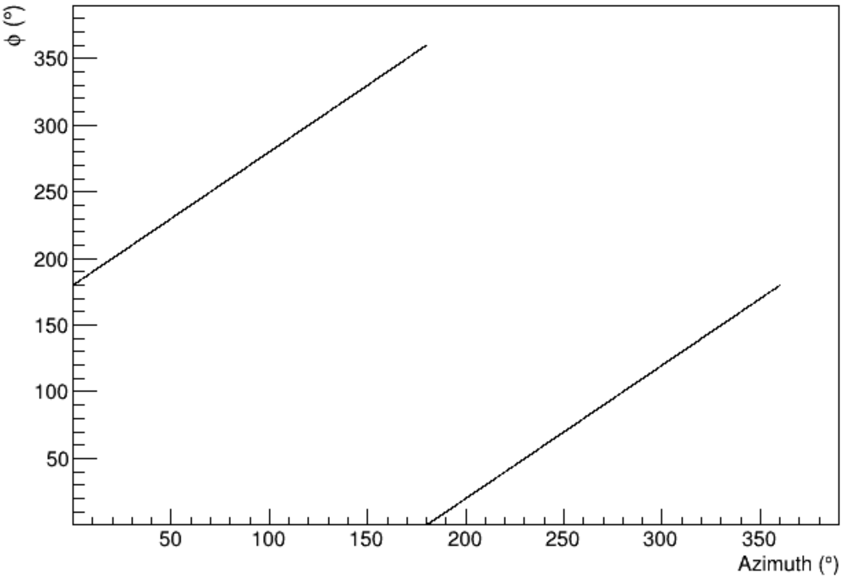

Figure 7.4.2: Azimuth vs. ϕ of the events for data recorded on June 21st 2011. The AAFit data set was used for this test.

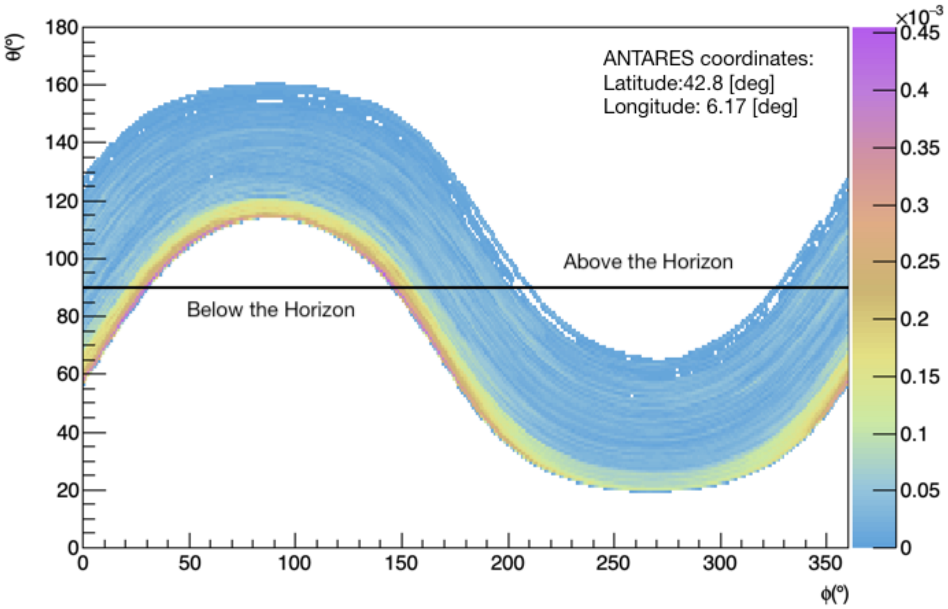

Figure 7.4.3: Sun map with respect to the position of ANTARES telescope.

Chapter 8

Analysis and Results

The purpose of this work is to perform indirect searches for dark matter from the Sun, using data collected by the ANTARES neutrino telescope between 2007 and 2019, for a total of 10.45 years of detector lifetime. In this chapter the steps done in this analysis are presented, and finally upper limits on the dark matter-nucleon cross section are shown. In addition, in order to put these results into a global context, a comparison between the results obtained in this work and other experiments is also shown.
The first goal of the analysis is to find the optimization of the selection parameters based on signal and background simulations. After that it will be possible to proceed with having a look at the telescope data. This analysis is conducted in a "blind" way, i.e. the real coordinates of the events are only looked after all optimisations are done on simulations and data with fake directions, in order to avoid biases in the analysis setup.
This work searches for neutrino signal from dark matter annihilation and this is done considering the three decay channels: $b\bar{b}$, $\tau^+\tau^-$, W^+W^-. All the computations are done considering the three muon track reconstruction strategies described in the previous chapter.

8.1 Binned analysis strategy

The analysis strategy chosen for this search follows the so-called *binned method.* This analysis method aims at emphasising the signal over the background by means of successive selection cuts. In the particular case of searches for neutrino events from an astrophysical source, a directional cut from the source itself allows to reduce the background contamination coming from a more isotropic distribution. This, in fact, is the case when considering the background induced by atmospheric events in a neutrino telescope.
In the particular case of indirect searches of dark matter from the Sun, the neutrino flux from the source can be estimated by evaluating how many

events could be detected when selecting a limited angular region around the Sun. By comparing the number of events observed in real data from this particular direction to the background expectations, the results of this optimised search can be translated into a neutrino flux estimation, from which the DM cross section can be evaluated.

This whole procedure relies on the definition of a statistical method for the computation of the number of the signal event from the source. The method of choice is based in this work on the Feldman and Cousins statistics [126]. From these, an estimation of neutrino detection efficiency is needed to move from a number of signal events to a physical flux. This efficiency is summarized in the detector acceptance, which depends on the detector neutrino effective area and the dark matter annihilation spectra in the Sun.

8.2 Acceptance

The ANTARES acceptance is computed via a convolution of the detector (anti-)neutrino effective area and the spectra of the different annihilation channels. The acceptance can be expressed as:

$$Acc(M_{WIMP}) = \bar{A}_{eff}(M_{WIMP}) = \frac{\sum_{j=\nu,\bar{\nu}}(\int_0^{M_{WIMP}} A^j_{eff}(E_j)\frac{dN_j}{dE_j}dE_j)}{\int_0^{M_{WIMP}} \frac{dN_\nu}{dE_\nu}dE_\nu + \frac{dN_{\bar{\nu}}}{dE_{\bar{\nu}}}dE_{\bar{\nu}}} \tag{8.2.1}$$

where $dN_{\nu,\bar{\nu}}/dE_{\nu,\bar{\nu}}$ is the energy spectrum of the (anti-)neutrinos at the surface of Earth, simulated using WimpSim [157] (see Section 6.7.2) for each of the considered channels, $b\bar{b}$, $\tau^+\tau^-$, W^+W^-. A_{eff} is the effective area of the ANTARES detector as function of the (anti-)neutrinos energy for events selected by the analysis.

8.2.1 Effective areas

The effective area represents the efficiency of the detector to detect a neutrino flux of a given energy. The effective area is dependent on the configuration of the detector and it is computed using Monte Carlo simulations. These accurate Monte Carlo simulations (as described in the previous chapter) try to reproduce the time-dependent behaviour of the detector, including its loss of efficiency with time, thus guaranteeing the proper computation of the detector effective area.

The neutrino effective area for a neutrino telescope as ANTARES can be expressed by:

$$A^\nu_{eff}(E_\nu, \theta_\nu, \phi_\nu) = \frac{N_x(E_\nu, \theta_\nu, \phi_\nu)}{N_{gen}(E_\nu, \theta_\nu, \phi_\nu)} \cdot V_{gen} \cdot \rho N_A \cdot \sigma(E_\nu) \cdot P_{Earth}(E_\nu, \theta_\nu) \tag{8.2.2}$$

where N_x is the number of events that are selected after triggering, reconstruction and eventually quality selection; N_{gen} is the number of generated events in the Monte Carlo simulations for that specific energy (E_ν)/ zenith(θ_ν)/ azimuth (ϕ_ν); V_{gen} is the generation volume of the simulations, ρ is the matter density and N_A is the Avogadro number; $\sigma(E_\nu)$ is the neutrino cross section at that energy and finally $P_{Earth}(E_\nu, \theta_\nu)$ is the absorption probability for the neutrino when crossing the Earth. This formula is valid also for the computation of anti-neutrinos.
Under the framework of the ANTARES simulations, as described in Section 7.1, the event generator produces a parameter called w_2 that, taking into account how neutrino events are simulated, allows for a re-weighting procedure. This $w2$ weight, when multiplied by a differential energy flux, reproduces the expected number of events in a given livetime. This weight w_2 is defined as:

$$w_2(E_\nu, \theta_\nu) = V_{gen} \cdot I_\theta I_E \cdot E^\Gamma \cdot \rho N_A \cdot \sigma(E_\nu) \cdot P_{Earth}(E_\nu, \theta_\nu) \cdot F \qquad (8.2.3)$$

where I_θ and I_E are the geometry and energy phase space factors for the neutrino generation, F is the number of seconds in a year and the exponent Γ is the neutrino generation spectral index; for the specific case of this analysis it is equal to 1.7. w_2 includes most of the parameters of the Equation 8.2.2 Thus the Equation 8.2.3 can be written as:

$$V_{gen} \cdot \rho N_A \cdot \sigma(E_\nu) \cdot P_{Earth}(E_\nu, \theta_\nu) = \frac{w_2(E_\nu, \theta_\nu)}{F \cdot I_\theta I_E \cdot E^\Gamma} \qquad (8.2.4)$$

Then Equation 8.2.4 can be substituted in Equation 8.2.2 of the area and we obtain the new equation for the effective area as function of the energy bin in which we are performing the effective area calculation $[E_m, E_M]$:

$$A^\nu_{eff}(E_\nu, \theta_\nu, \phi_\nu) = \frac{N_x(E_\nu)}{k(E_M^{1-\Gamma} - E_m^{1-\Gamma})} \cdot \frac{w_2(1-\Gamma)}{F \cdot I_\theta \cdot E^\Gamma} \qquad (8.2.5)$$

where k is the overall number of generated events with energies between E_m and E_M, E_m, E_M are respectively the minimum and maximum value of the energy bin.

8.3 Evaluation of the backgrounds

The ANTARES neutrino telescope collects on average 1-3 atmospheric neutrinos/day. In the meanwhile the average trigger rate of the experiment is of the order of 10 Hz and it is mainly due to atmospheric muon events reaching the detector depths. On the contrary, the expected signal from dark matter annihilation in the Sun is much smaller. It is thus necessary to differentiate interesting events from background ones.

The main sources of background in such detector are atmospheric neutrinos and atmospheric muons, as described in Sections 2.3.1, 2.3, and whose simulations are presented in Section 7.1.1, 7.1.2. Two different approaches can be exploited in order to compute these backgrounds, either using Monte Carlo simulations or using data themselves. Indeed, when searching for events from a certain region of the sky, the arrival direction of data can be scrambled in order to mimic different data sets where no signal is present. This scrambling procedure consists of attributing to each event a different time within the detector exposure, while keeping fixed its local coordinates. In this way its celestial coordinates are randomised, while still providing a realistic determination of the background detection. On the other hand, a re-weighting procedure can be used with simulated events to reproduce the expectation from the atmospheric muons and neutrino fluxes. The usage of data at this stage removes the uncertainties on the flux calculations in the weighting procedure.

In addition to the cut on the quality parameter, which removes the badly reconstructed events, a directional cut is necessary since the signal is unidirectional while the background is almost isotropically distributed in the region close to the source. So, the background can be further reduced by concentrating on a cone around the direction of the Sun.

In this work, the computation of the number of expected events is divided into two steps: first I computed the background distribution for each quality parameter considered; then this background distribution is fitted to precisely evaluate the number of events for different cone or aperture angle. In the first step, in order to compute the expected background from data, data are scrambled. In this way, hundreds of event skymaps are generated and used as pseudo-data.

In the case of the AAFit and BBFit multiline reconstruction strategies the angular separation Ψ is given by the angular distance between the reconstructed direction (θ_r, ϕ_r) and the Sun's position (θ_s, ϕ_s). In the case of BBFit singleline events, where only the zenith is reconstructed, Ψ is just the difference between θ_r and θ_s. In Figure 8.3.1 the distribution of the Ψ angle is shown for events reconstructed with the AAFit strategy. Different colors are used to show different quality parameter (λ) cuts. The cut on the quality cut parameter, λ for AAFit and χ^2 for BBFit, eliminates the low quality events which have higher probability to be badly reconstructed.

The second step consists in the computation of the cumulative distribution of the background, which is followed by a fit of this on this distribution, considering a specific range of cone angles, in order to estimate the number of background events that are expected within a given value of Ψ. The function used to fit for all quality cut is an exponential, with the exception of some quality cut for BBFit singleline where a sum of two exponential has been used. Then the fit parameters have been used to compute the number of background events for specifics cone/aperture angle. The Ψ region con-

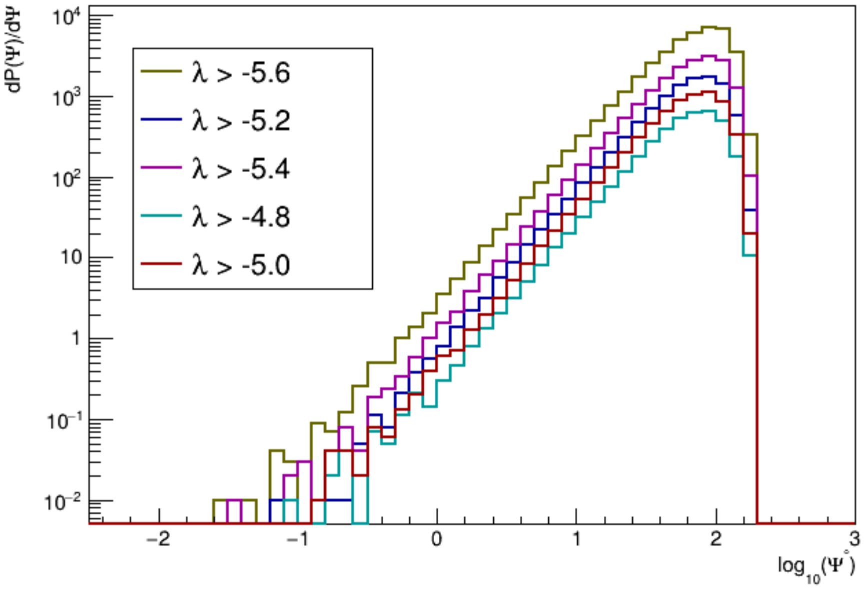

Figure 8.3.1: Ψ angle distribution for different AAFit quality paramenter cuts.

sidered is in the range corresponding to 1 to 15 degrees.
In Figure 8.3.2 an example of the fit applied on a cumulative for the AAFit case which has the cut on lambda $\lambda > -5.4$ is reported.

8.4 Sensitivity estimation

On the basis of the background estimation and acceptance previously computed, the Model Rejection Factor (MRF) procedure [153] is used to optimize the search window opening angle around the sources and the track quality cut parameters. This procedure allows to find the optimal selection cut as the one which minimises the sensitivity of the experiment, that is, the minimum flux coming from a source to which the experiment can be sensitive at a pre-defined confidence level. The neutrino flux sensitivity for a given channel can be written as:

$$\bar{\Phi}_{\nu_\mu+\bar{\nu}_\mu,90\%} = \frac{\bar{\mu}_{90\%}}{\bar{A}_{eff}(M_{DM}) \cdot T_{eff}}, \tag{8.4.1}$$

where $\bar{\mu}_{90\%}$ is the average upper limit at 90% of confidence level, computed using a Poisson distribution in the Feldman-Cousins approach [126]. This term depends on the expected background and the number of observed events

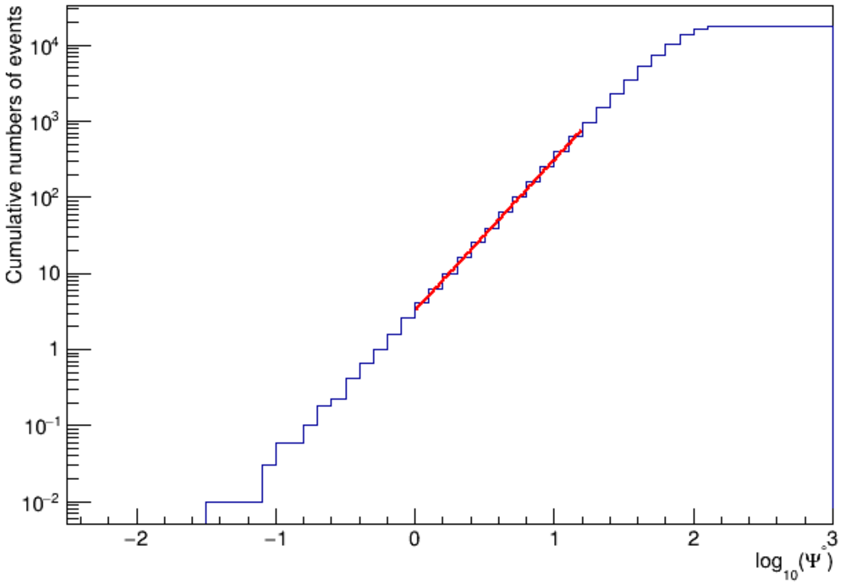

Figure 8.3.2: Fit on the cumulative of AAFit for the cut $\lambda > -5.4$.

in a hypothetical experiment. The total live-time T_{eff} of the detector and the acceptance for a given mass of Dark Matter particle M_{DM} and annihilation channel are at the denominator.

8.4.1 Choice of the best cut

Different cuts have been considered for each of the three reconstruction strategies, where the quality cut parameter and the angular separation from the Sun have been varied. In particular, for the AAFit strategy, the λ parameter has been varied in steps of 0.2 from -4.8 to -5.8 and the angular distance from 1° to 6° in steps of 1°. For the BBFit multiline strategy, the χ^2 parameter has been scanned in the range 1.1 to 1.8 in steps of 0.1, and the angular distance from 1° to 7° in steps of 1°. Finally, for the BBFit singleline strategy, the range of analysed χ^2 goes from 0.6 to 1.2 in steps of 0.1 with the angular distance moving from 4° to 12° in steps of 1°. All these computations are performed for each analysed channel and dark matter mass ranging from $50\,\mathrm{GeV/c^2}$ to $3\,\mathrm{TeV/c^2}$[1]. For each of these the aforementioned ingredients (effective area, spectra with which the acceptance is evaluated, and the background estimation) are built. Overall, around 100 combination

---

[1] DM mass test values are, in $\mathrm{GeV/c^2}$: 50, 100, 150, 176, 200, 250, 350, 500, 750, 1000, 1500, 2000, 3000.

of selection cuts have been analysed for each selected DM mass in order to find for each of them the optimal cut minimising the sensitivity. The estimated number of background events for the tested cases is given in the Appendix C.

For each of these set of cuts, the effective areas have been calculated, separately for neutrinos and anti-neutrinos considering their arrival direction with respect to the Sun. This is done taking the events along the path of the Sun (Figure 7.4.3) and defining the angular separation as the aperture of a cone (for AAFit and BBFit multiline) or a zenith band (for BBFIt singleline) centered on the Sun position at any given time, in the same way as described above for the evaluation of the background.

In Figure 8.4.1 the effective areas computed for neutrinos (solid lines) and for the anti-neutrinos (dashed lines), for the different considered strategies, are reported: for AAFit $\lambda > -5.4$ and cone angle 3°, for BBFit singleline $\chi^2 < 1.0$ and aperture angle 7°, for BBFit multiline $\chi^2 < 1.5$ and cone angle 4°. The values shown in this example are some of the ones used in the optimizations. It can be noted that the effective areas for neutrinos are different from the ones for anti-neutrinos; this can be attributed to their different cross-sections. The neutrino energy range considered in this study is up to 3 TeV since at higher energies neutrinos are absorbed in the Sun, as explained in Chapter 6. The computation is done considering the live time of the detector from 2007 to the end of 2019.

As said before, the spectrum-averaged effective area, Equation 8.2.1, can be built from these effective areas with the WimpSim spectra shown in Section 6.7.2. This constitutes the detector acceptance. Figure 8.4.2 shows some examples of the acceptances as a function of the WIMP mass for the different reconstruction strategies, for the optimised cuts, for all the three considered channels. It is possible to observe from the plot that for low masses, in general, BBFit singleline yields a larger acceptance; for this reason this reconstruction strategy can provide a better sensitivity with respect to the other two strategies. In addition, it can be noted that BBFit multiline and AAFit have a similar behavior; this is due to the multiline approach of their algorithms. The visible differences between the computed acceptances are not only due to the reconstruction strategy, but also to the individual annihilation channel spectrum: $\tau^-\tau^-$ and W^+W^- have a harder spectra thus producing higher energy neutrinos that are easier to detect; instead, the spectrum of $b\bar{b}$ is softer due to the semi-leptonic decay of this channel, and these lower energy neutrinos are penalized in the detection efficiency.

In the same way, for different combination of selection cuts, the background is also evaluated. This background evaluation and the acceptances are inserted into Equation 8.4.1. As a result, a neutrino flux sensitivity value is obtained for each combination of quality parameter and angular separation, for each WIMP mass and for each annihilation channel.

The final sensitivity values obtained were compared to find the minimum

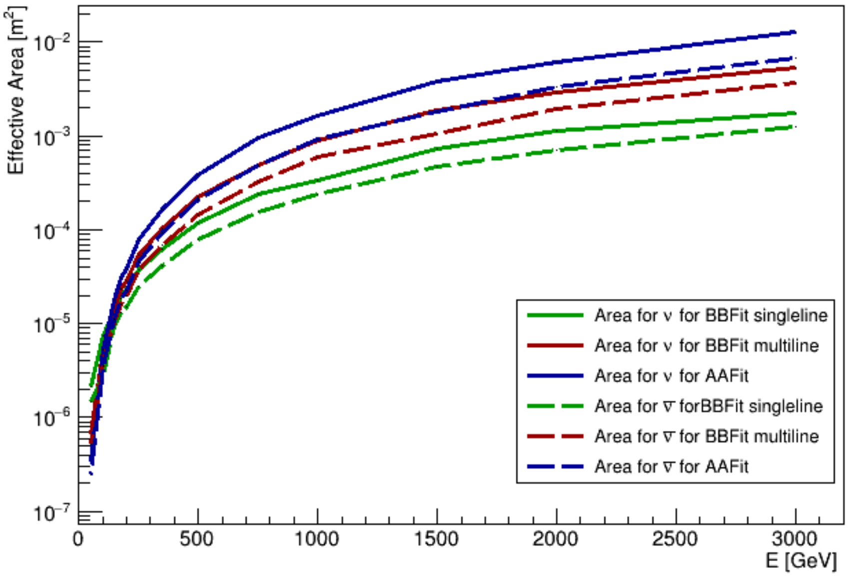

Figure 8.4.1: Effective Area as function of the neutrino energy computed for the three different reconstruction strategies separately for neutrinos (solid lines) and anti-neutrinos (dashed lines). In blue AAFit, in green BBFit singleline and in red BBFit multiline. The cuts for which these effective areas are valid are reported in the text.

value of the sensitivity which correspond to the optimal set of selection cuts. In Figure 8.4.3 an example of the optimisation results for the AAFit strategy assuming a dark matter mass of 1000 GeV is shown. From all these comparisons, it can be seen that for low masses BBFit singleline has better sensitivities, instead for intermediate masses BBFit multiline is better and finally for higher masses AAFit has better sensitivities. A reasonable choice of the final selection has been agreed upon, with the consensus of the ANTARES collaboration. Table 8.1 resumes the best cuts and the reconstruction strategies used in order to obtain the best sensitivity for each channel. Figures 8.4.4, 8.4.5, 8.4.6 show the obtained sensitivities, for $b\bar{b}$, $\tau^+\tau^-$ and W^+W^- respectively, with the three reconstruction strategies. In particular scanning all the analysed WIMP masses, a combination of the three strategies produces the best sensitivities for $b\bar{b}$ and $\tau^+\tau^-$ channels; instead, for W^+W^- only BBFit multiline and AAFit are used.

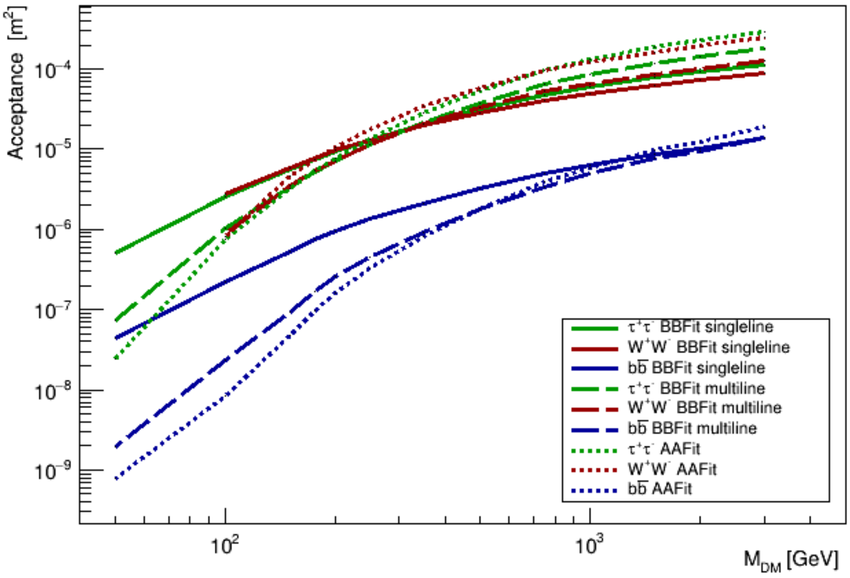

Figure 8.4.2: The Acceptance as function of the WIMP mass computed for the three reconstruction strategies for each channel. With solid lines are represented the acceptances for BBFit singleline, with dashed lines the ones for BBFit multiline and with dotted lines the acceptances computed for AAFit. The lines in blue represent $b\bar{b}$, the lines in green $\tau^+\tau^-$ and in red W^+W^-.

Table 8.1: Tables with selected cuts for each channels and mass range.

Channel	Mass range (GeV)	Strategy	Quality parameter	Cone/Aperture angle
$b\bar{b}$	M < 150	BBFit singleline	χ^2 = 1.0	8
$b\bar{b}$	150 ≤ M ≤ 500	BBFit multiline	χ^2 = 1.5	4
$b\bar{b}$	M ≥ 500	AAFit	λ = -5.4	3
$\tau^+\tau^-$	M = 50	BBFit singleline	χ^2 = 1.0	7
$\tau^+\tau^-$	50 < M ≤ 176	BBFit multiline	χ^2 = 1.5	4
$\tau^+\tau^-$	M ≥ 200	AAFit	λ = -5.4	3
W^+W^-	100 ≤ M ≤ 150	BBFit multiline	χ^2 = 1.5	3
W^+W^-	M ≥ 176	AAFit	λ = -5.4	3

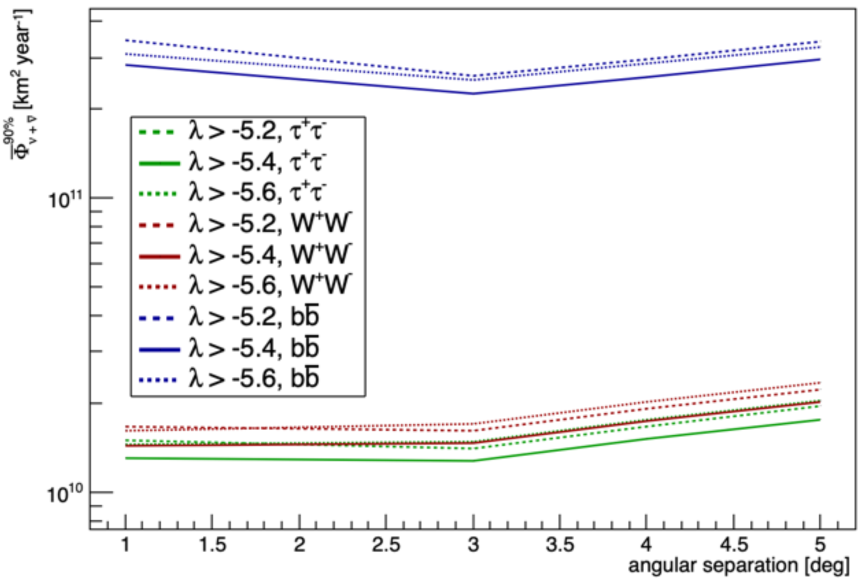

Figure 8.4.3: Optimization study for the AAFit strategy assuming a dark matter mass of 1000 GeV . The neutrino flux sensitivity is shown as a function of the angular separation selection. Three different value of λ parameter are shown for the three channel ($b\bar{b}$ (in blue), W^+W^- in red, $\tau^+\tau^-$ in green).

8.5 Systematic uncertainties

In an analysis like this there are different sources of systematic errors, which can be divided into two groups: those are related to the astrophysical conditions and those linked to the detector operation and performance.
Uncertainties on the astrophysical parameters, such as the DM density and velocity distribution, will affect the WimpSim simulations. Similarly, the Sun's properties enter these uncertainties. Their effect [20] can be included in the acceptance of the detector, and amount to a variation few percent each. The second type of uncertainties concerns the detector performance and the processes happening in it such as the propagation of photons, neutrino interaction cross section quantum efficiencies of the PMTs and timing uncertainties. These are usually estimated to be affecting the detector acceptance by about 6%, as in [55].
Including also these detector uncertainties, a conservative global uncertainty on the acceptance of 15% is assumed. Given the definition of the sensitivity, Equation 8.4.1, this has a direct scaling effect on it.
From the same formula, the second source of uncertainties on the sensitivity

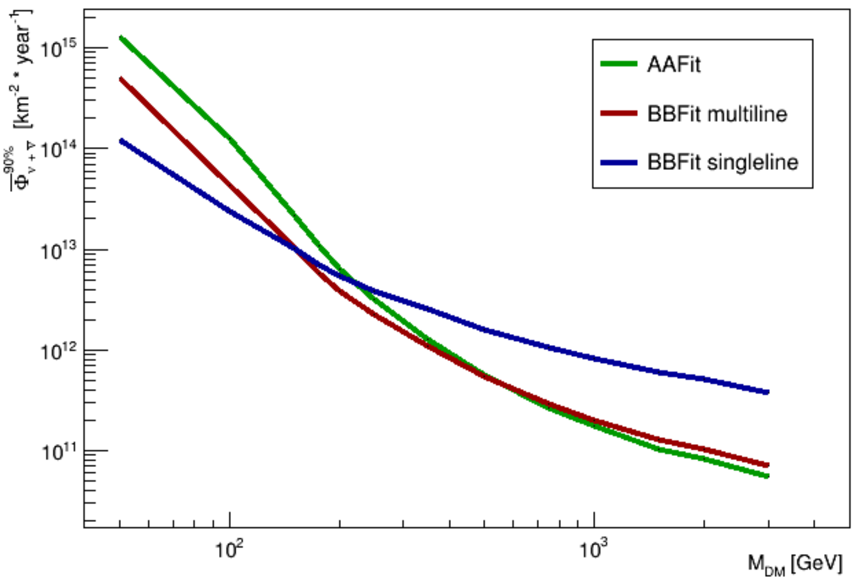

Figure 8.4.4: Comparison of the sensitivities of $\tau^+\tau^-$ channel for the selected cuts of the three strategies.

is the uncertainty on $\mu_{90\%}$. This uncertainties are generated by the computation of the expected number of events from the background. Indeed, even though using data for the estimation of background events reduces systematics from the simulation of background events, the fitting procedure described in Section 8.3 also carries some uncertainties. Considering the average uncertainties on the fit procedure exploited for the background estimation, a $\sim 11\%$ error is estimated on the number of background events. This is then inputted to the computation of $\mu_{90\%}$. It should be noted that the effect of the background uncertainty on $\mu_{90\%}$ is not linear and thus a 11% variation of the number of background events will not be a 11% variation of $\mu_{90\%}$. For the two cases, upper and lower limit errors have been computed and subsequently the sum in quadrature was carried out among these errors in order to obtain an upper and lower limit on the sensitivity values. The results of these computations will be shown in the next sections as error bands around the obtained upper limits.

8.6 Unblinding

As explained above, the analysis is first performed and optimized using blinded data. These data do not contain all the relevant information of the

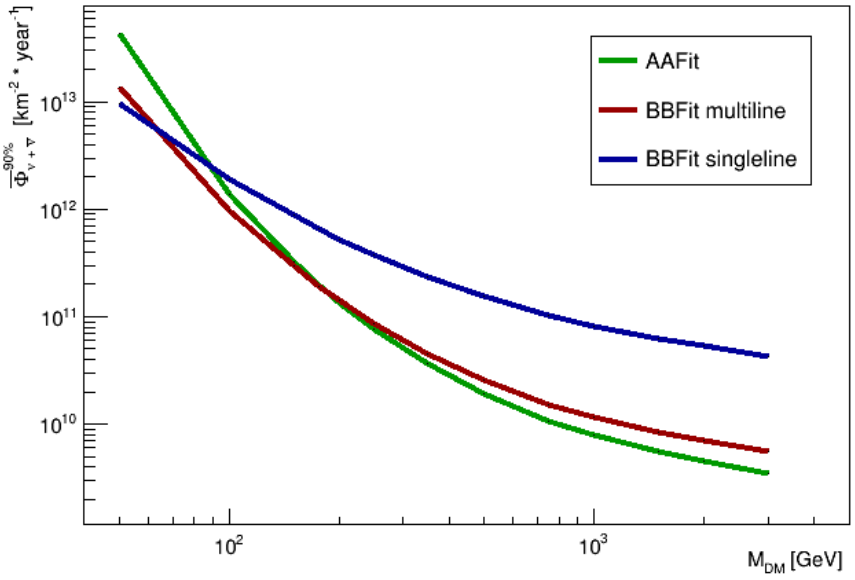

Figure 8.4.5: Comparison of the sensitivities of W^+W^- channel for the selected cuts of the three strategies.

detected events; in particular, a random time is attributed to each event, so that the local coordinates (θ and ϕ) cannot be correlated with the celestial coordinates of the genuine neutrino event origin. This allows to avoid biases in the optimisation of the selection cuts.
Once data are unblinded and the number of events is computed, no excess of events is observed from the true direction of the Sun. Table 8.2 shows for each strategy, channel and selection cut the expected number of background events and the observed number of events after unblinding. An over-estimation of the background is observed in all cases. The effect of this on the estimation of the upper limits will be pointed out in the next section. Then different checks have been performed:

- the code to compute the events of unblinded data has been run with blinded data;
- the number of events from blinded data, with 100 maps with scrambled directions, has been re-calculated with a linear scale on the angular separation Ψ to check if biases were introduced by the logarithm scale fit of the background distribution.

In both of these two cases the number of events retrieved from the selected cone/aperture angles is smaller than the the number of estimated background

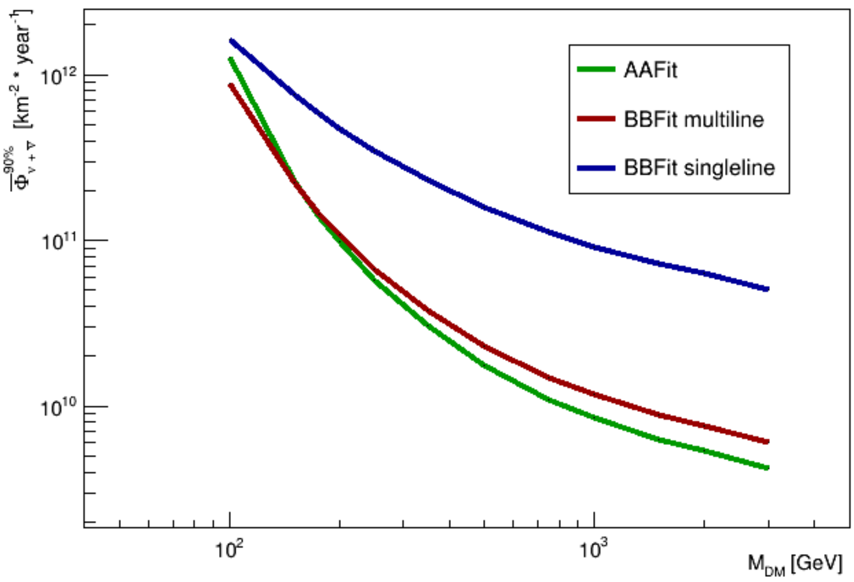

Figure 8.4.6: Comparison of the sensitivities of $b\bar{b}$ channel for the selected cuts of the three strategies.

events computed by the fit, and used in the sensitivity estimation.
In addition to these checks, other checks have been done using Monte Carlo simulations. In this case the sets of data for neutrino and muons have been processed separately to compute the number of events, with 100 maps with scrambled directions, and this was compared with the number of events of unblinded data. No excess of events has been observed also there. In the Figures 8.6.1, 8.6.2, 8.6.3 the comparison between real data, scrambled data and MC simulations for the three reconstruction strategies are reported.

8.6.1 Neutrino flux upper limits

Since no excess of events has been observed, the upper limit would be below the experiment's sensitivity. In all analysis of ANTARES and following the convention generally used in deep-sea neutrino telescopes, when such is the case, the 90% confidence level upper limits are set to be equal to the sensitivities. In Figure 8.6.4 these upper limits on the neutrino flux from the Sun produced by Dark Matter annihilation are shown, for the three channels considered, $b\bar{b}$, $\tau^+\tau^-$, W^+W^-, using the cuts resumed in Table 8.1.

Table 8.2: Tables with the comparison between expected events computed from the background and the observed events.

Strategy	Channel	Quality parameter	Cone/Aperture angle	Observed events	Expected events
AAFit	$b\bar{b}$,$\tau^+\tau^-$, W^+W^-	λ = -5.4	3	29	30.31
BBFit multiline	$b\bar{b}$	$\chi^2 = 1.5$	4	20	27.09
	$\tau^+\tau^-$	$\chi^2 = 1.5$	4	20	27.09
	W^+W^-	$\chi^2 = 1.5$	3	10	15.45
BBFit singleline	$b\bar{b}$	$\chi^2 = 1.0$	8	867	948
	$\tau^+\tau^-$	$\chi^2 = 1.0$	7	760	827
	W^+W^-	$\chi^2 = 1.0$	6	666	707

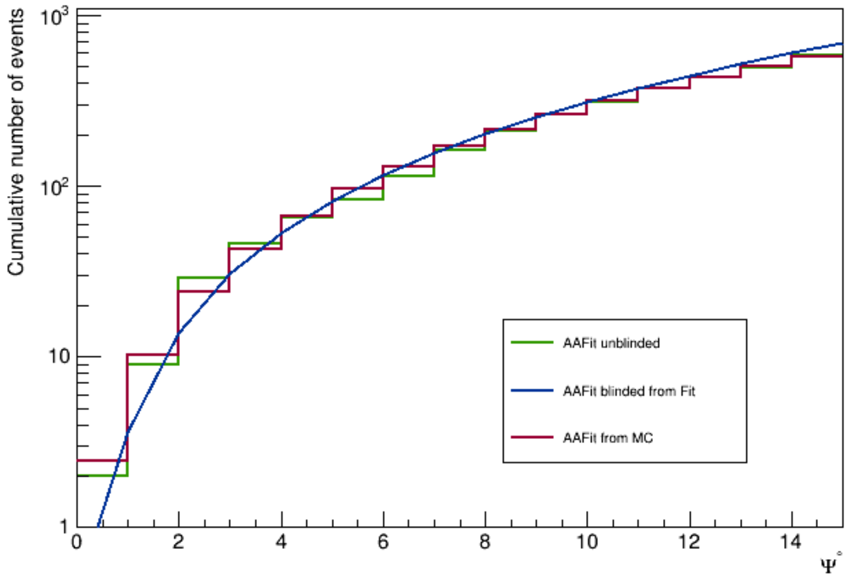

Figure 8.6.1: Cumulative number of events as a function of the angular separation for the AAFit reconstruction strategy. With a blue line the distribution for scrambled data is shown, in red the histogram of real data and in green the histogram of MC simulations are shown.

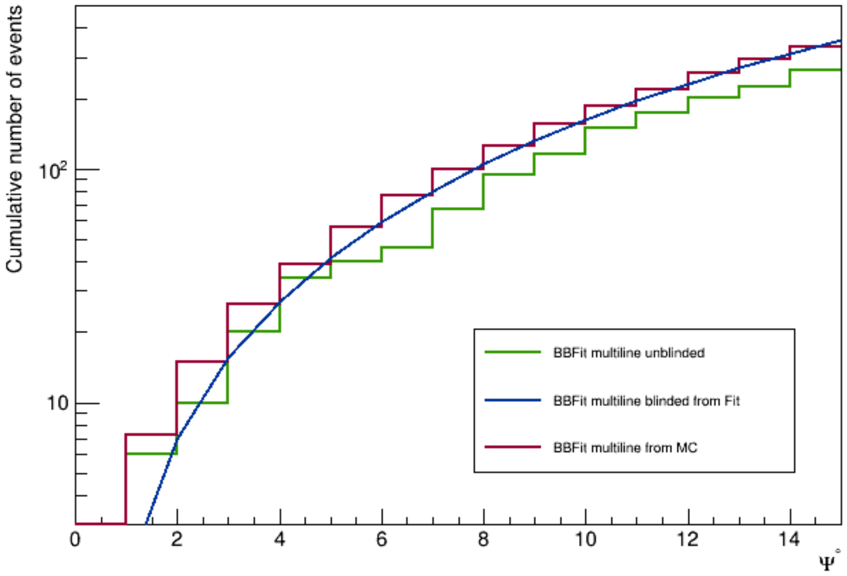

Figure 8.6.2: Cumulative number of events as a function of the angular separation for the BBFit multiline reconstruction strategy. With a blue line the distribution for scrambled data is shown, in red the histogram of real data and in green the histogram of MC simulations are shown.

8.7 Cross section

Once the neutrino flux upper limits are computed, these can be translated into cross section upper limits, through the conversion factors computed with the WimpSim program. [157] [213]. These factors, assuming the equilibrium between annihilation and capture via scattering, include the mean square distance between Sun and Earth and the number of neutrinos per annihilation. The dark matter upper limit cross section is computed for two cases explained in Chapter 6: spin dependent and spin independent.

8.7.1 Comparison with previous publication

In this subsection the results of this work and the last publication related to a similar work done with ANTARES [30] are compared. The analysis of the last publication is an indirect search of the dark matter towards the Sun but using an unbinned method based on likelihood maximisation and the data set from 2007 to 2012. The reconstruction strategies considered are the same used in the work of this thesis.
Figure 8.7.1 shows the comparison between the two analysis for the spin de-

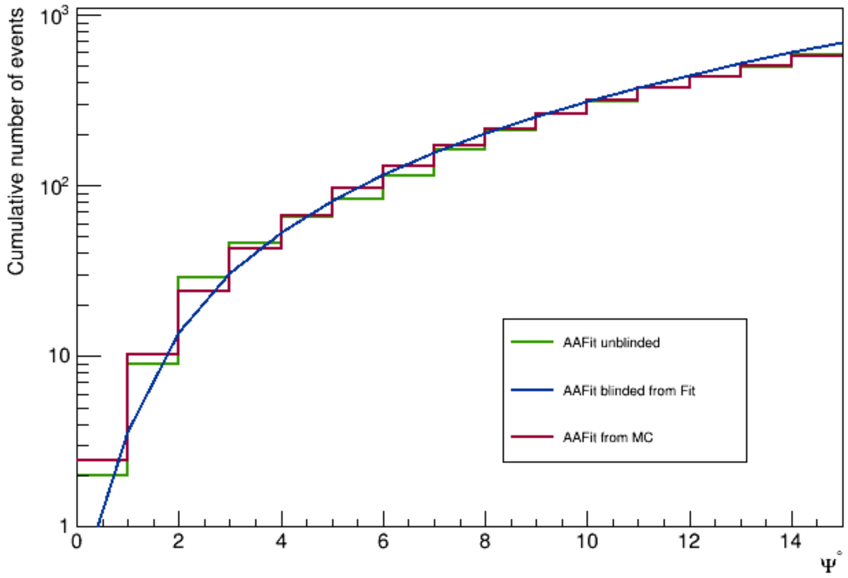

Figure 8.6.3: Cumulative number of events as a function of the angular separation for the BBFit singleline reconstruction strategy. With a blue line the distribution for scrambled data is shown, in red the histogram of real data and in green the histogram of MC simulations are shown.

pendent cross-section case and Figure 8.7.2 the case of the spin independent cross-section. The results of the work of this thesis are presented with solid lines, while with dashed lines the results of the last ANTARES publication are shown [30].

It is possible to deduce that the new results show an evident improvement, which is more than a factor of 2 and apparently better than what could be expected by the sole increase of the livetime. What we can observe here is that an unbinned analysis performs better at higher masses, instead the binned method performs better at low masses. This can be understood by the fact that the unbinned analysis considers the background distribution over the whole sky and weights it by the angular resolution of the events within the likelihood, while the binned analysis cuts the background distribution at a certain cone angle or zenith band, searching for a optimum bin. At low energies the angular resolution worsens and, in the case of the unbinned analysis, more background enters the estimation while for the binned case the cut on the angular separation reduce the impact of further away events in the background estimation by construction.

To better understand the improvements of the results achieved with this

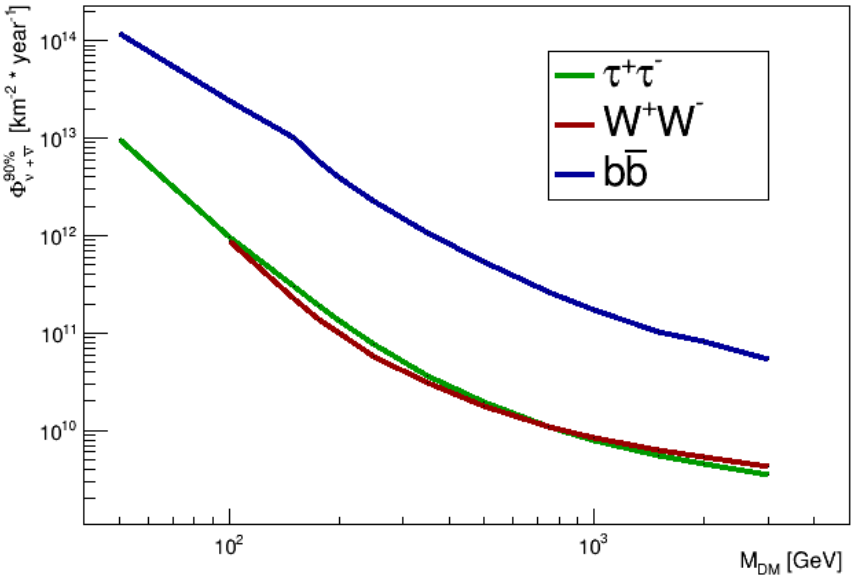

Figure 8.6.4: Upper limits on the flux for the indirect search of dark matter towards the Sun, using ANTARES data from 2007 to the end of 2019.

work and the differences between binned and unbinned method, the same analysis of this thesis has been replicated considering a data set of data from 2007 to 2012 to match the data-set of the previous publication. The best cuts obtained for the analysis are also considered for this check. In Figure 8.7.3 a comparison between the spin dependent cross section of the unbinned analysis (dashed lines) and the binned analysis (solid lines) are shown; both with data set from 2007 to 2012. Analogously, in Figure 8.7.4 the comparison for the spin independent cross section case is shown. The inclusion of systematic effects, described above and whose influence will be further displayed later in this chapter, do not modify these conclusions.

8.8 Comparison with other experiments

The results obtained in this thesis are also compared to the results published by other experiments. As it is explained in the Section 6.5, there are two types of experiments which can detect dark matter: the ones looking for direct detection and those that make indirect searches. The two approaches have different strengths and weakness. Some direct detection experiments are sensitive only to spin dependent or spin independent cross sections, while indirect experiments can study both. Also, in particular cases such as in-

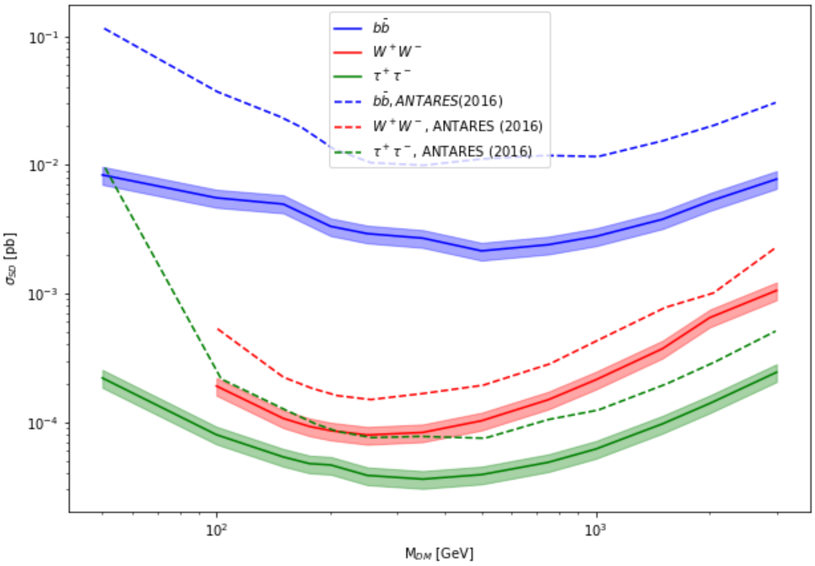

Figure 8.7.1: Limits on the spin-dependent cross section comparison between this work (solid lines) and the last publication (dashed lines) [30], for the three channels considered: $b\bar{b}$ (blue), $\tau^+\tau^-$ (green) and W^+W (red).

direct searches using high resolution experiments as gamma-ray telescopes, particular annihilation channels can be identified.
In Figure 8.8.1 the upper limits for the cross-section spin dependent obtained with different experiments are presented; as reference is taken the last publication of these. The results achieved in this thesis are really close to the ones of IceCube (2016) [19], for all three channels but in particular for $b\bar{b}$. Also IceCube improved its results recently using the Deep Core array in the inner parts of the detector [24], and produced competitive SD cross-sections for masses ranging from 10 GeV to hundreds GeV for $b\bar{b}$. However, for the annihilation channel $\tau^+\tau^-$, above dark matter masses of the order of 100 GeV the ANTARES results are better than the IceCube-Deep Core ones. A direct dark matter searches SD cross section is put as reference, because it presents a competitive spin dependent cross-section at low WIMP masses. ANTARES, for its characteristics, cannot compete at such low masses. In addition, it is very interesting to compare the results obtained in this work using ANTARES data with the simulation of ORCA sensitivity with 115 lines and five years of data taking; this results was presented at the ICRC2019 conference [166]. From this comparison, it is possible to deduce that KM3NeT/ORCA, once completed, will be more sensitive to the

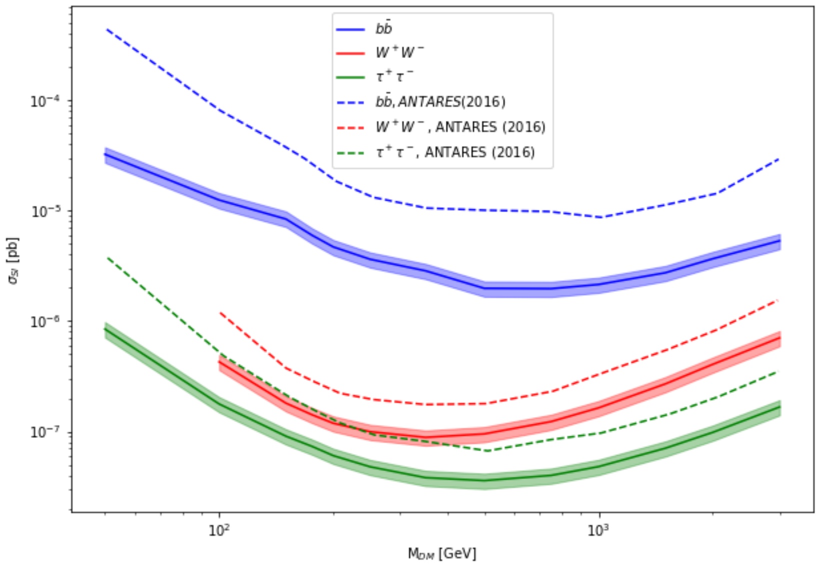

Figure 8.7.2: Limits on the spin-independent cross section comparison between this work (solid lines) and the last publication (dashed lines) [30], for the three channels considered: $b\bar{b}$ (blue), $\tau^+\tau^-$ (green) and W^+W (red).

neutrino flux of dark matter annihilation from the Sun at low masses (between 10 GeV and 100 GeV) with respect to ANTARES, with only 5 years of simulated data with respect to the 13 years of data taking considered in this thesis. In conclusion, KM3NeT/ORCA will be very competitive in the future in these DM searches.

Figure 8.8.2 shows the upper limits for the spin independent cases obtained with different experiments. As for the case of spin dependent cross section upper limits, the last publication of these experiments is taken as reference, and the three channels are shown with the same colors. Similarly to the SD case, also for the SI cross-section the results achieved in this work are really close to the ones of IceCube (2016) [19], showing a really similar behaviour of the limits. In addition, it is very interesting to compare the results obtained in this work using ANTARES data with the simulation of ORCA sensitivity with 115 lines and five years of data taking; this results was presented at ICRC2019 conference [166]. As already said above, the KM3NeT/ORCA sensitivity on the spin independent cross section is very competitive with few years of the completed detector.

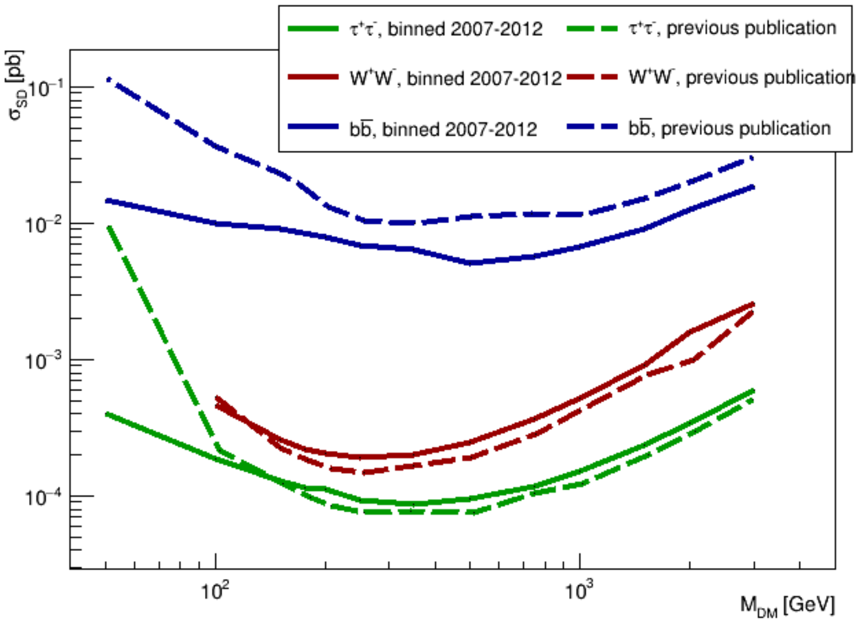

Figure 8.7.3: Limits on the spin-dependent cross section comparison between this work considering data from 2007 to 2012 (solid lines) and the last publication (dashed lines) [30], for the three channels considered: $b\bar{b}$ (blue), $\tau^+\tau^-$ (green) and W^+W (red).

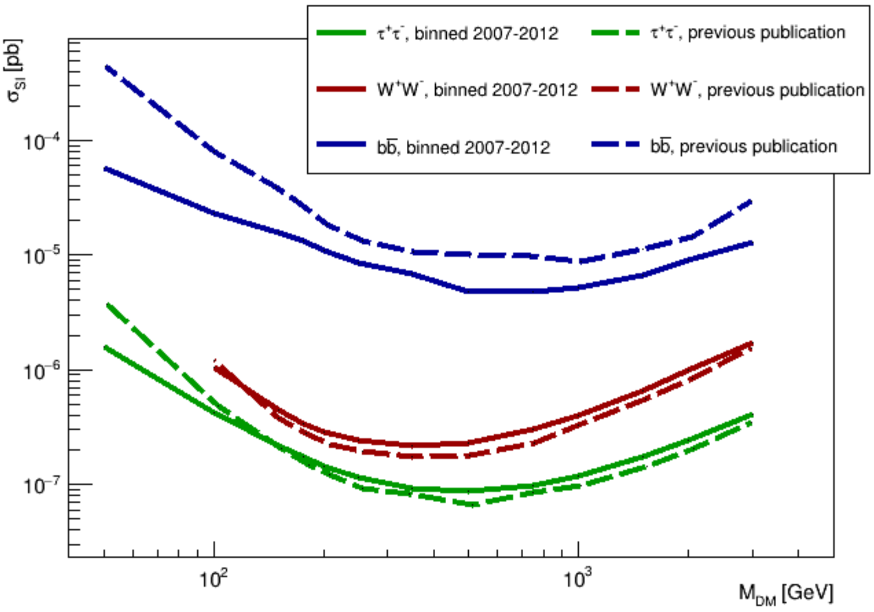

Figure 8.7.4: Limits on the spin-independent cross section comparison between this work considering data from 2007 to 2012 (solid lines) and the last publication (dashed lines) [30], for the three channels considered: $b\bar{b}$ (blue), $\tau^+\tau^-$ (green) and W^+W (red).

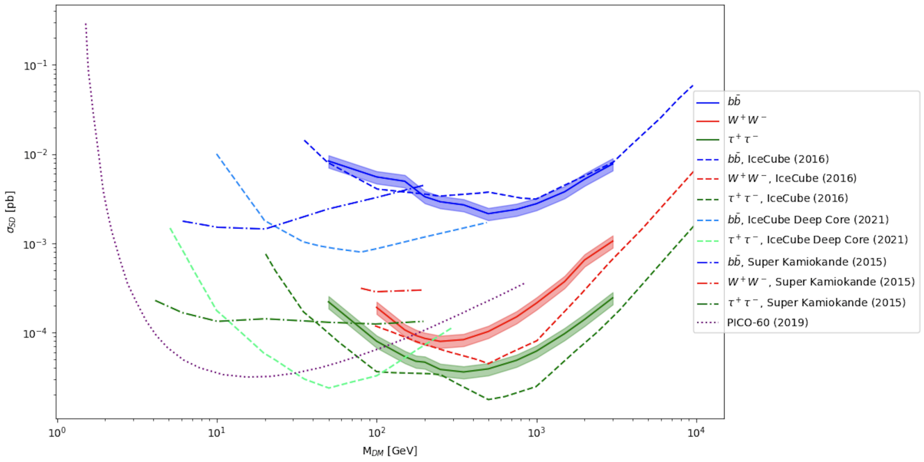

Figure 8.8.1: Limits on the spin–dependent WIMP–nucleon scattering cross–section as a function of WIMP mass for the $b\bar{b}$ (blue), $\tau^+\tau^-$ (green) and W^+W (red) channels. Limits given by other experiments are also shown: IceCube [19], [24], PICO-60 [64], SuperKamiokande [106].

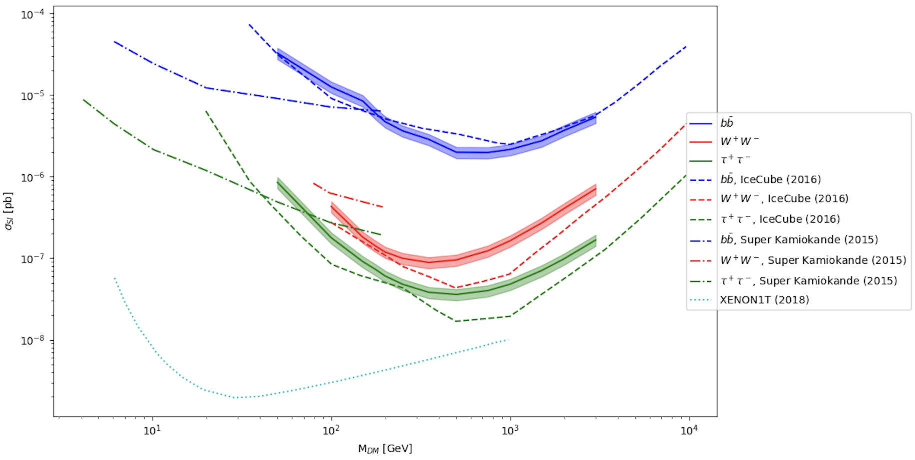

Figure 8.8.2: Limits on the spin–independent WIMP–nucleon scattering cross–section as a function of WIMP mass for the $b\bar{b}$ (blue), $\tau^+\tau^-$ (green) and W^+W (red) channels. Limits given by other experiments are also shown: IceCube [19], XENON 1T [72], SuperKamiokande [106].

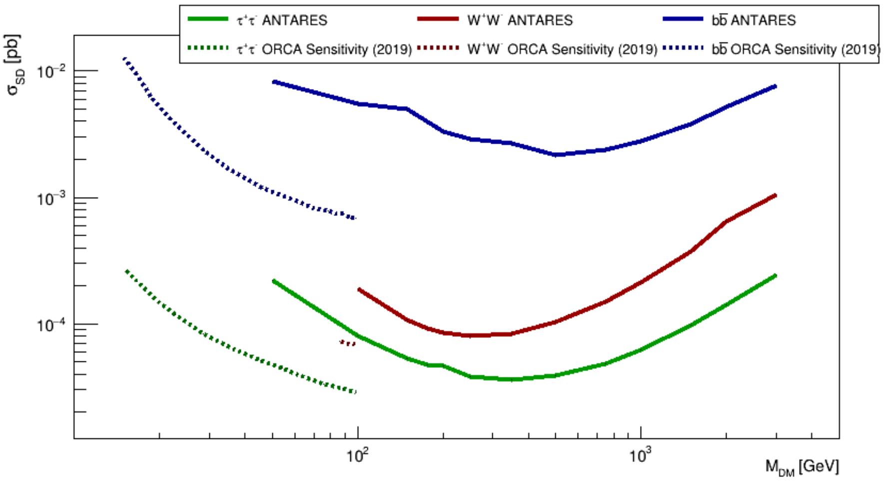

Figure 8.8.3: Comparison between the limits on the spin–dependent WIMP–nucleon scattering cross–section as a function of WIMP mass between the work of this thesis and the sensitivity of KM3NeT/ORCA [166], for the $b\bar{b}$ (blue), $\tau^+\tau^-$ (green) and W^+W (red) channels.

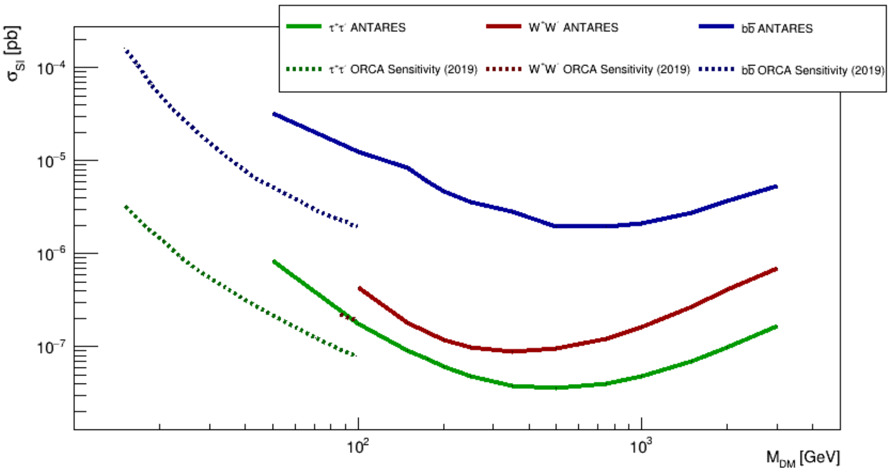

Figure 8.8.4: Comparison between the limits on the spin–independent WIMP–nucleon scattering cross–section as a function of WIMP mass between the work of this thesis and the sensitivity of KM3NeT/ORCA [166], for the $b\bar{b}$ (blue), $\tau^{+}\tau^{-}$ (green) and $W^{+}W$ (red) channels.

Summary and Conclusions

The new window of observation on the Universe opened by neutrino telescopes has shown in the last years many possibilities for discovery. ANTARES and its successor, KM3NeT, have played and will play a significant role from their privileged position in the Mediterranean Sea. ANTARES has taken data for fifteen years showing that undersea neutrino telescope can yield interesting results on many astrophysical subject. The two sites of the KM3NeT infrastructure are seeing the construction phases of the experimental apparatus and the first lines are already operational in both detectors. In particular in the French site, KM3NeT/ORCA, consists now of ten detection lines and KM3NeT/ARCA in the Italian site has now nine detection lines reaching an effective area similar to the one of ANTARES.

This thesis reports on both my technical work in collaboration with KM3NeT and the development of a physics analysis I conducted using ANTARES data. The construction phases of a new experiment are important and delicate, in particular the accurate calibration of single components, their assembling, as well as the calibration and tests of the Digital Optical Modules (DOMs) and Detection Units (DUs) before the deployment constitute a necessary passage towards the realization of the best possible detector. After the installation of the lines on the sea-bed it is still very important also to monitor the functioning of all the parts; this is especially important not only to guarantee a correct data acquisition but also to obtain the best accuracy in the reconstructions of the neutrino signals.

My contribution to KM3NeT has been mainly dedicated to compasses, as it has been described in Chapter 5. The calibration of compasses hosted on the electronic boards of the DOMs is really important. In one year I have calibrated around 110 CLBs; since a single DU contains 18 DOMs, for a total of 19 CLBs per DU, I contributed to the construction of nearly six lines. Along this process, studies on the effect on the calibration from different environmental conditions have been carried out.

Once the DUs are deployed under the sea, they are exposed to sea currents which can displace and/or rotate the DOMs. Compasses data allow to monitor some of these movements. The compass monitoring consists of computing and checking the Yaw, Pitch and Roll values to control any change in the orientation of each DOM. In this way it is possible to check for correspondences between strong sea currents and these movements. I studied the displacement of the DOMs in each line of KM3NeT/ORCA. This has shown that the Pitch and Roll values are not much affected by strong sea currents, while the analysis of Yaw values indicates that a DOM can twist by few degrees in the case of DOMs positioned in the lower part of a DU, and up to 20/30 degrees in higher floors. The reconstruction of the positions of the DOMs under the sea is possible under the assumption of a mechanical model for the DU. I contributed to the development of the DU Line Fit. In particular I worked on the part of the code in which compass data are retrieved in the same way as I did for the monitoring. The reconstruction of the DOM positions from acoustic data can be indeed complemented with the orientation information coming from compass measurements. This work in the DU Line Fit is also part of the thesis of D. Diego-Tortosa, a PhD student of the KM3NeT group at Universitat Politècnica de València with whom I collaborated.

Beyond this technical work I have been also actively taking part to the development of data analysis with the ANTARES neutrino telescope. The main physics topic of my thesis has been the analysis of the ANTARES neutrino telescope data in an indirect search for Dark Matter towards the Sun. Massive objects can capture dark matter particles. One of the best places to look at is the Sun since it is very massive and quite close. Moreover, the dark matter capture and annihilation rates are at equilibrium. Under these conditions, measuring the spectra of standard model particles from the dark matter annihilation can allow to set constraints on the dark matter scattering cross sections. My analysis has been developed using 13 years of data collected by the ANTARES neutrino telescope, as it is described in Chapter 8. The strategy followed in the search for WIMP-WIMP annihilation in the Sun used a binned method, based on the minimisation of the sensitivity flux of ANTARES to such a signal. Data have been selected in order to have up-going events from the direction of the Sun. The Model Rejection Factor procedure was used to optimize the search window radius around the source and the track quality parameters. The energy spectra of the (anti-)neutrinos at the surface of Earth is simulated using WimpSim and the channels $b\bar{b}$, $\tau^+\tau^-$, W^+W^- have been considered, assuming 100% of branching ratios in these channels. The final results I obtained improve the ones achieved by the last ANTARES publication by a factor of about 2. An article with the material of this study is in preparation.

Resumen y Conclusiones

La nueva ventana de observación del Universo abierta por los telescopios de neutrinos ha mostrado en los últimos años muchas posibilidades de nuevos descubrimientos. ANTARES y su sucesor, KM3NeT, han jugado y jugarán un papel importante desde su posición privilegiada en el Mar Mediterráneo. ANTARES ha tomado datos durante quince años y ha demostrado que el telescopio submarino de neutrinos puede arrojar resultados interesantes en muchos temas astrofísicos. Las dos localizaciones de la infraestructura KM3NeT están en su fase de construcción del aparato experimental y las primeras líneas ya están operativas en ambos detectores. En particular, KM3NeT/ORCA, en Francia, consta ahora de diez líneas de detección y KM3NeT/ARCA, en Italia, tiene ahora nueve líneas de detección que alcanzan un área efectiva similar a la de ANTARES. En esta tesis se describe mi trabajo técnico en la colaboración KM3NeT y el desarrollo de un análisis físico que realicé utilizando datos de ANTARES.

Las fases de construcción de un nuevo experimento son importantes y delicadas, en particular la calibración precisa de los componentes individuales, su integración, así como la calibración y las pruebas de los Módulos Ópticos Digitales (DOM) y las Unidades de Detección (DU) antes del despliegue constituyen un paso necesario hacia la realización del mejor detector posible. Después de la instalación de las líneas en el fondo marino, sigue siendo muy importante controlar también el funcionamiento de todas las partes; esto es especialmente importante no sólo para garantizar una correcta adquisición de datos sino también para obtener la mayor precisión en las reconstrucciones de las señales de neutrinos. Mi contribución a KM3NeT se ha dedicado principalmente a los sensores de orientación, como se ha descrito en el Capítulo 5. La calibración de estos sensores, alojados en las tarjetas electrónicas CLBs de los DOM, es realmente importante. En un año he calibrado alrededor de 110 CLBs; dado que una sola DU contiene 18 DOM, para un total de 19 CLBs por DU, contribuí a la construcción de casi seis líneas. En esta tesis se han llevado a cabo estudios sobre el efecto de la calibración en diferentes condiciones ambientales. Cuando las DUs se despliegan bajo el mar están expuestos a las corrientes marinas que pueden desplazar y/o rotar los DOMs. Los datos de los sensores acelero-magnéticos permiten monitorizar algunos de estos movimientos. El monitoreo consiste en calcular y verificar los valores de Yaw - Pitch - Roll para controlar cualquier cambio en la orientación de cada DOM. De esta forma es posible comprobar las correspondencias entre las corrientes marinas y estos movimientos. Estudié el desplazamiento de los DOMs en cada línea de KM3NeT/ORCA demostrando que los valores de cabeceo y balanceo no se ven prácticamente afectados por las corrientes marinas, mientras que el análisis de los valores de guiñada indica que un DOM puede torcerse hasta unos pocos grados en el caso de DOMs colocados en la parte inferior de una DU y hasta 20 o 30 grados en pisos superiores. La reconstrucción de las posiciones de los DOMs bajo el mar es posible bajo el supuesto de un modelo mecánico para la DU y contribuí al desarrollo del modelo “DU Line Fit”. En particular, trabajé en la parte del código en la que se recuperan los datos de los sensores de orientación de la misma manera que lo hice para el monitoreo. De hecho, la reconstrucción de las posiciones del DOM a partir de datos acústicos se puede complementar con la información de orientación proveniente de estos sensores. El trabajo en este modelo también forma parte de la tesis de D. Diego-Tortosa, estudiante de doctorado del grupo KM3NeT de la Universitat Politècnica de València, con quien colaboré.

Más allá de este trabajo técnico también he participado activamente en el desarrollo de análisis de datos con el telescopio de neutrinos ANTARES. El tema principal de física de mi tesis ha sido el análisis de los datos del telescopio de neutrinos ANTARES en una búsqueda indirecta de Materia Oscura hacia el Sol. Los objetos masivos pueden capturar partículas de materia oscura. Una de las mejores opciones por su cercanía es el Sol, donde las tasas de captura y aniquilación de materia oscura están en equilibrio. En estas condiciones, la medición de los espectros de las partículas del modelo estándar de la aniquilación de la materia oscura puede permitir establecer restricciones en las secciones transversales de dispersión de la materia oscura. Mi análisis se ha desarrollado utilizando 13 años de datos recopilados por el telescopio de neutrinos ANTARES, como se describe en los Capítulos 7 y 8. La estrategia seguida en la búsqueda de la aniquilación de WIMP-WIMP en el Sol utilizó un método binned, basado en la minimización del flujo de sensibilidad de ANTARES a tal señal. Los datos han sido seleccionados para tener eventos ascendentes desde la dirección del Sol. Se optimizó la apertura angular de búsqueda alrededor de la fuente y los parámetros de calidad de reconstrucción de la traza mediante el método de factor de rechazo al modelo. Se ha usado WimpSim para simular los espectros de energía de los (anti)neutrinos en la superficie de la Tierra para los canales de aniquilación a quarks b, a bosones W y a leptones τ, suponiendo siempre el 100% para las relaciones de ramificación en estos canales. Los resultados finales obtenidos en esta tesis mejoran los presentados en la publicación previa de ANTARES en un factor 2, aproximadamente. Actualmente, se está preparando un artículo con el material de este estudio.

Appendix A

Compasses

For completeness of the Chapter 5, Section 5.3.2, the Yaw, Pitch and Roll value for the calm period and the two periods with strong sea current are reported. In Table A.1 the details of the periods considered are resumed.

Table A.1: In this table are shown the details of the three periods presented in this work. Period 0 is the one with low sea current velocity, while the other two, Period 1 and 2, are affected to a strong sea current with similar speed but different orientation.

	Data Period	Run	Peak period	Current Speed (m/s)	Current Orientation (°)
Period 0	07/02/20	7365	NO	NO	NO
	14/02/20	7418	NO	NO	NO
Period 1	22/02/20	7495	24/02/20	0.095	225
	02/03/20	7590	25/02/20	0.130	250
Period 2	07/06/20	8085	03/06/20	0.080	95
	30/05/20	8130	04/06/20	0.110	130

A.1 Additional plot for low sea current velocity period and the two period of strong sea current

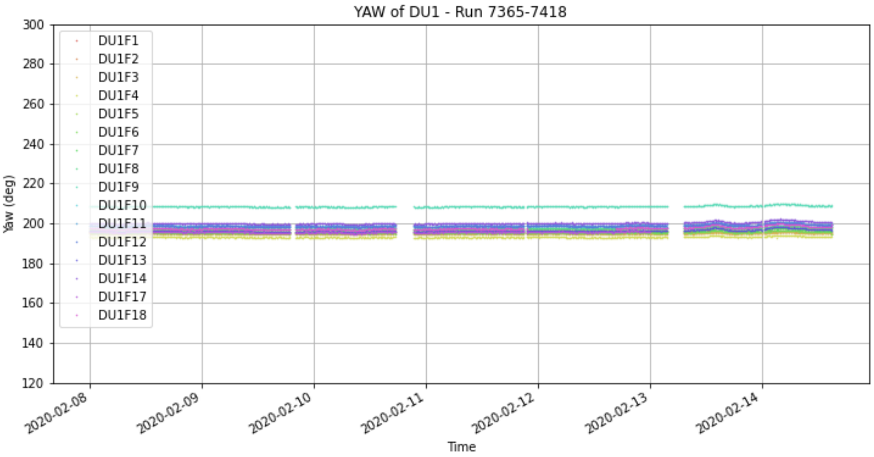

Figure A.1.1: Yaw of DU1 for Period 0.

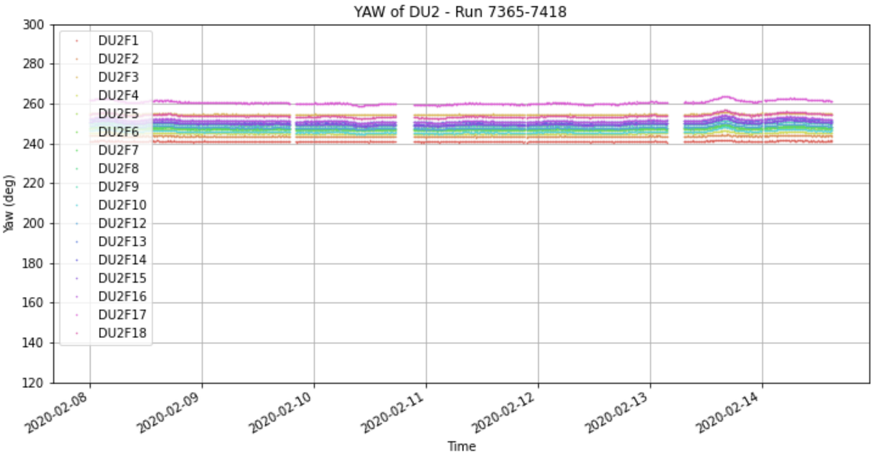

Figure A.1.2: Yaw of DU2 for Period 0.

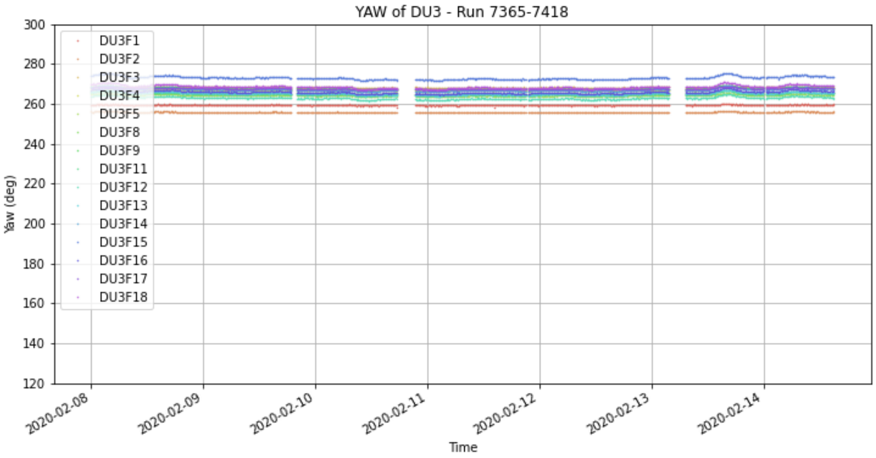

Figure A.1.3: Yaw of DU3 for Period 0.

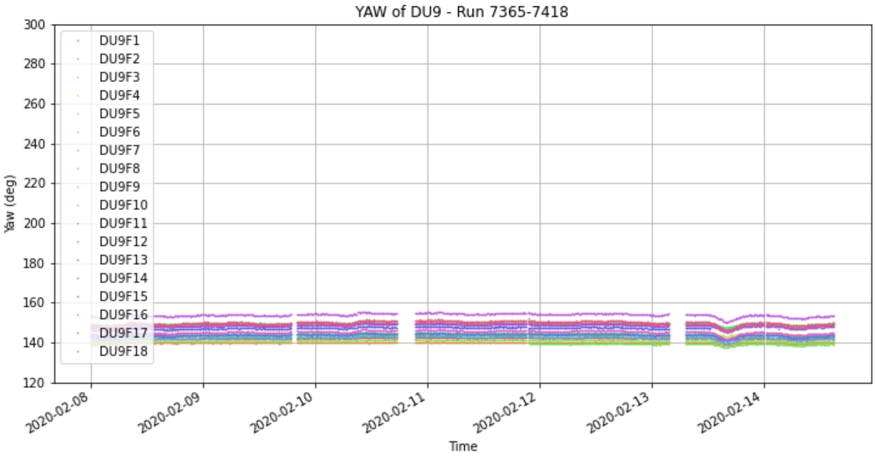

Figure A.1.4: Yaw of DU9 for Period 0.

A.2 Additional plot for Period 2

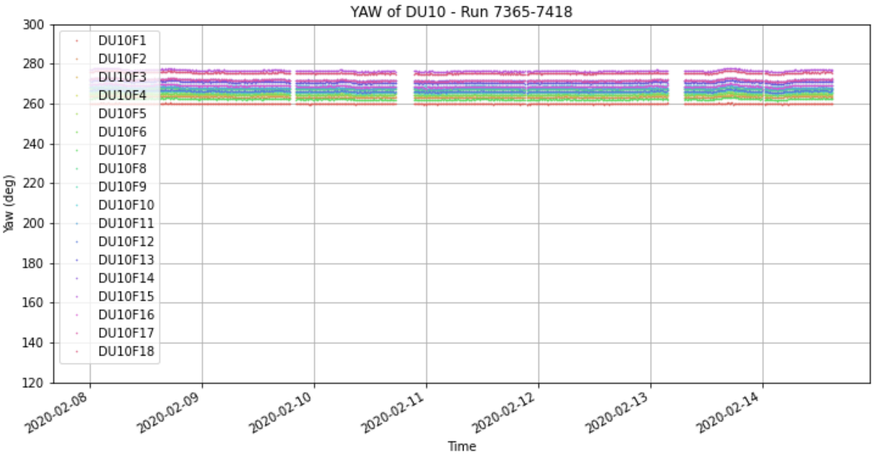

Figure A.1.5: Yaw of DU10 for Period 0.

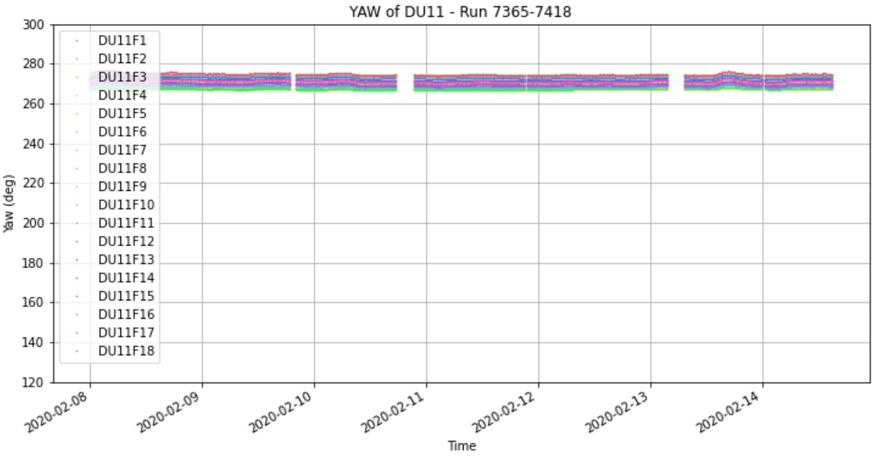

Figure A.1.6: Yaw of DU11 for Period 0.

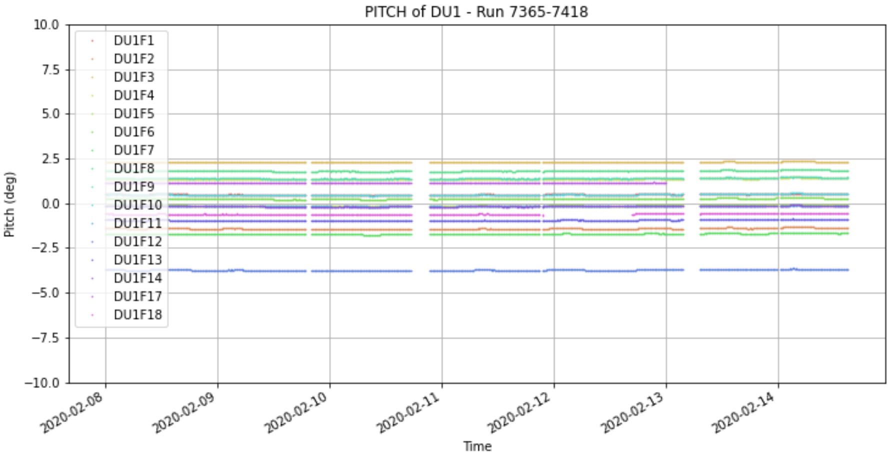

Figure A.1.7: Pitch of DU1 for Period 0.

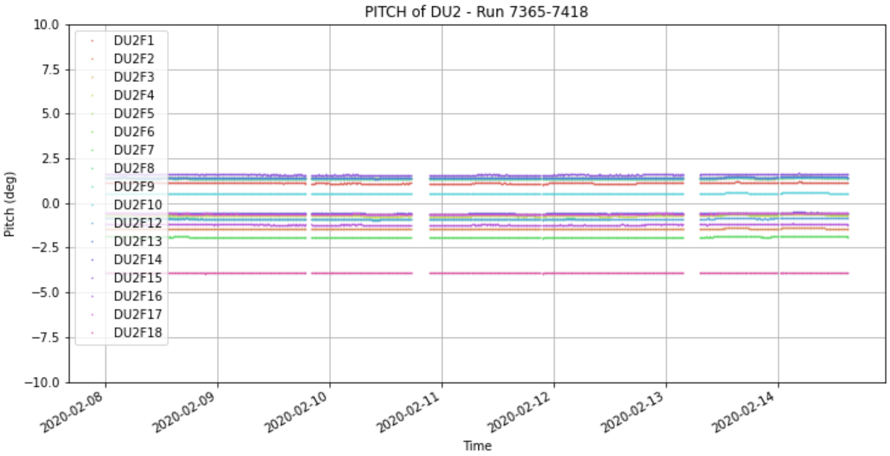

Figure A.1.8: Pitch of DU2 for Period 0.

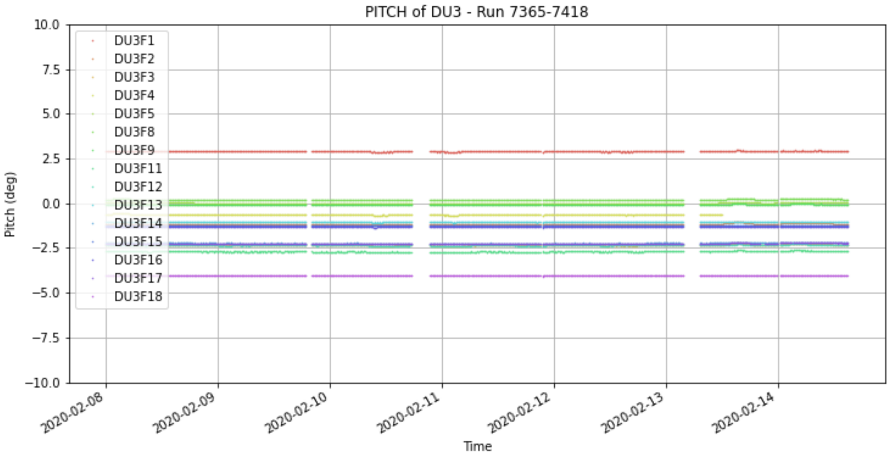

Figure A.1.9: Pitch of DU3 for Period 0.

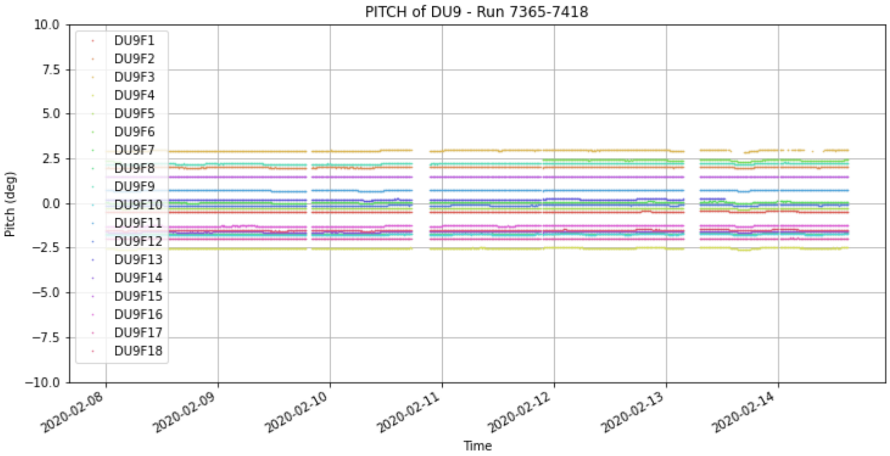

Figure A.1.10: Pitch of DU9 for Period 0.

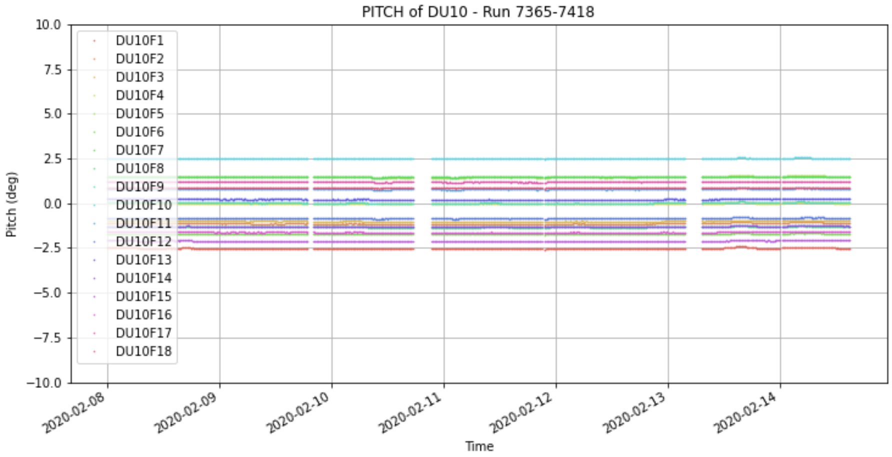

Figure A.1.11: Pitch of DU10 for Period 0.

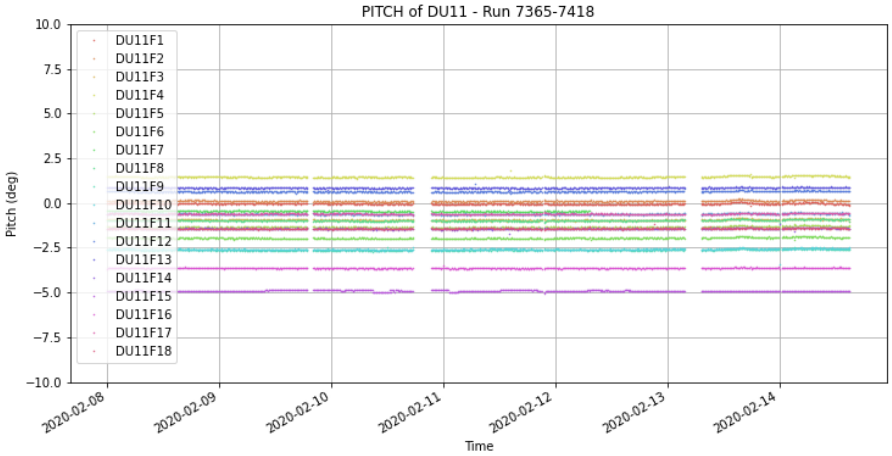

Figure A.1.12: Pitch of DU11 for Period 0.

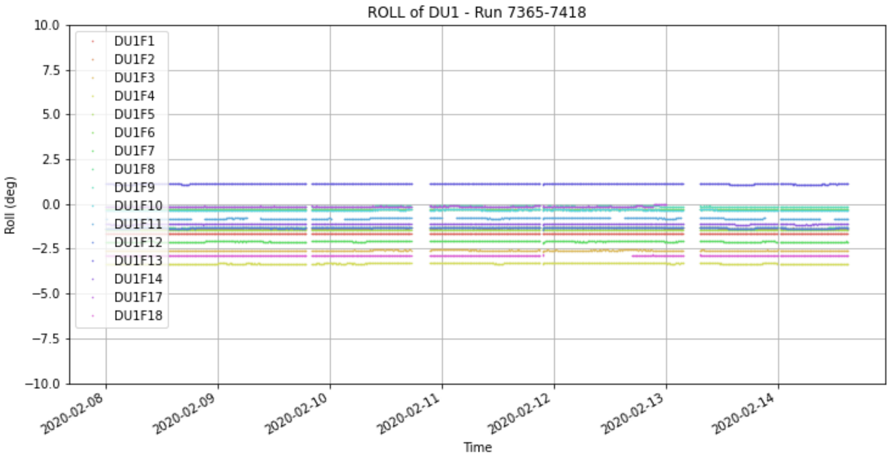

Figure A.1.13: Roll of DU1 for Period 0.

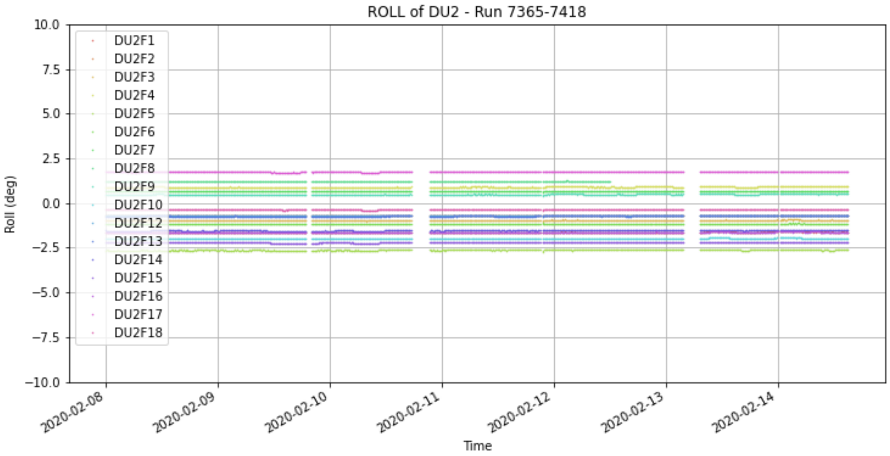

Figure A.1.14: Roll of DU2 for Period 0.

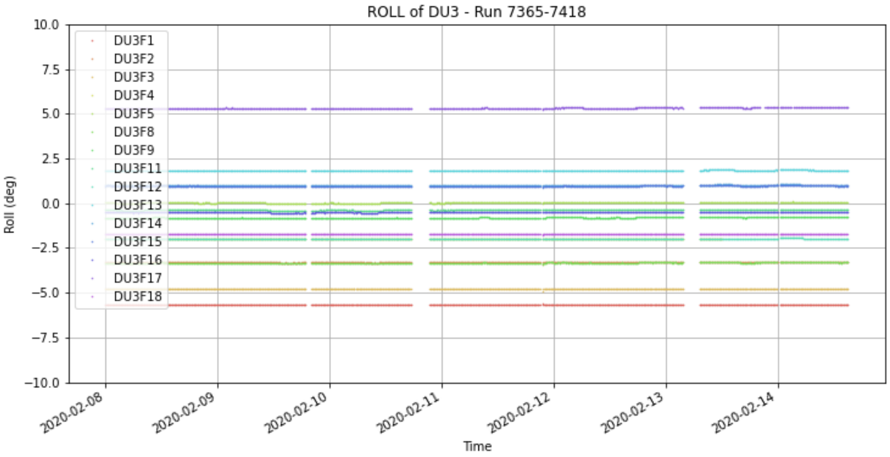

Figure A.1.15: Roll of DU3 for Period 0.

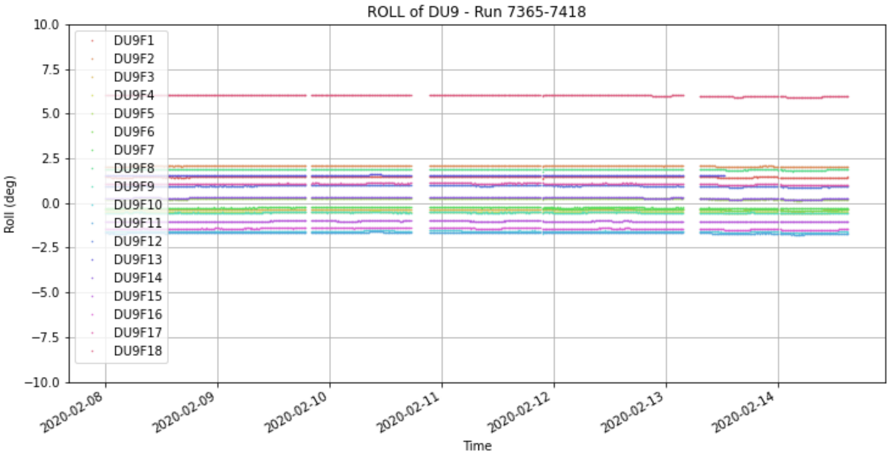

Figure A.1.16: Roll of DU9 for Period 0.

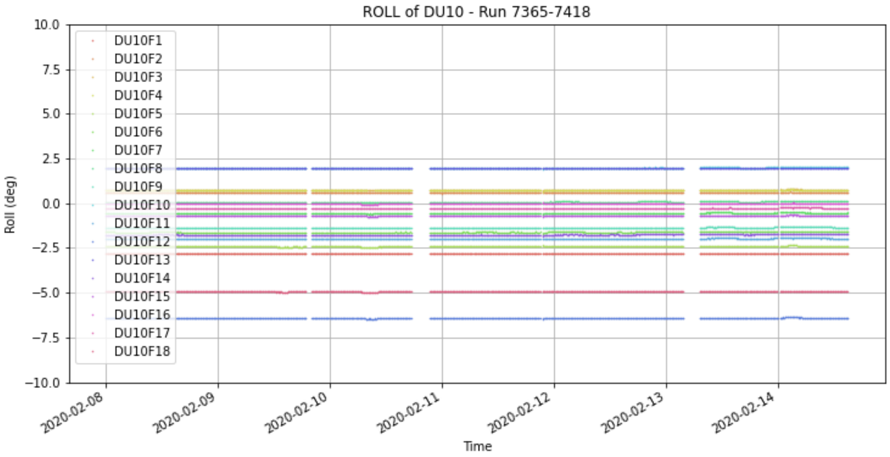

Figure A.1.17: Roll of DU10 for Period 0.

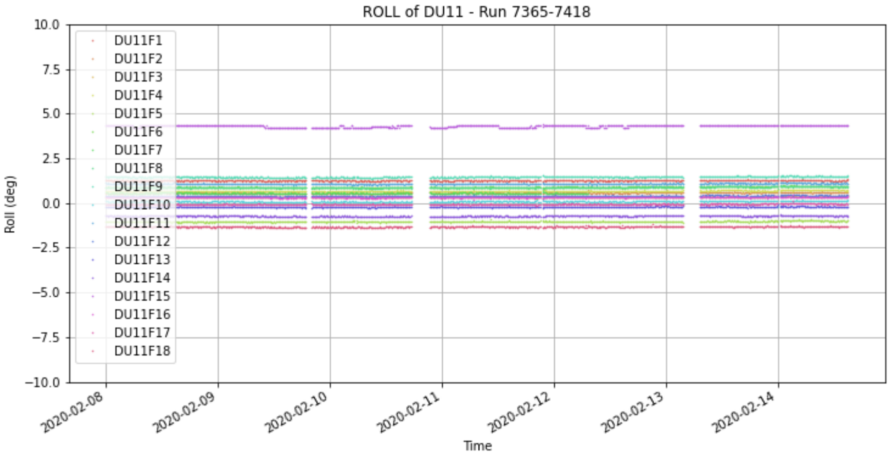

Figure A.1.18: Roll of DU11 for Period 0.

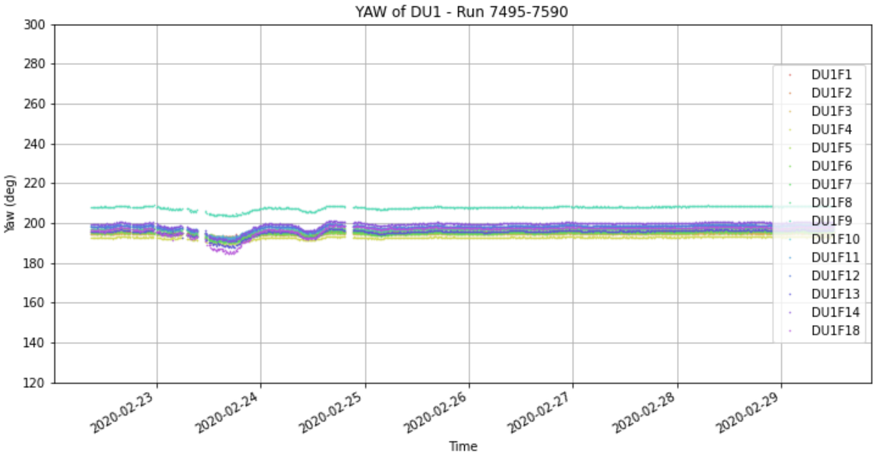

Figure A.1.19: Yaw of DU1 for Period 1.

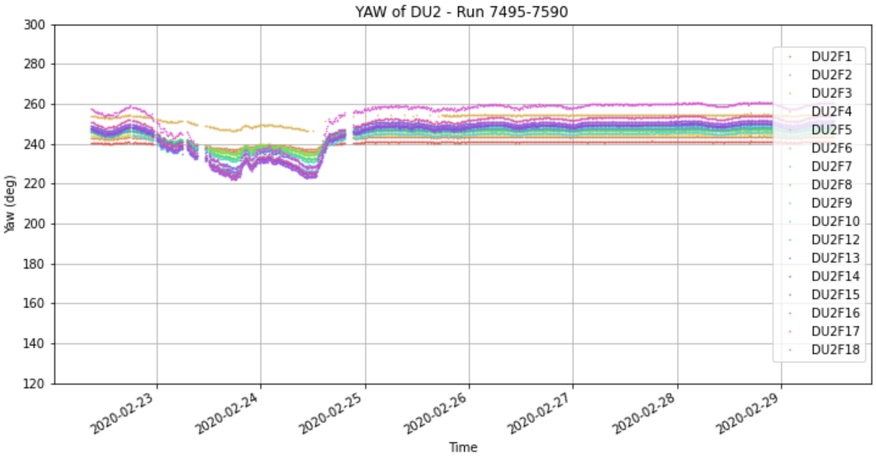

Figure A.1.20: Yaw of DU2 for Period 1.

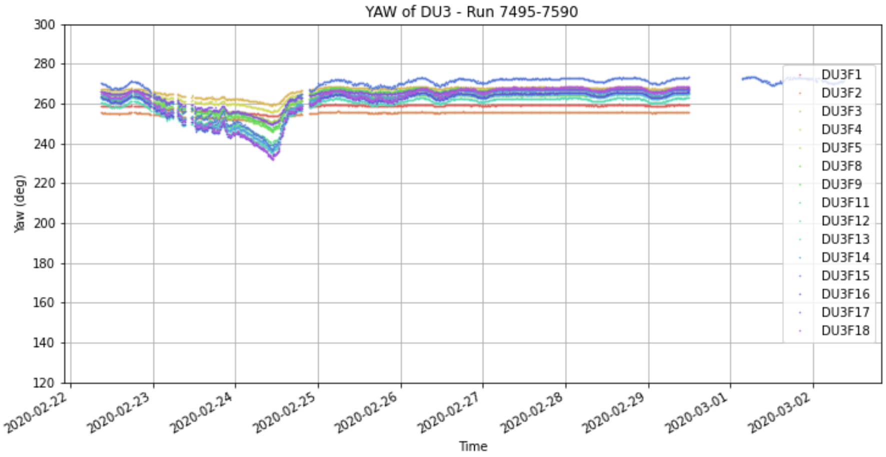

Figure A.1.21: Yaw of DU3 for Period 1.

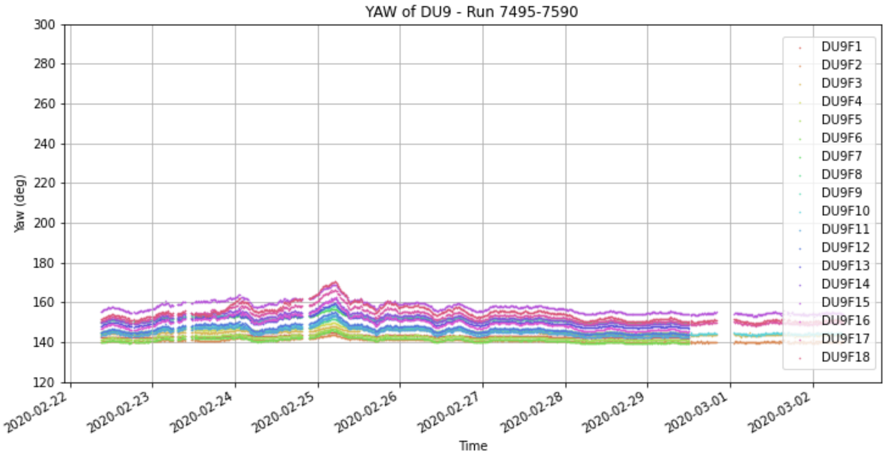

Figure A.1.22: Yaw of DU9 for Period 1.

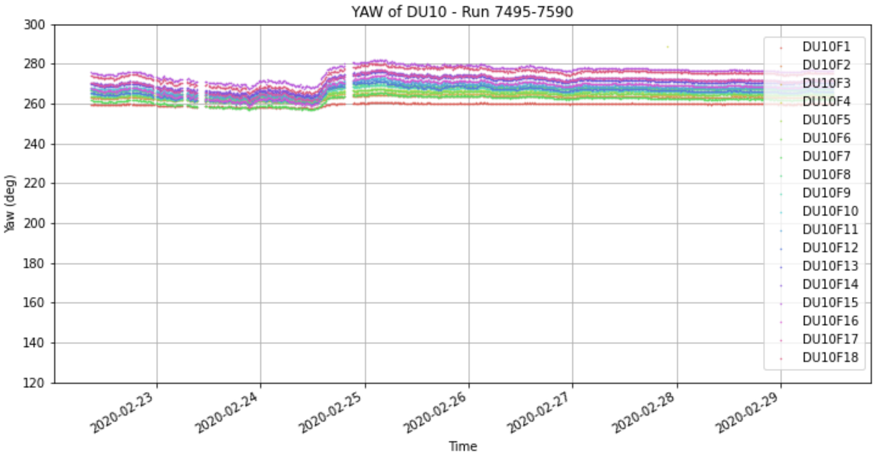

Figure A.1.23: Yaw of DU10 for Period 1.

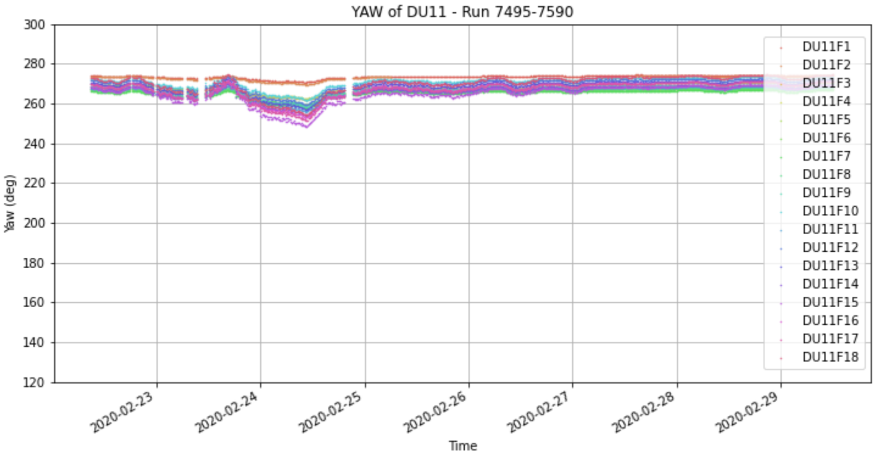

Figure A.1.24: Yaw of DU11 for Period 1.

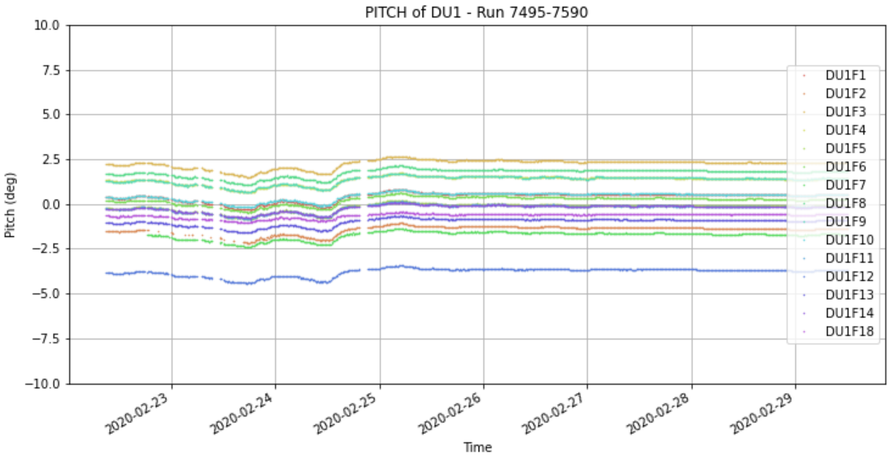

Figure A.1.25: Pitch of DU1 for Period 1.

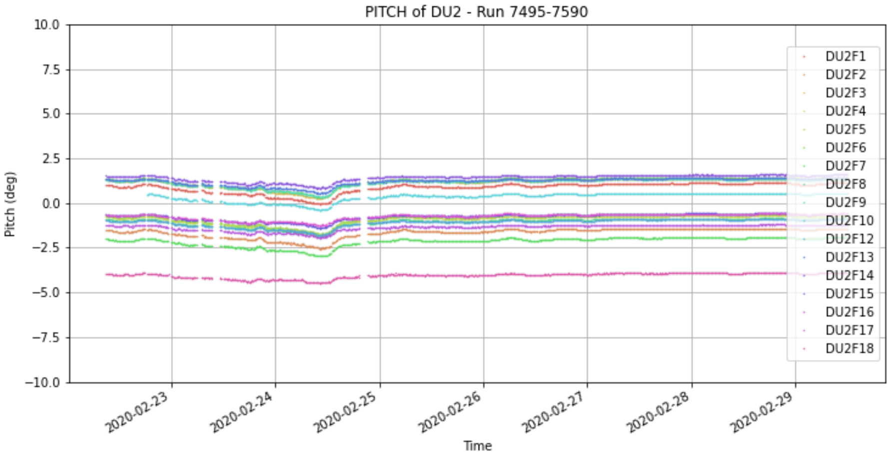

Figure A.1.26: Pitch of DU2 for Period 1.

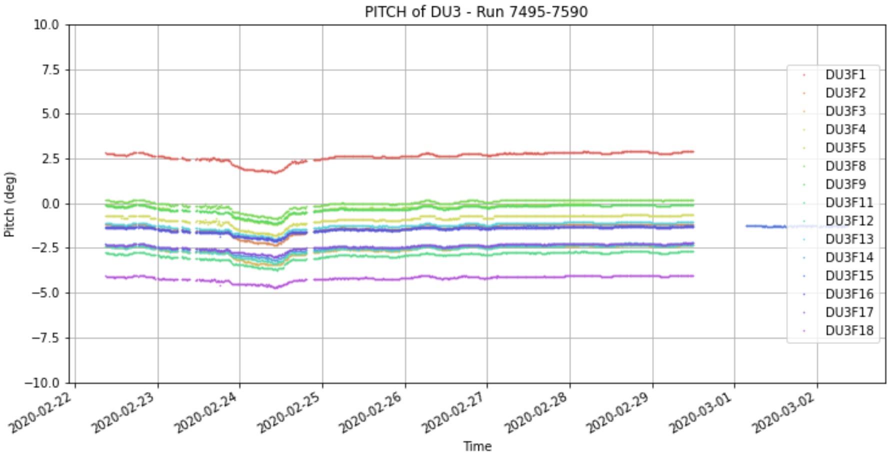

Figure A.1.27: Pitch of DU3 for Period 1.

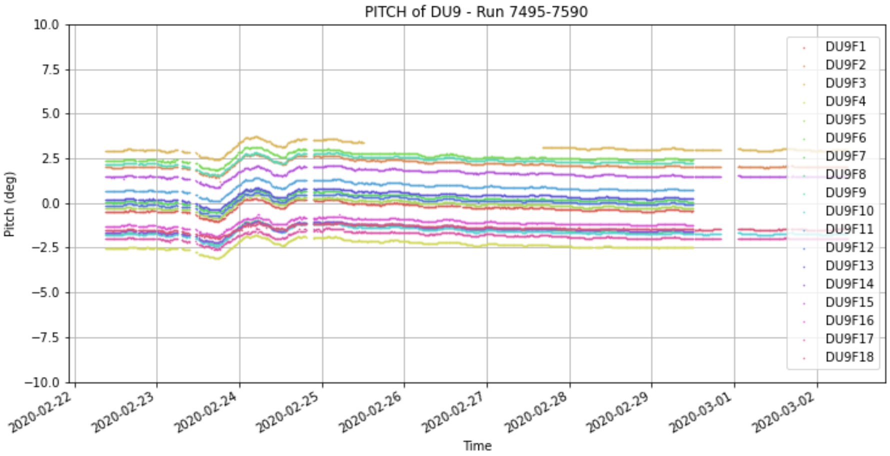

Figure A.1.28: Pitch of DU9 for Period 1.

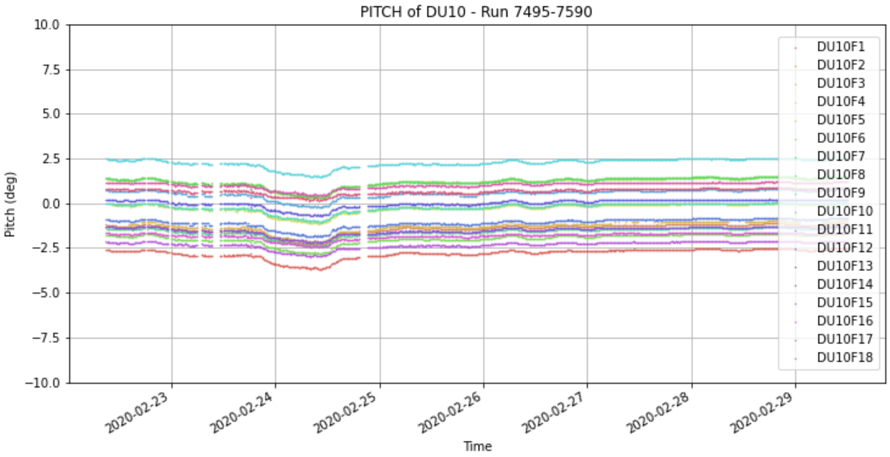

Figure A.1.29: Pitch of DU10 for Period 1.

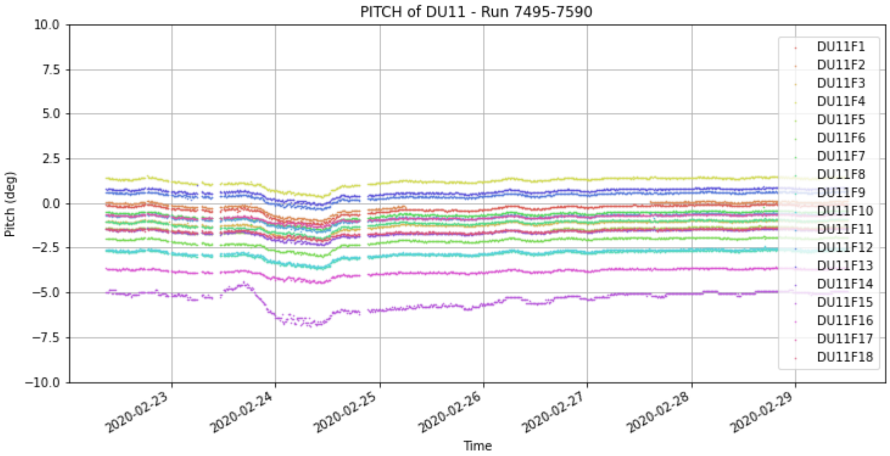

Figure A.1.30: Pitch of DU11 for Period 1.

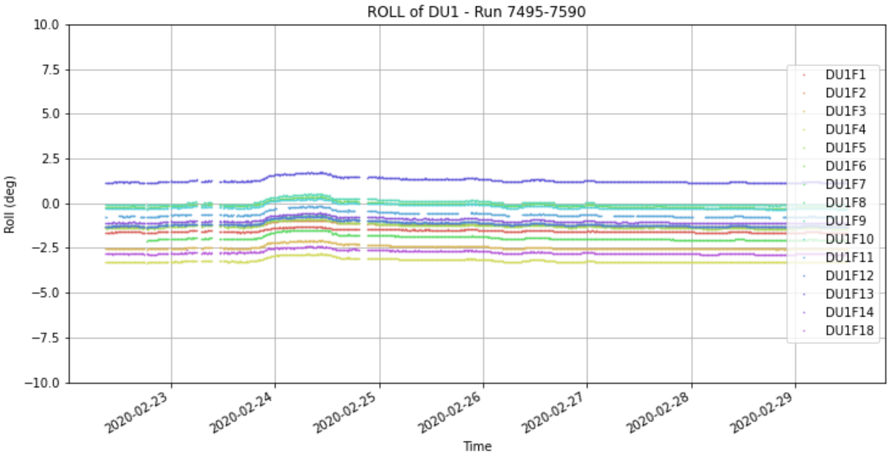

Figure A.1.31: Roll of DU1 for Period 1.

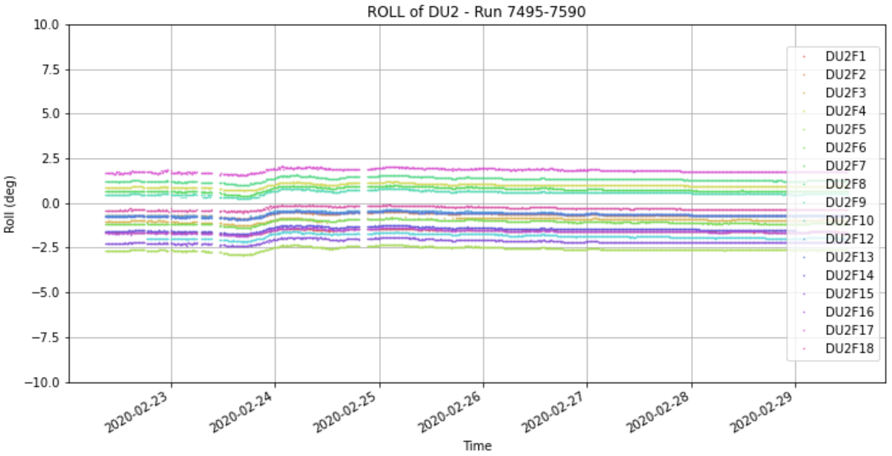

Figure A.1.32: Roll of DU2 for Period 1.

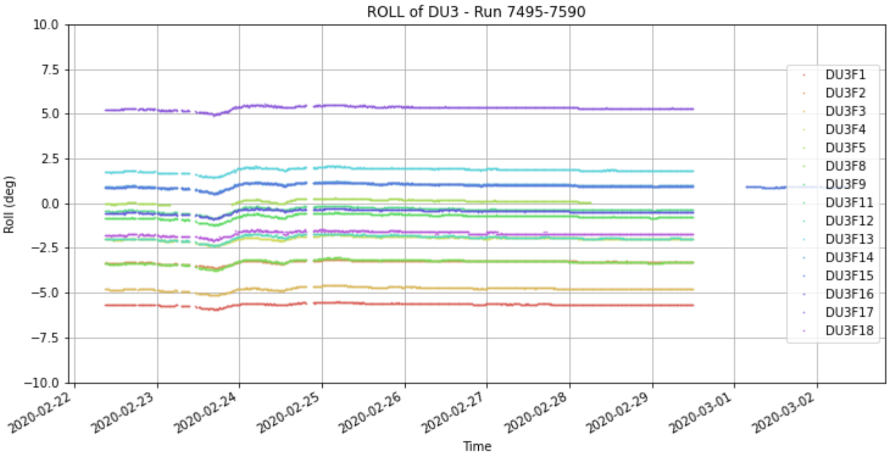

Figure A.1.33: Roll of DU3 for Period 1.

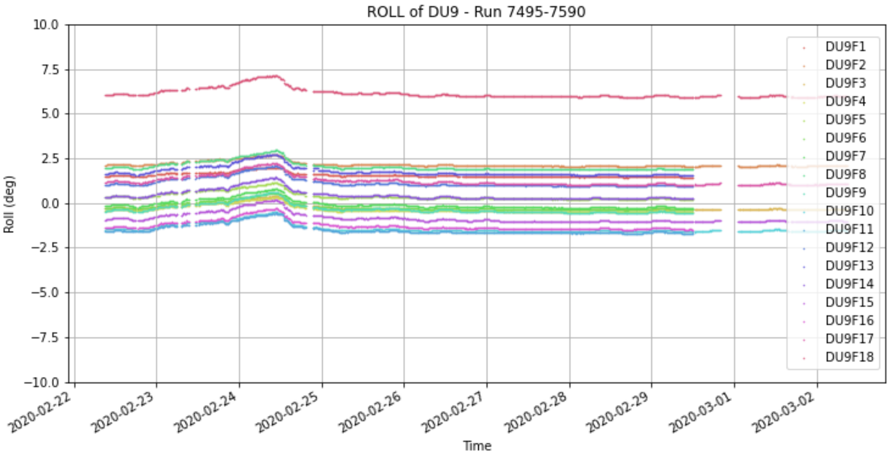

Figure A.1.34: Roll of DU9 for Period 1.

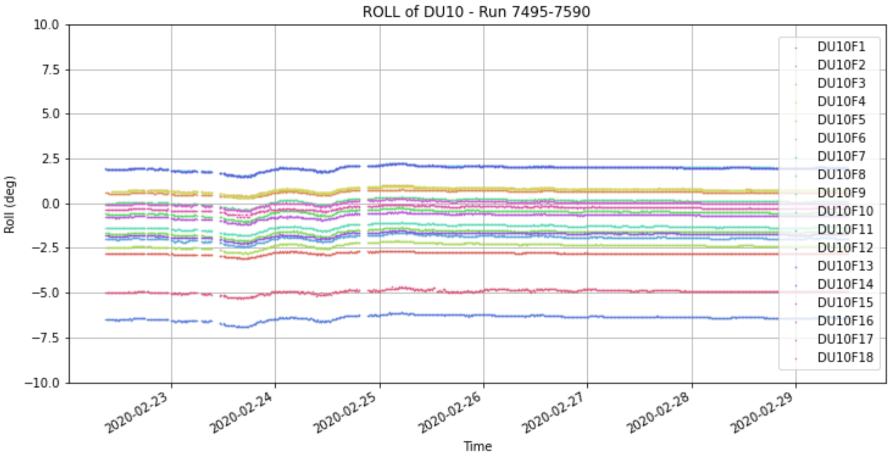

Figure A.1.35: Roll of DU10 for Period 1.

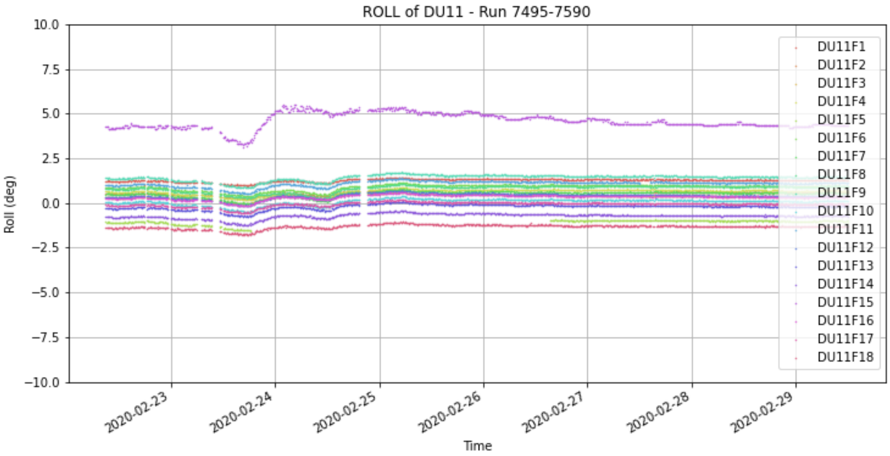

Figure A.1.36: Roll of DU11 for Period 1.

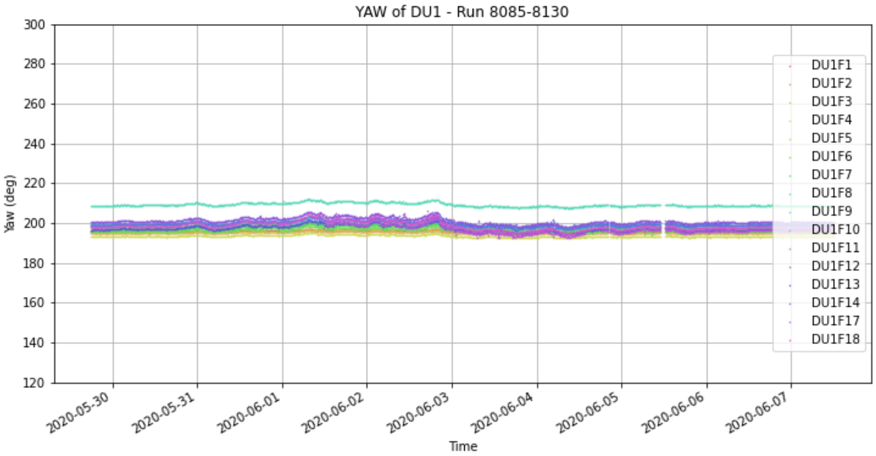

Figure A.2.1: Yaw of DU1 for Period 2.

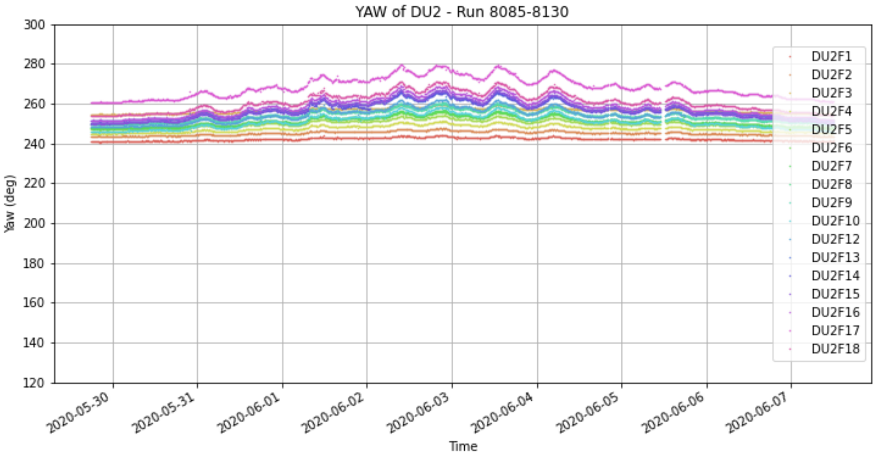

Figure A.2.2: Yaw of DU2 for Period 2.

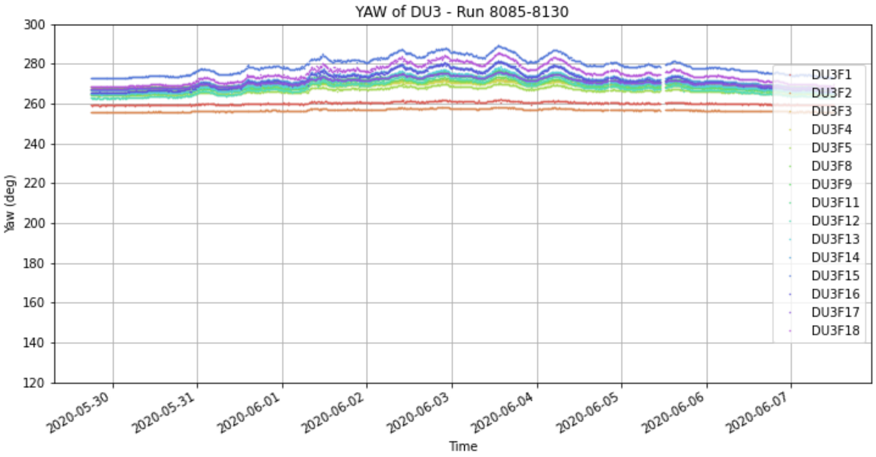

Figure A.2.3: Yaw of DU3 for Period 2.

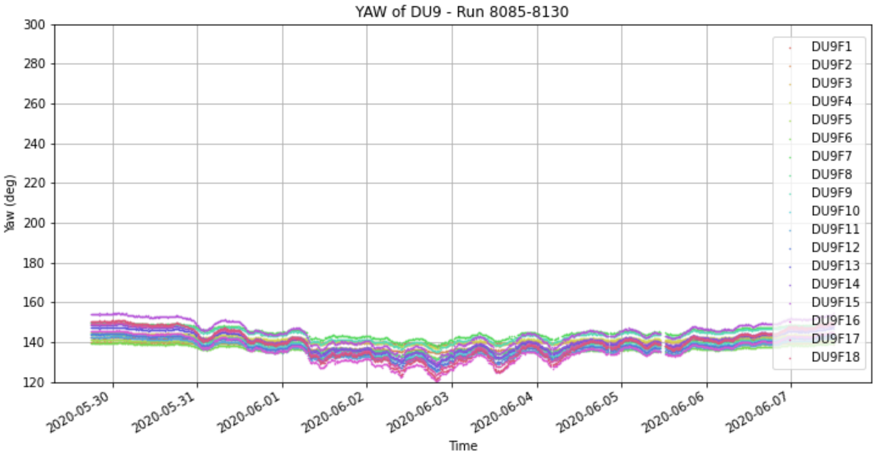

Figure A.2.4: Yaw of DU9 for Period 2.

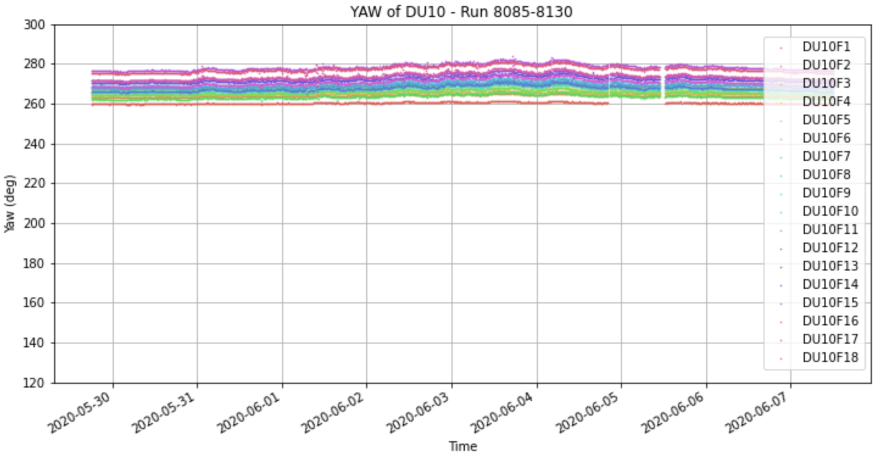

Figure A.2.5: Yaw of DU10 for Period 2.

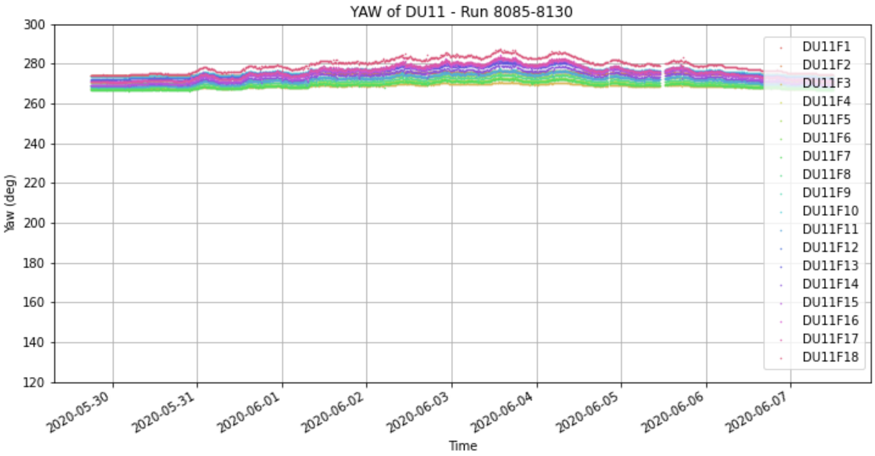

Figure A.2.6: Yaw of DU11 for Period 2.

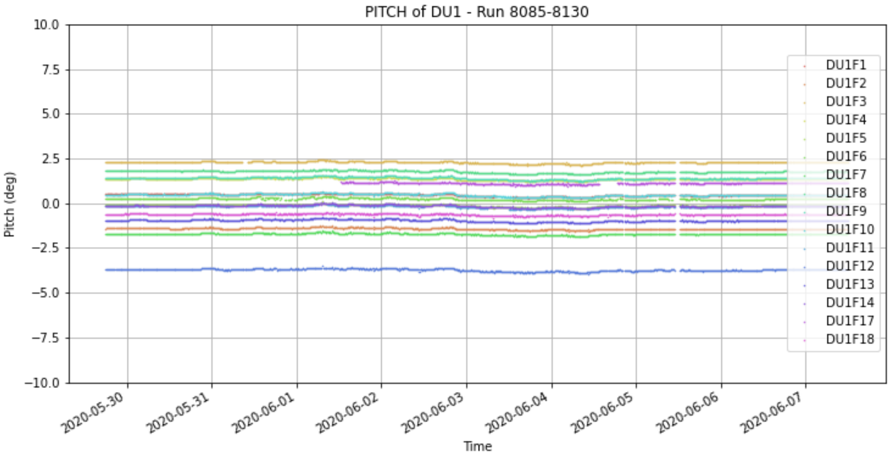

Figure A.2.7: Pitch of DU1 for Period 2.

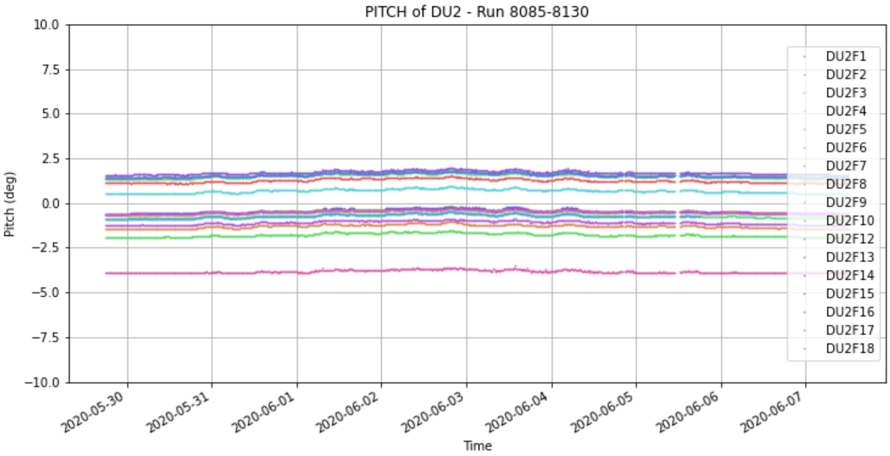

Figure A.2.8: Pitch of DU2 for Period 2.

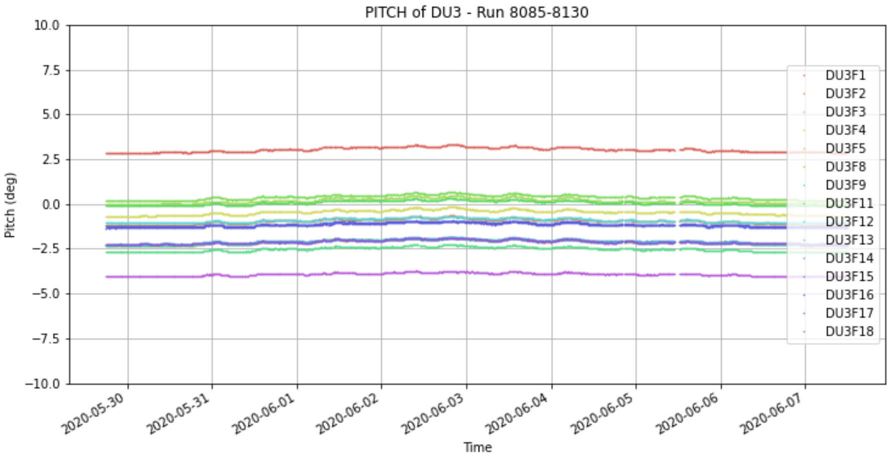

Figure A.2.9: Pitch of DU3 for Period 2.

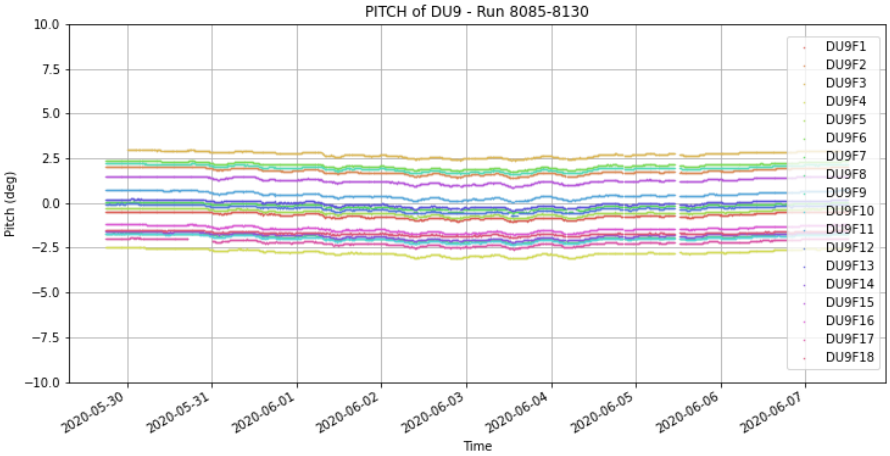

Figure A.2.10: Pitch of DU9 for Period 2.

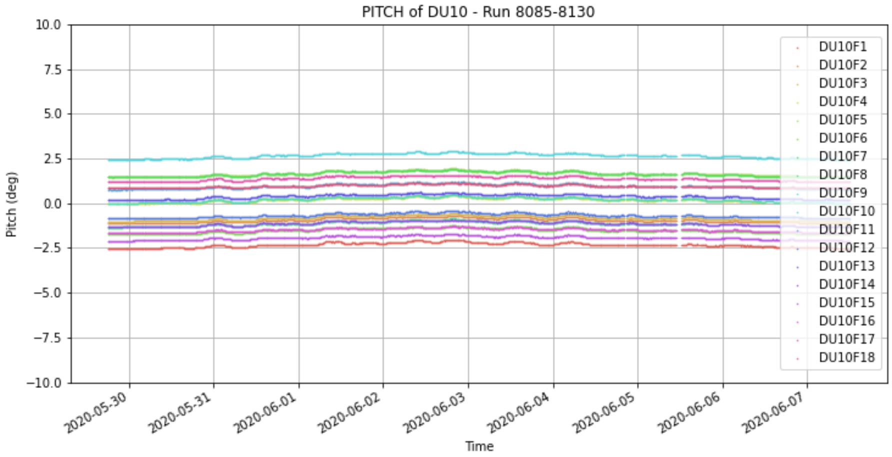

Figure A.2.11: Pitch of DU10 for Period 2.

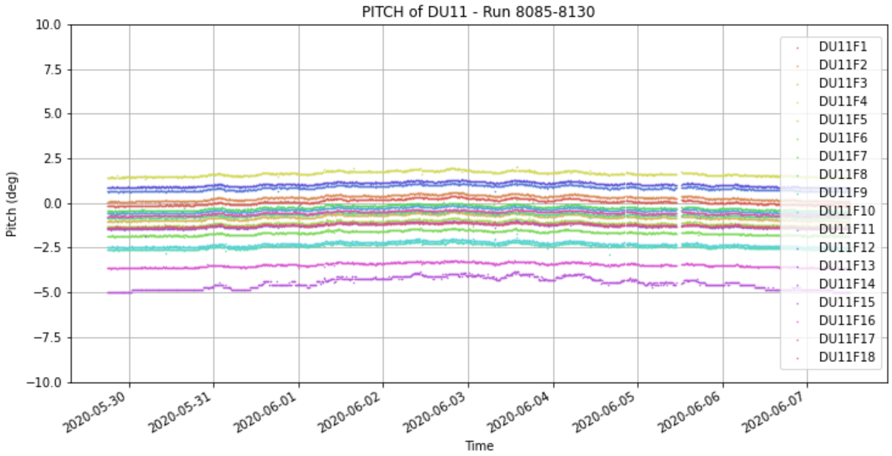

Figure A.2.12: Pitch of DU11 for Period 2.

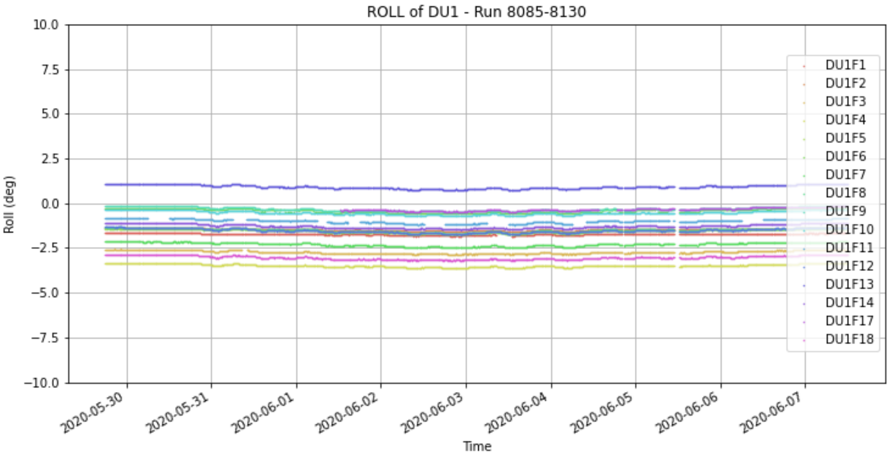

Figure A.2.13: Roll of DU1 for Period 2.

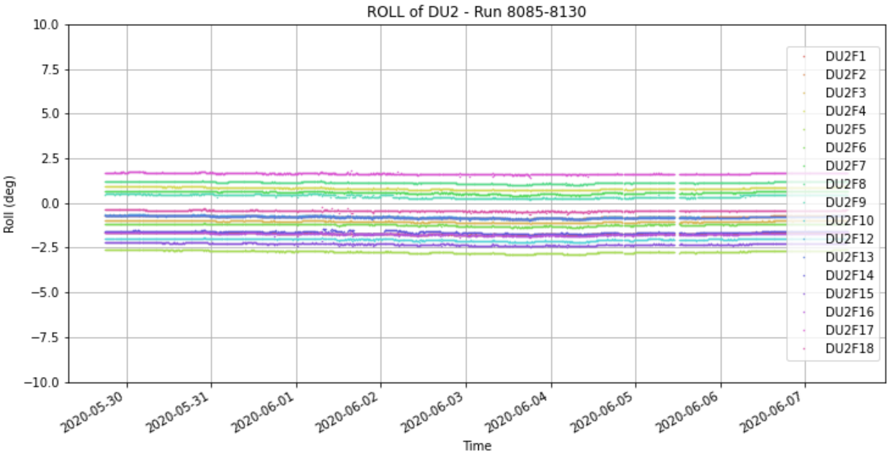

Figure A.2.14: Roll of DU2 for Period 2.

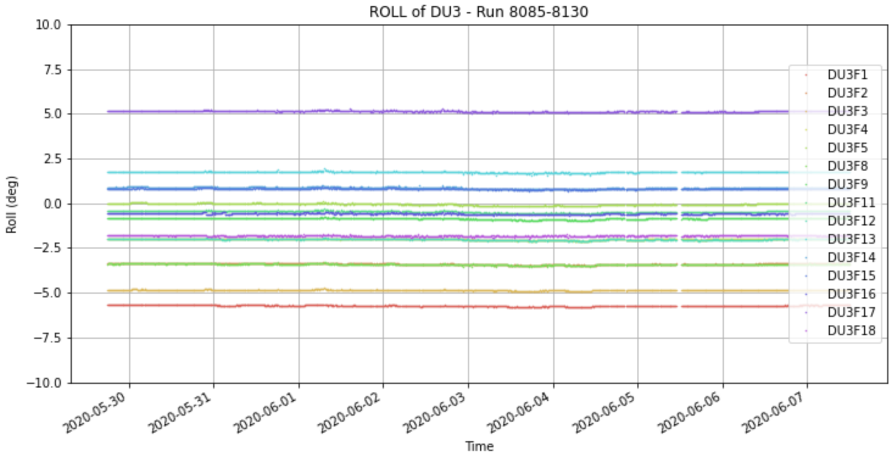

Figure A.2.15: Roll of DU3 for Period 2.

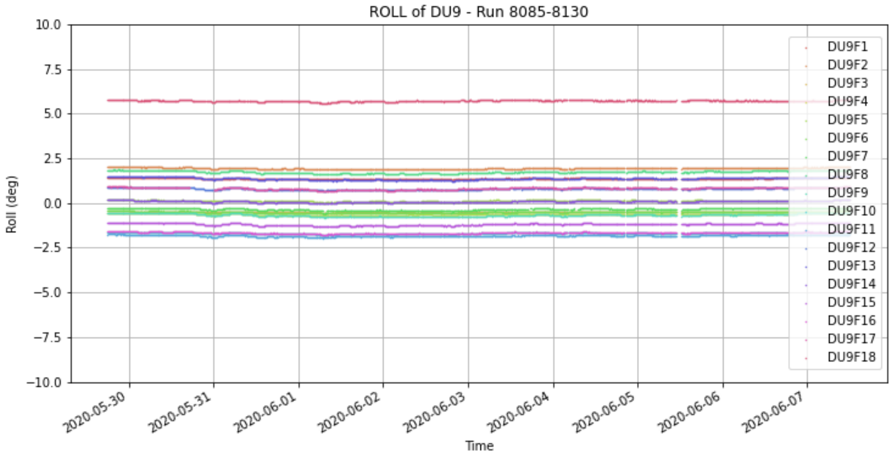

Figure A.2.16: Roll of DU9 for Period 2.

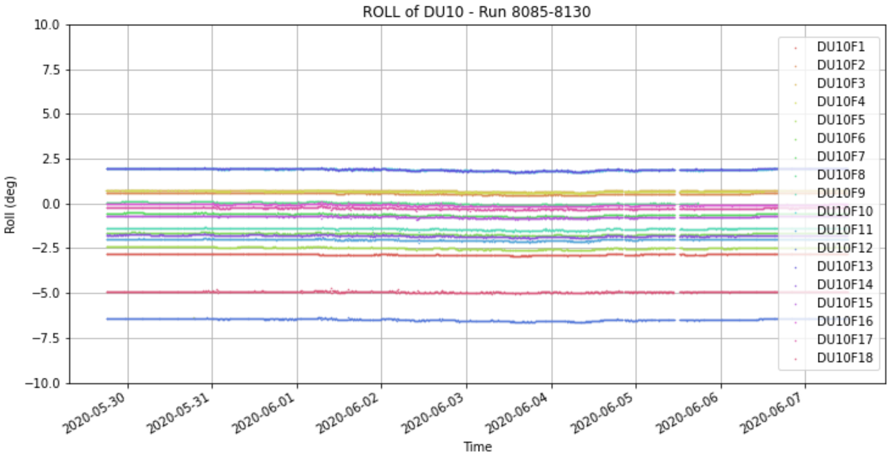

Figure A.2.17: Roll of DU10 for Period 2.

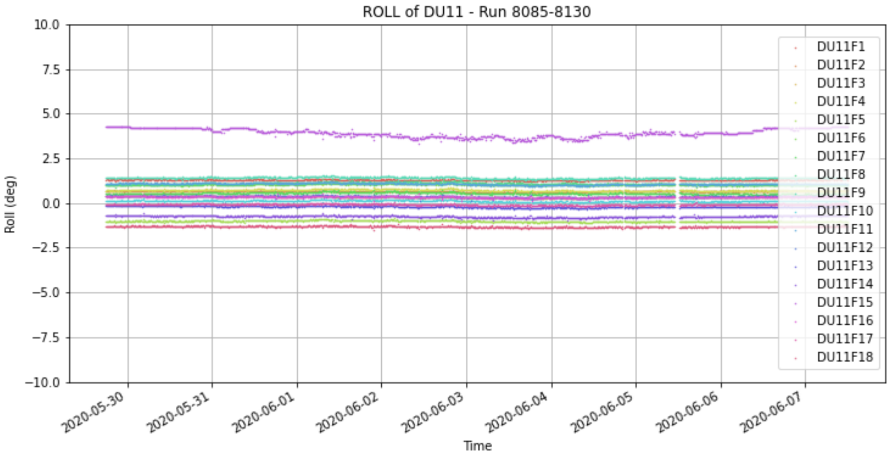

Figure A.2.18: Roll of DU11 for Period 2.

Appendix B

Compass calibration

B.1 Calibration

The motions of the CLB in the gimbals perform a series of eight full 360° rotations: six rotations around the x,y and z axes pus two rotations with an inclined, $\sim 45°$, z axis. Each rotation takes around 1 minute, in order to record enough data for the analysis.
The movements are these:

- CLB in horizontal position face up (Figure B.1(a))
- turn the CLB 90° with the face looking on your left (Figure B.1(b))
- turn the CLB 90°, face down (Figure B.1(c))
- turn the CLB in the vertical position again but looking at you right (Figure B.1(d))
- turn the CLB only 45° (Figure B.1(e))
- put the CLB in the initial position and using the internal handles put it in vertical looking at you (Figure B.1(f))
- turn the CLB of 180° in order to put it in vertical looking at your opposite side (Figure B.1(g))
- turn the the CLB only 45° (Figure B.1(h))
- leave the CLB in this 45° position and using the external handles rotated of 45° (Figure B.1(i)

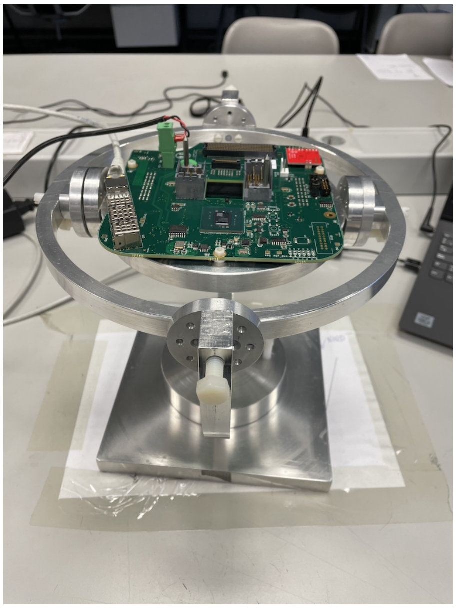

(a) 1.

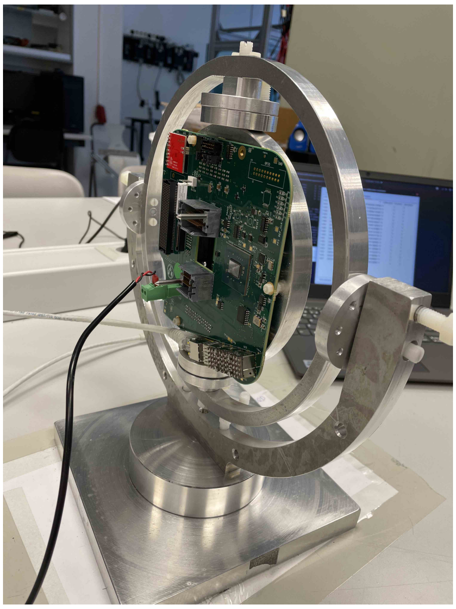

(b) 2

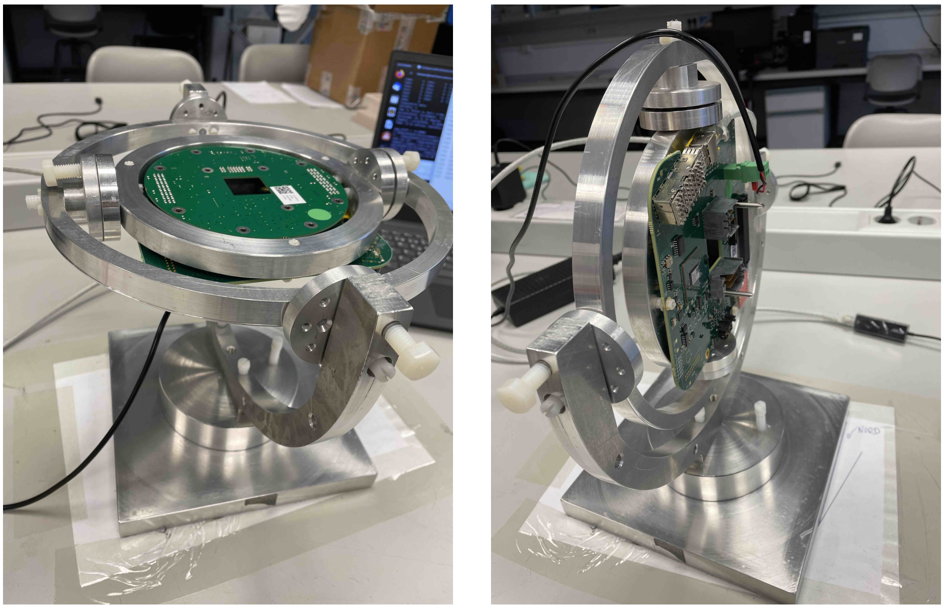

(c) 3

(d) 4

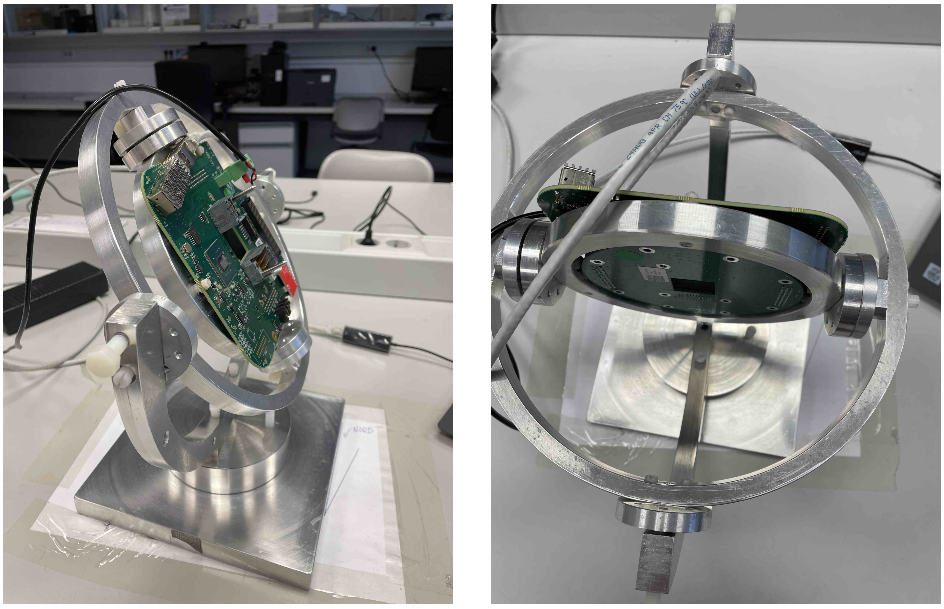

(e) 5.

(f) 6

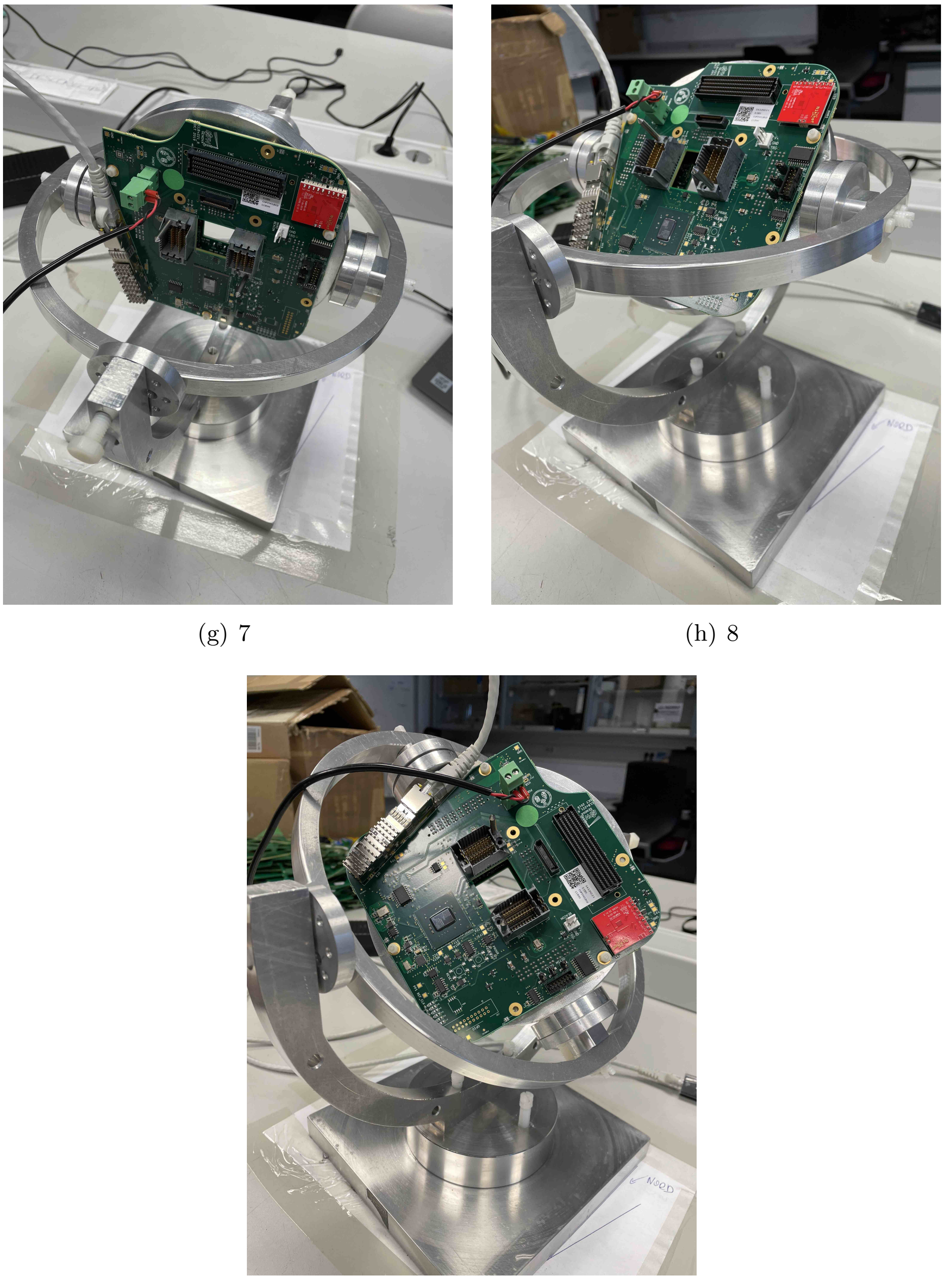

(g) 7

(h) 8

(i) 9

Appendix C

Tables

C.1 Tables with expected events

Table C.1: Table with the numbers of expected events for the BBFit single-line strategy.

Quality parameter	Cone/Aperture angle	Expected events
$\chi^2 = 0.9$	4	271
	5	342
	6	414
	7	486
	8	590
	9	631
	10	705
$\chi^2 = 1.0$	4	467
	5	587
	6	707
	7	827
	8	948
	9	1069
	10	1190
$\chi^2 = 1.1$	4	785
	5	977
	6	11696
	7	1360
	8	1551
	9	1741
	10	1931

Table C.2: Table with the numbers of expected events for the BBFit multiline strategy.

Quality parameter	Cone/Aperture angle	Expected events
$\chi^2 = 1.4$	1	1.5
	2	5.8
	3	12.9
	4	22.7
	5	35.1
	6	50.2
$\chi^2 = 1.5$	1	1.8
	2	7.0
	3	15.4
	4	27.1
	5	41.9
	6	59.7
$\chi^2 = 1.6$	1	2.2
	2	8.6
	3	18.9
	4	33.0
	5	51.0
	6	72.8

Table C.3: Table with the numbers of expected events for the AAFit strategy.

Quality parameter	Cone/Aperture angle	Expected events
λ =-5.2	1	2.1
	3	17.6
	4	30.8
	5	47.5
λ =-5.4	1	3.6
	3	30.3
	4	52.9
	5	81.5
λ =-5.6	1	8.7
	3	70.8
	4	122.5
	5	187.5

List of Acronyms

AB: Acoustic Beacon
ADCP: Acoustic Doppler Current Profiler
AHRS: Attiture Heading Reference System
AGN: Active Galactic Nuclei
ANTARES: Astronomy with a Neutrino Telescope and Abyss environmental RESearch
APS: Acoustic Positioning System
ARCA: Astroparticle Research with Cosmic in the Abyss
ARS: Analogue Ring Sampler
AVC: Amplitude to Voltage Converter
BH: Black Hole
BSS: Bottom String Socket
CC: Charge Current
CDM: Cold Dark Matter
C.L.: Confidence Level
CLB: Central Logic Board
CMB: Cosmic Microwave Background
CR: Cosmic Ray
CTD: Conductivity Temperature Depht sensor
DAQ: Data Acquisition
DM: Dark Matter
DOM: Digital Optical Module
DU: Detection Unit
FPGA: Field Programmable Gate Array
GC: Galactic Centre
GENHEN: GENerator of High Energy Neutrino
GRB: Gamma Ray Burst
GVD: Gigaton Volume Detector
HDM: Hot Dark Matter
HFLBL: High Frequency Long Base Line
JB: Junction Box
LCM: Local Control Module
LOM: Launcher of Optical Modules
MACHO: MAssive Compact Halo Object

MC: Monte Carlo
MEOC: Main Electro Optical Cable
MLCM: Master Local Control Module
MM: Mechanical Model
MOND: MOdified Newtonian Dynamics
MSSM: Minimal Supersymmetry Standard Model
NC: Neutral Current
NFW: Navarro-Frenk-White
OM: Optical Module
ORCA: Oscillation Research with Cosmic in the Abyss
p.e.: photo-electron
PMT: Photo Multiplier Tube
PWN: Pulsar Wind Nebulae
QA/QC: Quality Assurance / Quality Control
ROV: Remote Operated Vehicle
SC: Slow Control
SCM: String Control Module
SD: Spin Dependent
SI: Spin Independent
SM: Standard Model
SNO: Sudbury Neutrino Observatory
SNR: Supernova Remnant
SPL: Sound Pressure Level
SPM: String Power Module
SUSY: Super Symmetry
ToE: Time of Emission
ToT: Time over Treshold
TTS: Transit Time Spread
TVC: Time to Voltage Converter
UTM: Universal Transvers Mercator
WDM: Warm Dark Matter
WIMP: Weakly Massive Interactive Particle
YPR: Yaw, Pitch and Roll

Bibliography

[1] URL: http://www.phys.hawaii.edu/dumand/.

[2] URL: http://baikalweb.jinr.ru/.

[3] URL: https://icecube.wisc.edu.

[4] URL: http://antares.in2p3.fr/.

[5] URL: https://emso.eu.

[6] URL: https://www.km3net.org.

[7] URL: https://en.wikipedia.org/wiki/Attitude_and_heading_reference_system.

[8] URL: https://erddap.osupytheas.fr/erddap/index.html.

[9] URL: https://esahubble.org/images/heic1106c/.

[10] URL: https://esahubble.org/images/heic0814a/.

[11] URL: https://geant4.web.cern.ch/.

[12] URL: https://en.wikipedia.org/wiki/Universal_Transverse_Mercator_coordinate_system.

[13] Georges Aad et al. "Search for dark matter candidates and large extra dimensions in events with a photon and missing transverse momentum in pp collision data at $\sqrt{s} = 7$ TeV with the ATLAS detector". In: *Phys. Rev. Lett.* 110.1 (2013), p. 011802. DOI: 10.1103/PhysRevLett.110.011802. arXiv: 1209.4625 [hep-ex].

[14] Georges Aad et al. "Search for dark matter in events with a hadronically decaying W or Z boson and missing transverse momentum in pp collisions at $\sqrt{s} = 8$ TeV with the ATLAS detector". In: *Phys. Rev. Lett.* 112.4 (2014), p. 041802. DOI: 10.1103/PhysRevLett.112.041802. arXiv: 1309.4017 [hep-ex].

[15] M. G. Aartsen et al. "IceCube-Gen2: A Vision for the Future of Neutrino Astronomy in Antarctica". In: (Dec. 2014). arXiv: 1412.5106 [astro-ph.HE].

[16] M. G. Aartsen et al. "Measurement of the Atmospheric ν_e flux in IceCube". In: *Phys. Rev. Lett.* 110.15 (2013), p. 151105. DOI: 10.1103/PhysRevLett.110.151105. arXiv: 1212.4760 [hep-ex].

[17] M. G. Aartsen et al. "Neutrino emission from the direction of the blazar TXS 0506+056 prior to the IceCube-170922A alert". In: *Science* 361.6398 (2018), pp. 147–151. DOI: `10.1126/science.aat2890`. arXiv: `1807.08794 [astro-ph.HE]`.

[18] M. G. Aartsen et al. "Observation of High-Energy Astrophysical Neutrinos in Three Years of IceCube Data". In: *Phys. Rev. Lett.* 113 (2014), p. 101101. DOI: `10.1103/PhysRevLett.113.101101`. arXiv: `1405.5303 [astro-ph.HE]`.

[19] M. G. Aartsen et al. "Search for annihilating dark matter in the Sun with 3 years of IceCube data". In: *Eur. Phys. J. C* 77.3 (2017). [Erratum: Eur.Phys.J.C 79, 214 (2019)], p. 146. DOI: `10.1140/epjc/s10052-017-4689-9`. arXiv: `1612.05949 [astro-ph.HE]`.

[20] M. G. Aartsen et al. "Search for dark matter annihilations in the Sun with the 79-string IceCube detector". In: *Phys. Rev. Lett.* 110.13 (2013), p. 131302. DOI: `10.1103/PhysRevLett.110.131302`. arXiv: `1212.4097 [astro-ph.HE]`.

[21] M. G. Aartsen et al. "Search for Neutrinos from Dark Matter Self-Annihilations in the center of the Milky Way with 3 years of IceCube/DeepCore". In: *Eur. Phys. J. C* 77.9 (2017), p. 627. DOI: `10.1140/epjc/s10052-017-5213-y`. arXiv: `1705.08103 [hep-ex]`.

[22] R. Abbasi et al. "Determination of the Atmospheric Neutrino Flux and Searches for New Physics with AMANDA-II". In: *Phys. Rev. D* 79 (2009), p. 102005. DOI: `10.1103/PhysRevD.79.102005`. arXiv: `0902.0675 [astro-ph.HE]`.

[23] R. Abbasi et al. "Measurement of the atmospheric neutrino energy spectrum from 100 GeV to 400 TeV with IceCube". In: *Phys. Rev. D* 83 (2011), p. 012001. DOI: `10.1103/PhysRevD.83.012001`. arXiv: `1010.3980 [astro-ph.HE]`.

[24] R. Abbasi et al. "Search for GeV-scale dark matter annihilation in the Sun with IceCube DeepCore". In: *Phys. Rev. D* 105.6 (2022), p. 062004. DOI: `10.1103/PhysRevD.105.062004`. arXiv: `2111.09970 [astro-ph.HE]`.

[25] R. Abbasi et al. "The energy spectrum of atmospheric neutrinos between 2 and 200 TeV with the AMANDA-II detector". In: *Astroparticle Physics* 34.1 (2010), pp. 48–58. DOI: `10.1016/j.astropartphys.2010.05.001`.

[26] B. P. Abbott et al. "Multi-messenger Observations of a Binary Neutron Star Merger". In: *Astrophys. J. Lett.* 848.2 (2017), p. L12. DOI: `10.3847/2041-8213/aa91c9`. arXiv: `1710.05833 [astro-ph.HE]`.

[27] Hassan Abdalla et al. “Combined dark matter searches towards dwarf spheroidal galaxies with Fermi-LAT, HAWC, H.E.S.S., MAGIC, and VERITAS”. In: *PoS* ICRC2021 (2021), p. 528. DOI: `10.22323/1.395.0528`. arXiv: `2108.13646 [hep-ex]`.

[28] H. Abdallah et al. “Search for dark matter annihilations towards the inner Galactic halo from 10 years of observations with H.E.S.S”. In: *Phys. Rev. Lett.* 117.11 (2016), p. 111301. DOI: `10.1103/PhysRevLett.117.111301`. arXiv: `1607.08142 [astro-ph.HE]`.

[29] S. Adrian-Martinez et al. “Letter of intent for KM3NeT 2.0”. In: *J. Phys. G* 43.8 (2016), p. 084001. DOI: `10.1088/0954-3899/43/8/084001`. arXiv: `1601.07459 [astro-ph.IM]`.

[30] S. Adrian-Martinez et al. “Limits on Dark Matter Annihilation in the Sun using the ANTARES Neutrino Telescope”. In: *Phys. Lett. B* 759 (2016), pp. 69–74. DOI: `10.1016/j.physletb.2016.05.019`. arXiv: `1603.02228 [astro-ph.HE]`.

[31] S. Adrian-Martinez et al. “Measurement of the atmospheric ν_μ energy spectrum from 100 GeV to 200 TeV with the ANTARES telescope”. In: *Eur. Phys. J. C* 73.10 (2013), p. 2606. DOI: `10.1140/epjc/s10052-013-2606-4`. arXiv: `1308.1599 [astro-ph.HE]`.

[32] S. Adrian-Martinez et al. “The Positioning System of the ANTARES Neutrino Telescope”. In: *JINST* 7 (2012), T08002. DOI: `10.1088/1748-0221/7/08/T08002`. arXiv: `1202.3894 [astro-ph.IM]`.

[33] S. Adrián-Martınez et al. “The prototype detection unit of the KM3NeT detector”. In: *Eur. Phys. J. C* 76.2 (2016), p. 54. DOI: `10.1140/epjc/s10052-015-3868-9`. arXiv: `1510.01561 [astro-ph.IM]`.

[34] S. Adrián-Martınez et al. “Time calibration with atmospheric muon tracks in the ANTARES neutrino telescope”. In: *Astropart. Phys.* 78 (2016), pp. 43–51. DOI: `10.1016/j.astropartphys.2016.02.001`. arXiv: `1507.04182 [physics.ins-det]`.

[35] M. Ageron et al. “ANTARES: the first undersea neutrino telescope”. In: *Nucl. Instrum. Meth. A* 656 (2011), pp. 11–38. DOI: `10.1016/j.nima.2011.06.103`. arXiv: `1104.1607 [astro-ph.IM]`.

[36] Michel Ageron et al. “Indirect dark matter searches with neutrinos from the Galactic Centre region with the ANTARES and KM3NeT telescopes”. In: *PoS* ICRC2021 (2021), p. 537. DOI: `10.22323/1.395.0537`.

[37] N. Aghanim et al. “Planck 2018 results. I. Overview and the cosmological legacy of Planck”. In: *Astron. Astrophys.* 641 (2020), A1. DOI: `10.1051/0004-6361/201833880`. arXiv: `1807.06205 [astro-ph.CO]`.

[38] N. Aghanim et al. “Planck 2018 results. VI. Cosmological parameters”. In: *Astron. Astrophys.* 641 (2020). [Erratum: Astron.Astrophys. 652, C4 (2021)], A6. DOI: `10.1051/0004-6361/201833910`. arXiv: `1807.06209 [astro-ph.CO]`.

[39] P. Agnes et al. “DarkSide-50 532-day Dark Matter Search with Low-Radioactivity Argon”. In: *Phys. Rev. D* 98.10 (2018), p. 102006. DOI: `10.1103/PhysRevD.98.102006`. arXiv: `1802.07198 [astro-ph.CO]`.

[40] J. A. Aguilar et al. “A fast algorithm for muon track reconstruction and its application to the ANTARES neutrino telescope”. In: *Astropart. Phys.* 34 (2011), pp. 652–662. DOI: `10.1016/j.astropartphys.2011.01.003`. arXiv: `1105.4116 [astro-ph.IM]`.

[41] J. A. Aguilar et al. “Performance of the front-end electronics of the ANTARES neutrino telescope”. In: *Nucl. Instrum. Meth. A* 622 (2010), pp. 59–73. DOI: `10.1016/j.nima.2010.06.225`. arXiv: `1007.2549 [astro-ph.IM]`.

[42] J. A. Aguilar et al. “Study of large hemispherical photomultiplier tubes for the antares neutrino telescope”. In: *Nucl. Instrum. Meth. A* 555 (2005), pp. 132–141. DOI: `10.1016/j.nima.2005.09.035`. arXiv: `physics/0510031`.

[43] J. A. Aguilar et al. “The data acquisition system for the ANTARES Neutrino Telescope”. In: *Nucl. Instrum. Meth. A* 570 (2007), pp. 107–116. DOI: `10.1016/j.nima.2006.09.098`. arXiv: `astro-ph/0610029`.

[44] J. A. Aguilar et al. “Time Calibration of the ANTARES Neutrino Telescope”. In: *Astropart. Phys.* 34 (2011), pp. 539–549. DOI: `10.1016/j.astropartphys.2010.12.004`. arXiv: `1012.2204 [astro-ph.IM]`.

[45] J. A. Aguilar et al. “Transmission of light in deep sea water at the site of the ANTARES Neutrino Telescope”. In: *Astropart. Phys.* 23 (2005), pp. 131–155. DOI: `10.1016/j.astropartphys.2004.11.006`. arXiv: `astro-ph/0412126`.

[46] J. A. Aguilar et al. “Transmission of light in deep sea water at the site of the ANTARES Neutrino Telescope”. In: *Astropart. Phys.* 23 (2005), pp. 131–155. DOI: `10.1016/j.astropartphys.2004.11.006`. arXiv: `astro-ph/0412126`.

[47] M. L. Ahnen et al. “Limits to Dark Matter Annihilation Cross-Section from a Combined Analysis of MAGIC and Fermi-LAT Observations of Dwarf Satellite Galaxies”. In: *JCAP* 02 (2016), p. 039. DOI: `10.1088/1475-7516/2016/02/039`. arXiv: `1601.06590 [astro-ph.HE]`.

[48] M. L. Ahnen et al. “Limits to Dark Matter Annihilation Cross-Section from a Combined Analysis of MAGIC and Fermi-LAT Observations of Dwarf Satellite Galaxies”. In: *JCAP* 02 (2016), p. 039. DOI: `10.1088/1475-7516/2016/02/039`. arXiv: `1601.06590 [astro-ph.HE]`.

[49] S. Aiello et al. “Characterisation of the Hamamatsu photomultipliers for the KM3NeT Neutrino Telescope”. In: *JINST* 13.05 (2018), P05035. DOI: `10.1088/1748-0221/13/05/P05035`.

[50] S. Aiello et al. “Deep-sea deployment of the KM3NeT neutrino telescope detection units by self-unrolling”. In: *JINST* 15.11 (2020), P11027. DOI: `10.1088/1748-0221/15/11/P11027`. arXiv: `2007.16090 [astro-ph.IM]`.

[51] S. Aiello et al. “The KM3NeT multi-PMT optical module”. In: (Mar. 2022). arXiv: `2203.10048 [astro-ph.IM]`.

[52] S. Aiello et al. “The KM3NeT multi-PMT optical module”. In: (Mar. 2022). arXiv: `2203.10048 [astro-ph.IM]`.

[53] Sebastiano Aiello et al. “Architecture and performance of the KM3NeT front-end firmware”. In: *J. Astron. Telesc. Instrum. Syst.* 7.1 (2021), p. 016001. DOI: `10.1117/1.JATIS.7.1.016001`.

[54] M. Ajello et al. “Fermi Large Area Telescope Performance after 10 Years of Operation”. In: *Astrophys. J. Supp.* 256.1 (2021), p. 12. DOI: `10.3847/1538-4365/ac0ceb`. arXiv: `2106.12203 [astro-ph.IM]`.

[55] A. Albert et al. “ANTARES Search for Point Sources of Neutrinos Using Astrophysical Catalogs: A Likelihood Analysis”. In: *Astrophys. J.* 911.1 (2021), p. 48. DOI: `10.3847/1538-4357/abe53c`. arXiv: `2012.15082 [astro-ph.HE]`.

[56] A. Albert et al. “Long-term monitoring of the ANTARES optical module efficiencies using^{40}K decays in sea water”. In: *Eur. Phys. J. C* 78.8 (2018), p. 669. DOI: `10.1140/epjc/s10052-018-6132-2`. arXiv: `1805.08675 [astro-ph.IM]`.

[57] A. Albert et al. “Monte Carlo simulations for the ANTARES underwater neutrino telescope”. In: *JCAP* 01 (2021), p. 064. DOI: `10.1088/1475-7516/2021/01/064`. arXiv: `2010.06621 [astro-ph.HE]`.

[58] A. Albert et al. “Search for Dark Matter Annihilation in the Earth using the ANTARES Neutrino Telescope”. In: *Phys. Dark Univ.* 16 (2017), pp. 41–48. DOI: `10.1016/j.dark.2017.04.005`. arXiv: `1612.06792 [hep-ex]`.

[59] C. Alcock et al. “The MACHO project: Microlensing results from 5.7 years of LMC observations”. In: *Astrophys. J.* 542 (2000), pp. 281–307. DOI: `10.1086/309512`. arXiv: `astro-ph/0001272`.

[60] R. A. Alpher, H. Bethe, and G. Gamow. “The origin of chemical elements”. In: *Phys. Rev.* 73 (1948), pp. 803–804. DOI: `10.1103/PhysRev.73.803`.

[61] Rafael Alves Batista et al. “Open Questions in Cosmic-Ray Research at Ultrahigh Energies”. In: *Front. Astron. Space Sci.* 6 (2019), p. 23. DOI: 10.3389/fspas.2019.00023. arXiv: 1903.06714 [astro-ph.HE].

[62] Elena Amato and Barbara Olmi. “The Crab Pulsar and Nebula as Seen in Gamma-Rays”. In: *Universe* 7.11 (2021), p. 448. DOI: 10.3390/universe7110448. arXiv: 2111.07712 [astro-ph.HE].

[63] M. Ambrosio et al. “Measurements of atmospheric muon neutrino oscillations, global analysis of the data collected with MACRO detector”. In: *Eur. Phys. J. C* 36 (2004), pp. 323–339. DOI: 10.1140/epjc/s2004-01951-9.

[64] C. Amole et al. “Dark Matter Search Results from the Complete Exposure of the PICO-60 C_3F_8 Bubble Chamber”. In: *Phys. Rev. D* 100.2 (2019), p. 022001. DOI: 10.1103/PhysRevD.100.022001. arXiv: 1902.04031 [astro-ph.CO].

[65] P Amram et al. “Background light in potential sites for the ANTARES undersea neutrino telescope”. In: *Astropart. Phys.* 13 (2000), pp. 127–136. DOI: 10.1016/S0927-6505(99)00118-8. arXiv: astro-ph/9910170.

[66] P. Amram et al. “Sedimentation and fouling of optical surfaces at the antares site”. In: *Astropart. Phys.* 19 (2003), pp. 253–267. DOI: 10.1016/S0927-6505(02)00202-5. arXiv: astro-ph/0206454.

[67] P. Amram et al. “Sedimentation and fouling of optical surfaces at the antares site”. In: *Astropart. Phys.* 19 (2003), pp. 253–267. DOI: 10.1016/S0927-6505(02)00202-5. arXiv: astro-ph/0206454.

[68] P. Amram et al. “The ANTARES optical module”. In: *Nucl. Instrum. Meth. A* 484 (2002), pp. 369–383. DOI: 10.1016/S0168-9002(01)02026-5. arXiv: astro-ph/0112172.

[69] Raul E. Angulo and Oliver Hahn. “Large-scale dark matter simulations”. In: (Dec. 2021). DOI: 10.1007/s41115-021-00013-z. arXiv: 2112.05165 [astro-ph.CO].

[70] Dr J Floor Anthoni. URL: http://www.seafriends.org.nz/oceano/seawater.htm.

[71] P. Antonioli et al. “A Three-dimensional code for muon propagation through the rock: Music”. In: *Astropart. Phys.* 7 (1997), pp. 357–368. DOI: 10.1016/S0927-6505(97)00035-2. arXiv: hep-ph/9705408.

[72] E. Aprile et al. “Dark Matter Search Results from a One Ton-Year Exposure of XENON1T”. In: *Phys. Rev. Lett.* 121.11 (2018), p. 111302. DOI: 10.1103/PhysRevLett.121.111302. arXiv: 1805.12562 [astro-ph.CO].

[73] E. Aprile et al. "Excess electronic recoil events in XENON1T". In: *Phys. Rev. D* 102.7 (2020), p. 072004. DOI: 10.1103/PhysRevD.102.072004. arXiv: 2006.09721 [hep-ex].

[74] S. Archambault et al. "Dark Matter Constraints from a Joint Analysis of Dwarf Spheroidal Galaxy Observations with VERITAS". In: *Phys. Rev. D* 95.8 (2017), p. 082001. DOI: 10.1103/PhysRevD.95.082001. arXiv: 1703.04937 [astro-ph.HE].

[75] S. Archambault et al. "Dark Matter Constraints from a Joint Analysis of Dwarf Spheroidal Galaxy Observations with VERITAS". In: *Phys. Rev. D* 95.8 (2017), p. 082001. DOI: 10.1103/PhysRevD.95.082001. arXiv: 1703.04937 [astro-ph.HE].

[76] A. Avrorin et al. "The gigaton volume detector in Lake Baikal". In: *Nucl. Instrum. Meth. A* 639 (2011). Ed. by R. Forty et al., pp. 30–32. DOI: 10.1016/j.nima.2010.09.137.

[77] Howard Baer et al. "Dark matter production in the early Universe: beyond the thermal WIMP paradigm". In: *Phys. Rept.* 555 (2015), pp. 1–60. DOI: 10.1016/j.physrep.2014.10.002. arXiv: 1407.0017 [hep-ph].

[78] Josep Baeza Guzmán. "Calibración de sensores aceleromagnéticos del telescopio submarino KM3NeT". Universitat Politècnica de València, 2021. URL: http://hdl.handle.net/10251/173200.

[79] John N. Bahcall. "Solar models: An Historical overview". In: *AAPPS Bull.* 12.4 (2002). Ed. by F. von Feilitzsch and N. Schmitz, pp. 12–19. DOI: 10.1016/S0920-5632(03)01306-9. arXiv: astro-ph/0209080.

[80] John N. Bahcall and Raymond Davis. "Solar Neutrinos: A Scientific Puzzle". In: *Science* 191.4224 (1976), pp. 264–267. ISSN: 0036-8075. DOI: 10.1126/science.191.4224.264. eprint: https://science.sciencemag.org/content/191/4224/264.full.pdf. URL: https://science.sciencemag.org/content/191/4224/264.

[81] A. B. Balantekin and W. C. Haxton. "Neutrino Oscillations". In: *Prog. Part. Nucl. Phys.* 71 (2013), pp. 150–161. DOI: 10.1016/j.ppnp.2013.03.007. arXiv: 1303.2272 [nucl-th].

[82] C. M. Becchi and G. Ridolfi. *An introduction to relativistic processes and the standard model of electroweak interactions.* Springer, 2014. ISBN: 978-3-319-06130-6.

[83] W. Bednarek. "Neutrinos from the pulsar wind nebulae". In: *Astron. Astrophys.* 407 (2003), pp. 1–6. DOI: 10.1051/0004-6361:20030929. arXiv: astro-ph/0305430.

[84] K. G. Begeman, A. H. Broeils, and R. H. Sanders. "Extended rotation curves of spiral galaxies: Dark haloes and modified dynamics". In: *Mon. Not. Roy. Astron. Soc.* 249 (1991), p. 523. DOI: 10.1093/mnras/249.3.523.

[85] A. R. Bell. "Cosmic ray acceleration in pulsar-driven supernova remnants." In: 257 (1992), pp. 493–500. DOI: 10.1093/mnras/257.3.493.

[86] Igor Belolaptikov et al. "Neutrino Telescope in Lake Baikal: Present and Nearest Future". In: *PoS* ICRC2021 (2021), p. 002. DOI: 10.22323/1.395.0002. arXiv: 2109.14344 [astro-ph.HE].

[87] Maria Benito, Fabio Iocco, and Alessandro Cuoco. "Uncertainties in the Galactic Dark Matter distribution: An update". In: *Phys. Dark Univ.* 32 (2021), p. 100826. DOI: 10.1016/j.dark.2021.100826. arXiv: 2009.13523 [astro-ph.GA].

[88] V. Berezinsky et al. "Searching for relic neutralinos using neutrino telescopes". In: *Astropart. Phys.* 5 (1996), pp. 333–352. DOI: 10.1016/0927-6505(96)00035-7. arXiv: hep-ph/9603342.

[89] Lars Bergstrom, Joakim Edsjo, and Paolo Gondolo. "Indirect detection of dark matter in km size neutrino telescopes". In: *Phys. Rev. D* 58 (1998), p. 103519. DOI: 10.1103/PhysRevD.58.103519. arXiv: hep-ph/9806293.

[90] Gianfranco Bertone, Dan Hooper, and Joseph Silk. "Particle dark matter: Evidence, candidates and constraints". In: *Phys. Rept.* 405 (2005), pp. 279–390. DOI: 10.1016/j.physrep.2004.08.031. arXiv: hep-ph/0404175.

[91] Daniel Biehl et al. "Cosmic-Ray and Neutrino Emission from Gamma-Ray Bursts with a Nuclear Cascade". In: *Astron. Astrophys.* 611 (2018), A101. DOI: 10.1051/0004-6361/201731337. arXiv: 1705.08909 [astro-ph.HE].

[92] Samoil M. Bilenky. "Neutrinos". In: (Mar. 2001). arXiv: physics/0103091.

[93] Julien Billard et al. "Direct Detection of Dark Matter – APPEC Committee Report". In: (Apr. 2021). arXiv: 2104.07634 [hep-ex].

[94] Mattias Blennow, Joakim Edsjo, and Tommy Ohlsson. "Neutrinos from WIMP annihilations in the Sun including neutrino oscillations". In: *Nucl. Phys. B Proc. Suppl.* 221 (2011). Ed. by Geoffrey Mills et al., pp. 37–38. DOI: 10.1016/j.nuclphysbps.2011.03.089.

[95] Mattias Blennow, Joakim Edsjo, and Tommy Ohlsson. "Neutrinos from WIMP annihilations using a full three-flavor Monte Carlo". In: *JCAP* 01 (2008), p. 021. DOI: 10.1088/1475-7516/2008/01/021. arXiv: 0709.3898 [hep-ph].

[96] H. Blood et al. “DUMAND: The Ocean as a Neutrino Detector”. In: *International Neutrino Conference 1976*. June 1976, pp. 688–702. DOI: 10.1007/978-3-322-90614-4_68.

[97] Hans Böhringer and Gayoung Chon. “Constraints on neutrino masses from the study of the nearby large-scale structure and galaxy cluster counts”. In: *Mod. Phys. Lett. A* 31.21 (2016), p. 1640008. DOI: 10.1142/S0217732316400083. arXiv: 1610.02855 [astro-ph.CO].

[98] Antonio Boveia et al. “Summarizing experimental sensitivities of collider experiments to dark matter models and comparison to other experiments”. In: *2022 Snowmass Summer Study*. June 2022. arXiv: 2206.03456 [hep-ph].

[99] Ronald Bruijn. “KM3NeT Readout and Triggering”. In: *EPJ Web Conf.* 207 (2019). Ed. by C. Spiering, p. 06007. DOI: 10.1051/epjconf/201920706007.

[100] Jatan Buch et al. “PPPC 4 DM secondary: A Poor Particle Physicist Cookbook for secondary radiation from Dark Matter”. In: *JCAP* 09 (2015), p. 037. DOI: 10.1088/1475-7516/2015/9/037. arXiv: 1505.01049 [hep-ph].

[101] E. V. Bugaev et al. “Atmospheric muon flux at sea level, underground and underwater”. In: *Phys. Rev. D* 58 (1998), p. 054001. DOI: 10.1103/PhysRevD.58.054001. arXiv: hep-ph/9803488.

[102] A. Burkert. “The Structure of dark matter halos in dwarf galaxies”. In: *Astrophys. J. Lett.* 447 (1995), p. L25. DOI: 10.1086/309560. arXiv: astro-ph/9504041.

[103] G. Carminati, A. Margiotta, and M. Spurio. “Atmospheric MUons from PArametric formulas: A Fast GEnerator for neutrino telescopes (MUPAGE)”. In: *Comput. Phys. Commun.* 179 (2008), pp. 915–923. DOI: 10.1016/j.cpc.2008.07.014. arXiv: 0802.0562 [physics.ins-det].

[104] Bernard J. Carr. “Primordial black holes as a probe of cosmology and high energy physics”. In: *Lect. Notes Phys.* 631 (2003). Ed. by Domenico J. W. Giulini, Claus Kiefer, and Claus Lammerzahl, pp. 301–321. DOI: 10.1007/978-3-540-45230-0_7. arXiv: astro-ph/0310838.

[105] T. Chiarusi and M. Spurio. “High-Energy Astrophysics with Neutrino Telescopes”. In: *Eur. Phys. J. C* 65 (2010), pp. 649–701. DOI: 10.1140/epjc/s10052-009-1230-9. arXiv: 0906.2634 [astro-ph.HE].

[106] K. Choi et al. “Search for neutrinos from annihilation of captured low-mass dark matter particles in the Sun by Super-Kamiokande”. In: *Phys. Rev. Lett.* 114.14 (2015), p. 141301. DOI: 10.1103/PhysRevLett.114.141301. arXiv: 1503.04858 [hep-ex].

[107] Douglas Clowe, Anthony Gonzalez, and Maxim Markevitch. "Weak lensing mass reconstruction of the interacting cluster 1E0657-558: Direct evidence for the existence of dark matter". In: *Astrophys. J.* 604 (2004), pp. 596–603. DOI: `10.1086/381970`. arXiv: `astro-ph/0312273`.

[108] C Compère et al. "Kinetics of conditioning layer formation on stainless steel immersed in seawater". In: *Biofouling* 17.2 (2001), pp. 129–145. DOI: `10.1080/08927010109378472`. URL: `https://doi.org/10.1080/08927010109378472`.

[109] R. Coniglione et al. "KM3NeT Time Calibration". In: *PoS* ICRC2019 (2021), p. 868. DOI: `10.22323/1.358.0868`.

[110] Jan Conrad et al. "Fermi Gamma-ray Space Telescope sees first light". In: *CERN Cour.* 48N9 (2008), pp. 13–15.

[111] Craig J. Copi, David N. Schramm, and Michael S. Turner. "Big bang nucleosynthesis and the baryon density of the universe". In: *Science* 267 (1995), pp. 192–199. DOI: `10.1126/science.7809624`. arXiv: `astro-ph/9407006`.

[112] Alessandro Cuoco. "Signatures of Dark Matter in Cosmic-Ray Observations". In: *J. Phys. Conf. Ser.* 1468.1 (2020). Ed. by Masayuki Nakahata, p. 012095. DOI: `10.1088/1742-6596/1468/1/012095`. arXiv: `1911.06082 [astro-ph.HE]`.

[113] Dıdac D. Tortosaon. "Monitoring and Reconstruction of the Shape of the Detection Units in KM3NeT Using Acoustic and Compass Sensors". In: *Sensors* 20.18 (2020), p. 5116. DOI: `10.3390/s20185116`.

[114] *Dark Matter and Dark Energy: A Challenge for Modern Cosmology*. Vol. 370. Astrophysics and Space Science Library. Jan. 2011. DOI: `10.1007/978-90-481-8685-3`.

[115] Alessandro De Angelis and Mario Pimenta. *Introduction to Particle and Astroparticle Physics: Multimessenger Astronomy and its Particle Physics Foundations*. Undergraduate Lecture Notes in Physics. Heidelberg: Springer Nature, 2018. ISBN: 978-3-319-78180-8.

[116] A Dekel and J. Silk. "The origin of dwarf galaxies, cold dark matter, and biased galaxy formation". In: *Astrophys. J.* 303 (1986), pp. 39–55. DOI: `10.1086/164050`.

[117] Scott Dodelson and Lawrence M. Widrow. "Sterile-neutrinos as dark matter". In: *Phys. Rev. Lett.* 72 (1994), pp. 17–20. DOI: `10.1103/PhysRevLett.72.17`. arXiv: `hep-ph/9303287`.

[118] Leanne D. Duffy and Karl van Bibber. "Axions as Dark Matter Particles". In: *New J. Phys.* 11 (2009), p. 105008. DOI: `10.1088/1367-2630/11/10/105008`. arXiv: `0904.3346 [hep-ph]`.

[119] K. Eguchi et al. "First results from KamLAND: Evidence for reactor anti-neutrino disappearance". In: *Phys. Rev. Lett.* 90 (2003), p. 021802. DOI: `10.1103/PhysRevLett.90.021802`. arXiv: `hep-ex/0212021`.

[120] J. Einasto. "On the Construction of a Composite Model for the Galaxy and on the Determination of the System of Galactic Parameters". In: *Trudy Astrofizicheskogo Instituta Alma-Ata* 5 (Jan. 1965), pp. 87–100.

[121] John R. Ellis, R. A. Flores, and J. D. Lewin. "Rates for Inelastic Nuclear Excitation by Dark Matter Particles". In: *Phys. Lett. B* 212 (1988), pp. 375–380. DOI: `10.1016/0370-2693(88)91332-9`.

[122] John R. Ellis et al. "Dark matter in the light of LEP". In: *Phys. Lett. B* 245 (1990), pp. 251–257. DOI: `10.1016/0370-2693(90)90143-T`.

[123] Carmelo Evoli. *The Cosmic-Ray Energy Spectrum.* Dec. 2020. DOI: `10.5281/zenodo.4396125`. URL: `https://doi.org/10.5281/zenodo.4396125`.

[124] Lord Rayleigh F.R.S. "XXXIV. On the transmission of light through an atmosphere containing small particles in suspension, and on the origin of the blue of the sky". In: *The London, Edinburgh, and Dublin Philosophical Magazine and Journal of Science* 47.287 (1899), pp. 375–384. DOI: `10.1080/14786449908621276`. URL: `https://doi.org/10.1080/14786449908621276`.

[125] F. Feinstein. "The analogue ring sampler: A front-end chip for ANTARES". In: *Nucl. Instrum. Meth. A* 504 (2003). Ed. by P. Bourgeois et al., pp. 258–261. DOI: `10.1016/S0168-9002(03)00773-3`.

[126] Gary J. Feldman and Robert D. Cousins. "A Unified approach to the classical statistical analysis of small signals". In: *Phys. Rev. D* 57 (1998), pp. 3873–3889. DOI: `10.1103/PhysRevD.57.3873`. arXiv: `physics/9711021`.

[127] Jonathan L. Feng. "Dark Matter Candidates from Particle Physics and Methods of Detection". In: *Ann. Rev. Astron. Astrophys.* 48 (2010), pp. 495–545. DOI: `10.1146/annurev-astro-082708-101659`. arXiv: `1003.0904 [astro-ph.CO]`.

[128] E. Fermi. "Versuch einer Theorie der β-Strahlen.I / Towards the Theory of β-Rays". In: *Z. Phys.* 88 (1934), p. 161.

[129] Enrico Fermi. "On the Origin of the Cosmic Radiation". In: *Phys. Rev.* 75 (1949), pp. 1169–1174. DOI: `10.1103/PhysRev.75.1169`.

[130] Brian D. Fields, Katherine Freese, and David S. Graff. "Massive compact halo objects viewed from a cosmological perspective: Contribution to the baryonic mass density of the universe". In: *New Astron.* 3 (1998), pp. 347–361. DOI: `10.1016/S1384-1076(98)00015-3`. arXiv: `astro-ph/9804232`.

[131] Brent Follin et al. “First Detection of the Acoustic Oscillation Phase Shift Expected from the Cosmic Neutrino Background”. In: *Phys. Rev. Lett.* 115.9 (2015), p. 091301. DOI: `10.1103/PhysRevLett.115.091301`. arXiv: `1503.07863 [astro-ph.CO]`.

[132] J. A. Formaggio and G. P. Zeller. “From eV to EeV: Neutrino Cross Sections Across Energy Scales”. In: *Rev. Mod. Phys.* 84 (2012), pp. 1307–1341. DOI: `10.1103/RevModPhys.84.1307`. arXiv: `1305.7513 [hep-ex]`.

[133] Patrick J. Fox et al. “LEP Shines Light on Dark Matter”. In: *Phys. Rev. D* 84 (2011), p. 014028. DOI: `10.1103/PhysRevD.84.014028`. arXiv: `1103.0240 [hep-ph]`.

[134] Y. Fukuda et al. “Evidence for oscillation of atmospheric neutrinos”. In: *Phys. Rev. Lett.* 81 (1998), pp. 1562–1567. DOI: `10.1103/PhysRevLett.81.1562`. arXiv: `hep-ex/9807003`.

[135] M. Fukugita and T. Yanagida. *Physics of neutrinos and applications to astrophysics*. Theoretical and Mathematical Physics. Berlin, Germany: Springer-Verlag, 2003. ISBN: 978-3-662-05119-1. DOI: `10.1007/978-3-662-05119-1`.

[136] Luigi Antonio Fusco. “Search for a diffuse flux of cosmic neutrinos with the ANTARES neutrino telescope”. In: *PoS* ICRC2021 (2021), p. 1126. DOI: `10.22323/1.395.1126`.

[137] T. K. Gaisser and M. Honda. “Flux of atmospheric neutrinos”. In: *Ann. Rev. Nucl. Part. Sci.* 52 (2002), pp. 153–199. DOI: `10.1146/annurev.nucl.52.050102.090645`. arXiv: `hep-ph/0203272`.

[138] Thomas K. Gaisser, Ralph Engel, and Elisa Resconi. *Cosmic Rays and Particle Physics: 2nd Edition*. Cambridge University Press, June 2016. ISBN: 978-0-521-01646-9.

[139] Graciela Gelmini and Paolo Gondolo. “DM Production Mechanisms”. In: (Sept. 2010), pp. 121–141. arXiv: `1009.3690 [astro-ph.CO]`.

[140] T. Geralis. “CAST results and Axion review”. In: *44th Rencontres de Moriond on Electroweak Interactions and Unified Theories*. 2009, pp. 391–398. arXiv: `0905.4273 [hep-ex]`.

[141] Carlo Giunti and Chung W. Kim. *Fundamentals of Neutrino Physics and Astrophysics*. 2007. ISBN: 978-0-19-850871-7.

[142] Carlo Giunti and T. Lasserre. “eV-scale Sterile Neutrinos”. In: *Ann. Rev. Nucl. Part. Sci.* 69 (2019), pp. 163–190. DOI: `10.1146/annurev-nucl-101918-023755`. arXiv: `1901.08330 [hep-ph]`.

[143] Andrew Gould. “Direct and Indirect Capture of Wimps by the Earth”. In: *Astrophys. J.* 328 (1988), pp. 919–939. DOI: `10.1086/166347`.

[144] Andrew Gould. “Resonant Enhancements in WIMP Capture by the Earth”. In: *Astrophys. J.* 321 (1987), p. 571. DOI: `10.1086/165653`.

[145] N. Grevesse and A. J. Sauval. “Standard Solar Composition”. In: *Space Sci. Rev.* 85 (1998), pp. 161–174. DOI: 10.1023/A:1005161325181.

[146] K. Griest and D. Seckel. “Cosmic Asymmetry, Neutrinos and the Sun”. In: *Nucl. Phys. B* 283 (1987). [Erratum: Nucl.Phys.B 296, 1034–1036 (1988)], pp. 681–705. DOI: 10.1016/0550-3213(87)90293-8.

[147] David Griffiths. *Introduction to elementary particles.* 2008. ISBN: 978-3-527-40601-2.

[148] Francis Halzen. “High-energy neutrino astrophysics”. In: *Nature Phys.* 13.3 (2016), pp. 232–238. DOI: 10.1038/nphys3816.

[149] D. Heck et al. “CORSIKA: A Monte Carlo code to simulate extensive air showers”. In: (Feb. 1998).

[150] Adriaan Jacob Heijboer. *Track Reconstruction and Point Source Searches with ANTARES. PhD Thesis.* Universiteit van Amsterdam, 2004.

[151] C. de los Heros. “Getting there: From AMANDA to IceCube”. In: *PoS* HEP2005 (2006). Ed. by Gaspar Barreira, p. 023. DOI: 10.22323/1.021.0023.

[152] Victor F. Hess. “Über Beobachtungen der durchdringenden Strahlung bei sieben Freiballonfahrten”. In: *Phys. Z.* 13 (1912), pp. 1084–1091.

[153] Gary C. Hill and Katherine Rawlins. “Unbiased cut selection for optimal upper limits in neutrino detectors: The Model rejection potential technique”. In: *Astropart. Phys.* 19 (2003), pp. 393–402. DOI: 10.1016/S0927-6505(02)00240-2. arXiv: astro-ph/0209350.

[154] W. Hofmann. “The High Energy Stereoscopic System (HESS) project”. In: *AIP Conf. Proc.* 515.1 (2000). Ed. by B. L. Dingus, M. H. Salamon, and D. B. Kieda, p. 500. DOI: 10.1063/1.1291416.

[155] Morihiro Honda et al. “Calculation of atmospheric neutrino flux using the interaction model calibrated with atmospheric muon data”. In: *Phys. Rev. D* 75 (2007), p. 043006. DOI: 10.1103/PhysRevD.75.043006. arXiv: astro-ph/0611418.

[156] G. Ingelman, A. Edin, and J. Rathsman. “LEPTO 6.5: A Monte Carlo generator for deep inelastic lepton - nucleon scattering”. In: *Comput. Phys. Commun.* 101 (1997), pp. 108–134. DOI: 10.1016/S0010-4655(96)00157-9. arXiv: hep-ph/9605286.

[157] J. Elevant J. Edsjö and C. Niblaeus. *WimpSim Neutrino Monte Carlo.* URL: http://wimpsim.astroparticle.se/.

[158] J.D. Jackson. *Classical Electrodinamics (3rd ed.)* John Wiley, 1998. ISBN: 978-0-471-30932-1.

[159] Ronnie Jansson and Glennys R. Farrar. “THE GALACTIC MAGNETIC FIELD”. In: *The Astrophysical Journal* 761.1 (Nov. 2012), p. L11. DOI: `10.1088/2041-8205/761/1/l11`. URL: `https://doi.org/10.1088/2041-8205/761/1/l11`.

[160] Gerard Jungman and Marc Kamionkowski. “Neutrinos from particle decay in the sun and earth”. In: *Phys. Rev. D* 51 (1995), pp. 328–340. DOI: `10.1103/PhysRevD.51.328`. arXiv: `hep-ph/9407351`.

[161] Gerard Jungman, Marc Kamionkowski, and Kim Griest. “Supersymmetric dark matter”. In: *Phys. Rept.* 267 (1996), pp. 195–373. DOI: `10.1016/0370-1573(95)00058-5`. arXiv: `hep-ph/9506380`.

[162] N. N. Kalmykov, S. S. Ostapchenko, and A. I. Pavlov. “Quark-Gluon String Model and EAS Simulation Problems at Ultra-High Energies”. In: *Nucl. Phys. B Proc. Suppl.* 52 (1997). Ed. by H. Rebel, G. Schatz, and J. Knapp, pp. 17–28. DOI: `10.1016/S0920-5632(96)00846-8`.

[163] Edward W. Kolb and Michael S. Turner. *The Early Universe*. Vol. 69. 1990. ISBN: 978-0-201-62674-2. DOI: `10.1201/9780429492860`.

[164] Robert Lahmann. “Neutrino Detection, Position Calibration and Marine Science with Acoustic Arrays in the Deep Sea”. In: *Nucl. Instrum. Meth. A* 725 (2013). Ed. by G. Anton et al., pp. 32–37. DOI: `10.1016/j.nima.2012.12.107`. arXiv: `1304.0697 [astro-ph.IM]`.

[165] Paolo Lipari. “The lifetime of cosmic rays in the Milky Way”. In: (July 2014). arXiv: `1407.5223 [astro-ph.HE]`.

[166] Daniel Lopez-Coto, Sergio Navas, and J. D. Zornoza. “Dark Matter Searches from the Sun with the KM3NeT-ORCA detector”. In: *PoS* ICRC2019 (2020), p. 536. DOI: `10.22323/1.358.0536`.

[167] E. Lorenz. “The MAGIC telescope project”. In: *AIP Conf. Proc.* 515.1 (2000). Ed. by B. L. Dingus, M. H. Salamon, and D. B. Kieda, p. 510. DOI: `10.1063/1.1291417`.

[168] Ziro Maki, Masami Nakagawa, and Shoichi Sakata. “Remarks on the unified model of elementary particles”. In: *Prog. Theor. Phys.* 28 (1962), pp. 870–880. DOI: `10.1143/PTP.28.870`.

[169] William J. Marciano and Zohreh Parsa. “Neutrino electron scattering theory”. In: *J. Phys. G* 29 (2003), pp. 2629–2645. DOI: `10.1088/0954-3899/29/11/013`. arXiv: `hep-ph/0403168`.

[170] M. A. Markov and I. M. Zheleznykh. “On high energy neutrino physics in cosmic rays”. In: *Nucl. Phys.* 27 (1961), pp. 385–394. DOI: `10.1016/0029-5582(61)90331-5`.

[171] M. Masip. “High energy neutrinos from the Sun”. In: *Astropart. Phys.* 97 (2018), pp. 63–68. DOI: `10.1016/j.astropartphys.2017.11.003`. arXiv: `1706.01290 [hep-ph]`.

[172] Nick E. Mavromatos, Mairi Sakellariadou, and Muhammad Furqaan Yusaf. "Can the relativistic field theory version of modified Newtonian dynamics avoid dark matter on galactic scales?" In: *Phys. Rev. D* 79 (2009), p. 081301. DOI: `10.1103/PhysRevD.79.081301`. arXiv: `0901.3932 [astro-ph.GA]`.

[173] P. Meszaros. "The Fireball model of gamma-ray bursts". In: *Prog. Theor. Phys. Suppl.* 143 (2001). Ed. by F. Takahara, T. Nakamura, and N. Shibazaki, pp. 33–49. DOI: `10.1143/PTPS.143.33`.

[174] Gustav Mie. "Beiträge zur Optik trüber Medien, speziell kolloidaler Metallösungen". In: *Annalen der Physik* 330.3 (Jan. 1908), pp. 377–445. DOI: `10.1002/andp.19083300302`.

[175] M. Milgrom. "A Modification of the Newtonian dynamics as a possible alternative to the hidden mass hypothesis". In: *Astrophys. J.* 270 (1983), pp. 365–370. DOI: `10.1086/161130`.

[176] Alessandro Montanari, Emmanuel Moulin, and Denys Malyshev. "Search for dark matter annihilation signals from the Galactic Center with the H.E.S.S. Inner Galaxy Survey". In: *PoS* ICRC2021 (2021), p. 511. arXiv: `2108.10302 [astro-ph.HE]`.

[177] G. Morlino, P. Blasi, and E. Amato. "Gamma Rays and Neutrinos from SNR RX J1713.7-3946". In: *Astropart. Phys.* 31 (2009), pp. 376–382. DOI: `10.1016/j.astropartphys.2009.03.007`. arXiv: `0903.4565 [astro-ph.HE]`.

[178] Kohta Murase. "Active Galactic Nuclei as High-Energy Neutrino Sources". In: *Neutrino Astronomy: Current Status, Future Prospects*. Ed. by Thomas Gaisser and Albrecht Karle. 2017, pp. 15–31. DOI: `10.1142/9789814759410_0002`. arXiv: `1511.01590 [astro-ph.HE]`.

[179] Julio F. Navarro, Carlos S. Frenk, and Simon D. M. White. "The Structure of cold dark matter halos". In: *Astrophys. J.* 462 (1996), pp. 563–575. DOI: `10.1086/177173`. arXiv: `astro-ph/9508025`.

[180] P. Padovani et al. "Active galactic nuclei: what's in a name?" In: *Astron. Astrophys. Rev.* 25.1 (2017), p. 2. DOI: `10.1007/s00159-017-0102-9`. arXiv: `1707.07134 [astro-ph.GA]`.

[181] R. D. Peccei and Helen R. Quinn. "CP Conservation in the Presence of Instantons". In: *Phys. Rev. Lett.* 38 (1977), pp. 1440–1443. DOI: `10.1103/PhysRevLett.38.1440`.

[182] Arno A. Penzias and Robert Woodrow Wilson. "A Measurement of excess antenna temperature at 4080-Mc/s". In: *Astrophys. J.* 142 (1965), pp. 419–421. DOI: `10.1086/148307`.

[183] Chiara Poirè and Dìdac Diego-Tortosa. "KM3NeT Detection Unit Line Fit reconstruction using positioning sensors data". In: *PoS* ICRC2021 (2021), p. 1052. DOI: `10.22323/1.395.1052`.

[184] B. Pontecorvo. “Inverse beta processes and nonconservation of lepton charge”. In: *Zh. Eksp. Teor. Fiz.* 34 (1957), p. 247.

[185] Alan W. P. Poon et al. “Neutrino observations from the Sudbury Neutrino Observatory”. In: *AIP Conf. Proc.* 610.1 (2002). Ed. by E. Norman, L. Schroeder, and G. Wozniak, pp. 218–230. DOI: `10.1063/1.1469931`. arXiv: `nucl-ex/0110005`.

[186] Georg G. Raffelt. “Astrophysical axion bounds”. In: *Lect. Notes Phys.* 741 (2008). Ed. by Markus Kuster, Georg Raffelt, and Berta Beltran, pp. 51–71. DOI: `10.1007/978-3-540-73518-2_3`. arXiv: `hep-ph/0611350`.

[187] Lisa Randall and Raman Sundrum. “A Large mass hierarchy from a small extra dimension”. In: *Phys. Rev. Lett.* 83 (1999), pp. 3370–3373. DOI: `10.1103/PhysRevLett.83.3370`. arXiv: `hep-ph/9905221`.

[188] Elisa Resconi. “The Pacific Ocean Neutrino Experiment”. In: *37th International Cosmic Ray Conference*. Nov. 2021. arXiv: `2111.13133 [astro-ph.IM]`.

[189] G. Riccobene and A. Capone. “Deep seawater inherent optical properties in the Southern Ionian Sea”. In: *Astropart. Phys.* 27 (2007), pp. 1–9. DOI: `10.1016/j.astropartphys.2006.08.006`. arXiv: `astro-ph/0603701`.

[190] Giorgio Riccobene. *The Positioning system for KM3NeT*. Ed. by C. Spiering. 2019. DOI: `10.1051/epjconf/201920707005`.

[191] E. Richard et al. “Measurements of the atmospheric neutrino flux by Super-Kamiokande: energy spectra, geomagnetic effects, and solar modulation”. In: *Phys. Rev. D* 94.5 (2016), p. 052001. DOI: `10.1103/PhysRevD.94.052001`. arXiv: `1510.08127 [hep-ex]`.

[192] Massimo Ricotti, Jeremiah P. Ostriker, and Katherine J. Mack. “Effect of Primordial Black Holes on the Cosmic Microwave Background and Cosmological Parameter Estimates”. In: *Astrophys. J.* 680 (2008), p. 829. DOI: `10.1086/587831`. arXiv: `0709.0524 [astro-ph]`.

[193] Frank M. Rieger. “Cosmic Ray Acceleration in Active Galactic Nuclei - On Centaurus A as a possible UHECR Source”. In: *arXiv e-prints*, arXiv:0911.4004 (Nov. 2009), arXiv:0911.4004. arXiv: `0911.4004 [astro-ph.HE]`.

[194] P. F. de Salas et al. “On the estimation of the Local Dark Matter Density using the rotation curve of the Milky Way”. In: *JCAP* 10 (2019), p. 037. DOI: `10.1088/1475-7516/2019/10/037`. arXiv: `1906.06133 [astro-ph.GA]`.

[195] Dorothea Samtleben et al. “The Calibration Units of KM3NeT”. In: *PoS* ICRC2021 (2021), p. 1096. DOI: `10.22323/1.395.1096`.

[196] Geraldine Servant and Timothy M. P. Tait. "Is the lightest Kaluza-Klein particle a viable dark matter candidate?" In: *Nucl. Phys. B* 650 (2003), pp. 391–419. DOI: 10.1016/S0550-3213(02)01012-X. arXiv: hep-ph/0206071.

[197] J. Silk et al. *Particle Dark Matter: Observations, Models and Searches.* Ed. by Gianfranco Bertone. Cambridge: Cambridge Univ. Press, 2010. ISBN: 978-1-107-65392-4. DOI: 10.1017/CBO9780511770739.

[198] Sofia Sivertsson and Joakim Edsjo. "WIMP diffusion in the solar system including solar WIMP-nucleon scattering". In: *Phys. Rev. D* 85 (2012), p. 123514. DOI: 10.1103/PhysRevD.85.123514. arXiv: 1201.1895 [astro-ph.HE].

[199] Christian Spiering. "Towards high-energy neutrino astronomy". In: *The European Physical Journal H* 37.3 (2012), pp. 515–565. DOI: 10.1140/epjh/e2012-30014-2.

[200] Michel Spiro and Daniel Vignaud. "Neutrino physics and astrophysics". In: *Nucl. Phys. A* 654.1-2 (1999). Ed. by B. Frois, D. Goutte, and D. Guillemaud-Mueller, pp. C350–C372. DOI: 10.1016/S0375-9474(99)00263-8.

[201] M. Spurio. *Particles and Astrophysics - A Multi-Messenger approach.* Springer, 2015.

[202] Ignacio Taboada and Michelangelo V. D'Agostino. "Correlating prompt GRB photons with neutrinos". In: (Nov. 2007). arXiv: 0711.2277 [astro-ph].

[203] Christian Tamburini et al. "Deep-Sea Bioluminescence Blooms after Dense Water Formation at the Ocean Surface". In: *PloS one* 8 (July 2013), e67523. DOI: 10.1371/journal.pone.0067523.

[204] Marco Taoso, Gianfranco Bertone, and Antonio Masiero. "Dark Matter Candidates: A Ten-Point Test". In: *JCAP* 03 (2008), p. 022. DOI: 10.1088/1475-7516/2008/03/022. arXiv: 0711.4996 [astro-ph].

[205] Dídac D. Tortosa. "Mechanical Line Fit Model to Monitor the Position of KM3NeT Optical Modules from the Acoustic and Compass/Accelerometer Sensor System Data". In: *Proceedings* 42.1 (2020). DOI: 10.3390/ecsa-6-06583. URL: https://www.mdpi.com/2504-3900/42/1/33.

[206] S. Turck-Chièze. "The Standard Solar Model and beyond". In: *J. Phys. Conf. Ser.* 665.1 (2016), p. 012078. DOI: 10.1088/1742-6596/665/1/012078.

[207] Guido Van Rossum and Fred L. Drake. *Python 3 Reference Manual.* CreateSpace, 2009. ISBN: 1441412697.

[208] S. Viola, F. Simeone, and M. Saldaña. "Characterisation and testing of the KM3NeT acoustic positioning system". In: *EPJ Web Conf.* 116 (2016). Ed. by A. Capone et al., p. 03006. DOI: `10.1051/epjconf/201611603006`.

[209] Salvatore Viola. "KM3NeT acoustic positioning and detection system". In: *EPJ Web Conf.* 216 (2019). Ed. by G. Riccobene et al., p. 02006. DOI: `10.1051/epjconf/201921602006`.

[210] Patrick T. Wallace. *SLALIB: A Positional Astronomy Library.* Astrophysics Source Code Library, record ascl:1403.025. Mar. 2014. ascl: `1403.025`.

[211] Joachim Wambsganss. "Gravitational lensing in astronomy". In: *Living Rev. Rel.* 1 (1998), p. 12. DOI: `10.12942/lrr-1998-12`. arXiv: `astro-ph/9812021`.

[212] J. Wess and B. Zumino. "Supergauge Transformations in Four-Dimensions". In: *Nucl. Phys. B* 70 (1974). Ed. by A. Salam and E. Sezgin, pp. 39–50. DOI: `10.1016/0550-3213(74)90355-1`.

[213] G. Wikstrom and J. Edsjo. "Limits on the WIMP-nucleon scattering cross-section from neutrino telescopes". In: *JCAP* 04 (2009), p. 009. DOI: `10.1088/1475-7516/2009/04/009`. arXiv: `0903.2986 [astro-ph.CO]`.

[214] L. Wolfenstein. "Neutrino Oscillations in Matter". In: *Phys. Rev. D* 17 (1978), pp. 2369–2374. DOI: `10.1103/PhysRevD.17.2369`.

[215] Ya. B. Zel'dovich and I. D. Novikov. "The Hypothesis of Cores Retarded during Expansion and the Hot Cosmological Model". In: *Soviet Astron. AJ (Engl. Transl.),* 10 (1967), p. 602.

[216] F. Zwicky. "Die Rotverschiebung von extragalaktischen Nebeln". In: *Helv. Phys. Acta* 6 (1933), pp. 110–127. DOI: `10.1007/s10714-008-0707-4`.

[217] F. Zwicky. "On the Masses of Nebulae and of Clusters of Nebulae". In: *Astrophys. J.* 86 (1937), pp. 217–246. DOI: `10.1086/143864`.

[218] P. A. Zyla et al. "Review of Particle Physics". In: *PTEP* 2020.8 (2020), p. 083C01. DOI: `10.1093/ptep/ptaa104`.